Development and Optimization of heat pipe based Compound Parabolic Collector

By

Bala Abdullahi

B.Eng. (Mechanical Engineering), M.Eng. (Energy Engineering)

Thesis submitted in partial fulfilment for the requirements for the Degree of Doctor of Philosophy

School Of Mechanical Engineering

University Of Birmingham

Edgbaston, B15 2TT

June, 2015

Abstract

Compound Parabolic Concentrator (CPC) has advantages of possessing properties of flat plate and concentrating systems, high optical efficiency and wide applications. The performance of CPC solar collector is generally affected by the radiation available, its design and orientation. This thesis describes experimental and theoretical investigations of these parameters for different configurations of static symmetric CPCs with 2-5X concentration ratios for Kano, Nigeria.

A solar radiation model was developed to utilise global radiation measurements for characterizing solar radiation in terms of the clearness index, daylight hours, beam and diffuse radiation for regions in the northern hemisphere like Kano. Also, another model was developed to predict the optimum tilt angles for Kano using Engineering Equation Solver and the output of the solar radiation model. Results showed that tilting the collector to the monthly optimum angle gives the maximum radiation obtainable in each month with highest increase of 28.6 and 24.8% in December and January respectively. For seasonal tilt; the best angles were 27.05^{o} (October to March) and 0^{o} (April to September) while for fixed collector, tilting at 12.05^{o} (latitude) provides the highest performance.

Solar radiation analysis showed that Kano has significant diffuse radiation with up to 47% in some months; therefore CPC collectors offer high potential in harnessing solar energy. Using advanced ray tracing technique, detailed investigations of the effects of acceptance angle, receiver radius, truncation, collector length and orientation were carried out on the CPC performance. Results showed that compound parabolic collector can achieve daily average optical efficiencies of 76.5% and 64.4% for acceptance angles of 60^{o} and 40^{o} respectively. With truncation of 70%, daily average optical efficiency of 86.2% and 75.4% were achieved respectively and best truncation levels for different CPC configurations

were determined. Also novel idea of using double and elliptical receivers in single concentrator was studied and results showed respectively 15% and 17% improvement in optical efficiency compared to single circular receiver.

Thermosyphon heat pipes offer effective heat transfer mechanism to exploit the solar radiation. The flow and heat transfer in a thermosyphon heat pipe receiver was investigated experimentally and by Computational Fluid Dynamic (CFD) in Ansys Fluent where the effects of heat input, water flow rate and inclination angle on the thermal resistance and temperature distributions were studied. Results showed that the overall thermal resistance decreases with the increase in heat input while the performance of the pipe increases until it reached its limit and the pipe's average effectiveness was found to be 90%. Also the performance of the thermosyphon heat pipe increases with inclination angle especially at low heat inputs.

Using an in house solar simulator developed in this work, optical and thermal performance of the developed CPC fitted with heat pipe (HPCPC) was experimentally investigated at various radiation levels, inclination angles and CPC reflectivity. Results showed that the HPCPC can function well with thermosyphon inclination angle up to 40^{o} where it gives maximum efficiency at 10^{o} of 76% and for angles between 20 – 30^{o} of 72% and at 45^{o} it has 66% which is higher than that at zero degrees angle (60%). Increasing the CPC reflectivity from 60% to 80% gave an increase in the heat transfer rate up to 27%.

Solar energy can be used to generate cooling using heat powered sorption technologies. Therefore, the outcome of this work shows the potential of using this developed system in Kano environment for cooling applications where 10 arrays of 10 HPCPCs with acceptance angle of 30^{o} can produce 11kW of heat suitable for cooling load of 5kW at a Coefficient of Performance of around 0.5.

Acknowledgement

All praises are due to Allah (who taught man that which he knew not) for his guidance, blessing and assistance to me to the completion of this thesis. May His Mercy and blessing be upon our noble Prophet (SAWA) and his households (AS).

My sincere gratitude goes to my supervisor **Dr R. K. Al-dadah** for her patience, guidance and support throughout this work. I am deeply indebted to her for invaluable ideas, support, encouragement and revising my work.

I am grateful to **Dr S. Mahmoud** for his invaluable suggestions and novel ideas, support and revision of my work. I would like to thank Mr Simon Rowan for constructing my experimental rigs and solving any technical issue. My gratitude to all my teachers and entire staff of Mechanical Engineering who helped me in the course of this study such as R. Hood (for manufacturing my HPCPC), Dr Haider and Aydin for helping me in reflectivity and spectral measurements.

My sincere appreciations go to my parents; **Abdullah Hassan** and **late Lubabatu Abdullahi** (May Allah have mercy on her) for their upbringing, love and supports that enable me to reach this status. I cannot say enough words to my wife **Amina Sani Bala** and my children, sisters, brothers, nieces, nephews; Rabila, Asma'u, Ali, Fatima, Hassan, Muhammad, Hussain (to mentioned few) for their patient and prayers during my study.

I am grateful to all my elders/friends back home like **Mukhtar A.**, **Halilu A. Gwarzo**, **A. Rabiu**, A. Yusuf, and Muhd. Isa etc., to my friends in Birmingham; Dr Ahmed Elsayed, Kiyarash, Abdulmaged, Abdalqader, Adel, Abdurrahman, Aminu, Akilu, Auwal and Atiku, etc. Kind regards to my friends at HW University and University of Exeter; Dr Nazmi (for reflectivity measurements), Dr Ali I., Dr Hasan and Dr Nabin. Finally, I acknowledge the financial supports from KUST, Wudil and TETFUNDS, Abuja- Nigeria.

Publications

A. Journal

1. B. Abdullahi, R.K. Al-dadah, S. Mahmoud, **Optical performance of double receiver Compound Parabolic Concentrator**, Energy Procedia 61 (2014): 2625 – 2628
2. B. Abdullahi, R.K. Al-dadah, S. Mahmoud , R. Hood, **Optical and Thermal performance of double receiver Compound Parabolic Concentrator**, Applied Energy Journal (Accepted subject to minor revision).
3. B. Abdullahi, R.K. Al-dadah, S. Mahmoud, **Optimum Collector tilt angle and truncation level of heat pipe based Compound Parabolic Collector for Kano, Nigeria,** Energy Journal (Under review).
4. B. Abdullahi, A. El-Sayed, R.K. Al-Dadah, S. Mahmoud, A. Mahrous, **Experimental and Numerical Investigation of Thermosyphon Heat Pipe Performance at various inclination angles,** Applied Energy Journal (Under review).
5. B. Abdullahi, R.K. Al-dadah, S. Mahmoud, H. Butt **Optical and thermal performance of heat pipe based Compound Parabolic Collector**, Solar Energy Journal (Under preparation).

B. Conference Papers

1. B. Abdullahi, R.K. Al-dadah, S. Mahmoud, **Effect of Acceptance angle on the design and performance of a heat pipe based Compound Parabolic Collector at Kano, Nigeria,** International Conference on Renewable Energies and Power Quality (ICREPQ'13) Bilbao (Spain), 2013.
2. B. Abdullahi, R.K. Al-dadah, S. Mahmoud, K. Rahbar, A. O. Algareu, **Effect of slope angle and the truncation level on heat pipe based compound parabolic collector for Kano, Nigeria,** International Conference on Applied Energy ICAE, Pretoria, South Africa 2013.
3. A. O. Algareu, S. Mahmoud, R.K. Al-Dadah, B. Abdullahi, A. Aldihani, **Effects of geometry on the optical efficiency of small scale solar concentrator,** International Conference on Applied Energy ICAE, Pretoria, South Africa 2013.
4. B. Abdullahi, R.K. Al-dadah and S. Mahmoud, **Optimization of optical performance of heat pipe based Compound Parabolic Collector (HPCPC) for Kano, Nigeria using ray tracing technique,** Second Mechanical Engineering Symposium, University of Birmingham, UK, 2013.
5. B. Abdullahi, R.K. Al-dadah, S. Mahmoud, **Optical performance of double receiver Compound Parabolic Concentrator,** International Conference on Applied Energy ICAE, Taipei, Taiwan, 2014.

Dedication

To my beloved father and all my loved ones,

To my wife and children,

And to the soul of my beloved mother

Table of Contents

List of Figures

List of Tables

Nomenclature

A	Area (m^2), Aperture (m), maximum efficiency (%)
A_i	Anisotropic index
AM	Air mass
C	Concentration ratio
C_p	Specific heat capacity (J/ (kg.K)
COP	Coefficient of Performance
CPC	Compound Parabolic Concentrator/collector
CS	Continuous Simulator
D	Diameter (m)
ΔT	Temperature difference
E	Apparent energy (J/kg)
F'	Collector efficiency factor
F''	Collector Flow Factor
F_R	Heat removal Factor
F_v	Interface – induced volumetric force (N/m^3)
F	Intercept/correction Factor
f	Frequency (H)
FR	Fill ratio
FS	Flashed simulator
g	Gravitational force (m/s^2), gap dimension (m)
G	Incident ray on the aperture (W/m^2)
h	Convective heat transfer coefficient ($W/(m^2.K)$

h	Truncated height of HPCPC
H	Full height of HPCPC
HPCPC***x***R***y***	Heat pipe based Compound Parabolic Collector with ***x*** acceptance angle and ***y*** receiver radius
H_o	Daily average extraterrestrial global radiation (J/m^2)
H	Daily average global radiation (J/m^2)
$\overline{H}_o$	Monthly average extraterrestrial global radiation (J/m^2.day)
$\overline{H}$	Monthly average global radiation (J/m^2.day)
I	Electric current (A)
I, i	Hourly (instantaneous) radiation, incident rays
K_{eff}	Effective thermal conductivity
K_T	Clearness index
L	Length (m)
l	Secondary phase
$\dot{m}$	Mass flow rate (kg/s)
n_i	Av. number of reflections
N	Daylight hours (h)
$\overline{N}$	Maximum duration of active sunshine
P	Pressure (Pa)
P	Gap loss
P_{in}	Power input (W)
PS	Pulsed simulator
E	Energy (W)

q	Irradiance (W/m^2)
$\overline{R}$	Relative humidity (%)
R_{th}	Thermal resistance (K/W)
r_D	Diffuse radiation correlation factor
r_h	Hemispherical radiation correlation factor
S	Absorbed radiation (W/m^2)
S_{sc}	Solar constant (W/m^2)
S_E	Energy source term (kg/sm^3)
S_m	Mass source term (kg/sm^3)
$S_{\bar{x}}$	Standard deviation of mean
t	Hour of the day (solar time) (h)
T	Temperature (K)
U_L	Overall heat loss coefficient
U	Uncertainty (%)
V	Electric voltage (V),
V	Volume (m^3)
$\vec{v}$	Velocity vector (m/s)
$\bar{v}$	Magnitude of the velocity vector (m/s)

Greek symbols

α	Absorptivity, volume fraction
α_S	Altitude
β	Collector tilt angle (^{o})
δ	Solar declination (^{o})
Δ	Partial derivatives
ε	Emissivity
ϕ	Latitude (^{o})
γ	Surface azimuth angle (^{o}), intercept factor
γ_S	Solar azimuth angle (^{o})
η	Efficiency/Performance of thermosyphon (%)
μ	Dynamic viscosity (PaS)
π	Pi
θ	Acceptance angle (^{o})
θ_a	Half acceptance angle (^{o})
θ_{aT}	Half acceptance angle of truncated HPCPC (^{o})
θ_Z	Zenith angle (^{o})
$\overline{\theta}$	Ratio of maximum and minimum temperature
ρ	Density (kg/m^3), reflectivity
σ	Stefan – Boltzmann constant
σ_{lv}	Surface tension between liquid and vapour
τ	Transmittance

ω	Solar hour angle (^{o})
ω_S	Sunset hour angle (^{o})
ω'_S	Sun hour angle for tilt surface

Subscripts

a	Aperture (m), average, ambient
ann	Annulus
B	Beam
c	Condenser
cfd	Computational fluid dynamics
conv	Convective
cw	Cooling water
D	Diffuse
e	Evaporator, envelope
eff	Effective
expt	Experiment
G	Ground
h	Hemispherical radiation
i	Inlet
inc	Inclined
ins	Instability
l , *liq*	Liquid
m	Mass
max	Maximum
min	Minimum
N, n	Normal direction
nu	Non-uniformity

o	Optical, outer, outside
R	Reflector
r	Receiver
ref	Reflection
sat	Saturation
T	Tilt
tot	Total
u	Useful
v	Vapour
w	Water, width

CHAPTER ONE

1. Introduction

The activities of man at domestic and industrial levels depend largely on the availability and accessibility of energy and this makes energy to be part of our lives. The main objective of energy systems of any form is to provide energy services that are essential to man ranging from domestic such as cooking, cooling and heating to the industrial processes like construction and manufacturing. Energy can be obtained from many sources such as coal, fossil fuel, oil and gas, renewable sources such as solar, tides, hydro, etc.

Energy is needed by all societies for sustainability and development and for many decade most of the energies consumed by man are from burning fossil fuel. By 2040, the global energy demand is expected to grow by 37% and its supply mix to be divided into almost four equal parts between oil, gas, coal and low carbon sources [1]. The dependence of the world on the fossil fuel leads to the high cost of the fuel (known as energy crisis), air pollution, climatic change and environmental disasters. Climatic change leads to water shortage, damage caused by floods, storms, spread of disease and extinction of some species, etc. Another problem with the dependence on the conventional energy source is that the fossil fuels are exhaustible and with current consumption trend, it can finish within few decades [2].

It has been established that the climatic change associated with the global warming is due to the release of greenhouse gases (such as carbondioxide, methane, etc.) through burning of fossil fuel from cars, industries, electrical production, etc. [3] In order to reduce the impact of these environmental and social problems, the world community is taking some initiatives to

curtail the process. The Intergovernmental Panel on Climate Change (IPCC) aims to limit the global average temperature increase to 2^0C from the current rise of 3.6^{o}C [1] and meets to review this problem which led to agreements like Kyoto protocol. Thorough these agreement, the use of some compounds like CFCs were banned and this creates great challenges for some industries like refrigeration and air-conditioning [3]. Furthermore, the world is still faced with the problem of achieving sustainable energy system which is characterized as a system that meets a balance between the three main drivers namely supply security, economic and environment.

While the developed countries are facing the negative impact of excessive usage of conventional fossil fuel, others are facing inadequate, inefficient and unreliable energy supply. About 620 million people do not have access to electricity in sub –Saharan Africa, and the supply is inadequate, costly and unreliable for the few who have it [1]. It is estimated that about 730 million people [1] in this region depend on biomass for cooking which contributes to the air pollution that results in large number of death every year.

The use of clean energy like solar, wind, etc. have been identified as one of the solutions to the energy issues in the world [4, 5]. Recently the most used renewable energies are solar and wind due to their availability in most parts of the world, pollution free and installation flexibility. Solar energy is most promising, non-exhaustible and most exploitable in most part of the world compared to all other renewable sources due to its advantage of having less or no maintenance requirement, high potential applications in remote areas and enormous quantity of solar energy received per hour. The amount of energy released by sun in one hour (430 x 10^{20}J) was found to be more than the world consumption in 2001 (410 x 10^{20}J) [6, 7]. But the main issue with the development of solar energy technologies is the low efficiency which leads to high initial cost [7, 8].

1.1. Energy issues in Nigeria

Nigeria is one of the countries in the sub-Sahara situated between latitude of 4^{o} and 14^{o}N and longitude between 2^{o} and 15^{o} E. Like other countries in this region, it faces serious energy issues ranging from unbalanced energy consumption patterns, inefficient and unreliable supply to inadequate technological capacity and inefficient utilization. With the total area of $9.23X10^{11}m^{2}$ and the population of over 120 million according to 2006 National census which is estimated now to be between 175.4 and 178.5 million, the electricity supply of Nigeria is mostly below 4,000 MW [9]. According to the World Bank data, 2015, the annual average electric power consumption between 2010 and 2014 was 149 kWh per person (capita) in Nigeria against 5,472, 13,246 and 4,606 kWh for UK, US and South Africa respectively [10].

Since the introduction of electricity in 1896 in Lagos, its development is slow while the demand is increasing with the increase in the population [11]. Only 10% of the rural households and 30% of the whole population have access to electricity [12] and this forces most households (70 - 80%) [2] to rely on wood for their energy requirements. The excessive use of wood, reliance on personal power generators, coupled with about 79% of electricity generated from fossil fuel, Nigeria is put as 46^{th} country in the world in carbondioxide emission with 73.69 metric tons released in 2011 [12]. Also the use of wood leads to continuous cutting down of trees that causes desert encroachment, erosion and loss of soil fertility.

The insufficient energy supply in Nigeria leads to the regular power outage and make the power non-accessible to many people especially in the rural areas. This situation lead to either total collapse of some industries or relocation to other countries because of the high running cost due to the cost of fuel to run their private power generators. Kano (the most populous

state), is an agricultural area seriously affected by these energy issues leading to the poor production outputs and crop wastage.

Several attempts were taken to resolve the energy crisis in the country through the Energy Commission of Nigeria (ECN), which is mandated to produce and implement energy planning and policy coordination. One of the attempts is a project titled "Sustainable Energy Development for Sub-Saharan Africa, in collaboration with International Atomic Energy Agency (IAEA). Two IAEA's energy models; Model for the Analysis of Energy Demand (MAED) and Model for the Energy Supply Strategy Alternative and General Environmental impact (MESSAGE) were developed to predict energy supply and demand [9]. Four economic situations were considered in developing these models as shown in Figure 1.1. Based on such models, the energy projection and demand from 2005 to 2030 [9] were predicted as shown in Figures 1.1 and 1.2. Comparing the current supply (of less than 4,000 MW) with the projected demand of 2015, there is deficit of 24,360, 26,210, 27,240 and 60,200 MW for the reference, high growth, optimistic I and optimistic II scenarios respectively. It further shows that the current supply did not even meet the 2005 projection of 5,746 MW and this shows the seriousness of the situation.

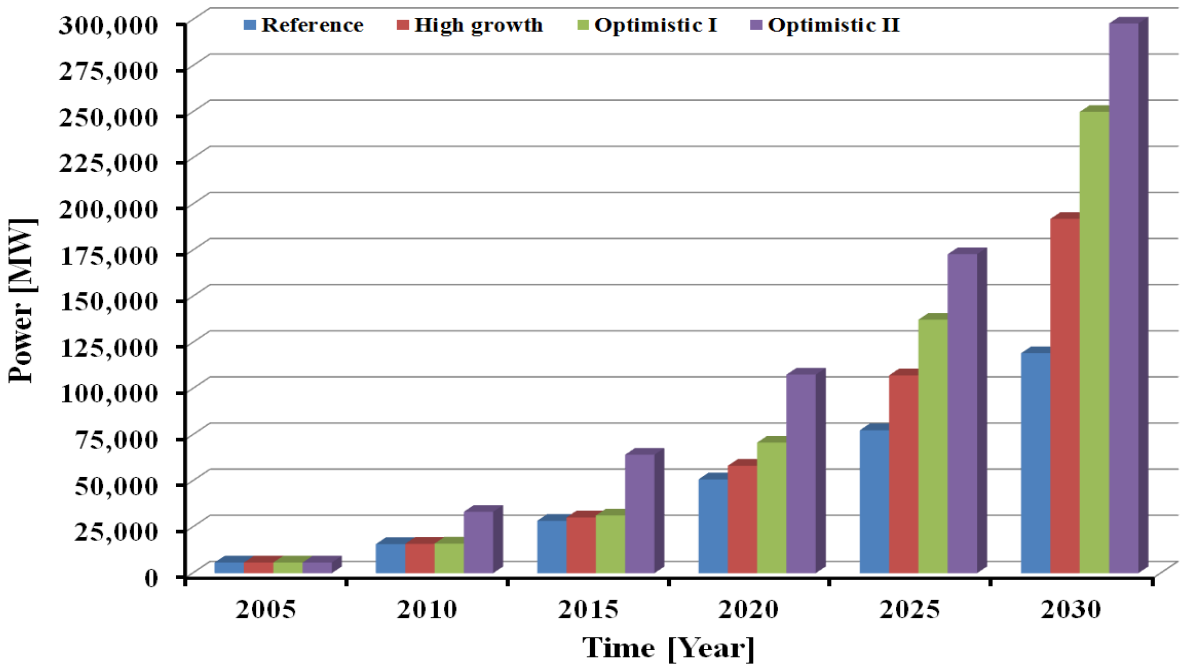

Figure 1.1 Electricity demand projection in Nigeria [9, 11]

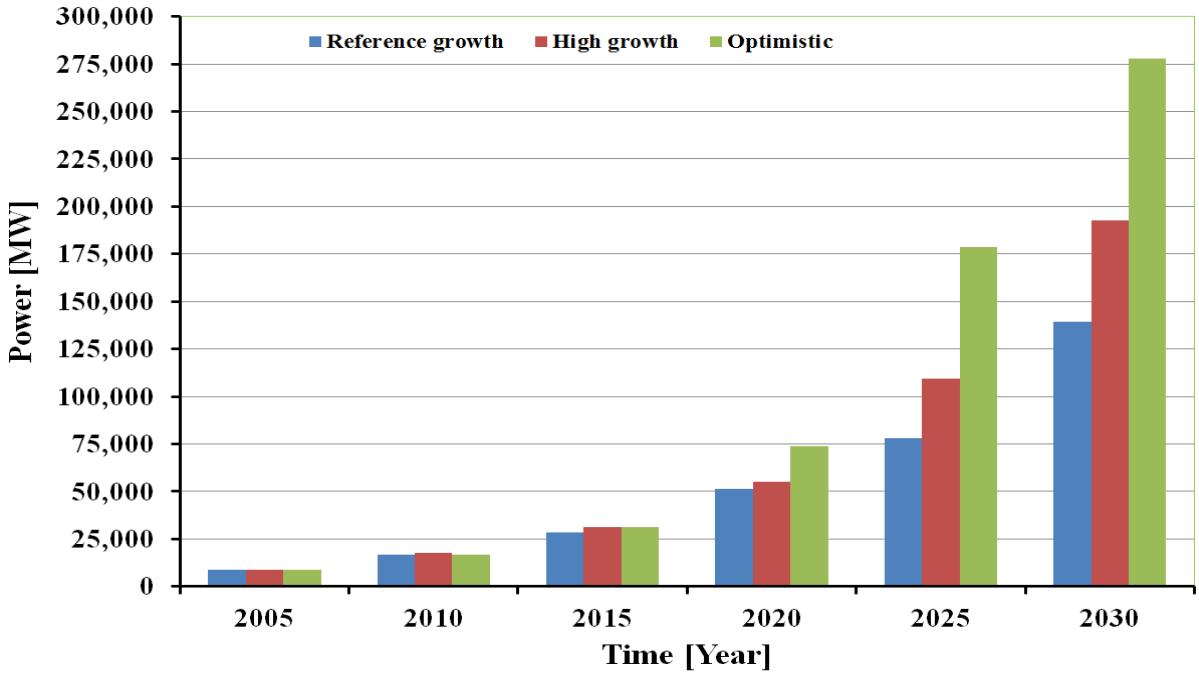

Figure 1.2 Projection of Electricity Supply in Nigeria [9]

Another attempt is the use of solar energy to complement the conventional sources since solar energy has great potential in Nigeria especially in the far north. Nigeria lies within sunshine belt receiving global solar radiation that varies from about 3.5 kWh/(m^2.day) in the south to more than 7 kWh/(m^2.day) in the far north, and average sunshine hours per day of 4 to 9 hours which also increases from south to north [9]. Studies have shown that if solar systems are installed to cover 1% of the country's area, solar electricity of 1.850 x 10^6 GWh can be generated per year which is more than 100 times the country's consumption [8]. Solar Photovoltaic (PV) is the fastest growing renewable energy in Nigeria with more than 15MW generation dispersed in different places as standalone [8]. The millennium development goals (MDG) program also contributed to the spread of PV installation especially in the rural areas. Few solar thermal systems such as solar cookers, solar dryers, and solar incubators were developed, but most of them for research purposes. But there is no PV or solar thermal that is connected to the national grid despite the solar potential in the country. Several factors contributed to the slow development of the solar systems in Nigeria including high cost, zero incentive, low awareness, inadequate research, etc. and this makes it impossible for the solar technology to meet the required input to the energy mix of 14% (2008), 23% (2015) and 36% (2030) as projected by presidential committee on power development [9].

1.2. Solar energy potentials in Kano state – Nigeria

Kano state (12.05^{o}N, 8.52^{o}E) has high solar radiation reaching up to a maximum of 26.78 MJ/m^2.day (7.44 kWh/m^2.day) and has the advantages of high average daylight and sunshine hours. But due to the problems stated in 1.1, the penetration of solar technology is still at infant stage despite the energy challenges facing the agricultural state. But still the issue of low efficiency and high cost of the systems remains the major problem to the development of

solar technology in such area and this can further be attributed to the lack of sufficient researches especially in the concentrating solar systems. Currently there is no report of a single concentrating either PV or thermal systems in operation in such area. Also less attention is given to the thermal systems which can be a good option in many applications like solar cooling and reservations.

Solar thermal concentrating systems can be used with relatively higher efficiency than PV in some applications like air-conditioning systems and in rural areas for preserving agricultural goods (refrigeration). Furthermore, utilizing solar thermal will greatly reduce the security and damage risks compared to the PV systems which tend to be stolen. It also has wider applications, relatively cheaper for some applications than PV and will be suitable to the climate of Kano.

Concentrators in the form of mirror surfaces are used in many thermal applications where higher temperature is required that cannot be delivered by flat plate collectors. They focus more energy either on a line (cylindrical) or on a point (spherical) by using optical devices which can be reflectors or refractors, continuous or segmented. Using concentrators also reduce the total area and the total cost of the system by reducing the number of the receivers required through the use of less expensive reflectors. Therefore, researches on the potentials of using concentrating solar systems in Kano in particular and Nigeria in general will help in boosting the solar applications in the region, which is one of the aims of this study.

1.3. Compound Parabolic Concentrator solar collector (CPC)

CPC is among the various types of concentrating solar thermal collectors. It has several advantages over other thermal collectors because it possesses the properties of both flat plate

and concentrating collector and has high optical and quantum efficiencies [13] . Generally the performance of CPC and any other solar collector depends on the radiation available, collector design and orientation. Many researches were conducted on these three factors with the aim of improving the efficiency of the CPC by considering one of these factors for a particular collector. Some are based on modification to the receiver [14, 15], modification to the reflector [16] and using special working fluid [17]. But it will be useful to consider a combination of these factors for a low concentration CPC (2 -5X), with the aim of improving their efficiencies, as described in this thesis.

1.4. Aims and Objectives

It has been shown that significant research has been reported on the performance enhancement of CPC, but most of them worked on either a particular parameter and/or a selected CPC geometry. Research on detailed investigation of low concentration CPCs which considers all the major parameters that affect its performance is lacking. However, it is necessary to optimize the family of low concentration CPC (2 - 5X) by considering all the three factors; radiation available, design and orientation for performance enhancement. Furthermore, very limited work was reported on the use of thermosyphon heat pipes in CPCs despite their effectiveness in heat transfer, most of the collectors utilize wicked heat pipes. Also as shown in section 1.2, despite the energy challenges in Kano- Nigeria and the solar potential, there is no single concentrating solar thermal or PV collector in operation either at domestic or industrial level. Few reports on solar applications in Nigeria are based on PV which apart from other issues, it is faced with the challenge of security and frequent damage.

The aim of this work is to investigate the means of enhancing the performance of a low concentrating heat pipe based compound parabolic solar collector by considering the three

major factors that affects the performance of collector; ***solar radiation available, design and the collector orientation*** which will lead to design and performance predictions of CPC solar collector for driving refrigeration and air conditioning systems for northwest states in Nigeria. It also aimed at fully modelling the solar radiation of Kano, Nigeria to serve as electronic platform for researches on solar energy in the region and similar locations. The collector is to operate under many climate conditions but with more emphasis to the climate of Kano, Nigeria and other northwest states in the country.

The present research is on the development and optimization of the performance of heat pipe based CPC to enhance its performance for different applications with the following objectives:

- Develop two computer models for modelling solar radiation and optimization of the collections for regions in the northern hemisphere, which leads to the selection of appropriate collector design and collector's optimum tilt angle
- Design, construct and evaluate the performance of an in-house continuous solar simulator for optical and thermal experiments of this work
- Conduct experiments to validate the optical simulation and test the thermal performance of the developed CPC
- Design optimization through:
  - Detailed characterization of the CPC (2 – 5 X) by developing a computer model to investigate the effects of key geometric parameters of the CPC
  - Conduct detailed optical simulations on CPC with acceptance angle of 20, 30, 40, 50 and 60^{o} with various receiver radii of 6, 11, 12.5, 22.5 and 25mm using the validated model to study the effect of parameters like acceptance angle, receiver radius, gap and truncation effects, receiver length and size, etc.

- To investigate a novel idea of using double receiver in a single CPC

❖ Conduct both experimental and numerical study (CFD) on the performance of thermosyphon heat pipe of 22mm diameter and 400mm length to study the effects of heat input, cooling water flow rate, inclination, etc. on its operation

❖ Study (by simulation and experiment) the effects of collector orientation and thermosyphon inclination in CPC with the aim of achieving maximum possible operation hours and best thermosyphon operation

❖ Design and predict the performance of CPC for powering solar refrigeration and air-conditioning systems for Kano- Nigeria by using the results of the studies carried out.

1.5. Thesis Outline

Generally, this thesis has two broad dimensions; details study on enhancing and optimizing the performance of CPC and exploring the potentials of solar radiation in Kano for various applications. The thesis starts with detailed literature review on the CPC including the design approach, performance enhancement technique and applications. Research on collector orientation, tilt angle as well as experimental and numerical studies of thermosyphon heat pipe were also reviewed. Detailed analysis was carried out for the development of solar radiation model using meteorological data of Birmingham, UK and Kano, Nigeria. Simulation and experimental studies conducted on the solar simulator and different configurations of CPC were then presented.

Detailed design of a test rig to investigate the performance of thermosyphon heat pipe was mentioned followed by numerical study (CFD) using Ansys Fluent. Advanced ray tracing technique was extensively utilised on the study of the effects of key parameters on the

performance of CPC. Optical and thermal experiments were conducted on the developed CPC under different operating conditions.

Lastly, the outcome of the analysis were used in predicting the optical and thermal performance of array of CPCs for proposed applications in solar refrigeration and air-conditioning systems for Kano, Nigeria. Hence, the contents of this thesis can be summarized as follows:

Chapter One contains brief discussion on the world's energy issues, Nigeria's energy issues and the solar potentials in Kano, Nigeria. It also contains brief introduction on the CPC and the general thesis overview.

Chapter Two reviews the research reported on the CPC, solar radiation models, experimental and numerical studies on the performance of thermosyphon.

Chapter Three presents detailed procedure for developing a solar radiation model using either global radiation or clearance index as input to predict beam and diffuse on horizontal and tilt surfaces, daylight hour, hourly radiation, etc. based on isotropic and anisotropic approaches. It also presents the optimization code developed in Engineering Equation Solver (EES) for parametric study and determining the optimum tilt angle for Kano.

Chapter Four describes the design, optical simulation, experimental evaluation and development of an in-house solar simulator for testing the CPC in this thesis.

Chapter Five presents the development of a computer program in excels spreadsheet for CPC geometric characterization. Two geometries of CPC with reflectivity of 60 and 80% were manufactured and used for optical testing and validating the simulations. It also presented detailed optical studies carried out using advanced ray tracing for the study of the effects of some parameters on the performance of CPC family considered in this work.

Chapter Six describes the test rig developed for studying the performance of thermosyphon heat pipe under different conditions, and the CFD model developed for studying its heat and mass transfer characteristics using Ansys Fluent together with user defined function (UDF). The validated model was used to study the effects of other parameters like pipe thickness.

Chapter Seven presents thermal performance of the CPC developed in chapter 5 fitted with a thermosyphon receiver. It also presented the performance prediction of array of the heat pipe based CPC under climatic condition of Kano for proposed applications in solar cooling systems like solar refrigeration and solar air-conditioning systems.

Chapter Eight describes the conclusions drawn from the studies conducted and proposed future works.

CHAPTER TWO

2. Literature review

2.1. Introduction

This chapter presents a detailed literature review of research work regarding compound parabolic solar collector (CPC). It begins with brief study of the basic principles and theoretical analysis of different types of CPCs. It also includes reviews on the solar radiation modelling, experimental and numerical studies on the thermal performance of thermosyphon heat pipe used as receiver in some solar collectors.

2.1.1. Solar technology

Solar technology is broadly divided into two categories; thermal and photovoltaic. Solar photovoltaic involves conversion of the solar radiation directly into electricity by the use of solar cells, while solar thermal refers to the process of converting solar radiation into heat by the use of a device called solar thermal collector. The outputs from such systems can be utilized for various applications such as cooking, direct heating, drying, waste treatment, desalination, water heating, etc. It can also be used for power generation, powering other systems like refrigeration, air conditioning, etc. Water heating is one of the earliest applications of solar energy where between 1920 and 1950, thousands of solar heating systems were installed in California and Florida [18].

Solar thermal collectors are heat exchangers that transform solar radiation into heat and transport the heat to a working fluid (which can be water, air, oil, etc.) flowing through it.

They consist of different components such as glazing, receiver, receiver plate and concentrator (in case of concentrating systems).

There are different types of collectors which are categorized based on their motion, design or operating temperatures as shown in Table 2.1. Also collectors can be categorized into concentrating and non- concentrating collectors. In terms of motion, solar collectors can be categorized as stationary, one and two axes tracking collectors. A non-concentrating collector has the equal area for capturing and absorption of solar energy while the concentrating counterpart consists of reflectors that focus incoming radiation onto the receiver. The non - concentrating collectors which includes flat plate and evacuated tube collectors are designed for applications requiring moderate temperature outputs up to 100^{o} C [19]. Flat plate collectors (FPC) have advantages of being inexpensive to manufacture and able to collect both beam and diffuse components of solar radiation. However, these collectors are greatly influenced by the weather conditions such as cloud, wind, moisture, etc. which lead to reduced performance and they cannot be utilized for high temperature applications [19]. For temperature requirement above 100^{o}C, concentrating systems are used. The concentration is achieved by including a reflecting surface between the radiation source (sun) and the receiving area.

2.2. Concentrating collectors

Concentrating collectors can be stationary or moving to track the sun on either one or two-axis as shown in Table 2.1. Sun tracking collectors have the following advantages [20]:

i. High efficiency due to low thermal losses as a results of small heat loss area
ii. High fluid temperature

iii. Possibility of having a good match between the intended application and the outlet temperature

iv. Smaller absorbing area and low cost of treating smaller area to maximise its absorption.

Table 2.1 Types of Solar collectors and their temperature ranges [20]

Configuration	Collector	Receiver	Concentration ratio	Temperature range (^{o}C)
Stationary	Flat-plate collector	Flat	1	30 – 80
	Evacuated tube collector	Flat	1	50 – 200
	Compound parabolic collector	Tubular	1- 5	60 – 240
One - axis tracking			5 - 15	60 – 300
	Linear Fresnel reflector	Tubular	10 – 40	60 – 250
	Cylindrical trough collector	Tubular	15 - 50	60 – 300
	Parabolic trough collector	Tubular	10 - 85	60 – 400
Two-axis tracking	Parabolic dish reflector	Point	600–2000	100 – 1500
	Heliostat field collector	Point	300–1500	150 – 2000

However, the tracking collectors have the following disadvantages [20]:

i. The system will be complex due to the tracking mechanism

ii. They capture little diffuse component of the radiation depending on their concentration ratio due to their small acceptance angles

iii. Usually periodic cleaning of the reflector is required

Concentrating collectors can be divided into imaging and non-imaging. When the sun's image is formed on the receiver it is called imaging collector which includes parabolic dish, parabolic trough, central receiver (or heliostat field collector) and linear Fresnel reflector (LFR) while the compound parabolic concentrator belongs to the non-imaging category (Figure 2.1). Non-imaging concentrators can meet low and medium concentration without tracking the sun and this makes them more affordable than imaging counterpart. Figure 2.1 shows different types of concentrating collectors.

2.2.1. Compound Parabolic Collector (CPC)

Compound parabolic concentrator is a non- imaging concentrator that concentrates all solar radiations falling on it within a wide range of angle. Its first design was individually proposed in 1966 by Hinterberger and Winston in USA, Baranov and Melnikov in USSR and Ploke in Germany, but its potential was realised in 1974 [19]. With non-imaging system, concentration of up to 4 can be achieved with totally stationary collector and this reduces material, labour and hence the total cost of the system coupled with increase in the efficiency.

Compound parabolic collector consists mainly of two halves of parabolas and a receiver situated along their line of symmetry. It is characterized by the acceptance angle, collector height and aperture width as shown in Figure 2.2.

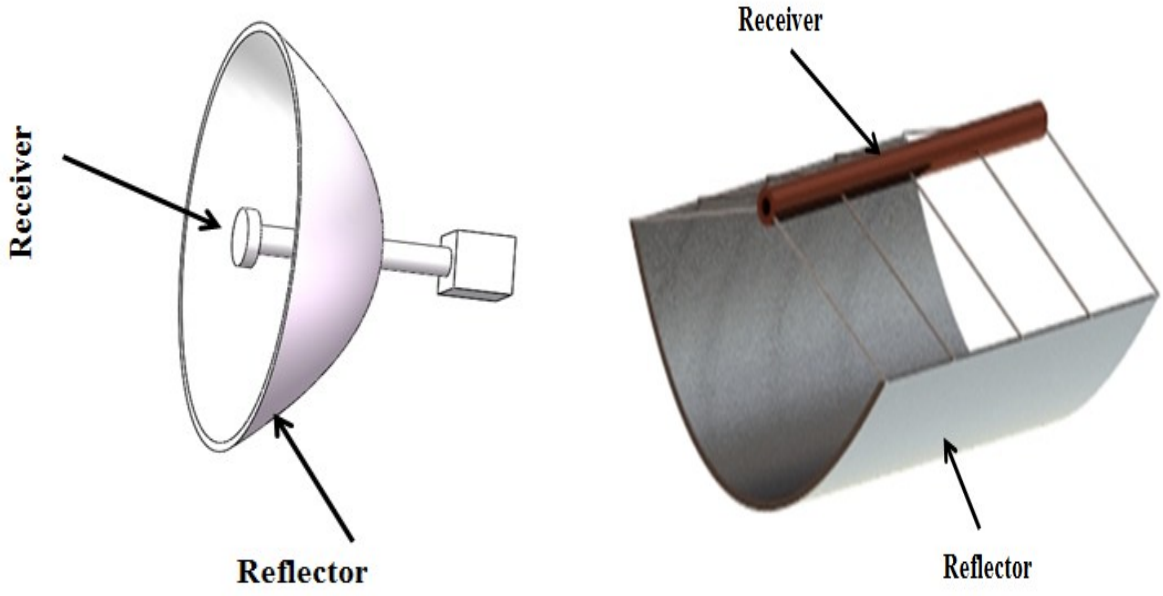

(a) Parabolic dish collector **(b) Parabolic trough**

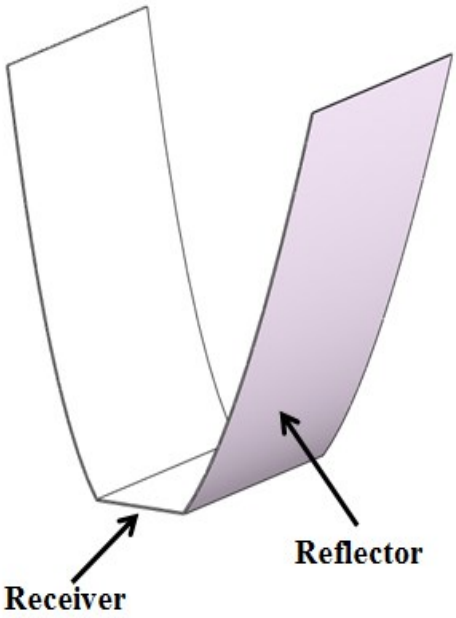

(c) Compound Parabolic Collector

Figure 2.1 Types of concentrating collectors [21]

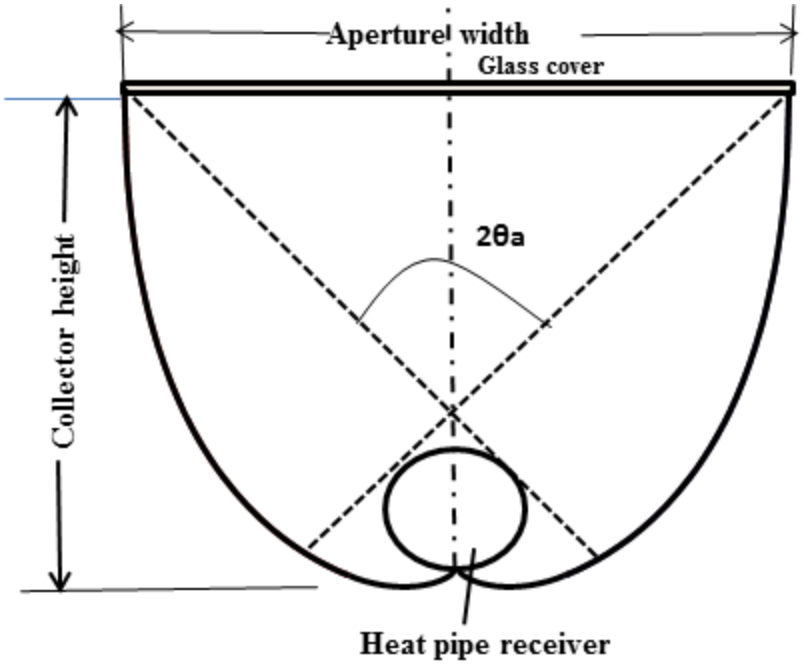

Figure 2.2 Compound Parabolic Collector

The followings are some terms used in describing concentrating collectors like CPC:

1) Acceptance angle, $2\theta_a$ – It is the maximum angle within which all radiations are concentrated on the receiver. The gain and loss of rays by the CPC depends on the incident angle of the rays compared with the acceptance half – angle (θ_a) of the CPC.
2) Aperture area, A_a – the opening plane of the CPC through which solar radiations enter the collector.
3) Receiver area, A_r – This is the area where solar radiation is received and the energy is transferred to the working fluid.
4) Geometric Concentration ratio – It is the ratio of the aperture area to the receiver area given as [18]:

$$C = A_a / A_r \tag{2.1}$$

5) Intercept factor (F) – It is the part of the energy intercepted by a receiver of a certain size.

The concentrator can be symmetric or asymmetric which can be fitted with the receiver of different configurations such as flat, tubular, wedge, bifacial, etc. as shown in Figure 2.3. Using tubular receiver in the CPC has the following advantages [22];

- Minimising the back losses and
- Low fabrication cost due to the availability of circular tubes

CPCs offer some unique advantages in addition to those enjoyed by other concentrating collectors as follows:

1. They concentrate solar radiation and they possess the properties of the flat plate collectors by being static and still collecting diffuse radiation
2. Minimizing errors of both the reflective surface and receiver tube alignment, which lead to the achievement of a low cost photoreactor [13]
3. They have high optical efficiency due to their ability to receive almost all the available radiation within their acceptance angle
4. High quantum efficiency because they do not receive a high flow of photons [13] .
5. Simple to construct and low cost, due to its ability to perform efficiently in static position
6. Wide range of applications such as in refrigeration, air-conditioning, electricity generation, etc.
7. CPC has high possible concentration allowable by thermodynamic limit for a certain acceptance angle.

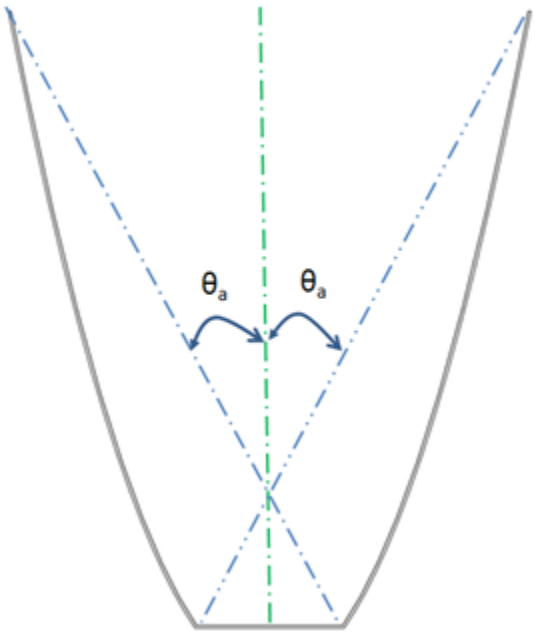

(a) Flat receiver

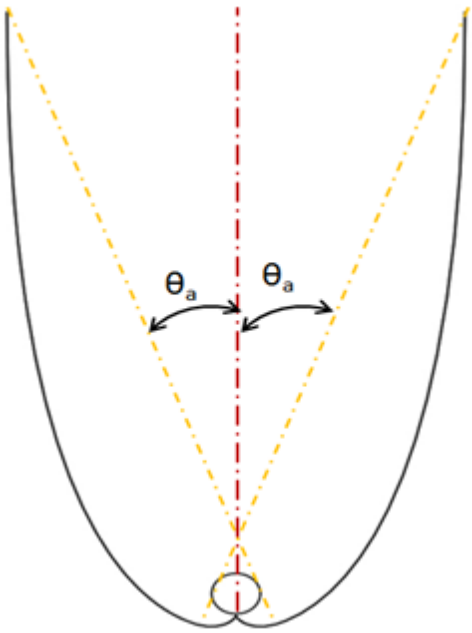

(b) Tubular receiver

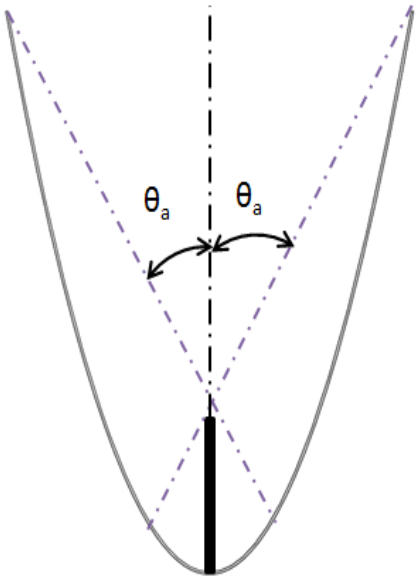

(b) Fin receiver

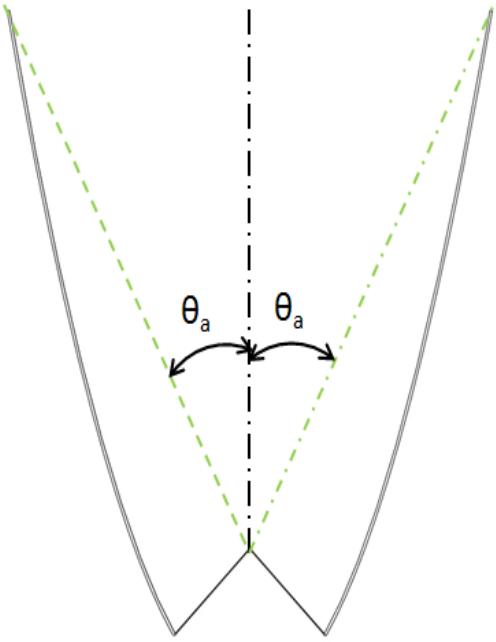

(d) Wedge receiver

Figure 2.3 Different receiver configurations of CPC [18]

2.2.2. Performance of CPC

The overall performance of CPC is evaluated in terms of its optical and thermal efficiencies which largely depend on many parameters like geometry, material properties, acceptance angle, solar radiation available, collector orientation, etc. Several attempts were made to define the optical efficiency of CPC which largely depends on the material properties of the reflector, glass cover (if present) and the receiver.

Rabl, 1985 suggested a simple equation for optical efficiency of CPC [18]:

$$\eta_o = \rho\tau\alpha\gamma \tag{2.2}$$

Where γ stands for intercept which depends on the accuracy of the construction and the geometric size, and its value varies between 0.9 and 1.0 [23]. While ρ, τ and α are respectively the reflectance of the concentrator, transmittance of the cover and the absorptivity of the receiver.

A modified correlation was proposed by El-Assay *et al.*, 1987 [24] to include the effects of the gap between the reflector and the receiver, g and the concentration ratio as:

$$\eta_o = A\frac{\left(C_{DB}/C + 1\right) \subseteq A}{C_{DB} + 1} \tag{2.3}$$

Where C is the concentration ratio and C_{DB} is the ratio of the diffuse to the beam radiation.

A is the maximum efficiency given as:

$$A = \tau\ \tau_e\alpha\ \rho\ PF \tag{2.4}$$

Where

τ = transmissivity of the glass cover

τ_e = transmissivity of the receiver envelope

ρ = reflectivity of the mirror

α = absorptivity of the receiver

P = gap loss = $1 - g/2\pi r_{ro}$ (r_{ro} = the receiver outer radius)

F = intercept factor given by [24];

$$F = \left[1 - (1 - \alpha_r)0.16\left(A_{ro}/A_{eo}\right)\right]^{-1} \tag{2.5}$$

Where A_{ro} and A_{eo} are the outer areas of the receiver and the envelope respectively. However, the optical efficiency of CPC can be determined using ray tracing technique (to be discussed in chapter five).

The instantaneous efficiency, η of a CPC is defined as the ratio of useful energy gain to the incident radiation on the aperture of the collector, G_a [20]:

$$\eta = Q_u / A_a G_a \tag{2.6}$$

Where the useful energy gain Q_u is given by [19]:

$$Q_u = F_R\left[SA_a - A_r U_L\left(T_i - T_a\right)\right] \tag{2.7}$$

The heat removal factor, F_R is given by [19]:

$$F_R = \frac{\dot{m} C_P}{A_a U_L}\left[1 - \exp\left(-\frac{A_a U_L F'}{\dot{m} C_P}\right)\right] \tag{2.8}$$

Collector flow factor, F'' is defined as [19]:

$$F'' = \frac{F_R}{F'} = \frac{\dot{m}C_P}{A_a U_L F'}\left[1 - \exp\left(-\frac{A_a U_L F'}{\dot{m}C_P}\right)\right] \tag{2.9}$$

The overall heat loss coefficient, U_L is obtained as [19]:

$$U_L = \frac{Q_{loss}}{A_r(T_r - T_a)} \tag{2.10}$$

The absorbed radiation, S can be estimated from the radiation and the optical characteristics of the concentrator and the receiver as [19, 20]:

$$S = A\left(G_{B,CPC}\tau_{C,B}\tau_{CPC,B}\alpha_B + G_{D,CPC}\tau_{C,D}\tau_{CPC,D}\alpha_D + G_{G,CPC}\tau_{C,G}\tau_{CPC,G}\alpha_G\right) \tag{2.11}$$

The first term in the equation 2.11 is the beam input to S, the second and third terms are the contributions of the diffuse and the ground- reflection respectively.

The terms $G_{B,CPC}$, $G_{D,CPC}$ and $G_{G,CPC}$ are determined by equations 2.12 – 2.15

1. $G_{B,CPC} = G_{BN}Cos\theta$ (F = 1) if $(\beta - \theta_a) \subseteq \tan^{-1}[\tan(\phi)\cos(Z)] \subseteq (\beta + \theta_C)$ (2.12)

$= FG_{BN}Cos\theta_a$ if the above condition is not satisfied (2.13)

2. $$G_{D,CPC} = \begin{cases} \frac{G_D}{C} \; if(\beta - \theta_a) \subset 90^o \\ \frac{G_D}{2}\left(\frac{1}{C} + Cos(\beta)\right) if(\beta + \theta_a) \supset 90^o \end{cases} \tag{2.14}$$

3. $$G_{G,CPC} = \begin{cases} 0 if(\beta + \theta_C) \subset 90^0 \\ \frac{G}{2}\left(\frac{1}{C} - Cos(\beta)\right) if(\beta + \theta_C) \supset 90^0 \end{cases} \tag{2.15}$$

Angle β is the collector aperture inclination angle with respect to the horizontal, so the ground reflection is only effective if the collector receiver sees the ground, i.e. $\beta + \theta_a \supset 90^o$.

The insolation, G_{CPC}, of a collector with concentration ratio C can be estimated as [20]:

$$G_{CPC} = G_B + \frac{1}{C} G_D \tag{2.16}$$

$$G_{CPC} = G_B - \left(1 - 1/C\right) G_D \tag{2.17}$$

Also it is convenient to express the absorbed radiation, S in terms of the G_{CPC} as [20]:

$$S = G_{CPC} \tau \ \tau_{CPC} \alpha \ = \left[G_a - \left(1 - \frac{1}{C}\right) G_D \right] \tau \ \tau_{CPC} \alpha \tag{2.18}$$

Or as [20]:

$$S = G_a \tau \ \tau_{CPC} \alpha \ \gamma \tag{2.19}$$

Where

$$\gamma = 1 - \left(1 - 1/C\right) G_D / G_t \tag{2.20}$$

Where τ_{cpc} is the effective transmissivity of the CPC and ɣ is the correction factor for diffuse component which accounts for the loss of diffuse radiation outside the acceptance angle of the CPC with the concentration ratio C.

2.2.3. Literature review on CPC

The literature on the CPC reviewed in this section is divided into three major parts; design approach, performance enhancement technique and applications.

2.2.3.1. Design approach

There are several designs of CPC in terms of the concentrator shape, receiver type, truncation and tracking. The two parabolas that concentrate radiation onto the receiver may be symmetric or asymmetric. The asymmetric CPC has high design and operational flexibility compared to the symmetric one but it has high average number of reflection and high requirement of the mirror precision [25].

The CPC can be fitted with different types of absorbers which can be of fin type (like bifacial, wedge, flat, etc.) or tubular as shown in Figure 2.3. Depending on the intended application, water storage tank, photoreactor and PV cell can also serve as receivers.

Performance investigation and heat transfer characterization of different designs of CPC were analysed based on either optical or thermal or both in order to select between different designs or improve their performances. A 1.9X CPC of 0.2 m^2 area was built and its thermal performance was determined using therminol 66 as the working fluid [17]. A pipe of 28mm outer diameter with selective surface and surrounded by a transparent Pyrex with vacuum of 10^{-4}Pa was used as the receiver. Under irradiance of 825 W/m^2 and ambient of 32^oC, the stagnation and operating temperature was found as 319^oC and 150^oC respectively with optical efficiency of 52%. Tatara *et al.*, 1991 investigated the performance of four different arrays of 1.24X- CPC connected in series with and without an acrylic cover plate. Some recommendations on the ways of reducing heat losses were made such as coating the absorber with selective surface, enveloping it with glass or acrylic and improving the side thermal insulation. The experimental results were used to generate efficiency against ratio of temperature difference and the global radiation ($\Delta t/G$) relationship and in each case a linear graph is obtained with intercept yielding optical efficiencies that range from 54.5% to 69.5% [26]. Fraidenraich *et al.*, 1999 studied the optical and thermal performance of non- evacuated

CPC solar collector with a cylindrical absorber with the heat loss coefficient expressed as function of temperature using a mathematical model. Heat loss linear coefficient was shown to be dependent on the solar insolation while the second degree coefficient was independent of the insolation. A linear plot of efficiency against the ratio of the square of the difference between the fluid inlet temperature and ambient to the insolation was proposed as a new way of presenting the thermal performance of CPC collector as shown in Figure 2.4.

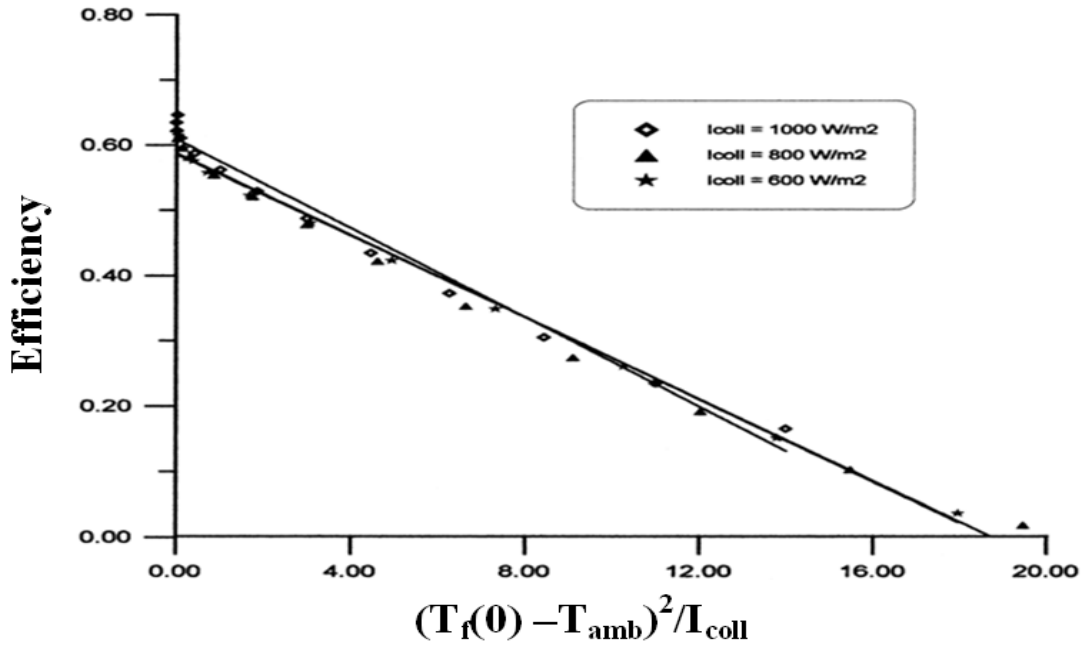

Figure 2.4 Efficiency of CPC solar collector [27]

The results of an indoor test of thermomax evacuated tube heat pipe collector and single sided coated evacuated tube heat pipe absorber integrated in CPC were presented by Nkwetta *et al.,* 2012 [28]. The performance of the two collectors was evaluated and compared based on the outlet temperature and daily energy collection at five different transverse angles ($0 - 40^{o}$). The concentrating collector outperformed the evacuated tube heat pipe collector with the mean outlet and inlet fluid temperature difference and energy collection efficiency by 305^{o}C and 25.42% respectively. Although the result is as expected but for a good comparison the

aperture areas of the two collectors should have been the same and wider range of incident angles ought to be tested.

Several attempts were made to define the optical and thermal behaviour of CPC both numerically and experimentally. Initially, the performance of CPC was presented based on the flat plate receivers. The work of Rabl 1976 is among the early research on the evaluation of the performance of CPC solar collectors [29]. Radiative, convective and conductive heat transfer mechanisms within the collector were presented in the form of correlations similar to those for flat plate absorber. It is assumed that the temperature distribution at the aperture and absorber is uniform, while that of the reflector may be higher near the absorber compared to the region near the aperture. Also the absorptivity is assumed to be independent of the acceptance angle. For calculation of optical efficiency, a simple technique for calculating the average number of reflections for radiation passing through CPC was presented.

The overall radiative heat transfer from the receiver to the reflector and from reflector to the aperture were given respectively as [29]:

$$q_{rR} = \varepsilon_{eff.rR} A_r \sigma \left(T_r^{\,4} - T_R^{\,4} \right) \tag{2.21}$$

$$q_{Ra} = \varepsilon_{eff-Ra} A_r \sigma \left(T^4{}_R - T^4{}_a \right) \tag{2.22}$$

Where σ is the Stefan-Boltzman constant given by 5.67 x 10^{-12} watts/(cm^2.K) and ε_{eff}, are the effective emissivity of the CPC within and outside the acceptance angle, while r, R and a stands for receiver, reflector and aperture respectively.

The well-known flat plate film coefficient was used for determining the convective heat transfer from the receiver to air in the CPC cavity and then from the air to the aperture neglecting all interactions with the reflector as given by [29]:

$$q_{conv-ra} = \frac{T_r - T_a}{1/(A_a U_a) + 1/(A_r U_r)} \tag{2.23}$$

Although this work lacks experimental data, it gives estimate of the optical and thermal performance at different acceptance angles and the effects of truncation and material properties. It also presents numerical examples for predicting the performance of the CPC solar collector. The shortcomings of this approach include restricting it to the receiver with envelope and the assumption of uniform temperature on the reflector and the cover. In practice, the temperature distributions on these surfaces are non-uniform as the reflector will be hotter near the receiver compared to the part near the cover.

Other works on the heat transfer characterization of CPC includes those of Abdel – *Khalil et al.,* 1978 at vertical position [30] and at various inclination angles Abdel-khalil and Li, 1978 [31]. However, the correlations proposed in their models involved many complicated terms such as logarithm and power terms.

Similarly, various approaches were reported for characterizing the heat transfer processes in CPC with tubular receiver. Hsieh, 1981 studied the thermal performance of the CPC by developing a mathematical model based on the assumptions that direct radiations within the acceptance angle are all reflected on the receiver and its direction depends on the geometry. The convective heat transfer coefficient is presented as [32]:

$$h = 1.32\left(\Delta T \big/ 2r_e\right)^{0.25} \tag{2.24}$$

Where ΔT (^{o}C) is the temperature difference between the envelope and the collector cover and r_e is the radius of the envelope. Equation 2.24 is linearized for easy use in the iteration process as [33]:

$$h = 3.25 + 0.0085\frac{T_e - T_a}{4r_e} \tag{2.25}$$

Apart from the numerical studies of the heat transfer performance of CPC, various experimental studies were reported for flat plate receivers [34-36] and tubular receivers [37-

39] etc. The general limitation of their experimental approaches is the direct heating of the receiver alone by either electric heater or heating wire which is different from the real heating by sun or solar simulator where both the concentrator and the receiver are heated. Also most of their approaches considered only the vertical orientation of the system neglecting the inclination and some neglected the contribution of the collector material properties.

A more generalized numerical and experimental approach of determining the convective heat transfer in CPC which includes both optical and thermal behaviour is presented by [40]. Ray tracing technique was employed for the optical analysis and the models considered both beam and diffuse radiation components absorbed by the glass cover, reflector and the absorber. Also the approach is more general compared to the previous as it considered receiver with and without envelop and with or without selective surfaces. The overall heat flow from the absorber to the enclosing surface was taken as [40]:

$$Q = A_r \varepsilon \sigma \left(T_r^{\,4} - T_e^{\,4} \right) \tag{2.26}$$

While the net fluxes (in or out), q_{net}, is given by [40]:

$$q_{net} = q_{tot} - h\left(T - T_e\right) \tag{2.27}$$

Experiments were conducted on different geometries of the collectors with half acceptance angles of 30, 45 and 60^o; each was integrated with 700mm long copper tube of 15mm external diameter. The tests were conducted under a solar simulator. The numerical results were validated with the results obtained using Mach – Zehnder interferogram (experimental) for different acceptance angles and inclined to different tilt angles and found to be in good agreement [40]. The performance of the CPC in this model was evaluated using different inputs such as insolation and material properties of the absorber, reflector and the glass cover. Despite the generalized nature of this model, it is shown to be valid when the system has large length – to cross sectional area, where the end effect is minimal.

The geometric and optical properties of fully illuminated inverted V shape receiver CPC with vertex angle greater or equal to the acceptance half angle, was analytically studied by [41]. Calculations of the energy obtained and cost benefit analysis were also carried out for different collector orientations and various vertex and acceptance angles. According to the authors, the results obtained has led to the best collector design for the Recife – PE city, Brazil with the concentration ratio between 1.0 and 1.2 for East – West orientation, acceptance and absorber vertex angles of 30^o and 65^o respectively. The performance of asymmetric and symmetric CPC with inverted and tubular receivers respectively was compared in terms of radiation conversion efficiency by[42]. The results showed that the asymmetric inverted absorber CPC (IACPC) outperformed the symmetric tubular CPC (TACPC) with 10 – 15% increase in the conversion efficiency. But the reason for the superior performance of the IACPC may be difficult to be attributed to the concentrators' shape; as they have different absorber shapes and also the TACPC has glass envelope around the receiver which will also affect its performance.

A yearly distribution insolation model for a 2D CPC was developed by Suzuki and Kobayashi, 1995 to determine its optimum acceptance angle [43]. The model considered the beam radiation distribution to be within $\pm 23.5^o$ of declination and diffuse of having uniform irradiance. The authors considered acceptance angle of 26^o as optimum regardless of the diffuse radiation intensity. Although the authors concluded that their optimized CPC could be used in most locations in the world, it should be understood that their model considered only radiation on the receiver. Also the optimum acceptance angle may differ in places far away from the equator (which is target in their model) due to factors like variation of the daylight hours and the beam tilt factors. Also other studies proposed wider angles , such as 30^o [44], 45^o [45] and 56^o [46].

Tchinda *et al.,* 1998 [47] presented analysis of heat transfer in axial direction of the absorber of the CPC collector. An explicit expression of the temperature of the heat transfer fluid as a function of the space co-ordinate in the flow direction and the time dependant solar intensity was proposed. Also the effects of parameters like inlet fluid temperature and mass flow rate, on dynamic behaviour of the collector were studied. The theoretical model proposed in the work was validated by comparing its results with experimental results obtained by Reed, 1979, Rabl *et al.*, 1980 and Scherz, 1977. Also Tchinda, 2008 [48] presented a mathematical model for computing the thermal performance of an air heater with a truncated CPC having a flat – one sided absorber. A computer code was used for predicting the performance of the heater using energy conservation equations. Influence of some parameters such as air mass flow rate, collector length and wind speed on the performance of the heater were discussed and reasonable agreement was reported between the numerical and the experimental results.

The choice between the collectors to be static or continuously tracking the sun is another important aspect of the CPC design. While using tracking system enhances the performance of a CPC, it adds cost and complexity of the whole system. Kim *et al.,* 2008 compared the thermal performance of stationary and sun tracking evacuated CPCs tested under real sun[49]. The thermal performance of the two collectors was evaluated both experimentally and numerically and the results showed an improvement of 14.94% in favour of tracking system. However, the authors did not take into consideration the cost and the complexity of the tracking compared to the stationary as whether the increase in the efficiency compensates for the added complexity and cost.

Grass *et al.*, 2004 presents a comparative study between evacuated stationary CPC with parabolic trough and evacuated tube collector with integrated tracking reflector. Possible losses were discussed and ways to reduce them were also analysed. The collectors were

characterized using ray tracing technique and experimental data and the results showed that the two non- tracking evacuated tube collectors show good efficiencies but with different characteristics for the acceptance of irradiation. Although the tracking collector performed satisfactory but still the tracking mechanism will add complication and more cost to the system. But the author claimed that the additional cost due to the tracking system will not exceed 50 €/m^2 aperture area [50]. The effects of using two - axis sun tracking system on the thermal performance of CPC was experimentally investigated by [51]. Two similar CPCs of 650mm parabolic trough were fabricated and tested; one fixed and inclined at 33^o while the other was attached with an automatic tracking system. Results from this study showed that the tracking increases the average water temperature in the collector and the energy collection at various flow rates. An improvement of up to 75% was reported in the energy collection when the flow rate is between 25 and 45 kg/hr. Although cost analysis of the two cases is absent in the paper, the use of tracking system should be recommended when the improvement obtained offset the additional costs.

Tripanagnostopoulos *et al.,* 1999 presented design, construction and performance testing of two water solar heaters utilising stationary asymmetric CPC, with two different receiver configurations; one with tubular receiver (CPC I) and another one with flat absorbers (CPC II). The two designs were found to perform efficiently as shown in Figure 2.5 where their efficiencies were plotted against the ratio of the temperature difference between water inlet and outlet temperature to the irradiance falling on the collectors. Results reported showed that the CPC I and II are suitable for direct water heating and with output water temperature always above 40^oC [52]. But the superiority of CPC II cannot be attributed to the geometry since the authors used different surface finish for the two receivers.

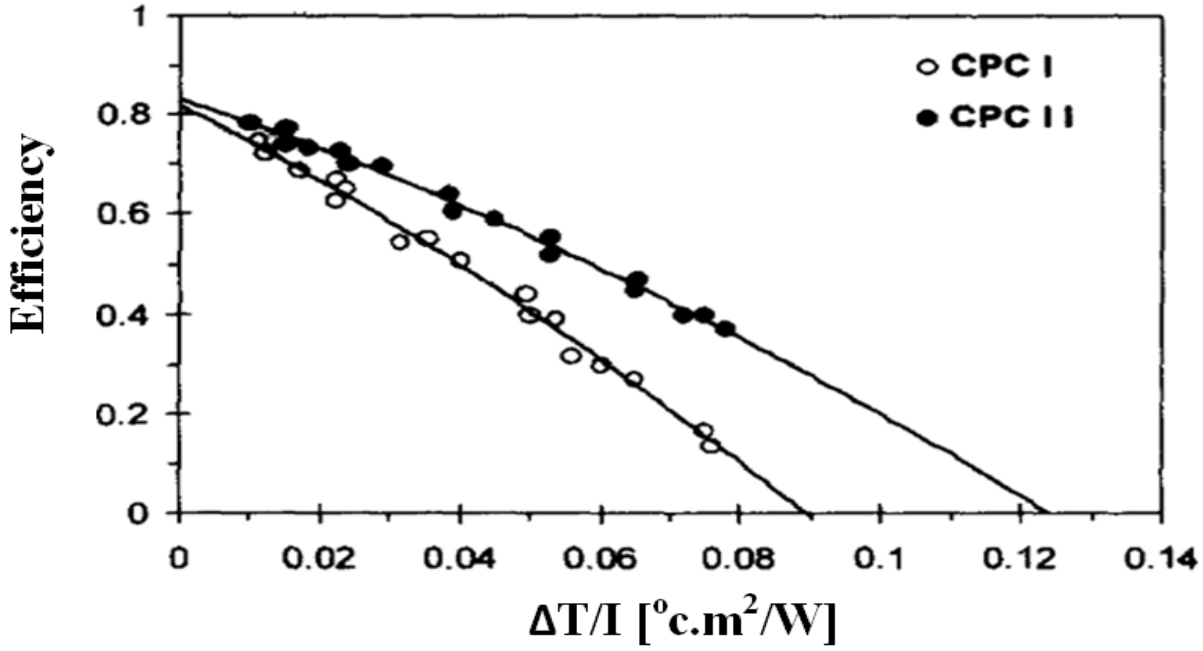

Figure 2.5 Efficeincy of the two designs of the asymmetric CPCs [52]

Tripanagnostopoulos *et.al*, 2000 tested two prototypes of stationary asymmetric truncated CPC with non-evacuated flat bifacial absorbers; one with one mirror absorber unit (CPC-S model) and the other with three smaller mirror-absorber (CPC-T model) integrated in one device [53]. Both faces of the absorbers were coated with different combination of coating materials to achieve best combination. Model CPC-S was tested with several combinations of absorber coating on both front and inverted surfaces such as selective/black, selective/selective, black/black, etc. and found that selective/selective flat bifacial absorber performed better than the others. The best combination was used for the tests of model CPC-T prototype and results compared to those of CPC-S. The reported results showed that maximum efficiency of 71% and stagnation temperature of 180^{o}C could be achieved. Also CPC-T model was found to be more efficient and suitable for practical use compared to CPC-S model.

Prototypes of six different collectors for stand-alone, roof and wall mounting were built and tested outdoor by Adsten *et al.,* 2005 [54]. Results showed that the roof mounted gave the highest annual energy output of 925 MJ/m^2 and the stand-alone with Teflon produced 781 MJ/m^2. Based on these results obtained, the authors claimed that this concentrator design concept can be used as concentrators for PV modules.

Farouk *et al.,* 1997 fabricated and tested an asymmetric CPC (full and truncated) at different absorber gap heights for the purpose of determining the optimum performance and the absorber configuration. The tests were conducted indoor using a solar simulator and under two conditions; with stagnant water in the receiver and without water. Maximum stagnation temperatures of 109 and 157^{o}C were obtained with and without water in the absorber respectively. Also the results showed that the overall performance is better for the higher gap configuration than for the lower at the testing range of inlet temperature of 20 -70^{o}C [16].

Two different types of solar collectors; a standard glazed flat plate and evacuated tube collector with external compound parabolic concentrator reflector were compared by measuring their efficiencies in steady-state and partial dynamic conditions using EN12975-2 test standards by Zambolin *et al*., 2010 [55]. The work included experimental measurements of the two collectors, generation of efficiency curves, daily efficiencies and characterizing the collectors based on the daily efficiencies obtained. Theoretical and experimental results showed that the evacuated tube with CPC reflector produced higher daily efficiency than the flat plate collector. But the two collectors have different gross and aperture areas reported as (5.16 and 3.9) and (4.76 and 3.5) for flat plate and evacuated tube respectively.

A maximum reflector collector (referred to MaReCo) with optical axes of 20^o and 65^o for upper and lower parabolas respectively was tested for the radiation distribution on the absorber [56]. Results showed an increase of 6 – 8% in efficiency when the thickness of the

absorber fin is increased from 0.5 to 1mm with average annual efficiency of 88% and 92% respectively.

2.2.3.2. Performance enhancement technique

The performance of the CPC can be enhanced in many ways mainly to maximize the radiation collection and minimize heat losses. Various techniques were employed by different authors to maximize the radiation collection and to have an effective heat transfer medium. To achieve the targets, the knowledge of the possible sources of losses and properties of materials are of paramount importance. The parameters associated with this include using special tube as receiver like heat pipe, modifying the reflector or the receiver and proper selection of the working fluid and materials for the collector as well as other means to enhance its overall efficiency.

Modification to the absorber of the CPC is one of the approaches employed for improving the performance of the collector. The thermal performance of two CPCs having one of the absorber modified by introducing two cavities of 4.5mm aperture at 43^{o} was compared by Azhari *et al.,* 1996 [14]. The modification was made to increase the efficiency by reducing losses from the receiver surface. Efficiencies of 32 and 50% were achieved for the conventional and modified configurations respectively. Another similar work on the optimization of tubular absorber of CPC was carried out in 1994 by Khonkar *et al.,* 1994 who created some cavities in the circumferential area with relatively high solar intensity. Ray tracing technique utilizing AutoCAD package was used to locate such areas where the cavities were made. The authors proposed some guidelines on the location of the cavity, cavity size, and possible combination of cavity radius and aperture width. They also presented analysis of the generation of CPC and tubular absorber profile, behaviour of rays within the CPC and the phenomena of the rays inside the CPC for different incident angles [57]. But in such study,

the authors considered incidence angles only between 0 and 10^{o} which may not be sufficient to cover the issue of hot spots which is usually more pronounced when the sun is far away from the zenith. Although considerable improvement has been reported from this approach, but the process has to be performed with greater care so that the receiver should not be deformed and flow of the working fluid should not be affected.

It has been shown that the non-uniformity of solar radiation on the flat absorber surface during some period of operations can be used to improve the efficiency of the collector as reported by Tripanagnostopoulos *et al.,* 1996. Studies were made on the design of asymmetric and symmetric CPC with flat absorbers which were divided into four sections as channels for the fluid flow. The absorber was divided into segments and the working fluid is passed through the channels with high concentration of radiation while other channels were kept at stagnation temperature. It is shown that temperature range of 100 – 200^{o}C can be achieved with simple concentrating collector [15]. The advantage of introducing transparent baffle into a non-evacuated CPC cavity was reported by Eames and Norton, 1995 [58]. The optical and thermal performance of this collector was evaluated numerically and experimentally using 15mm diameter receiver and three different dimensions of the baffles placed at different locations and orientations. Results showed improvement in the reduction of heat losses depending on the baffle's position and the CPC inclination angle. However, this approach will cause optical losses due to the presence of such baffle in the cavity and the authors reported 5% optical loss cause by the baffle.

The CPCs fitted with tubular receiver usually need to have a gap between the receiver and the tip of the reflector to avoid thermal loss due to conduction but such gap causes rays losses. The reflectors are usually modified to reduce such losses. Oommen *et al* 2002 developed CPC with "V" shape groove at the bottom of the reflector to suppress rays losses due to the gap

between the receiver and the concentrator. The experimental results of the optical and thermal performance of the prototype were evaluated and showed that its instantaneous efficiency is high even at higher operating temperature. The experimental and theoretical optical efficiencies were found as 0.59 and 0.63 respectively which are comparable within allowable range [59]. A CPC design which incorporated a curved inverted- Vee absorber fin was presented by [34] who aimed at optical efficiency enhancement through eliminating optical losses due to gap and enhancing heat transfer removal factor. A fin (BDED'B') is superimposed on the receiver covering the whole area of the involute hence it make use of only upper part of the reflector as shown in Figure 2.6. The results reported showed 3% and 28% respectively reduction of gap loss and average number of reflection which led to increasing the optical efficiency by 2%. The improvement recorded from this work is very low especially when compare with the logistics attached to the modifications.

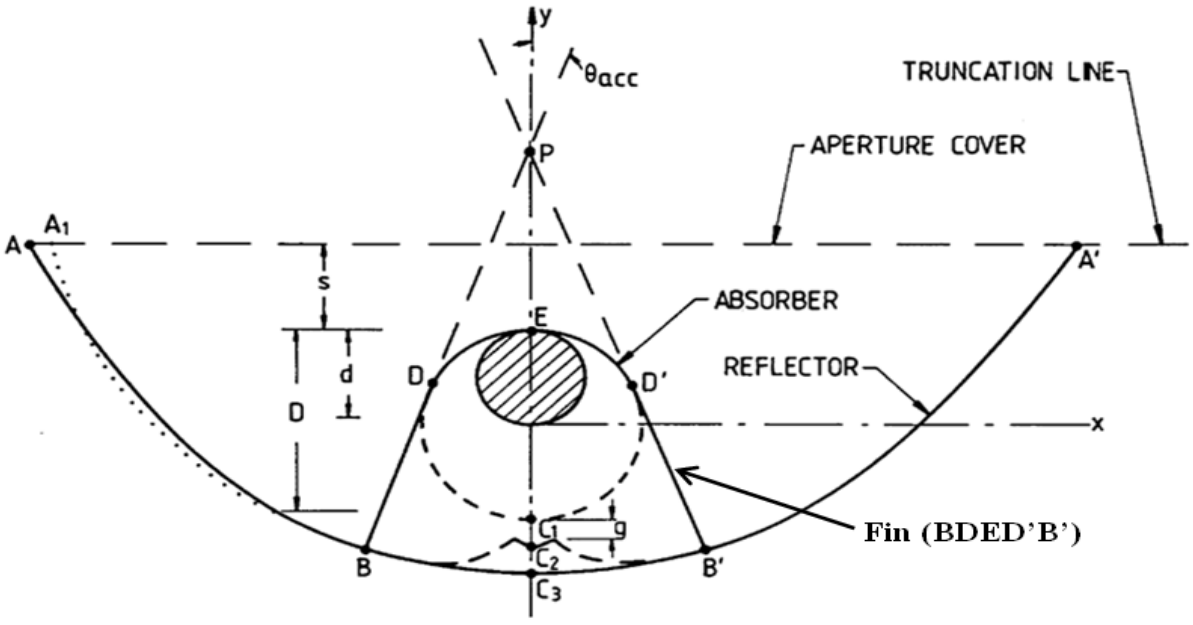

Figure 2.6 Schematic of curved inverted V- shape CPC [34]

A non-evacuated CPC with inverted V receiver was tested for its optical and thermal performance by Carvalho *et al*., 1995 [44]. Two different mechanisms for reducing heat losses were employed; applying Teflon film at the collector cover and the absorber as well as adding transparent insulator. The former yields improvement in heat loss reduction of 1.3 $W/^oCm^2$ while the later resulted in large reduction in optical efficiency and with only 1 $W/^oCm^2$ improvement in heat loss. Also the results reported showed optical efficiency of 74% and heat loss coefficient for E-W and N-S orientation of 4 and 4.3 respectively [44]. The optical performance of an inverted asymmetric CPC was simulated and optimised using a computer- based numerical ray tracing utilizing both beam and diffuse radiation [60]. This work studied the variation of the optical efficiency of the model with the parameters like gap height, mirror reflectivity, acceptance angle and the concentration ratio. Results showed that the optical efficiency increased with the increase in mirror reflectivity and acceptance angle while it decreased with the increase in the number of reflections and the increase in the height of the receiver gap.

Another approach employed to enhance the heat transfer in CPC is the use of heat pipe as the receiver. Heat pipes are used in solar systems to improve their performance usually by integrating them with evacuated tube tubular collector to achieve medium or high temperatures. Heat pipe is an effective heat transfer device that can deliver large amount of energy with small temperature difference by simultaneous evaporation and condensation. Due to its numerous advantages over other types of pipes in terms of high heat conduction, light weight, efficient heat transfer and design flexibility, it is used in many systems apart from solar.

A low concentration CPC with geometric concentration ratio of 2.92 and 1.95 for full and truncated reflector respectively was presented by Nkwetta *et al.,* 2012 [61]. The receiver is

tubular evacuated heat pipe of 15mm diameter enclosed in a white borosilicate glass tube. A 2D ray tracing technique was used in analysing the performance of such collector in terms of flux distribution, optical losses and efficiency at different incident angles. Results predicted 93.72% and 79.13% ray's acceptance and optical efficiency respectively between transverse angle of 0^o and 20^o. Since this work considered very small range of incident angles, it could have been good to explain if the intended collector will be adjusted periodically. Also since the authors used in house software, there is a need for validation either by experiment or by using more established software. Nkwetta and Smyth [62] presented the design, fabrication and testing of solar collector using heat pipe receiver of two different configurations; single sided (SSACPC) and double sided (DSACPC) coated receivers integrated into CPC with acceptance angle of 30^o and concentration ratios of 2 and 1.85 for full and truncated profiles respectively. Indoor testing was conducted using solar simulator at tilt angle of 60^o. The two designs were compared based on the collection efficiency, heat loss and energy collection rate. Results showed that the DSACPC outperformed the SSACPC in terms of the outlet temperature and thermal performance with average improvement of 42.4% in the fluid temperature increase.

A thermal analysis of an evacuated tube CPC air collector integrated with an open thermosyphon was reported by Liu *et al.,* [63]. The system consists of two solar air collectors in parallel using water – based copper (II) oxide nanofluid (system 1) and deionized water (system 2) as working fluids. Outdoor testing was conducted on the two systems and the results were compared based on the air outlet temperature and efficiency. Air outlet temperature above 170^oC at air mass flow rate of $7.6m^3/h$ was obtained from the collector using the nanofluid and with higher efficiency compared to that using water. Even though there is improvement when nanofluid is used but the challenge of determining the right

quantity and the cost of the nanoparticles to be used are issues which were not address in this paper and most of the related publications.

The thermal performance of evacuated heat pipe tube integrated into CPC was tested outdoor according to the ISO 9806 – 1 standard by Chamsa-ard *et al.*, 2014 [64], who also developed a numerical model to predict the energy production based on the atmospheric condition of Phitsanulok, Thailand. Their results showed 78%, 3.55 and 0.06 W/(m^{2o}C) thermal efficiency and heat loss coefficients a_1 and a_2 respectively and 286.16 kWh energy produced monthly. Apart from CPC collectors integrated with heat pipe, flat plate collectors are also integrated with heat pipes for various applications like powering vapour absorption system [65], solar water heaters and heat exchangers [66-70].

2.2.3.3. Collector orientation

Solar collectors are tilted to angle from horizontal to maximize the radiation collection. Usually, collectors in the northern hemisphere are orientated to face south inclined at certain angle to the horizontal and vice versa. This angle is usually referred as tilt or inclination angle, but throughout this thesis, it will be called tilt angle, β. The tilt is made to enable both flat plate and concentrating solar collector to collect most of the solar radiation received by the location. Various studies were conducted to find out the gain that can be achieved by tilting a surface in terms of radiation falling on it compared to horizontal position. These studies lead to the determination and recommendations of best tilt angle or sometimes the optimum for certain locations on the earth. This is dealt with fully in chapter three in this thesis.

Skeiker, 2009 presented a mathematical model for determining the optimum tilt angle at some selected locations in Syria and chosen latitudes. Results showed that for Damascus zone the

annual optimum tilt angle is 30.56^{o} for collector facing south. Also monthly adjustment yield improvement of 26% in solar radiation compared to horizontal alignment [71]. The authors recommended installation of the collector at the optimum seasonal angle and the angle to be adjusted at the end of each season and this gives 10% increase in the optical efficiency of the collector compared to annual tilt. Transient system simulation (TRNSYS) program was used by Shariah *et al*., 2002 to find the optimum tilt angle for thermosyphon solar water heater in Jordan. Using annual solar fraction as an indicator, the results showed the optimum tilt angle as latitude plus (0 to 10^{o}) and latitude plus (0 to 20^{o}) for northern and southern regions respectively [72]. The work is localised to Jordan but there is no mention of the latitude of the location in Jordan, which is vital as a guide to the readers.

Numerical model for predicting the optimum tilt angle of a stationary collector to be used in some parts of China was presented by Tang and Tong, 2004. Correlations in literature were used to determine the monthly, seasonal and annual radiation collections at various collector tilt angles. Results showed optimum angles for different locations as 0^{o} (horizontal) and latitude minus 3^{o} for south and north eastern regions respectively [73]. Gunerhan and Hepbasli, 2007 recommended tilt angle equal to the latitude of the location, ϕ, for maximum yearly radiation collection and ϕ -15^{o} and ϕ +15^{o} for maximum collection in summer and winter respectively [74]. Similar recommendations were given for Helwan in Egypt by Elminir *et al.,* [75]. Whereas other works reported their findings based on the consideration of a particular location, Jan and Frank, 1982 made general recommendations for the best tilt based on application where tilt equals to the latitude for solar water heating and equals to latitude plus 15^{o} for solar heating systems to favour winter sun [23].

Generally, there is no single angle that gives increase in the radiation collection throughout the year and also the best tilt angle varies from one region to another. This is due to the factors that affect the values of the best/optimum tilt angle:

1. the actual climatic condition of the region
2. the intended application of the system and
3. the intended maximization period i.e. year, season or month

Since it has been established that tilting a surface to a correct angle increases the radiation falling on it, attempts were made to study such effects on the CPC collector. A predictive thermal heat transfer model was developed by Farouk *et al*., 1995 in which the effect of the variation of inclination angle of CPCs on their performance was investigated. They utilised a line-axis symmetric compound parabolic collector (1.5X) in developing the theoretical model in which the variation of convective, radioactive, conductive and overall heat transfer coefficients and system efficiency under different conditions of angular inclinations, concentration ratio and solar insolation were studied. The results showed a 10% and 5% variation in the convective heat transfer and the CPC efficiency respectively due to the inclination angle [76]. Another numerical model was proposed for the study of the effects of collector tilt angle on the performance of CPC by Norton *et al.,* 1994 [77]. The study involved the determination of the collector efficiency and heat transfer coefficient at different tilt angles, concentration ratio and solar intensity. Results showed that as the concentration ratio increased, the thermal performance increased while the overall heat transfer coefficient decreased. Also the variation of the collector efficiency with the tilt angle was found to be less than 5% at 1.5X and this variation decreased as the concentration reached 3X.

Eames and Norton, 1993 presented a model predicting the optical and thermal behaviour of CPC with different acceptance and tilt angles [37]. A parametric study was conducted and the effects of the acceptance and tilt angles on the convective heat transfer was analysed. The themofluid behaviour of CPC with different tilt angles were predicted for full and truncated geometries. Formula for convective heat transfer was proposed which includes the effects of acceptance and inclination angles for full and truncated profiles.

2.2.3.4. Literature on experimental characterization of thermosyphon

Thermosyphon heat pipe's operation depends on the gravity effects to return the condensate to the evaporator for the cycle to continue. There are considerable works reported in the literature on the effects of inclining of thermosyphon heat pipe to angle relative to the horizontal, fill ratio, aspect ratio, working fluids, internal surface finish, etc. Some applications of solar systems require that the pipe be inclined to an angle from the horizontal to increase the exposure of the system to the maximum solar radiation [78-81].

Experiments were carried out on 1000mm long thermosyphon heat pipe with internal and external diameters of 14 and 16mm using distilled water as working fluid by Emami *et al*., 2008 [82]. The effects of filling ratio (between 20 and 60%), aspect ratio (of 15, 20 and 30) and inclination (between 15 and 90^{o}) were studied on the rate of heat transfer, condensation heat transfer coefficient and temperature distributions. The results showed that the performance of the pipe is best at 60^{o} and 45% filling factor for the aspects ratios and filling factors considered. But the condensation heat transfer was highest when the pipe is inclined between 30 and 45^{o} for all aspect ratios. The effects of inclination, concentration of nanoparticles and operating temperature on the performance characteristics of a copper thermosyphon was studied by Gabriela *et al*., 2011 [83]. Deionised water and nanofluids were used as the working fluid in the 2000mm long two phase closed thermosyphon. Results

reported from this study showed that the heat transfer rate increased with the increase in the inclination angle and the operating temperature also affects the heat transfer rate. Thermal resistance decreases with the increase in the angle and the thermal resistance of the nanoparticle solution is lower than that of the water. With water as working fluid the maximum evaporation and condensation heat transfer coefficient was reached at 60^o and 45^o respectively while the thermal resistance is smallest at 45^o. The overall thermal resistance is minimal at 90^o inclination when the concentration of the nanoparticles is 5.3%.

Jouhara *et al*., 2013 [84] studied the operational suitability of thermosyphon with 400mm long condenser section inclined at 12^o from the evaporator using ethanol-water mixture and azeotrope (mixture of fluid whose proportion cannot be changed by common distillation) as working fluids. The study showed the advantages of using azeotrope in obtaining uniform temperature distributions and lower thermal resistance. But the work did not show the clear effects of inclining the condenser. Experimental study on the effects of the thermosyphon inclination angles from 5^o to 90^o and fill ratio of 15, 22 and 30% was carried out by Noie *et al*., 2007 [85] using water as working fluid. The best performance of this pipe was found to be in the range of the inclination of 15^o to 60^o. Hahne and Gross, 1981 [86] presented work on the effects of the inclination angle on the transport behaviour of a closed two – phase thermosyphon made from steel and utilizing refrigerant R115 as the working fluid. Results showed that the maximum heat transfer rate was obtained between inclination angle of 40 and 45^o with the minimum at 90^o. But in this work, two parameters; angles and heat inputs were varied at the same time, which will make it difficult to deduce the effect of the inclination alone. Chehade *et al*., 2014 [87] studied the effects of fill ratio, inlet temperature and flow rate of the cooling water on the performance of two – phase closed loop thermosyphon. They reported the optimal condition as; fill ratio between 7 and 10%, inlet temperature of 5^oC and

flow rate of 0.7 l/min. But these values could be considered as optimum for the geometry they tested but not general for all thermosyphon. Different results on the best inclination angle for thermosyphon were reported as shown, this may be due to the various factors that affect its operation, geometry and operating conditions.

Since thermosyphon heat pipe requires being in vertical position or at a certain inclination angle (with the condenser at the top), then any concentrator integrated with such pipe must be inclined to certain angle. Details of the operation of the thermosyphon are given in chapter 6 of this thesis. This angle is different from the tilt angle of the surface discussed earlier and will be referred as inclination angle, β_{inc}, throughout this thesis. The heat pipe based CPC (HPCPC) may have two slope angles; tilt facing south or north (depending on the region) and inclination angle of the pipe facing east or west (for East- West orientation) as shown in Figure 2.7 But this will happened when the longest side of the collector is along the pipe length, hence oriented along the East – West direction.

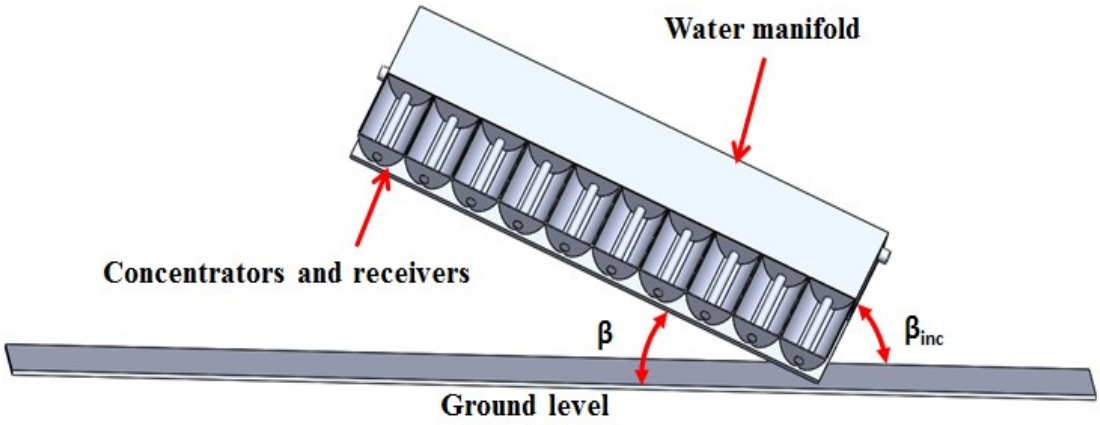

Figure 2.7 Collector tilt and thermosyphon inclination angles of HPCPC

2.2.3.5. Numerical studies on the performance of thermosyphon heat pipe - CFD

Apart from the experimental works reported above, numerical models were developed to investigate the effects of major parameters on the operation of thermosyphon heat pipes. This is due to the numerous parameters that affect its performance and experimental investigation is time and cost intensive. Asgar *et al.,* 2010 [88] presented experimental and CFD modelling of the flow and heat transfer in thermosyphon using volume of fluid (VOF) approach. The effects of heat inputs and fill ratio on the performance of the heat pipe were investigated using 1000mm long pipe. Results showed that the performance of the thermosyphon increased with the increase of heat input between 350W and 500W, but it decreased when the heat is above 500W. Also for the fill ratios tested; 0.3, 0.5 and 0.8, the best performance was found at the fill ratio of 0.5. Basaran and Kucuka, 2003 [89] studied the flow in a closed loop rectangular thermosyphon by a two – dimensional numerical model. SIMPLEX algorithm was used in solving the momentum and the energy equations for laminar flow. The authors reported that their model is appropriate for predicting flow characteristics and heat transfer of the thermosyphon loop at uniform temperature.

A two – dimensional model was developed by Zhang *et al.,* 2009 [90] for predicting the performance of a disk – shape flat two –phase thermosyphon which is utilized in cooling electronics. The vapour flow inside the tube was simulated as a single – phase flow where temperature distributions and vapour velocity were determined. Results showed that nucleate boiling and maximum vapour velocity occurred at the evaporator surface but boiling phenomenon rarely occurred close to the sidewalls. Although experimental and the numerical results are in agreement, the authors considered only vapour phase inside the tube. Asmaie *et al*., 2013 [91] developed a two – phase model for the flow and heat transfer in a

thermosyphon using deionized water and nanofluid mixture of copper(II) oxide with water as working fluid. CFD modelling was used for predicting the temperature distributions on the wall and the heat transfer coefficients of both the evaporator and condenser for the two working fluids. The CFD results were compared with the experimental results reported by Liu *et al*., 2012 [92] and were in good agreement especially at the adiabatic and condenser sections. Also better heat transfer, heat fluxes and lower average wall temperature were shown for the nanofluid compared to water.

A three – dimensional CFD model to simulate the flow boiling process of hydrocarbon feedstock heat exchanger of a steam cracker was developed by De Schepper *et al.,* 2009 [93]. VOF together with user defined functions (UDF) were used in modelling the convection section of the cracker. Also the authors proposed correlations for the interphase mass source term used in the governing equations for simulating the evaporation and boiling phenomena in the cracking furnace. CFD model was built for simulating the heat transfer in a two – phase closed thermosyphon using VOF approach by Fadhl *et al.,* 2013 [94]. UDF was added to the Ansys Fluent code in order to deal with the evaporation and condensation processes taking place in the thermosyphon. The temperature profiles obtained from the simulation was compared with the experimental results and was in agreement. But there is large deviation between the experimental thermal resistances and the simulation especially at low heat inputs.

2.2.3.6. Applications of the CPC

Compound parabolic concentrator has wide range of applications due to its advantages of simple design, high efficiency, great flexibility, etc. Its applications are found in water treatment, electricity generation, refrigeration, water and air heating as described in the following sections.

1. Water and Air heating systems

Various configurations of CPC solar collectors have been employed for the provision of hot water and air ranging from domestic to industrial requirements. Solar radiation is absorbed by the collector and is transferred to the working fluid in the form of heat. The heated water or air is moved from the collector to where it can be used directly or stored in a tank. The movement of the heat transfer fluid can be natural (Passive) or by force circulation (Active).The passive system can be thermosyphon or integrated collector storage systems while the active systems include direct circulation and integrated water heating systems.

Compound Parabolic Collectors are mostly utilised for direct circulation, integrated collector storage and indirect water heating systems and they offer economic benefit when compared with others utilising different types of collectors.

In the CPC indirect water heating systems, the heat is transferred to water by circulating the working fluid in a heat exchanger which can be located outside or inside the tank. While in direct circulation systems, water is pumped to the CPC collector where it gain energy and then the heated water is returned to the storage tank.

The use of air as the working fluid has some advantages and disadvantages compared to the liquid heating systems. The main advantage is that air is non-corrosive and requires no protection from freezing or boiling. But on other hand, it is difficult to control leakage of air, occupies large space and requires high parasitic power consumption compared to liquid systems [21]. Tripanagnostopoulos and Souliotis, 2004 compared the performance of solar water heaters with stationary compound parabolic concentrators (CPC) of asymmetrical and symmetrical reflectors having integrated collector storage (ICS) and a flat plate thermosyphon unit (FPTU). Four experimental models were constructed and tested outdoors to determine their mean daily efficiency and thermal losses during the night. Results showed that CPC with

asymmetric reflector has better preservation of heat in the night than symmetric counterpart [95].

An Integrated Collector Storage (ICS) solar water heater consisting of two concentric cylinders was designed and tested under real sun by Souliotis *et al*., 2008 [96]. It was analysed both optically and thermally with the aim of improving its performance based on the distribution of the irradiance on the receiver. The cylindrical absorber was mounted horizontally inside a stationary truncated asymmetric compound parabolic concentrating (CPC) reflector trough. Parameters investigated include the temperature profile in the inner storage tank, twenty four hours variation of stored water temperatures with no draw-off for the ICS and FPTU systems, the variation in the storage water temperatures and the mean water temperatures with no draw-off for the ICS and FPTU systems etc. In another publication by the same author, a comparison was made between an integrated collector storage solar heater (ICSSWH) and a flat plate thermosyphon unit (FPTU) [97]. The ICS system consisted of two concentric cylinders integrated into a truncated asymmetric CPC. Outdoor testing was conducted on the two systems and results showed that the operation of ICS is effective both in the day and night. It also showed similar thermal loss coefficient to the FPTU during night.

A solar water heating system was fabricated by Yadak *et al*., 1996 using CPC of 36^{o} acceptance angle which was installed on the roof of a two stories Department of physics, Mithila University. It was fabricated from local materials and tested at stagnation condition where the water temperature reached 92^{o}C achieving temperature rise of 16^{o}C [98]. Another ICS solar water heater was designed and fabricated with an inverted absorber integrated in the CPC cavity with secondary cylindrical concentrator and with different types of transparent baffles situated at different positions to reduce the thermal losses due to convection heat

transfer [99]. An indoor test was conducted using solar simulator to determine its performance with different baffle materials, sizes and positions. Results showed that the glass baffles at the top position of the aperture of the concentrator reduces the losses with insignificant optical loss. Other approach of using inverted absorber was reported by Rabl, 1976 [29]. Usually ICS systems suffer great convection losses especially at low insolation. Various techniques were employed to reduce such losses ranging from integrating heat retention devices either at the aperture [100, 101], within the collector cavity [102] or inside the vessel [103].

2. Refrigeration and air-conditioning

There are various ways where solar energy can be utilized to provide cooling either for refrigeration or air-conditioning. Solar refrigeration usually requires lower temperature than air conditioning systems and can be powered by the thermal energy obtained from the solar collector or electricity from photovoltaic. Some of the available solar cooling systems include solar electric refrigeration, solar thermal refrigeration, adsorption, absorption and solar desiccant. Numerous studies have been reported on the use of CPC solar collector for refrigeration and air conditioning with different approaches.

Gonzalez *et al*., 2009 presented a model to stimulate the operation of a solid-sorption chiller utilising methanol-activated carbon pair and a CPC solar collector. The model used first order differential equations in describing all parts of the refrigeration system such as absorber bed, condenser, evaporator, etc. The model was tested to validate its predictions using computer program and agreement between the two was shown as around 3.5% [104]. The same authors presented a tubular CPC configuration containing an adsorption bed inside the solar collector for energy collection to power an adsorptive refrigerator. A prototype was built and tested at Burgos, Spain using activated carbon-methanol pair as shown in Figure 2.8. Experimental

results showed that the coefficient of performance (COP) between 0.078 and 0.096 was achieved [105].

A solar sorption refrigerator consisting of two CPC reflectors, two tubular absorbers and a glazing is presented by Tamainot- Telto *et al,* 1999. The system was designed for solar power input of 500W and to provide a cooling power up to 120W equivalent to approximately refrigeration load of 10 MJ/day. The absorber made from seamless steel tube was described using a numerical model and it predicted a maximum bed temperature up to 172^{o}C when the unit is working under a daily solar radiation conditions [106]. Nkwetta *et al.,* 2012 [61] presented the optical performance of CPC for powering solar air –conditioning system. Results of the ray tracing simulation showed 93.72% ray's acceptance and 79.13% optical efficiency for incident angles between 0^{o} and 20^{o}. In another study, the potentials and advantages of using a CPC solar concentrator was explored by the same authors and the system was shown to attained temperature between 70^{o} and 120^{o}C [107].

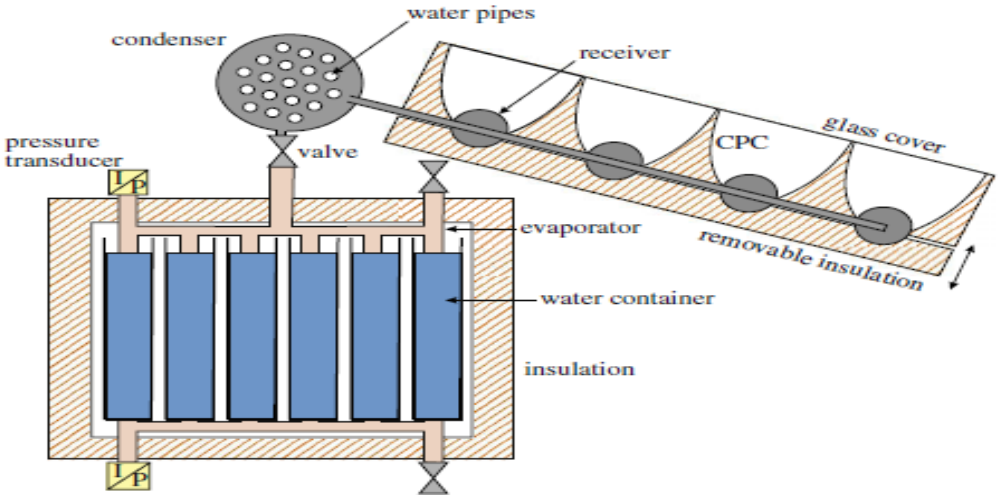

Figure 2.8 Schematic diagram of prototype of a solid - sortion chiller with CPC [104]

3. Water treatment

Treatment of water by removing hazardous materials, salt and other minerals is another area where CPC collector is utilized in the form of detoxification or desalination processes.

Desalination is any process that removes some amount of salt and other minerals from saline water (like sea water) to get fresh water that can be achieved by either phase-change or membrane technique.

Blanco *et al*., 1999 presented a prototype design and development of an efficient and simple system based on CPC for water treatment which led to the design and construction of a full-sized demonstration plant in Spain for the treatment of non-biodegradable contaminants. With CPC of aperture area of 100 m^2, the plant treats $2m^3$ of contaminated water in approximately two hours per batch depending on the solar intensity. Figure 2.9 shows one side of the demonstration plant [108]. Malato *et al.,* 2004 presented a CPC collector used in solar photocatalysis process for waste water treatment. Ray tracing simulations were used as a design tool for the optical configuration of such reactor. The authors reported that CPC with concentration ratio of 1 with static flat system has been proved to be a promising combination for the photochemical applications [109].

Figure 2.9 Water treatment demonstration plant in Spain [108]

A CPC was used in a pilot plant for the treatment of refractory textile waste water by heterogeneous and homogenous processes. Results reported by Vilar *et al.,* 2011 [110] showed that solar advanced oxidation process (AOP) is a promising technology for degrading refractory compounds and solar photo Fenton was found to be the most efficient of all the AOPs considered.

Ajona and Vidal, 2000 [111] reported a performance evaluation of a low cost CPC prototype for water detoxification and explored the feasibility of this concept as the basis for solar photocatalytic oxidation. Although present costs for the solar water detoxification system are higher than that of conventional technologies, potentially greater cost reductions are being investigated through the use of one-sun systems. The authors reported that a one sun (1000 W/m^2) CPC for water treatment was developed at the cost of $\$160/m^2$ and according to their projection, the cost can be as low as $\$50/m^2$ for mass production. The preliminary findings also showed that the overall treatment cost can be reduced by reducing the catalyst cost instead of the unit reactor cost.

Also the viability of a CPC solar photoreactor in water disinfection has been demonstrated by Fernandez *et al.,* 2005 [112]. Titanium (IV) oxide (TiO_2) photocatalysis process was employed with and without the support of catalyst and results obtained from the experiment showed that illuminated area of the CPC plays a vital role in the inactivation of bacteria by solar radiation.

4. CPC Solar Industrial heating processes and CPC with Photovoltaic

CPC solar collectors are capable of meeting the domestic and many industries energy demands for medium and high temperatures applications. Processes such as distillation, drying, sterilising, evaporation, preservation, etc. can all be integrated with solar thermal collectors depending on the delivery temperature required.

CPCs are utilised in the generation of electricity either by generating steam to run turbine or by coupling it with a photovoltaic cell for increasing the efficiency of the cell. The hybrid photovoltaic/thermal (PV/T) system refers to the solar thermal collector that utilises PV cells as the receiver for generating electric power and heat. The system can be made to generate both electricity and heat by providing cooling system that can dissipate the heat generated on the cells due to the concentration of the radiation.

A prototype of double-pass photovoltaic-thermal solar air collector with CPC and fins has been designed and fabricated by Mohd *et al*., 2005. The hybrid system consists of array of solar cells and fins attached to the back side of the absorber plate to enhance heat exchange to the flowing air as shown in Figure 2.10. The performance of the system was investigated over a range of operating conditions and found that it enhanced the power production from the solar cells. But the power output decreased with the increase of the flow temperature, which tend to lower the efficiency of the whole system. The temperature rise was found to be proportional to the radiation intensity and the combined efficiency raised from 39 to 79% as the flow rate increased from 0.015 to 0.16 kg/s at radiation of 500 W/m^2 [113].

A detailed parametric study on the optics and heat transfer in an asymmetric compound parabolic photovoltaic concentrator (ACPPVC) was presented by Mallick *et al.,* 2007 as shown in Figure 2.11 [114]. Various solar radiation intensities falling on the aperture of the concentrator were used and the PV cell temperatures were monitored. Results showed a reduction of 25.4K in the cell temperature was achieved with air flowing through a duct of 20mm wide at 1 m/s placed between the aperture and the concentrator. For the front and rear a temperature reduction of 34.2 K was predicted for the same condition. Other works reported on integrating CPC with PV cells are [115-118] mostly with asymmetric reflectors.

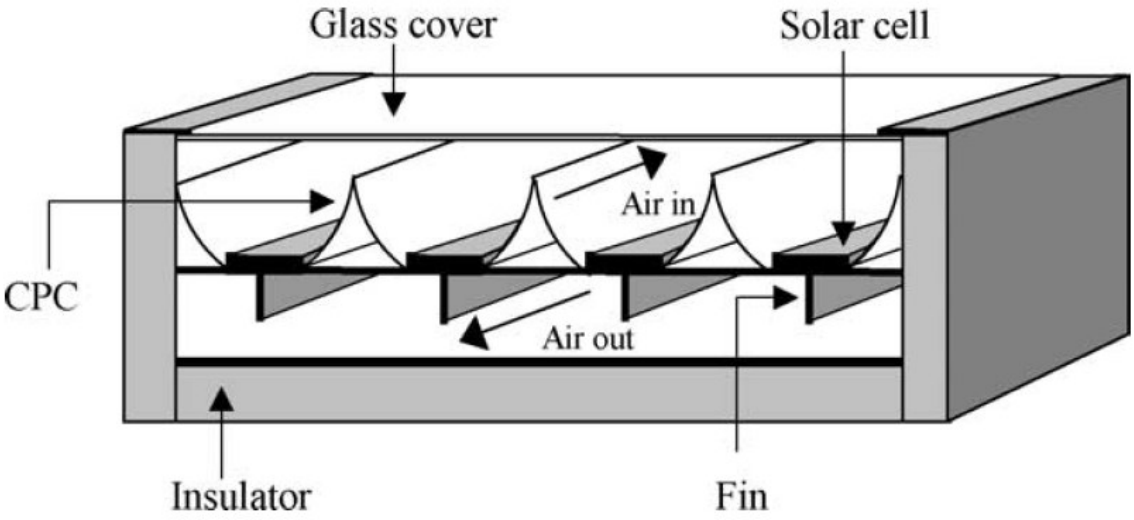

Figure 2.10 Double pass photovoltaic/thermal CPC solar collector with fins [113]

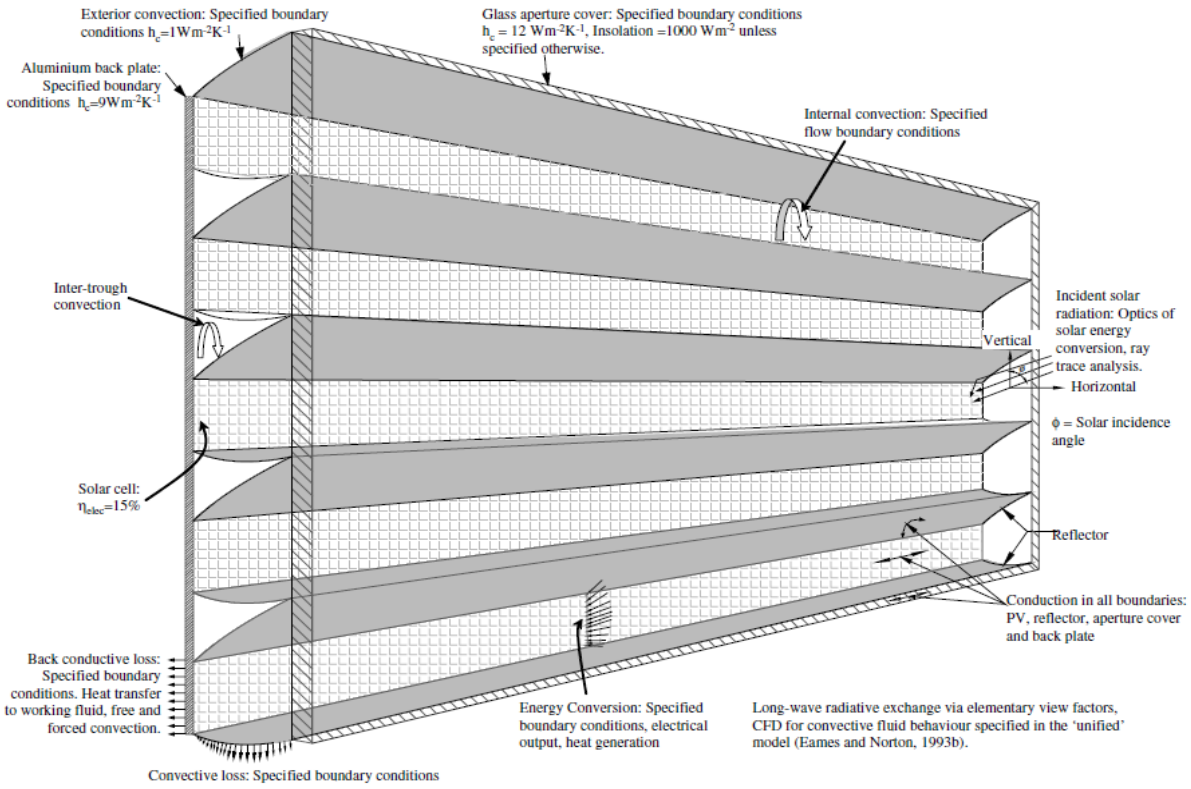

Figure 2.11 Schematic diagram of energy transfer mechanism of asymmetric CPC photovoltaic system [114]

5. CPC applications in photochemical, photo catalytic and medicine

Solar photocatalytic refers to the process of promoting specific catalytic reaction by collecting and delivering photons to a reactor through the use of solar collectors. The technology required in solar liquid-phase photochemical applications is similar in many aspects with the thermal applications, but unlike thermal, photochemical processes normally use only photons of short wavelengths to promote specific chemical reactions. The photocatalytic water splitting has been proven in many laboratories for efficient hydrogen production. Results reported in literature have shown that efficiencies in the order of 50%, 60% and even 90% have been achieved for the outdoor hydrogen production under direct solar light. Linkous *et al,* 1995 and Koca and Sahin, 2002 have successfully conducted works on the hydrogen production under sunlight [119] and [120].

A photocatalytic hydrogen production solar reactor utilizing compound parabolic concentrator (CPC) was designed and tested by Jing *et al.,* 2009. Preliminary results of the system performance showed a maximum hydrogen production rate of 0.164l/h per unit volume of the reaction solution [121]. McLouhlin *et al.,* 2004 reported the use of low cost CPC in photocatalytic disinfection of water using near UV light [122]. A pilot plant made up of CPC integrated with eight Pyrex tubes was tested at tilt angle of 37^0 using suspension titanium (IV) oxide (TiO_2) at different concentrations. Results showed that adding of TiO_2 caused improvement only when the concentration was 3mg/l. However, the paper ought to study the detail effects of the concentration of TiO_2 on the overall disinfection process.

2.2.3.7 Literature on solar radiation modelling

One of the important factors that affect the performance of any solar system is the availability of solar radiation in the location where it is installed. Meteorological agencies and solar stations measure the meteorological parameters like sunshine hour, temperature, humidity,

solar radiation, etc. at the location at certain intervals of minutes, hours or daily average. Global radiation is the most important data required in the design and performance evaluation of a solar system. Continuous and accurate measurements are often absent especially in developing countries; hence several attempts were made to correlate these parameters with one another to enable the determination of one parameter from the others. Sambo, 1986 proposed 12 different correlations for estimating the global solar radiation for Kano, Nigeria using sunshine hours, average daily temperature and relative and specific humidity for a period of five years. Among the equations obtained, the one with least root mean square error (RMSE) is [123]:

$$\left(\frac{\overline{H}}{H_o}\right) = 0.621 - 0.294\left(\frac{\bar{n}}{\overline{N}}\right) + 0.178\left(\frac{\bar{n}}{\overline{N}} - \overline{R} - \bar{\theta}\right) + 0.491\left(\frac{\bar{n}}{\overline{N}\bar{\theta}}\right) \tag{2.28}$$

While that with the smallest sum of percentage error is

$$\left(\frac{\overline{H}}{H_o}\right) = 0.567 + 0.054\left(\frac{\bar{n}}{\overline{N}}\right) - 0.182\left(\bar{\theta}\overline{R}\right) \tag{2.29}$$

Where $\bar{n}$, $\overline{R}$, $\overline{N}$, $\bar{\theta}$, $\overline{H}$, and $\overline{H_o}$ are the sunshine, relative humidity, maximum time when the sunshine data taker is active, maximum and minimum temperature ratio, global and extraterrestrial radiation respectively. Also the author Sambo, 1988 [124] presented the measured and predicted global and diffuse radiation for a period of one year (1985 – 1986). Kipp and zonen solarimeters with and without shadow ring were used for the measurement and the calculations were done using one of the correlations presented in [123]. The predicted and the measured values showed good agreement, but there is relatively scattered nature of the data which the author attributed it to the dust and rainy season in the location during the period of such measurements in 1985. Also the period of the measurements is short for generating correlations to be used for long time.

Three correlations for determining the global radiation from beam and diffuse components were proposed by Lam and Li, 1996 [125]. Measured global and other components at the University of Hong Kong of four years were used. The model was reported to have mean bias error (MBE) between 0.45 and 0.82% and root mean square error (RMSE) ranging from 7.76 to 14.86%. Khorasaniza and Mohammadi, 2013 [126] tested eleven correlations available in literature together with global radiation, sunshine duration, relative humidity and temperature in predicting monthly average global radiation in Tehran and five other cities in Iran. The model was classified into 3; function of sunshine duration only, function of sunshine duration, temperature and relative humidity, and as a function of relative humidity and ambient temperature [126]. Results showed for all the cities considered, the first two combinations tend to be the best models.

It can be seen that several numerical models exist for predicting solar radiation components from available data for different regions of the world such as for Hong Kong [127], Sao Paulo [128], East and West of Iran [129] and central Arid desert of Iran [130] etc.

Apart from the numerical prediction using correlations, other prediction tools like artificial neural network (ANN), fuzzy logic, etc. were extensively used for the modelling of solar radiation components. A model based on ANN was developed by Fadare, 2009 for predicting global solar radiation on horizontal surface of Nigeria using meteorological data of ten years for 195 locations. Latitudes, longitude, altitude, mean temperature, relative humidity, month and mean sunshine duration were used as inputs to the model while global radiation was considered as the output. Results showed a good agreement between predicted and measured data with global radiation between 7.01 and 5.62 to between 5.43 and 3.54 kWh/(m^2day) for the northern and southern regions respectively [131]. Other predictions of global radiation for Nigeria using ANN includes Alfa *et al.,* 2001 [132] for predicting hourly global radiation for

Bauchi city and Jiya and Alfa, 2002 [133] for global radiation mapping of the whole country. The use of data from only 31 stations for a period of only one year makes the accuracy of their results to be low.

A model for predicting global and diffuse radiation on a horizontal surface of five locations in Malaysia was presented by Khatib *et al.,* 2011 [134] using four different prediction tools; linear, fuzzy logic, non – linear and ANN. The inputs to their model are latitude, longitude, clearness index and day number. The results showed that ANN gives better results with mean absolute percentage error (MAPE) of 5.38 and 1.53 for global and diffuse respectively. Although good agreement was reported but the model's input exclude very important variables that are highly related to the radiation such as sunshine duration and temperature.

2.3 Summary

From the literature survey conducted, the following conclusions are put forward:

- The performance of CPC is affected by many parameters which can be grouped into three; solar radiation available, collector design and orientation. Therefore, it would be beneficial to investigate the effects of most of these parameters on a class of CPC (like 2 – 5X) for better understanding and possible optimization.
- Although there are several performance enhancement techniques reported but all of them are limited either to particular CPC or specific aspect of CPC like working fluid, selective coating, modifying the receiver or reflectivity, etc. But it would be better to investigate a combination of such parameters in order to optimize its performance.
- Different models were reported for predicting the global solar radiation in some regions in the world using different methods but detailed of modelling the various

components like beam, diffuse, tilt factors, etc. is limited. Therefore, it would be beneficial to have a model for full radiation characterization for a region in developing countries like Nigeria.

- Heat pipes and thermosyphons are used as receivers for CPC to enhance heat transfer; hence studies on their thermal characteristics were reported for better understanding of their operations. Various reports on parameters affecting the performance of thermosyphon both numerically and experimentally are available, but some are conflicting like effects of inclination angle of the pipe. Hence it will be beneficial to investigate such parameters in detail for better design of the heat pipe based compound parabolic collector (HPCPC)
- Generally, tracking the sun was found to be a good option for improvement of the overall efficiency of the CPC, the use of such mechanism should be recommended based on the intended application and only when the enhancement obtained offset the additional cost and other logistics due to tracking. But most of the works reported failed to compare the cost of the mechanism with its gain.
- Some works are presented for a particular region and an application, in order to contribute to their energy requirements. Therefore, it would be beneficial to carry out a work to address energy issues in developing countries (like Nigeria) where the problem is enormous.

CHAPTER THREE

3. Modelling of Solar radiation and Optimization of the collection

3.1. Introduction

In chapter two the literature review showed that the solar radiation modelling involves mostly generating correlations for predicting global radiation on horizontal surfaces. Therefore, there is a need to develop a model to predict the beam and diffuse radiation on both horizontal and tilt surfaces from the measured global. Also there is no report on the detailed solar characteristics and optimum tilt angle for Kano, which creates gaps in maximizing the collection of the solar radiation falling on its surfaces, which is addressed in this work.

This chapter deals with the fundamentals of solar radiation, the modelling process of the various radiation components, the effects of the collector tilt and optimization of radiation collection. A model was developed in Microsoft Excel ® (referred as Solrad) using correlations available in literature for predicting the monthly and hourly beam, diffuse and ground reflection using the measured global radiation for northern hemisphere regions. The model also predicts the tilt factors for every month, clearness index, hourly incident angles and the effects of the collector tilt angles. Measured global radiation for Birmingham, UK was used for testing the model and the results were compared with published results in literature. The solar radiation characteristics of Kano, Nigeria were fully modelled leading to the determination of the monthly, seasonal and annual optimum tilt angle for the region. The optimization was carried out using Golden Section Search (GSS) and Quadratic

approximation methods in EES for the twelve months which led to the determination of optimum tilt angles for Kano.

3.2. Solar radiation

Sun is huge nuclear reactor constantly forming helium by fusion of hydrogen nuclei together and this process leads to the generation of large amount of energy in form of electromagnetic waves. Sun releases 4 X 10^{26} W of energy, but the radiation strike the earth surface at approximately 8 X 10^{16} W [18]. This energy travels 150 million km from the sun to the earth in the form of electromagnetic radiation at a speed of 300,000 km/s [18]. The total amount of radiation received at the top of the atmosphere is supposed to be constant over a year and it is termed as solar constant. This is the solar radiation receives by a surface vertical to the direction of radiation at mean distance between sun and the earth (1.495 X 10^{11} m) [18].

The amount of radiation that reaches different regions on the earth varies due to the latitude and seasonal variation. Longitudinal difference includes sunlight duration, angle of incidence of sun rays and atmospheric attenuation. The reduction of solar radiation as it pass through the atmosphere is due to scattering and absorption by dust particles, air molecules and other greenhouse gases like carbon dioxide, methane, water vapour, etc. (Figure 3.1). Also the amount of radiation falling at a particular region is further influenced by the local condition of the atmosphere such as cloud. The amount of the radiation that reaches the earth without scattering by the atmosphere is called beam or direct radiation while diffuse is the radiation component received after scattering, also known as sky radiation. The sum of these two components is usually termed as global radiation.

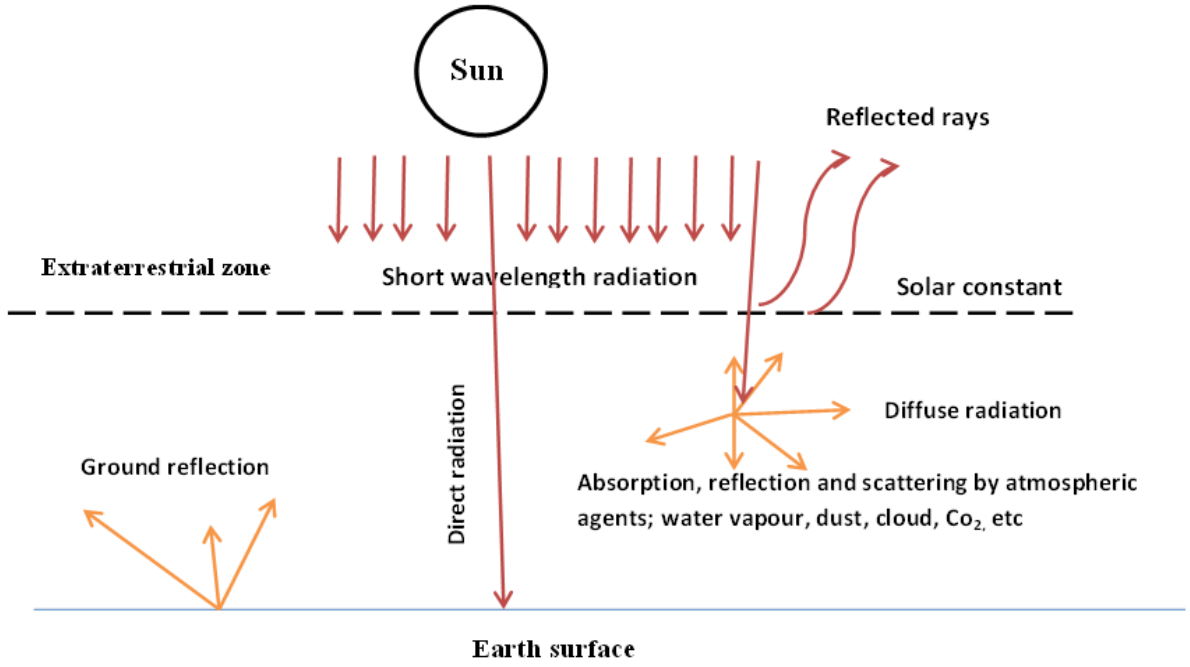

Figure 3.1 Radiation from the sun to the earth surface [135]

The total energy of the solar rays coming from atmosphere incident on a certain location at particular latitude depends on the following:

- Air mass (AM) through which the sun radiation passes through, and it depends on the angle of the incident ray from the vertical (i.e. from the zenith). AM is the measure of the amount of reduction in the intensity of the rays as they pass through the atmosphere, given by [135]:

$$AM = 1/Cos\,\theta \tag{3.1}$$

  Where θ is the angle between the vertical position (zenith) and the ray, hence AM is 1 when the sun is at zenith.

- The declination of the sun or its altitude over the horizon which depends on the day of the year as shown in Figure 3.2

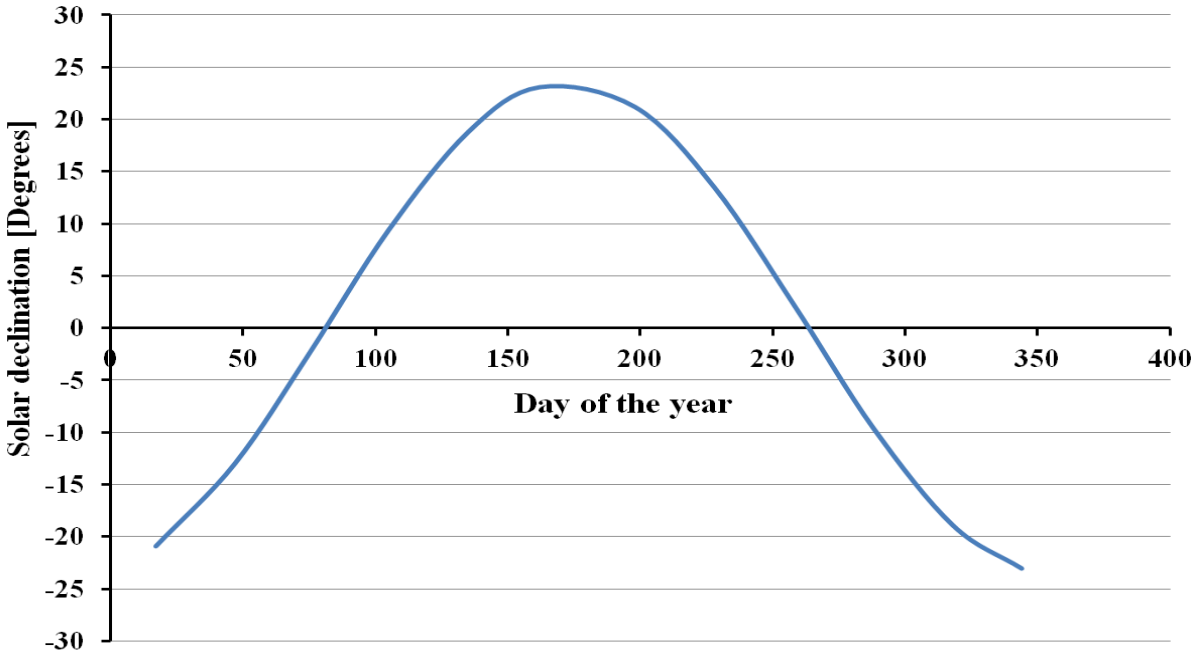

Figure 3.2 Variation of solar declination with the days of the year

3.2.1. Solar angles

There are many parameters that are used to describe the relationship between the sun and plane on the earth's surface such as solar declination, solar altitude, azimuth, zenith angles, etc. as shown in Figure 3.3. These angles are used in calculating the radiation striking the earth surface.

Solar declination, δ refers to the angle between the sun rays and a plane passing through the equator having values between -23.45^{o} and 23.45^{o}, as shown in Figure 3.2. Solar azimuth angle, γ_S is the angular movement of the projection of beam radiation on horizontal surface from south and this displacement is positive for west to south and negative for east to south.

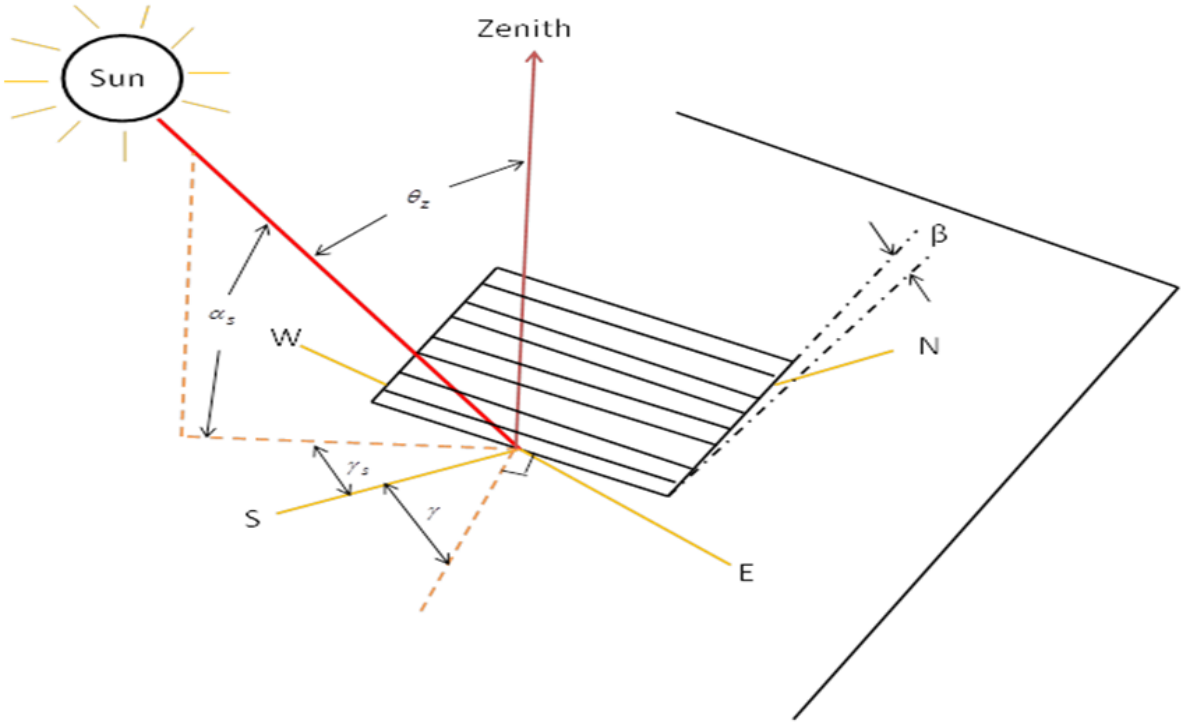

(a)

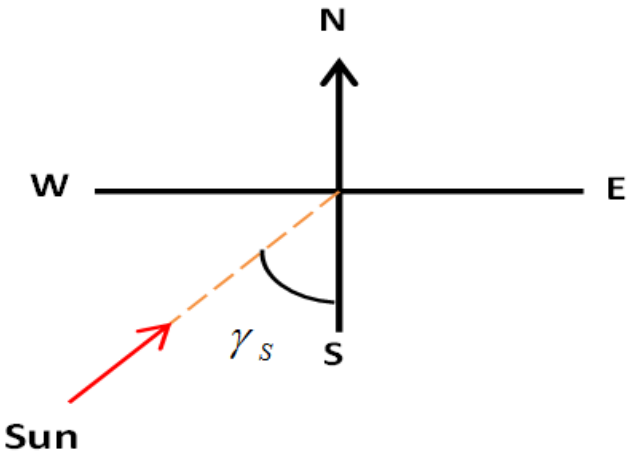

(b)

Figure 3.3 Sun angles relative to (a) a tilted surface and (b) azimuth angle on a plane surface [19]

The surface azimuth, γ is the diversion of such projection from local meridian and has a range of -180^o $\leq \gamma \leq$ 180^o. The altitude, α_S is the angle between the sun's ray and the

horizontal plane and its values depends on the solar declination, hour angle and the latitude. Solar hour angle gives the sun's position relative to the noon at a certain time and location with values of zero, negative and positive when the sun is at noon, before noon and after noon respectively.

3.2.2. Extraterrestrial Solar radiation

Extraterrestrial radiation is the radiation received outside the atmosphere and it is the maximum theoretical value that could be received if there is no absorption, reflection and scattering by the atmosphere constituents. The annual average value of extraterrestrial radiation is called the solar constant, G_{sc} and its value was estimated by different groups ranging from 1322 W/m^2 to 1394 W/m^2. The value of 1367 W/m^2 (with an uncertainty of 1%) will be used throughout this thesis which is the value adopted by World Radiation Centre [19].

The value of extraterrestrial radiation varies due to two factors; the variation in the amount of radiation emitted by the sun and the variation of the earth – sun distance, and it's value just outside the atmosphere is given as [19]:

$$G_o = G_{sc}\left(1 + 0.033\cos\frac{360n}{365}\right) \tag{3.2}$$

Where G_{sc} the solar constant and n is the nth day of the year

The solar radiation incident on a horizontal plane outside the atmosphere can be calculated by [19]:

$$G_o = G_{sc}\left(1 + 0.033\cos\frac{360n}{365}\right)\cos\theta_z \tag{3.3}$$

Where θ_Z is the zenith angle given by [19] as:

$$\cos\theta_z = \cos\phi\cos\delta\cos\omega + \sin\phi\sin\delta \tag{3.4}$$

Daily extraterrestrial radiation, H_O (J/m^2) on the horizontal earth surface at any time between sunrise and sunset can be calculated by combining equations 3.3 and 3.4 as:

$$H_o = \frac{86{,}400G_{sc}}{\pi}\left(1 + 0.033\cos\frac{360n}{365}\right)X\left(\cos\phi\cos\delta\sin\omega_s + \frac{\pi\omega_s}{180}\sin\phi\sin\delta\right) \tag{3.5}$$

Where ϕ is the latitude of the location ($-90^o \le \phi \le 90^o$) and δ is the solar declination which depends on the day of the year, n, (n = 1 for 1st January,) given by [18] as:

$$\delta = (23.45^o)\sin[360^o(284+n)/365] \tag{3.6}$$

The sunset hour angle, ω_s, is [19]:

$$\omega_S = \cos^{-1}[-\tan\phi\tan\delta] \tag{3.7}$$

The number of daylight hours is given by [19] as:

$$N = \frac{2}{15}\cos^{-1}(-\tan\phi\tan\delta) \tag{3.8}$$

The solar hour angle w, changes by 15^o per hour given by [19]:

$$w = \left(\frac{360}{24}\right)t \tag{3.9}$$
$$= 15t$$

Where t is the hour of the day (solar time)

Daily values of the extraterrestrial radiation are calculated and averaged to give the monthly

average extraterrestrial radiation on a horizontal surface, $\overline{H_O}$, for a particular month. However, for latitude in the range of +60 to -60, $\overline{H_O}$ can be calculated with equation 3.5 using *n* and δ for the mean day of the month (i.e. the day having H_o closest to the $\overline{H_O}$) [19]. Table 3.1 shows the mean day of each month, *n* and the corresponding δ.

Table 3.1 Recommended mean days for months and Values of *n* for each month [19]

Month	***n* for *i*th Day of Month**	**Date**	**n, Day of year**	**δ , Declination**
January	*i*	17	17	-20.9
February	31 + *i*	16	47	-13.0
March	59 + *i*	16	75	-2.4
April	90 + *i*	15	105	9.4
May	120 + *i*	15	135	18.8
June	151 + *i*	11	162	23.1
July	181 + *i*	17	198	21.2
August	212 + *i*	16	228	13.5
September	243 + *i*	15	258	2.2
October	273 + *i*	15	288	-9.6
November	304 + *i*	14	318	-18.9
December	334 + *i*	10	344	-23.0

3.2.3. Terrestrial Solar radiation

Since some of the short wavelength solar radiation are absorbed, reflected and scattered when passing through the atmosphere, then the amount that strike a surface (like solar collector) on the earth's surface is of interest because it is the amount to be utilized. This is called terrestrial or hemispherical solar radiation which amount to about one third of the extraterrestrial [19] but depends on the location, condition of the sky, time of the year, etc.

Terrestrial solar radiation is usually divided into two components; beam or direct radiation and diffuse radiation. Beam radiation is the component that passes the atmosphere without being absorbed, scattered or reflected, hence it has a definite direction. The geometric relationship between a plane on earth and the incoming beam radiation (ie sun's position relative to such plane) is described by angles like surface azimuth, slope, incidence, zenith angles, etc. as shown in Figure 3.3. While diffuse has no definite direction due to the scattering, reflection and absorption, it suffered before reaching the earth's surface. Radiation from some surfaces on the earth's referred to as ground reflection is also considered as diffuse. The sum of these radiation components will be considered as the global radiation throughout this thesis.

Global radiation on horizontal surfaces are usually measured in many regions in the world, but only few stations especially in developing countries give the beam and diffuse components separately. The measuring instruments for the hemispherical radiation are generally of two types; Pyranometer and pyrheliometer. Pyranometer measures global radiation due to its ability to accept radiation from the whole hemisphere while pyrheliometer accepts radiation from only one direction hence is used for beam radiation measurement. But

both of them operate based on the response in terms of temperature rise of black absorber when heated by the sun.

In a situation where global radiation is missing, other meteorological data like sunshine hours, temperature, clearness index, etc. are used to numerically calculate it values as discussed in chapter two. Also when global component or clearness is available for a certain location, beam and diffuse components can be estimated as described in the next section. Monthly average Clearness index, $\overline{K_T}$, is an important parameter for determining the global radiation according to the following equation [18]:

$$\overline{K_T} = \frac{\overline{H}}{\overline{H_O}} \tag{3.10}$$

Where $\overline{H}$, is the monthly average global radiation on horizontal surface and $\overline{H_O}$ is the monthly average extraterrestrial radiation.

3.3. Mathematical Modelling of Solar radiation

The performance of a solar collector depends largely on the availability of solar radiation which is the input to the collector for it to deliver the required outputs. Modelling of solar radiation is performed to determine the required data from the available ones and to find the effects of tilt angle on the radiation falling on a particular surface.

3.3.1. Prediction of monthly average diffuse and beam components on horizontal surface

Since the evaluation of solar collector performance requires the beam and diffuse components separated, and these data are mostly absent, correlations described by Rabl,1958 [18] and

others can be utilized to predict them from measured global radiation. Splitting of the global radiation into its beam and diffuse is very important as [19]:

1. The calculation of radiation falling on surfaces of different orientation requires separation of these components and
2. The prediction of the performance of concentrating collector for long period is usually based on the beam component

The ratio of the monthly diffuse, $\overline{H_D}$, to the mean global radiation is given by [18]:

$$\frac{\overline{H_D}}{\overline{H}} = 0.775 + 0.00606(w_s - 90) - [0.505 + 0.00455(w_s - 90)]\cos(115\overline{K_T} - 103) \quad (3.11)$$

The monthly average beam component $\overline{H_B}$, can be calculated by [136]:

$$\overline{H_B} = \overline{H} - \overline{H_D} \quad (3.12)$$

Several other correlations exist for the ratio of diffuse to the hemispherical radiation like Erbs et al, 1982, for $w_s \subseteq 81.4^o$ and $0.3 \subseteq \overline{K_T} \subseteq 0.8$ [18, 19] as:

$$\frac{\overline{H_D}}{\overline{H}} = 1.391 - 3.560\overline{K}_T + 4.189\overline{K}_T{}^2 - 2.137\overline{K}_T{}^3 \quad (3.13)$$

While for $w_s \supset 81.4^o$ and $0.3 \subseteq \overline{K_T} \subseteq 0.8$, the ratio is given by [18, 19]:

$$\frac{\overline{H_D}}{\overline{H}} = 1.311 - 3.022\overline{K_T} + 3.427\overline{K}_T{}^2 - 1.821\overline{K_T}^3 \quad (3.14)$$

Where $\overline{K}_T$ is the monthly average clearness index given by equation 3.10.

3.3.2. Prediction of hourly average diffuse and beam components on horizontal surface

Predicting the hourly hemispherical radiation falling on a horizontal surface involves converting the monthly/daily average into hourly instantaneous values. This enables the performance of a solar collector to be evaluated with the solar hour angle. The daily average clearness index K_T, is the ratio of the daily average hemispherical radiation, H, to the daily average extraterrestrial radiation H_O, thus:

$$K_T = H / H_O \tag{3.15}$$

Similarly the hourly clearness index is defined as [19]:

$$k_T = I / I_o \tag{3.16}$$

Where I and I_o are the average instantaneous (hourly) terrestrial and extraterrestrial radiations respectively and can be determined by using correlations proposed by Rabl,1985 [18] as follows:

$$I_o = \frac{12X3600}{\pi} G_{sc}\left(1+0.033\cos\left(360n/365\right)\right)X\left[\cos\phi\cos\delta\left(\sin w_2 - \sin w_1\right)+\frac{\pi\left(w_2-w_1\right)}{180}\sin\phi\sin\delta\right] \tag{3.17}$$

The hourly diffuse, I_D and hemispherical radiation, I_h components can be predicted from the monthly average as [18]:

$$\overline{I_D} = r_D\left(w, w_s\right)\overline{H_D} \tag{3.18}$$

$$\overline{I_h} = r_h\left(w, w_s\right)\overline{H} \tag{3.19}$$

Where

$$r_D(w,w) = \frac{\lambda}{\tau_{day}} \frac{\cos w - \cos w_s}{\sin w_s - (\lambda w_s / 180^o)\cos w_s} \tag{3.20}$$

$$r_h(w,w_s) = (a + b\cos w) r_D(w,w_s) \tag{3.21}$$

The sunset hour angle w_s is given by the equation 3.7, τ_{day} is the length of the day (24 hours) and the solar hour angle w is given by equation 3.9. While the coefficients a and b are given by [18]:

$$a = 0.4090 + 0.5016 Sin(w_s - 60^o) \tag{3.22}$$

$$b = 0.6609 - 0.4767 Sin(w_s - 60^o) \tag{3.23}$$

When τ_{day} is in seconds (86,400), then $\overline{I_d}$ and $\overline{I_h}$ will be in W/m^2, and the average hourly beam radiation at normal incidence can be deduced from [18]:

$$\overline{I_B} = \frac{\overline{I_h} - \overline{I_D}}{Cos\theta_z} \tag{3.24}$$

For solar collectors with low concentration (C < 10), like CPC which accepts significant amount of diffuse radiation the instantaneous hemispherical radiation is [18]:

$$I = I_B \cos\theta + \frac{I_D}{C} \tag{3.25}$$

The effective irradiance on the aperture of high concentration solar collector (C ≥ 10) which accepts a small amount of diffuse radiation would be [18]:

$$I = I_B \cos\theta \tag{3.26}$$

Where C is the concentration ratio and Θ is the incident angle of the sun rays on the collector aperture and it is given for a surface sloped at an angle of β in the northern hemisphere by [19]:

$$Cos\theta = Cos(\phi - \beta)Cos\delta Cos\omega + Sin(\phi - \beta)Sin\delta \quad (3.27)$$

3.3.3. Radiation on inclined surfaces

Solar collectors are usually tilted to maximize solar radiation collection especially the beam component (since diffuse comes from all directions).The value for the best tilt angle depends on the location and the time of the year as reported in the literature. However, some authors like Jan and Frank suggested general guidelines on the choice of tilt angle which is made based on the application as; 15^o greater than the latitude for solar heating of buildings and tilt angle equals to the latitude for solar water heating systems [23]. Solar radiation on inclined surfaces is not readily available for most location because most of the weather stations record data for only horizontal surfaces hence correlations are used to convert the horizontal radiation to that on sloped surfaces.

3.3.3.1. Hourly radiation on inclined surface

There are many approaches for calculating the total radiation on a tilted surface and they differ on the way they treat diffuse radiation. The simplest model is the one where beam radiation is assumed to be predominant and the sum of diffuse and ground reflected radiations is the same for all orientations. Other models are the isotropic and anisotropic sky models which are more accurate than the first approach.

Isotropic diffuse model considers the radiation on tilted surface to be made up of beam, isotropic diffuse and radiation diffusely reflected from the ground. This provides an

improvement to the first model and the calculation is simple but it underestimate the total radiation on a sloped surface. Based on this assumption, the solar radiation on a tilted surface for an hour is given by [19]:

$$I_T = I_B R_B + I_D\left(\frac{1+\cos\beta}{2}\right) + I\rho_G\left(\frac{1-\cos\beta}{2}\right) \tag{3.28}$$

The ratio of the total radiation on the tilted surface, I_T to the total radiation on horizontal surface is given by [19]:

$$\mathrm{R} = \frac{\mathrm{Totalradiationonthetiltedsurface}}{\mathrm{Totalradiationonahorizontalsurafce}} = I_T \big/ I \tag{3.29}$$

Then

$$R = \frac{I_B}{I} R_B + \frac{I_D}{I}\left(\frac{1+\cos\beta}{2}\right) + \rho_G\left(\frac{1-\cos\beta}{2}\right) \tag{3.30}$$

The ratio of beam radiation on tilted surface, $I_{B,T}$ to that on a horizontal surface, I_B at any time can be calculated as [19]:

$$R_B = \frac{I_{B,T}}{I_B} = \frac{I_{B,n}Cos\theta}{I_{B,n}Cos\theta_Z} = \frac{Cos\theta}{Cos\theta_Z} \tag{3.31}$$

Where $I_{B,n}$ is the direct radiation on a surface which is normal to the direction of its propagation.

For the northern hemisphere such ratio is given by [19]:

$$R_B = \frac{Cos(\phi-\beta)Cos\delta Cos\omega + Sin(\phi-\beta)Sin\delta}{Cos\phi Cos\delta Cos\omega + Sin\phi Sin\delta} \tag{3.32}$$

The ratio of the hourly diffuse radiation to the hourly hemispherical radiation can be determined using Erbs *et al.*, 1982 correlations once the hourly hemispherical radiation is known[18]:

$$\frac{I_D}{I} = \begin{cases} 1.0 - 0.09K_T & for\ k_T \leq 0.22 \\ 0.9511 - 0.1604k_T + 4.388k_T^2 - 16.638k_T^3 + 12.336k_T^4 & for\ 0.22 < k_T \leq 0.8 \\ 0.165 & for\ k_T > 0.8 \end{cases} \quad (3.33)$$

Anisotropic model proposed by Hay, Davies, Klucher, Reindl (called HDKR model) provides an improvement to the isotropic as it takes account of circumsolar diffuse, diffuse from the horizon and horizon-brightening as shown in Figure 3.4.

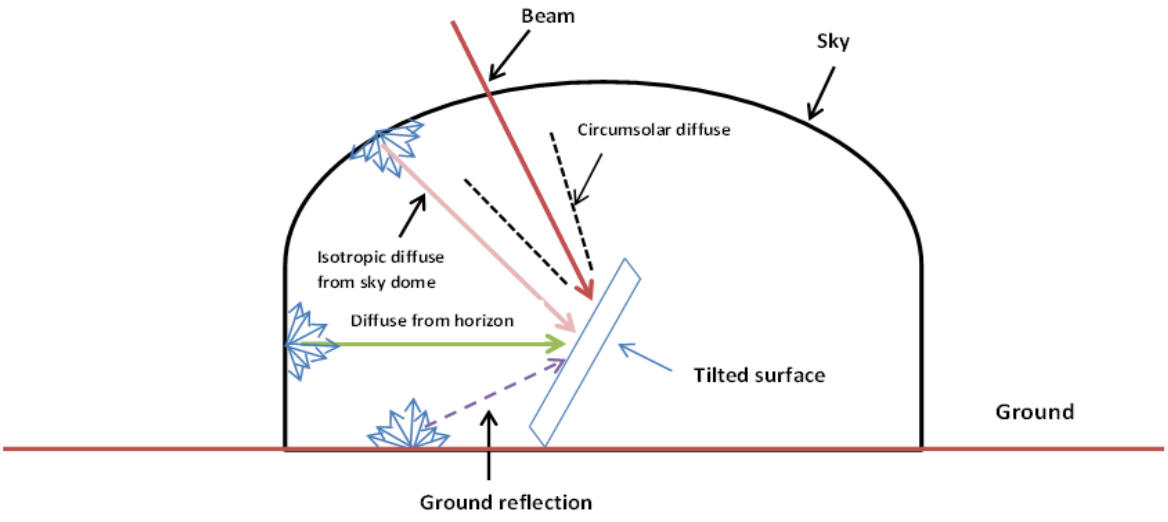

Figure 3.4 Direct, diffuse and ground radiation on a sloped surface (Anisotropic sky) [19]

Based on this model, the hourly total radiation on the tilted surface is [19]:

$$I_T = (I_B + I_D A_i) R_B + I_D (1 - A_i) \left[\frac{1 + \cos\beta}{2} \right] \left[1 + f Sin^3 \left(\frac{\beta}{2} \right) \right] + I \rho_G \left(\frac{1 - \cos\beta}{2} \right) \quad (3.34)$$

where A_i is the anisotropy index which depends on the transparency of atmosphere for passing of direct radiation given by [19]:

$$A_i = I_B / I_o \quad (3.35)$$

and the correction factor, f estimates the cloudiness of the atmosphere and is given as [19]:

$$f = \sqrt{\frac{I_B}{I}} \quad (3.36)$$

3.3.3.2. Monthly average radiation on inclined surface

For the determination of monthly average daily radiation on tilted surface, two popular methods exist; the isotropic and the K-T methods, but isotropic is the most widely used [19]. The monthly average total radiation on a tilted surface is the sum of the monthly average beam $\overline{H_{BT}}$, diffuse $\overline{H_{DT}}$ and ground reflection, $\overline{H_{GT}}$ as follows [137]:

$$\overline{H_T} = \overline{H_{BT}} + \overline{H_{DT}} + \overline{H_{GT}} \quad (3.37)$$

The monthly average direct (beam) radiation on tilted surface can be determined from [137]:

$$\overline{H_{BT}} = \left(\overline{H_T} - \overline{H_{DT}} \right) \overline{R_B} \quad (3.38)$$

Where $\overline{R_B}$ is the ratio of the monthly average daily beam radiation on the tilted surface to that on the horizontal surface known as tilt factor.

While the monthly average diffuse on tilted surface is given by [137]:

$$\overline{H_{DT}} = \overline{H_D}\,\overline{R_D} \tag{3.39}$$

The ratio of the diffuse on the tilted surface to that on the horizontal, $\overline{R_D}$ depends on the model employed, hence different values were proposed like isotropic model by Liu and Jordan, and given as [19]:

$$\overline{R_D} = \left(\frac{1+Cos\beta}{2}\right) \tag{3.40}$$

Based on this model proposed by Liu and Jordan,1962 [138] and later extended by Klein [139], the monthly mean solar radiation on an unshaded tilted surface can be expressed as [19]:

$$\overline{H_T} = \overline{H}\left(1-\frac{\overline{H_D}}{\overline{H}}\right)\overline{R_B} + \overline{H_D}\left(\frac{1+Cos\beta}{2}\right) + \overline{H}\rho_G\left(\frac{1-Cos\beta}{2}\right) \tag{3.41}$$

And

$$\overline{R} = \frac{\overline{H_T}}{\overline{H}} = \left(1-\frac{\overline{H_D}}{\overline{H}}\right)\overline{R_B} + \frac{\overline{H_D}}{\overline{H}}\left(\frac{1+Cos\beta}{2}\right) + \rho_G\left(\frac{1-Cos\beta}{2}\right) \tag{3.42}$$

$\overline{R_B}$, depends on the transmittance of the atmosphere and its value can be taken for surfaces that are sloped towards the equator in the northern hemisphere (i.e. ɣ = 0) as [138]:

$$\overline{R_B} = \frac{Cos(\phi-\beta)Cos\delta Sin\omega' + \left(\lambda/180\right)\omega'_s Sin(\phi-\beta)Sin\delta}{Cos\phi Cos\delta Sin\omega'_s + \left(\lambda/180\right)\omega'_s Sin\phi Sin\delta} \tag{3.43}$$

Where w'_s is the sunset hour angle for the tilted surface for the mean day of the month, given by [19]:

$$\omega'_s = \min\begin{bmatrix} Cos^{-1}(-\tan\phi\tan\delta) \\ Cos^{-1}(-\tan(\phi-\beta)\tan\delta) \end{bmatrix} \quad (3.44)$$

"min" implies to the smaller of the two in the brackets.

Where is no information on the properties of the material near a solar collector, the recommended value for ρ_G, is 0.7 and 0.2 with and without snow respectively [18].

3.3.4. Modelling results and discussions

A mathematical model (Solrad model) was built using the correlations described in the previous sections in a Microsoft Excel® spreadsheet to determine atmospheric parameters such as daylight hours, incident angles, clearness index, solar hour angles, monthly and hourly average beam, diffuse and ground reflection for both horizontal and tilted surfaces, for regions in the northern hemisphere. The main input to this model is only the monthly average global radiation on horizontal surface, but in the absence of such data, clearness index can also be used. Also optimization of solar radiation falling on a tilt surface was carried out using Golden Section Search (GSS) and Quadratic approximation methods in the Engineering Equation Solver (EES) for the determination of monthly and seasonal optimum angles.

Meteorological data of Birmingham (52.48^{o}N, 1.88^o W) UK, obtained from Atomwide limited, for the period of six years (2006 to 2012) was used for testing the model. The station use Vantage Pro2 Plus instruments for the recording of the atmospheric data. There is no detailed discussion on the results for Birmingham, because it is only used for validation of the model, so that it can be used for all regions in the northern hemisphere. Upon validation, the model was used to characterize the climatic condition of Kano, by using measured daily

average global radiation on horizontal surface obtained from Nigerian Meteorological Agency, NMA [140].

3.3.4.1. Modelling results for solar radiation in Birmingham, UK

Measured global radiation data on horizontal surface recorded in half hour interval (in W/m^2) from Atomwide station, was used as input to the model for testing its performance. Monthly average was calculated and converted to $MJ/(m^2.day)$ to conform with the units of the set up as shown in Figure 3.5.

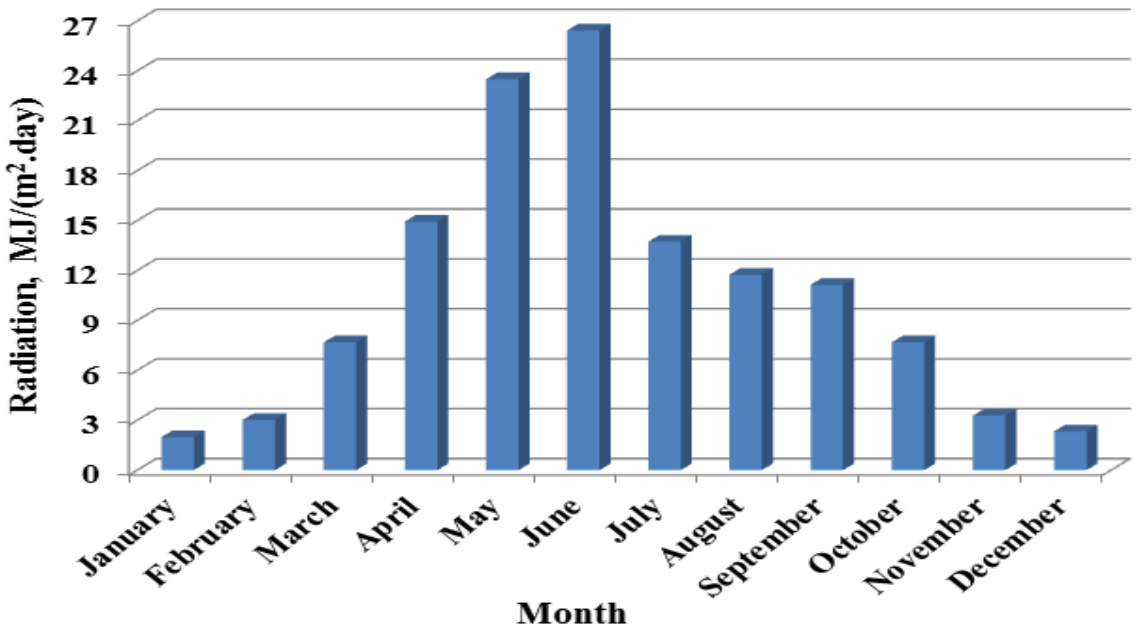

Figure 3.5 Monthly average Global radiations on the horizontal surface of Birmingham, UK

The monthly average daylight hours obtained from this model is shown in Figure 3.6 and is of good agreement with what is measured for Birmingham. Also the monthly tilt factors obtained from this model was compared by those reported by Jan and Frank,1982 [23] for different latitudes and the results are in good agreement as shown in Figure 3.7 with deviation

of 4% and 7% for the tilt equal to the latitude of Birmingham and 90^{o} inclination respectively.

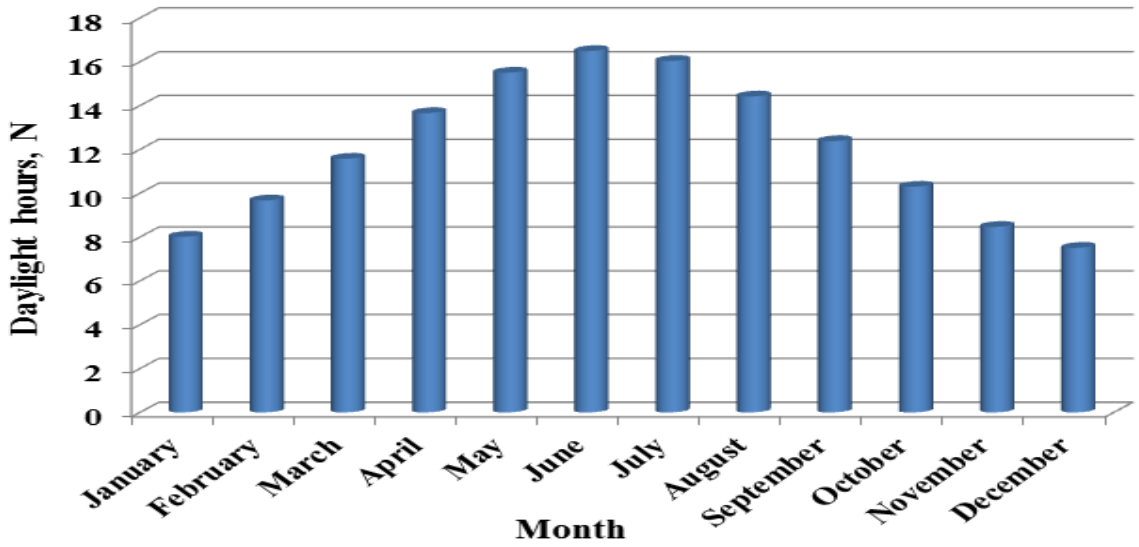

Figure 3.6 Monthly daylight hours of Birmingham

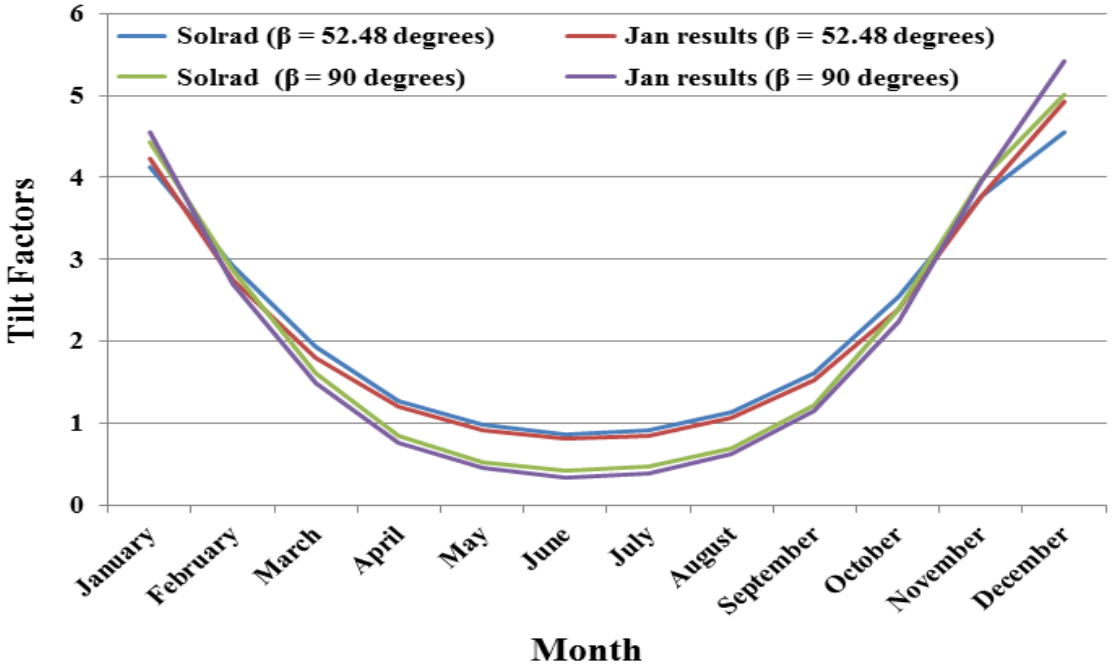

Figure 3.7 Comparison of the monthly beam radiation tilt factors for different models

3.3.4.2. Modelling results for Kano, Nigeria

Using daily average global radiation obtained from NMA, the radiation parameters for Kano were predicted using the model described in 3.3. Radiation data of Kano for 37 years (1971 to 2008) were obtained from the agency and were averaged to monthly values. However, data of 2008 was used in the model because it is the latest available for this research and it showed a difference of 5.8% when compared with the whole 37 years data average.

Monthly average radiation was obtained by averaging the daily measured data as shown in Figure 3.8. From this Figure, it can be seen that the region receives significant amount of radiation throughout the year with the highest values in March (26.78 MJ/ (m^2.day). This is due to the latitude of Kano which favours longer sunlight hour, incident angles of the rays and seasonal variation.

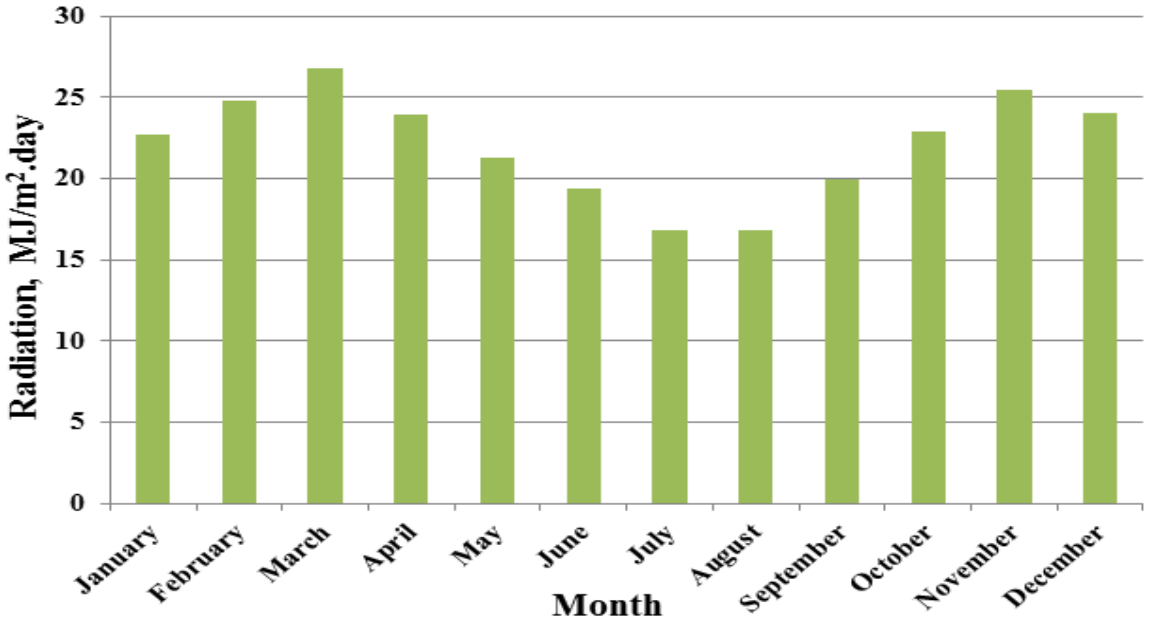

Figure 3.8 Measured monthly average global radiation on horizontal surface (Kano)

Analysis of the radiation falling on a surface of a solar collector at a slope other than the horizontal requires separate treatment of direct and diffuse radiation components. Also the

predictions of long term performance of specific concentrating system are usually based on the direct component available. Hence the beam and diffuse components were predicted from the global and are showed in Figure 3.9 and the clearness index is presented in Figure 3.10. It can be seen that significant amount of diffuse component is obtained between April and September where the percentage lies between 34 and 47% with the peak in July and August. This period corresponds to the raining season where the sky is usually covered with clouds which cause the scattering of the incoming radiation.

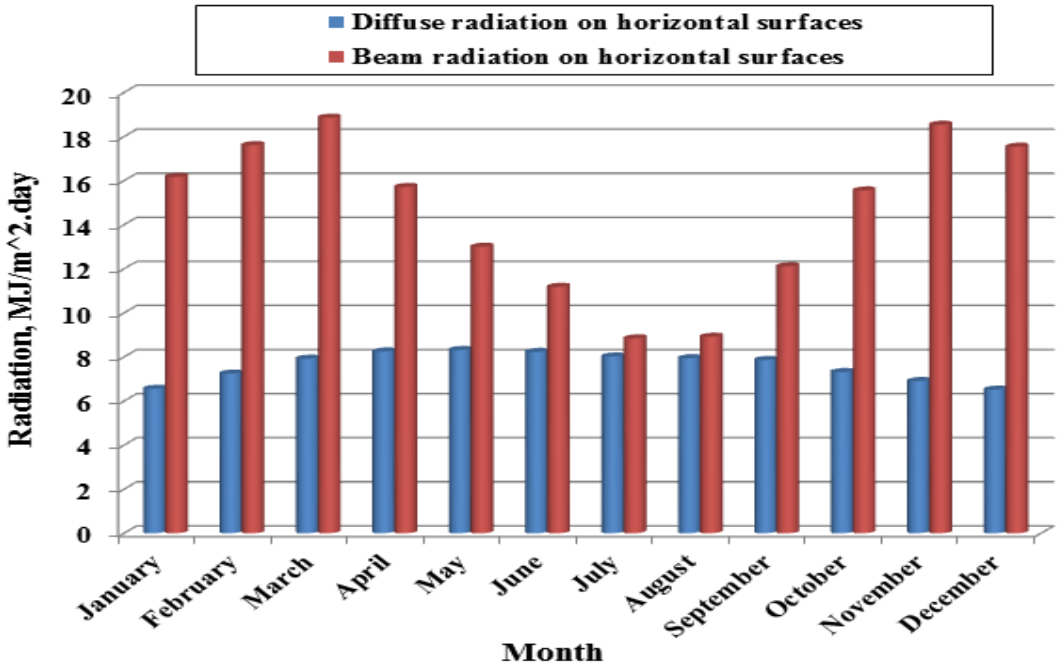

Figure 3.9 Monthly average predicted beam and diffuse radiation on horizontal surface of Kano

These results can further be justified with the low values of clearness during this period as shown in Figure 3.10 where the values tend to be declining from the mid of March through August and increase from the mid of September. The annual average clearness index is 0.63 with highest value of 0.81 in November. These results further show that solar collector

capable of receiving significant amount of diffuse radiation like low concentrating CPC will be a good choice for this region.

The region also shows no significant difference in the daylight hours throughout the year, as shown in Figure 3.11. The length of the days tends to be longer during the months of April through September with the highest in June (12.7 hours) and this corresponds to wet and warm season. However, the difference is not significant and the annual average daylight hour is 12.00.

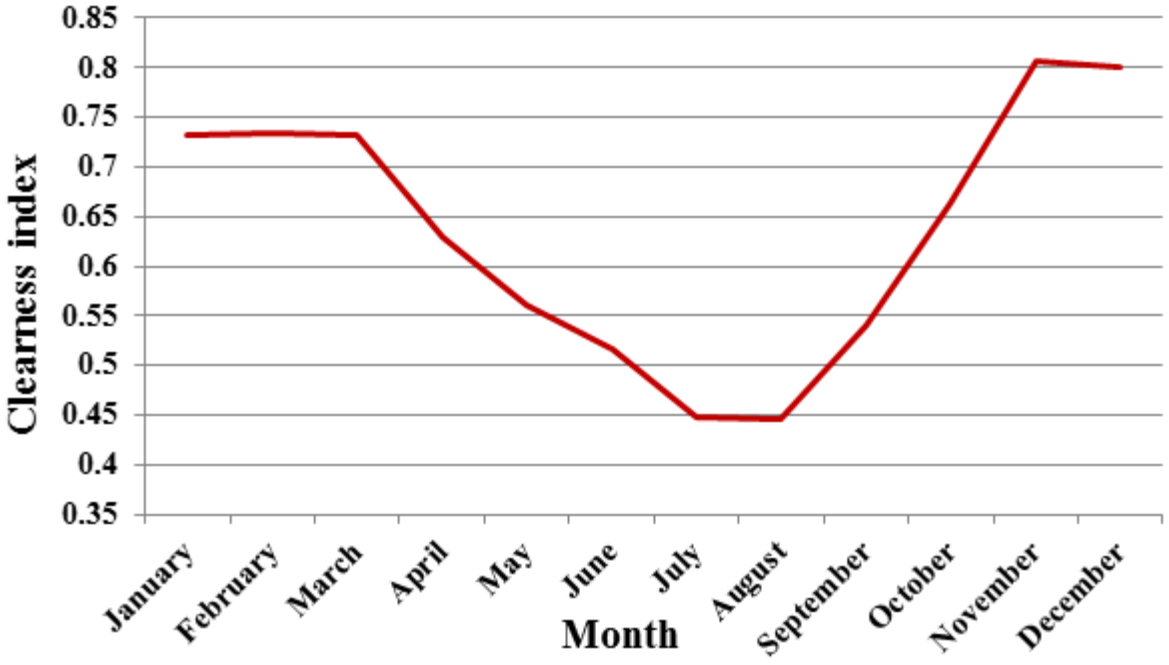

Figure 3.10 Monthly average clearness index on the surface of Kano

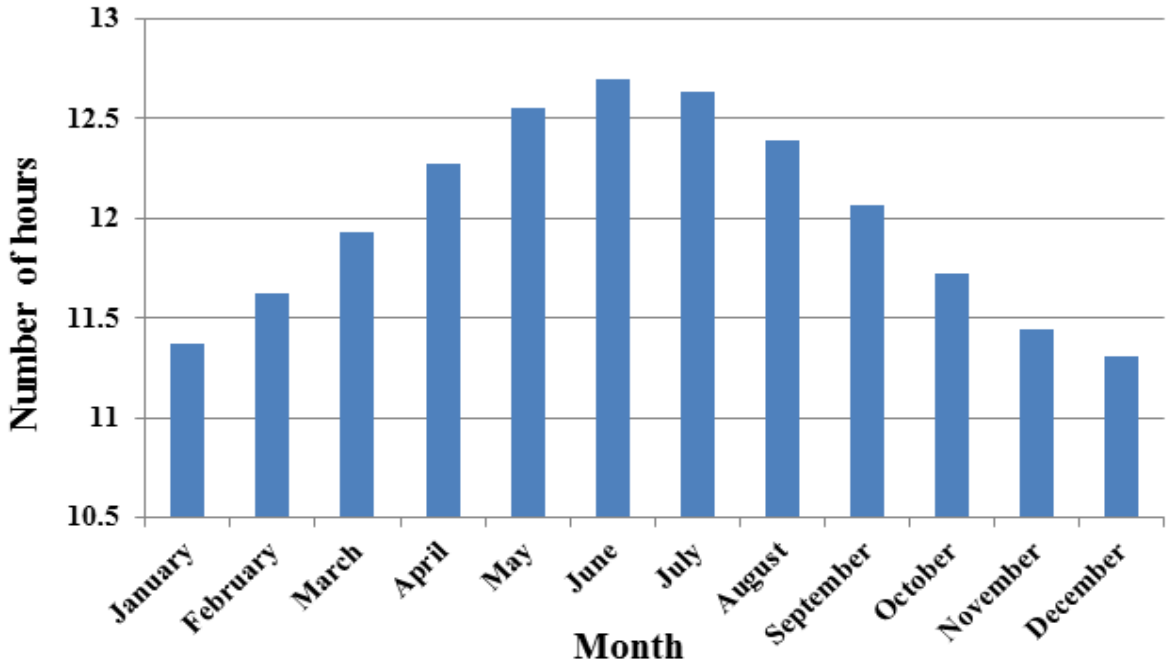

Figure 3.11 Monthly average Daylight hours of Kano

In order to investigate the effects of tilting a solar collector at an angle, β relative to the horizontal, eight different tilt angles, related to the latitude of Kano (as shown in Table 3.2) were simulated and the value of the monthly global radiation is obtained for each case and compared with the horizontal orientation as presented in Figure 3.12. It can be seen from such figure that the monthly average global radiation varies with the change of the tilt angle throughout the year. But the results show that there is no particular angle that gives increase in the radiation for all the months due to the variation of the monthly tilt factor (as shown in Figure 3.13) and ground reflection. The two figures show similar patterns, which further show the dependency of the radiation received by a tilted surface on the tilt factor. The fluctuation of the beam tilt factor throughout the year is attributed to the variation of the sunset hour angle which in turn depends on the solar declination that varies with the day of the year.

Table 3.2 Collector tilt angles simulated and their relationship to the latitude of Kano

S/N	Tilt angle, β /^{o}	Relation to the latitude
1	0	$\beta = \phi - 12.05^o$
2	2.05	$\beta = \phi - 10^o$
3	10	$\beta = \phi - 2.05^o$
4	12.05	$\beta = \phi$
5	22.05	$\beta = \phi + 10^o$
6	27.05	$\beta = \phi + 15^o$
7	42.05	$\beta = \phi + 30^o$
8	57.05	$\beta = \phi + 45^o$

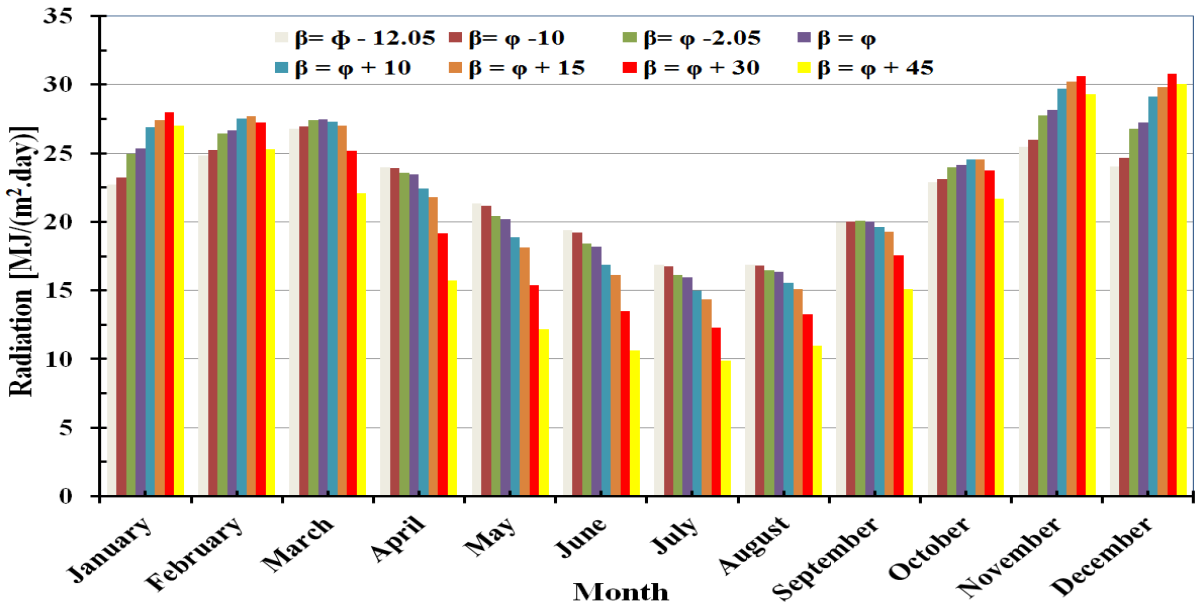

Figure 3.12 Monthly average global radiation at different tilt angles

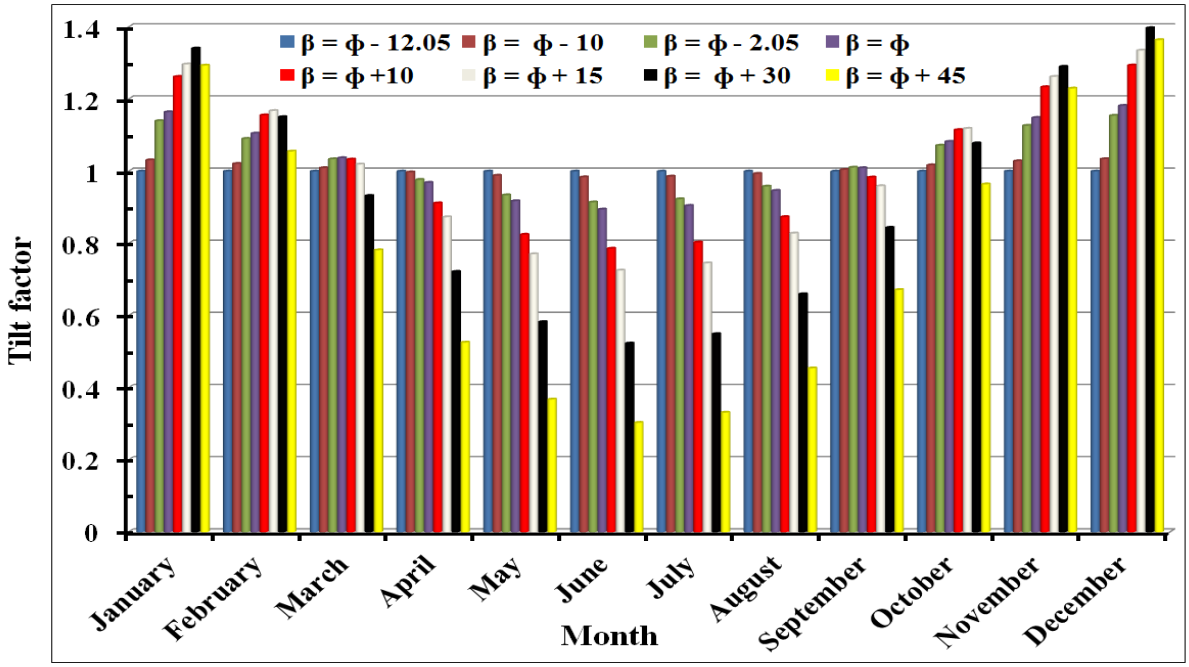

Figure 3.13 Monthly average tilt factors for different tilt angles

From the modelling results in Figures 3.12 and 3.13, the following can be deduced on the effects of tilt angles for Kano:

1) Generally, there is increase in global radiation compared to the horizontal orientation from October to March as the tilt angle increases up to $\beta = \phi + 15^o$ with the maximum and minimum increase in December (24.1%) and March (0.84 %) respectively. But for the month of March, the amount starts decreasing when $\beta > \phi$, which shows that the optimum tilt for such month lies between $\beta = \phi$ and $\beta = \phi + 10^o$. However, when the tilt angle is greater than $\beta = \phi + 15^o$, the trends for other months changes as follows:

   i. There is increase in radiation at $\beta = \phi + 30^o$ compared to $\beta = \phi + 15^o$ for November, December and January, but decreases when $\beta = \phi + 45^o$. This shows that the optimum tilt for these months lies between these extremes (ie $\beta = \phi + 30^o$ and $\beta = \phi + 45^o$).

ii. The radiation decreases when $\beta = \phi + 30^o$ compared to $\beta = \phi + 15^o$ in October and February and this shows that the optimum tilt angle lies between these angles.

2) There is a decrease in the global radiation as the tilt angle increases in the months of April to August, with the highest loss of 45.23% in June when $\beta = \phi + 45^o$. Hence zero degrees (horizontal) is the best for these months.

3) March and September tends to be transition months as they show irregular patterns as the tilt angle increases;

   i. For March, there is insignificant increase in global radiation as tilt angle increases but reaches maximum of 2.5% at $\beta = \phi$. It decreases for any angle greater than the latitude.

   ii. For September, there is insignificant increase in the global for all tilt angles equal or less than the latitude with highest (0.52%) at $\beta = 10^o$. The radiation decreases for any angle greater than the latitude.

Due to the trends of these results, more investigations are required for the determination of optimum collector tilt angle for Kano. Hence parametric studies and optimization for the determination of the optimum tilt for the months, season and the year were carried out in the next sections of this chapter.

3.3.4.3. Results of hourly radiation

Hourly values of the radiation components are usually needed for estimating the performance of solar collectors, although the actual values depend on the sunshine hour and the nature of the sky. Isotropic and anisotropic sky approaches were used in modelling the hourly hemispherical, beam and diffuse on both horizontal and inclined surfaces from the measured

global radiation on a horizontal surface in Kano. For isotropic sky approach, eleven hours (which is the minimum daylight hours) were considered for each month and the average solar hour angles, w, for the mean days were used. While for anisotropic approach, the radiation between two hours is determined by considering the midpoints of such hours (w_1 and w_2) with w_2 being larger as shown in the Table 3.3.

Table 3.3 Solar hour angles for anisotropic approach

Hours angles interval/^{0} (w_1 and w_2)	**Solar hour angle/^{o}, at the Midpoint of the interval**
Between -75 & -60	-67.5
Between -60 & -45	-52.5
Between -45 & -30	-37.5
Between -30 & -15	-22.5
Between -15 & 0	-7.5
Between 0 & 15	7.5
Between 15 & 30	22.5
Between 30 & 45	37.5
Between 45 & 60	52.5
Between 60 & 75	67.5

The hourly hemispherical radiation on horizontal surface was predicted from the global values for each month as shown in Figure 3.14. For this orientation, the two approaches gave the same results because there is no slope and they have the same trends as the monthly average obtained in the preceding section.

Figure 3.14 shows increase in the radiation as the sun moves towards the zenith (with peak at the zenith) and decreases as the sun moves away with least values at the sunrise and sunset. But the intensity depends on the time of the year and the nature of the atmosphere in the region under consideration and this account for the variation throughout the year as seen in the figure.

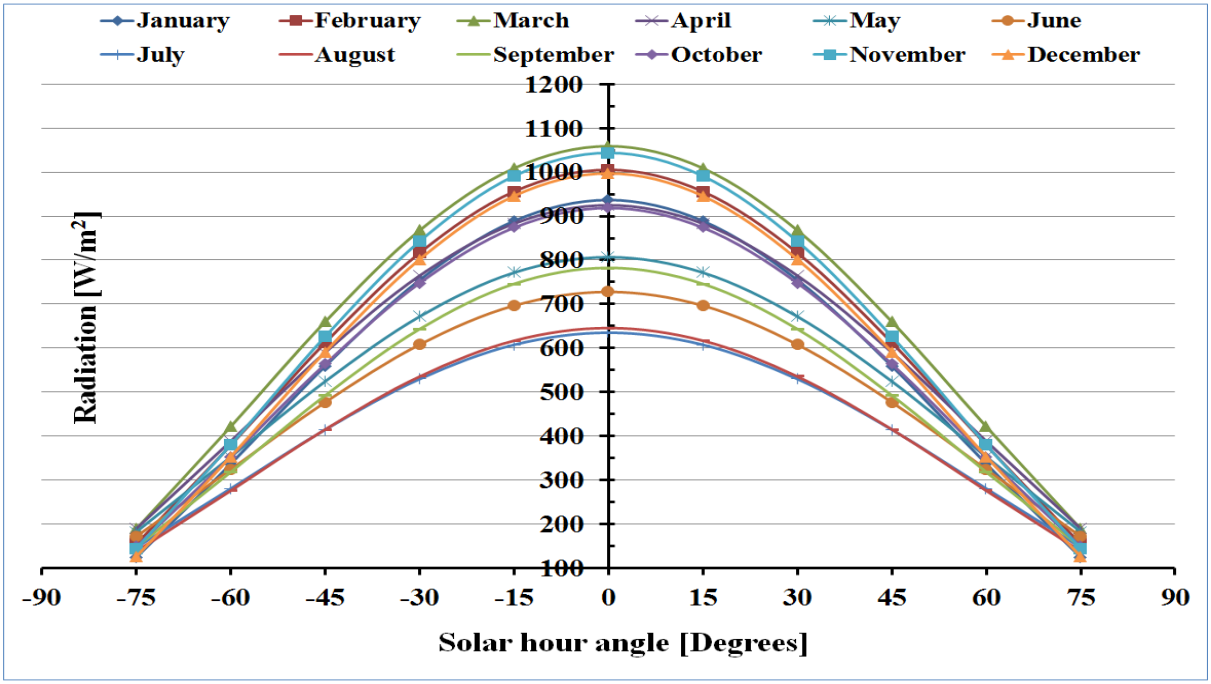

Figure 3.14 Predicted hourly radiation falling in Kano for all months at β = 0

The two approaches were compared by the results of hourly total radiation obtained at tilt angle equals to the latitude of Kano as shown in Figure 3.15 for December and June. It can be seen from the figure that an improvement was achieved in the predicted radiation on the

surface by using anisotropic approach compared to isotropic but it is more in December than in June. This is due to the modifications made to the isotropic by taking into account the circumsolar diffuse and horizon brightness instead of taking diffuse component as isotropic.

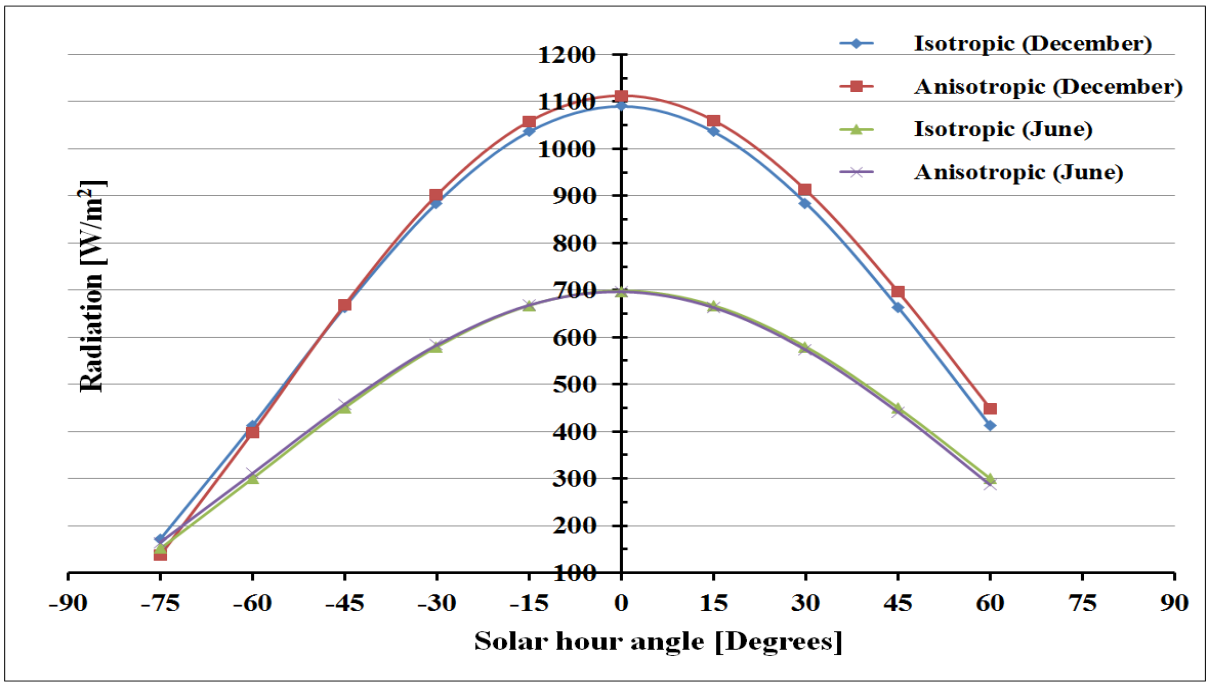

Figure 3.15 Predicted hourly total radiation obtained by the two approaches

Since anisotropic model gives an improvement in the radiation on tilted surface, the approach is used to study the effects of collector tilt angle on the hourly radiation falling on surfaces tilted to five different angles from the horizontal. Two out of the twelve months were presented; one in the winter (December) and the other in summer (June). The effects of the tilt angle on hourly radiation follows similar trends to that of the monthly average presented in the foregoing discussions. In December, the hourly radiation increases with the increase in the tilt angle with $\beta = \phi + 15^{o}$ as the best among the range tested with a daily average increase of 26% as shown in Figure 3.16.

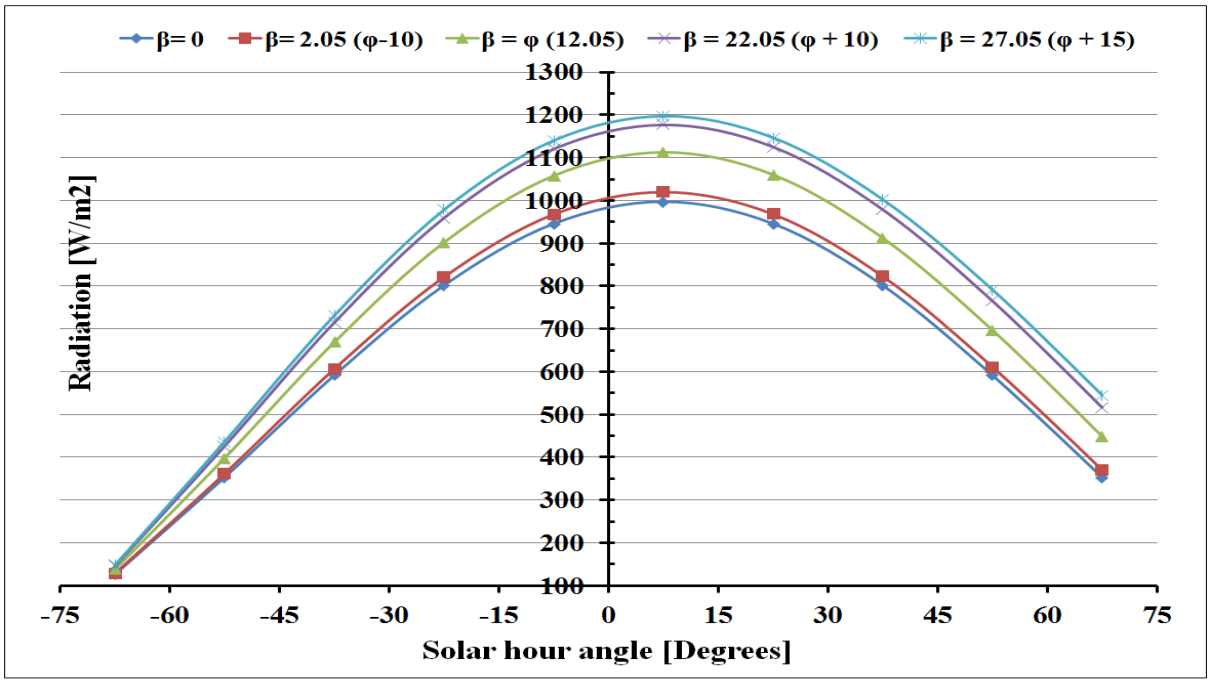

Figure 3.16 Predicted hourly hemispherical radiation in Kano at different tilt angles (December)

But on the other hand, the radiation falling on each hour of June in Kano is decreasing as the tilt angle of the collector increases and the best orientation being horizontal ($\beta = 0$) as shown in Figure 3.17. This is also similar to the trends obtained for the monthly average radiation on tilt surfaces for the summer months. A solar collector tilted to an angle of 27.05^{o} (ie $\beta = \phi + 15^{o}$) in June, will experience a daily average loss in radiation of 19% compared to the horizontal position.

The results of hourly radiation agreed well with that of the monthly average and it also emphasizes the need for more iteration in order to determine the optimum tilt angle for every month.

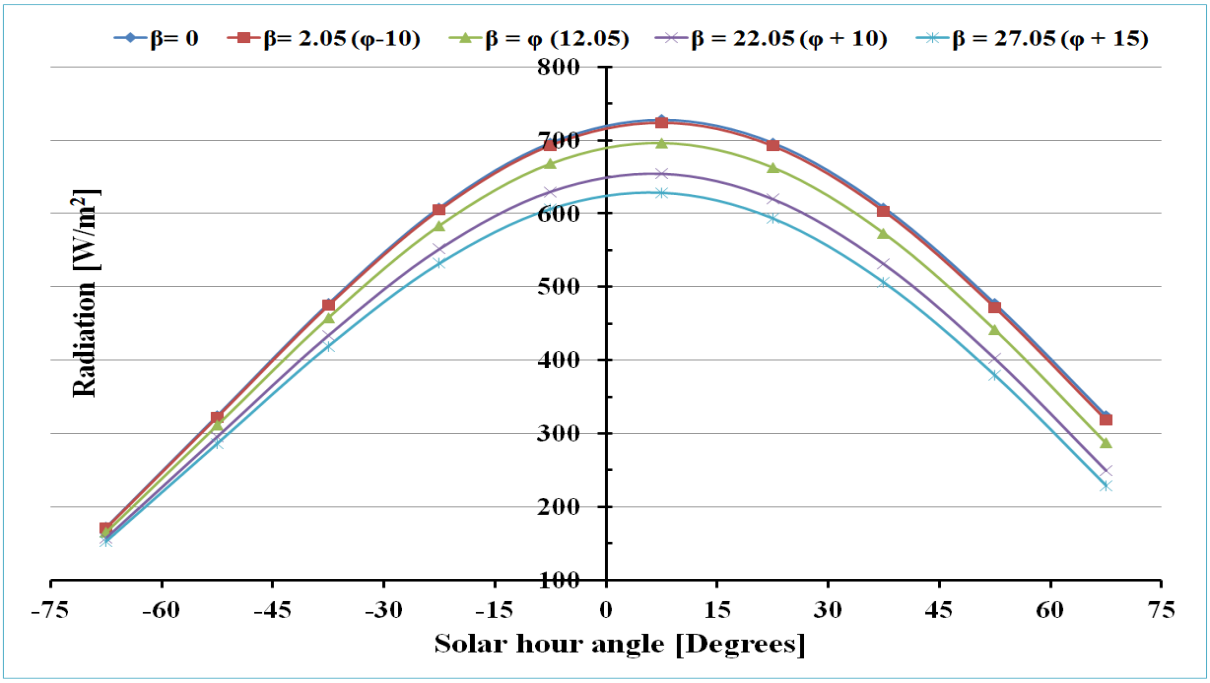

Figure 3.17 Predicted hourly hemispherical radiation in Kano at different tilt angles (June)

3.4. Monthly optimum tilt angle of Kano

The results of section 3.2 showed that there is no single tilt angle that gives increase in the radiation falling on a surface throughout the year and the trends in some months show that the optimum can be obtained between certain ranges of tilt angles. In this section, genetic algorithm in Engineering Equation Solver (EES) is used in determining the optimum tilt angle for Kano within the ranges identified in the previous sections. The model will be called Eesrad model in this thesis.

3.4.1. Effects of tilt angle on the global radiation using Eesrad model

Parametric studies was first carried out for all the months and the global radiation was determined from 0^o to 80^o tilt angles using the measured radiation on horizontal surface, mean day and solar declination of each month. The program code of the developed model is shown in Appendix A and the result of the parametric study is presented in Figure 3.18. From the

Figure, it can be seen that the global radiation reach peak value for each month after which it starts decreasing and these ranges corresponds to those found in the Solrad model, hence the two models show a good agreement. But the advantage of Eesrad over Solrad model is that it simulates wider range of angles with less computational times and the optimum tilt for each month can easily be obtained. It can also be seen that all the summer months (From April to August) show a similar trend of decreasing radiation as the tilt angle increases while for other months, there is increase and then decrease in the radiation depending on the tilt angle and the month of the year.

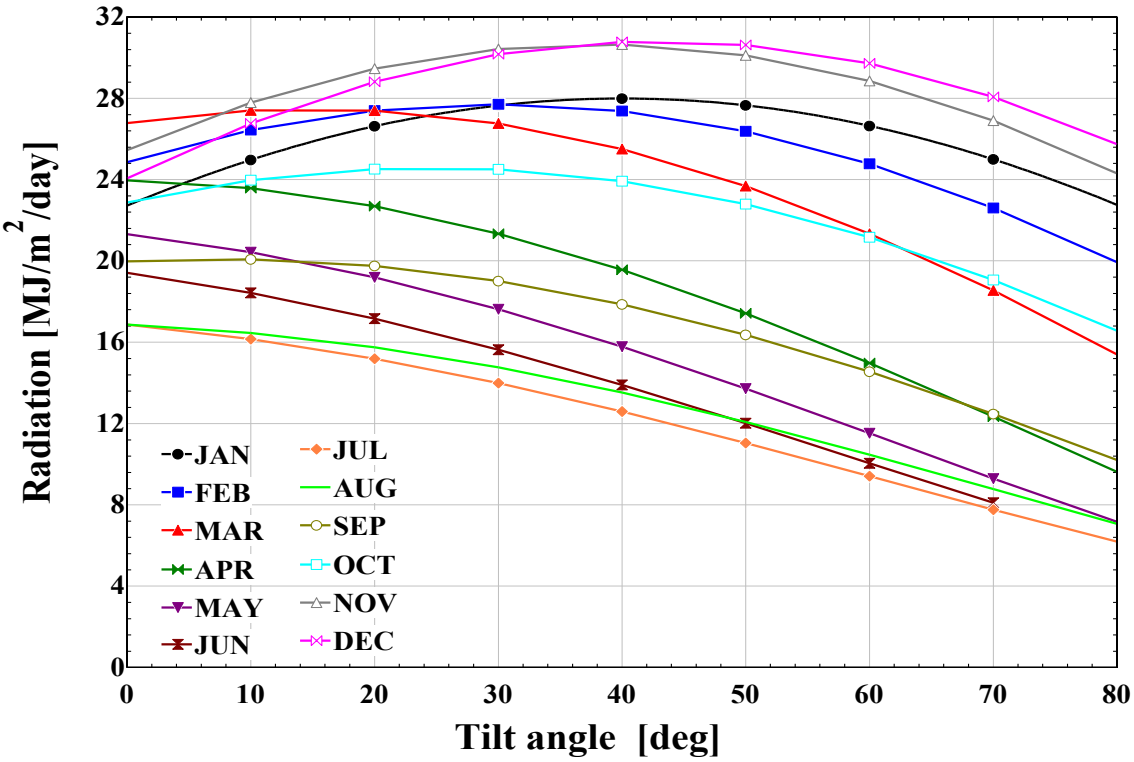

Figure 3.18 Monthly average global at different tilt angles

3.4.2. Optimum tilt angles

Using Golden Section Search (GSS) and Quadratic approximation methods in EES, the optimization was carried out for the twelve months. The global radiation at tilt was set as the

objective function (to be maximized) while the tilt angle was selected as the independent variable. The maximum function calls and relative convergent tolerance were set as 400 and 1.00E-09 respectively to maximize the accuracy of the results. Figures 3.19 and 3.20 show the results of the optimization process for winter and summer months respectively. From the two figures, it can be seen that a steady state is reached at the optimum angles after few iterations showing the optimum tilt angles and the corresponding values of the global radiation for each month.

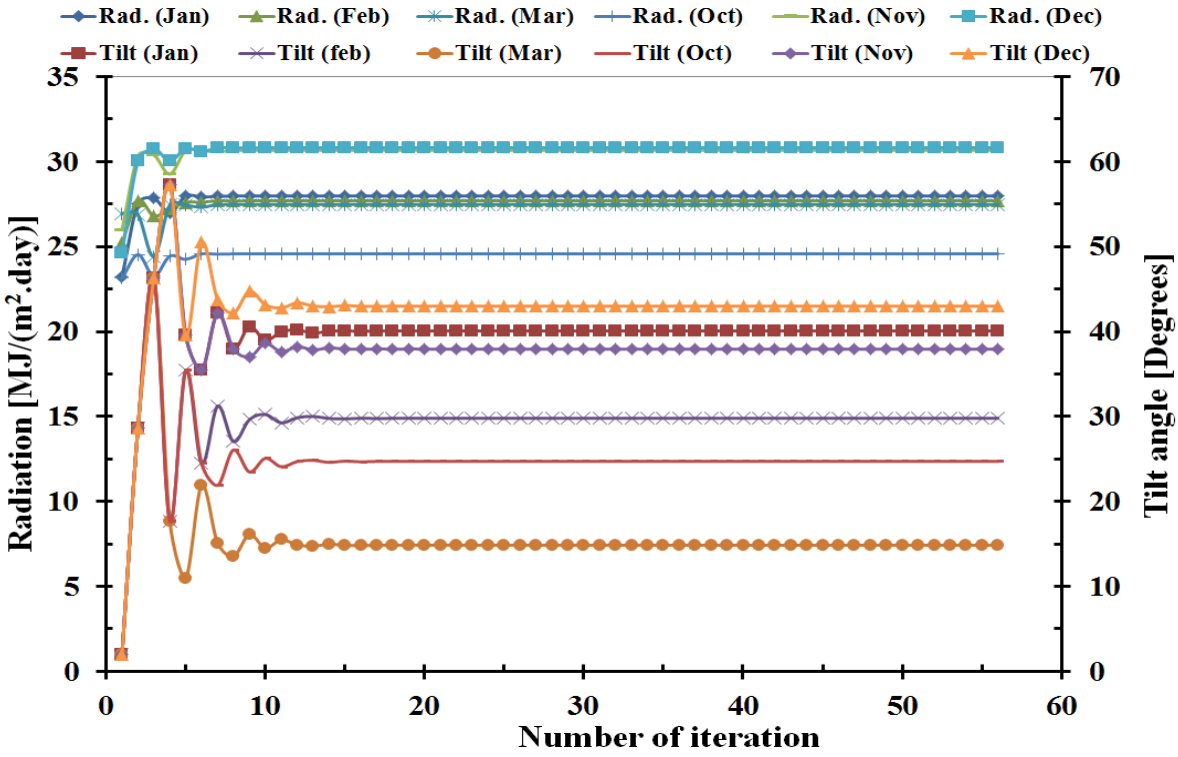

Figure 3.19 Monthly optimum tilt angles and the corresponding radiation values against the number of iterations (winter)

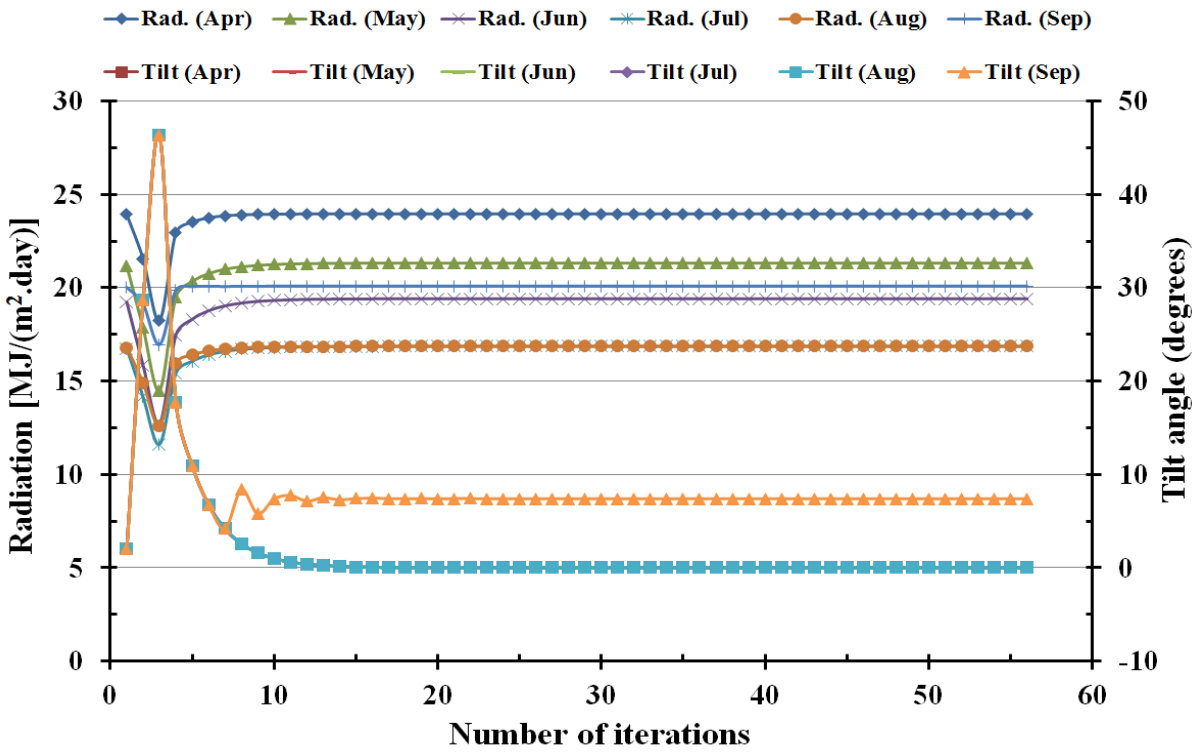

Figure 3.20 Monthly optimum tilt angles and corresponding radiation values against the number of iterations (summer)

It can also be seen that the optimum angles obtained for each month falls within the range previously suggested by the Solrad model, which further shows the agreement of the two models and the accuracy of the predicted optimum angles. From April to August zero degrees is shown to be optimum (Figure 3.20) while for October to February, their optimum angles ranging from 24.72^{o} to 43^{o} (Figure 3.20) with December having the largest (43^{o}). March and September have 14.86^{o} and 7.41^{o} as optimum respectively.

3.4.3. Solar Energy received in Kano

The solar energy to be received by a surface in Kano when it is horizontal, sloped to the latitude and to the optimum tilt angles of every month for an average of eleven daylight hours is shown in Figure 3.21. Comparing $\beta = \beta_{opt}$ and $\beta = 0$, gives 28.6% and 24.8% increase in energy receive in December and January respectively. For $\beta = \beta_{opt}$ and $\beta = \phi$, January and

December will still have the highest increase of 11% and 13.2% respectively. While 13.7% and 12.4% increase in energy receive in December and January will be achieved when comparing $\beta = \phi$ and $\beta = 0^o$ but with loss in performance from April to August; highest in June (5.2%). Comparison of the percentage increase in solar energy received in Kano between the optimum and other angles is shown in Figure 3.22.

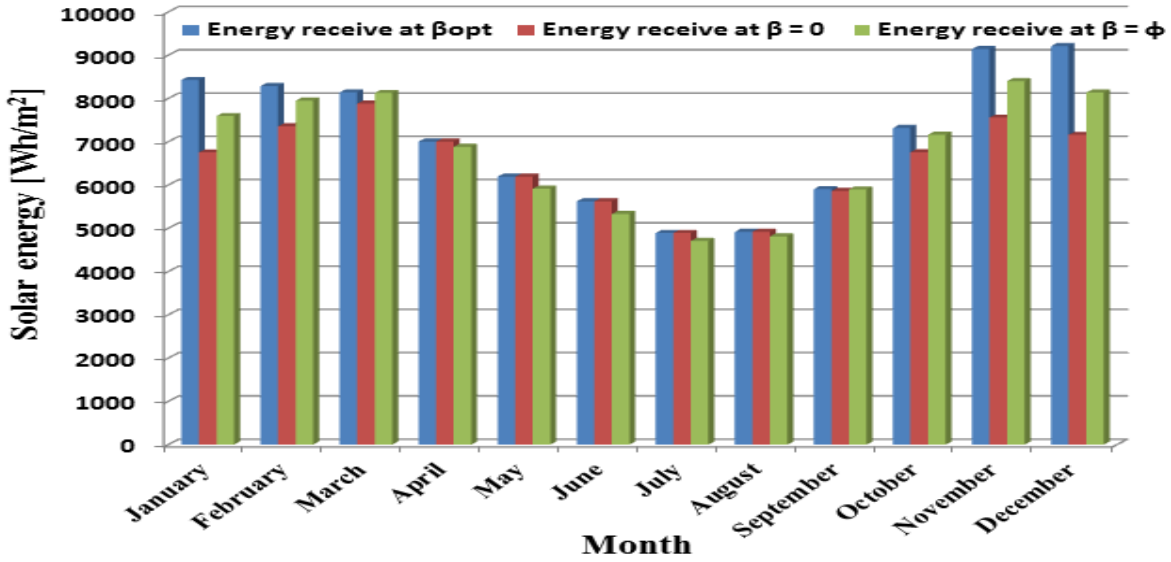

Figure 3.21 Daily average solar energy receive at different tilt angles for each month

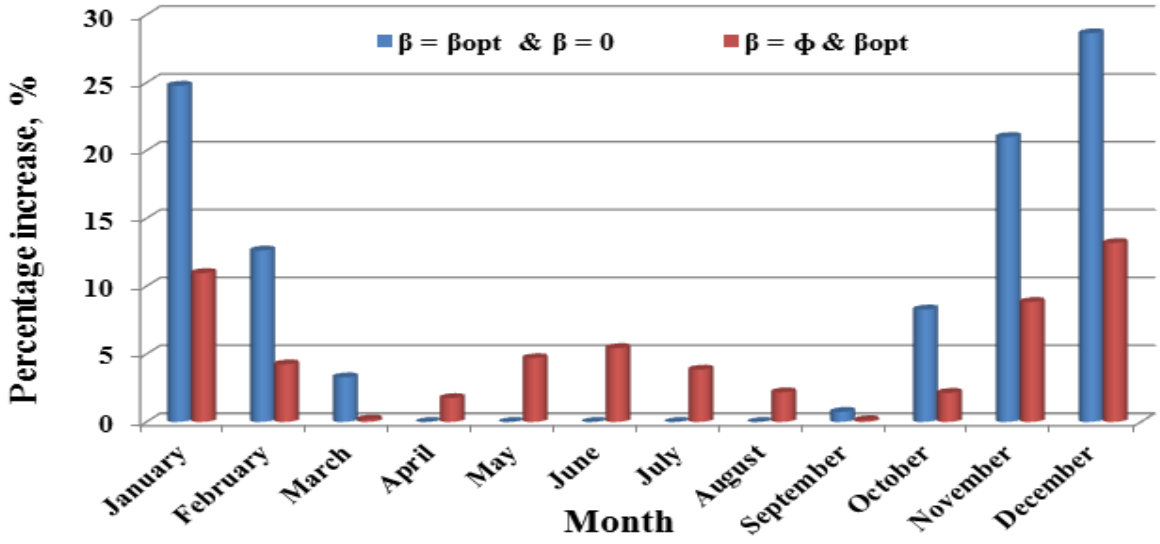

Figure 3.22 Comparison of percentage increase in the energy received between optimum tilt and other angles

3.5. Summary

Most of the weather stations in the world (inclusive of those in Nigeria) measure weather condition such as global radiation on horizontal surfaces, sunshine hours, temperature, humidity, etc. but only few stations records diffuse and beam separately and also only few measure these components on tilted surfaces. In Nigeria, there is no report of any weather station that measures diffuse/beam or radiation on tilted surface. As seen in chapter 2, few attempts were made to model global radiation from other weather data for Kano, but no work was reported for fully modelling its weather condition (despite its huge solar potentials) like predicting the beam, diffuse, tilting effects, optimum tilt angles, etc., hence the aim of this chapter. This chapter presented an overview of the solar radiation models reported in the literature. Mathematical model (Solrad model) was developed for modelling solar radiation components in the northern hemisphere, tested using global radiation of Birmingham, UK and used in modelling the weather conditions of Kano, Nigeria. Optimization was carried out using another model developed in Engineering Equation Solver (Eesrad model) which led to the determination of monthly, seasonal and annual optimum tilt angles for Kano.

Based on the results obtained from the two models and the analysis carried out in this chapter, the following conclusions can be drawn for Kano's radiation characteristics:

a) Kano has high radiation falling on its surface almost throughout the year with maximum value in March [26.78 MJ/(m^2.day)] and minimum value in August [16.86 MJ/ (m^2.day)], annual average clearness index and daylight hours of 0.63 and 12.00 respectively.

b) The amount of diffuse radiation component is significant in some months with July having highest (47.55%) and the least in December (27.1%)

c) Tilting a solar collector to an angle relative to the horizontal surface of Kano affects the amount of the radiation falling on it depending on the tilt factors.

d) The choice of the best tilt angle for Kano depends on whether the collector will be fixed or adjusted (monthly or seasonally). The following recommendations are put forward for Kano:

    1) Fixed collector: For the collector to be fixed at an angle throughout the year without adjustment, the best tilt is to the latitude of Kano ($\beta = \phi = 12.05^{o}$) because of uniformity and having radiation gain in seven month (highest of 13.2% in December) and annual average of 7.3%. It will experience radiation loss in five month (maximum of 6.7%) and annual average of 4.7%. Another option for fixed collector is zero degrees tilt ($\beta = 0^{o}$) and the choice between the two will depend on the cost of the tilt mechanism and the type of the solar system.

    2) Monthly adjustment: The optimum angle for each month has been determined and the collector can be tilted to such angles shown in Figures 3.19 and 3.20 to maximise the radiation collected. This is best option because there will be significant radiation gain throughout the year with 28.6 and 24.8% in December and January respectively. Also the maximum radiation obtainable in each month is received and there will be no radiation loss throughout the year.

    3) For seasonal tilt:

- $\beta = 27.05^{o}$ ($\phi + 15^{o}$) is the best angle for the months between October and March, with the highest increase in December (24%) and seasonal average of 14%.

- $\beta = 0$ ($\phi - 12.05^{o}$) is the best angle for the months between April and September. This is due to the significant amount of diffuse component in these months (as shown in Figure 3.9) and the best angle for capturing it is horizontal orientation, because it is distributed randomly in the sky. Also in these months (especially June to September), the northern hemisphere is tilted towards the sun, thus sun rays hit normal to the surface.

The monthly tilt is the best if the collector is to be adjusted; this is because it achieves the maximum radiation obtainable in each month without radiation loss throughout the year. Since the same sloping mechanism will be required by seasonal and monthly options, and the former gives more advantages, then it should be recommended for Kano but with additional labour for the adjustment every month.

4) A solar collector sloped to the optimum monthly tilt angles in Kano will receive 85,054.85 Wh/m^2 (monthly average of 7, 087.9 Wh/m^2) annually based on 11 sunshine hours.

CHAPTER FOUR

4. Design and Manufacturing of a Continuous Solar Simulator

4.1. Introduction

The test of solar systems can be done outdoor (under real sun) or indoor by the use of a device called solar simulator. To enable testing of the HPCPC to be developed in this work, a solar simulator is required so that the test can be done at any time and under different amount of irradiance. This chapter gives details of the optical design, manufacturing, assembling and characterization of a continuous solar simulator developed in the University of Birmingham, UK. It begins with basic theory on the concept of solar radiation spectrum and design considerations for a solar simulator. Detailed investigations on the performance of different reflectors were carried out, but as initial stage of the work an off - the shelf lamp with elliptical reflector was used due to time and budget constraints, but the study conducted can be used for the manufacturing of large area simulator.

4.2. Solar spectrum

Solar energy travels from the sun to the earth in the form of electromagnetic waves. Electromagnetic waves are waves consisting of electric and magnetic fields and transport energy. They are characterised by wavelength, λ, and frequency, f and distribution of these waves makes the electromagnetic spectrum (Figure 4.1).

Solar radiation received on the ground has most of its energy between wavelengths of 0.29 to 3 μm which are found in the ultraviolet light, visible and infrared radiation. Over 90% are from visible light and near infrared while less than 10% is ultraviolet distributed as follows as shown in Figure 4.1 [19]:

- Ultraviolet – 8% Wavelength less than 380nm
- Visible light – 43% Wavelength between 380nm and 750nm
- Infrared – 49% Wavelength between 750nm and 1mm

As explained in chapter three, the solar radiation reaches the earth in two forms; beam and diffuse and the intensity of solar radiation received on the earth surface differs from one region to another. The magnitude also changes with the time throughout the day due to the length of the path that the rays travel before reaching the surfaces and this is defined by the air mass AM (as explained in section 3.1).

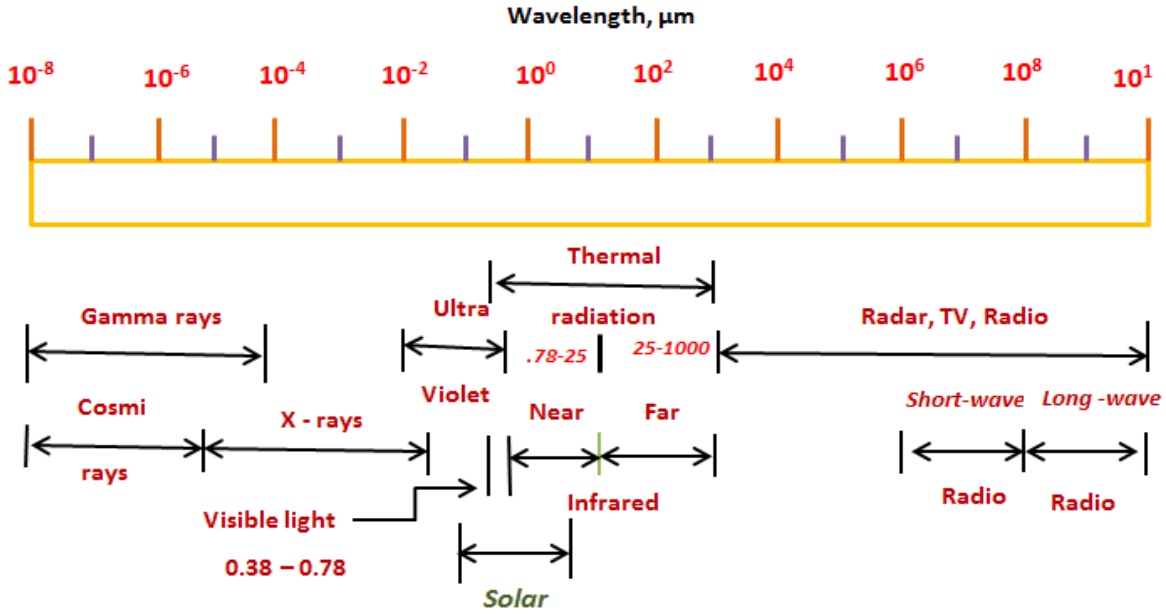

Figure 4.1 Electromagnetic radiation spectrums [19]

4.3. Solar simulator

Solar simulator is a device that produces illumination close to that of the real sun. According to the ASTM E927 and IEC 904 -9 standards, solar simulator has to simulate the solar radiation and spectrum. It consists of all or some of the following:

- Light source and associated power supply
- Reflector to house the lamp
- Optical filter to modify the output beam (optional)
- Necessary controls to operate the simulator and adjusting irradiance

Using solar simulator offers many advantages in solar energy research because it allows testing of solar systems independent of the weather condition. Other advantages compared to the use of real sun are:

- ability to control solar intensity to suit various regions
- steady state can be achieved
- accelerates solar research since testing of solar systems can be done at any time of the day or year
- ability to control other climatic conditions like wind and temperature
- Possibility of repeating tests on solar systems under the same conditions of intensity, temperature and wind

However, using solar simulator in testing solar systems is faced by problems of spectral match with that of the sun, achieving collimated rays and the uniformity of the flux on the receiver. Hence the flux distributions on the receiver, collimation of the rays and the light spectrum distributions are the issues and the challenges that require attention while designing a solar simulator.

4.3.1. Types and classifications of solar simulator

There are basically three types of solar simulators; steady state (or continuous), pulse or flash. Continuous simulator (CS) refers to the simulator where the illumination continues throughout the testing period. They are usually designed for wide range of intensity ranging from less than one sun (1000W/m^2) to numerous suns by utilizing number of lamps [141]. Flashed simulator (FS) provides illumination at an interval of few milliseconds and hence high intensity can be achieved. It is aimed to avoid unnecessary heating of the testing system, but its spectrum and intensity tends to be transient due to the nature of its operations. Pulsed simulator (PS) is an intermediary between the continuous and the flashed whereby it uses shutter to close and open a continuous source of light. The pulse can be in the order of 100 to 800 milliseconds [141].

The lamp life for the PS is between 40,000 to 1 million flashes while CS has 1000 hours of continues working [141]. Due to the short flash duration of PS (between 2 and 10ms), the test cell must be able to respond within short time [141]. Both pulsed and continuous simulators are used for high and low concentration photovoltaic applications.

In order to assess the performance of SS especially the commercial brands, they are usually classified based on the acceptable tolerance for the three characteristics of their operations; spectral match, non-uniformity and temporal instability. They are classified into Class A, Class B and Class C based on the three international standards; American (ASTM E927), European (IEC 904-9) and Japanese (JIS C 8912 & JIS C 9833) standards.

4.3.2. Spectral match

The spectrum of solar simulator is required to resemble that of the sun with minimum deviation set by the international standards. For industrial testing, the AM is standardized as

AM0 (radiation in space), AM1D, AM1G, AM1.5D, AM1.5G, AM2D and AM2G, where D and G means direct and global respectively and this is due to the effects of latitude, altitude, time of the day, etc. on the air mass (AM). But AM1.5G is taken as the standard sun spectrum for non-space applications. All the three international standards gave the same allowable tolerance of spectral match for the three classes as presented in Table 4.1. Optical filters are usually used to correct the spectral mismatch especially in commercial simulators, but this increases the total cost of the device. Also informations about the spectrum of the different lamps are provided by the manufacturers as a guide for spectrum match.

Table 4.1 Spectral match tolerance based on ASTM, IEC and JIS [142, 143]

CLASS	SPECTRAL MATCH	PERCENTAGE, %
A	0.75 – 1.25	±25
B	0.6 – 1.4	±40
C	0.4 – 2.0	+100/-60%

4.3.3. Temporal instability

It is a measure of the ability of the light from a simulator to stay stable for a period of time like 1 minute, 1 hour, etc. Instability of a solar simulator T_{ins} can be calculated from [144]:

$$T_{ins} = \frac{q_{\max} - q_{\min}}{q_{\max} + q_{\min}} x100\% \tag{4.1}$$

Where $q_{\max}$ and $q_{\min}$ are the maximum and minimum irradiance measured in W/m^2 at the selected point on the target receiver at the specified time. Table 4.2 shows the allowable tolerance for the percentage instability according to the international standards.

Table 4.2 Temporal instability tolerance [142, 143, 145]

CLASS	ASTM	IEC	JIS
A	≤2%	≤2%	≤1%
B	≤5%	≤5%	≤3%
C	≤10%	≤10%	≤10%

4.3.4. Non - uniformity

This is a measure of the nonuniformity of the radiation from a solar simulator on the target surface and it is the most difficult requirement to meet by a simulator. The non-uniformity, S_{nu} of a solar simulator can be determined by [144]:

$$S_{nu} = \frac{\dot{q}_{\max} - \dot{q}_{\min}}{\dot{q}_{\max} + \dot{q}_{\min}} x100\% \tag{4.2}$$

Where $\dot{q}_{\max}$ and $\dot{q}_{\min}$ are the maximum and minimum irradiance measured over the target area. The international standards determine the simulator class based on the non-uniformity tolerance as shown in Table 4.3.

Table 4.3 Non-uniformity tolerance [142, 143, 146]

CLASS	ASTM	IEC	JIS
A	≤3% (for area ≥ 30x30cm)	≤2% (for area ≤ 30x30cm)	≤2%
B	≤5%	≤5%	≤3%
C	≤10%	≤10%	≤10%

According to the ASTM standard, the number of the mapping points should be at least 36 while for IEC it should be 64.

4.4. Brief literature review of solar simulators

Apart from commercial solar simulators manufactured by different companies, various types were developed and reported in literature for testing solar systems at different research institutions. Some are designed for non-concentrating applications and are characterized by uniformly distributed parallel rays while others are for delivering high flux on a target receiver. This section will present few of such simulators that are mainly developed in- house for research purposes. The choice of the reflector, lamp, intensity and the overall design are dictated by the intended applications of the simulator, which translate the basic requirements of the testing facility.

Optical properties of different shapes are utilized in the selection of the reflector depending on the intended application. Parabolic shapes are usually used for simulators designed for testing concentrating and multijunction systems where the rays are required to hit the target at normal angles. It is known that rays from a source of light placed at the focal point of parabola radiate parallel to its axis of symmetry. While ellipsoidal reflectors are usually utilized in high flux solar simulators because of its properties that all rays originating from one of its focus must pass through the other focus before they disperse.

High flux solar simulators are designed to concentrate flux on small target hence creating high power and are usually for solar thermal, thermochemical, high concentration PV (HCPV) and advanced high- temperature testing. Table 4.4 shows some high flux simulators reported in literature with the lamp and reflector types used.

Table 4.4 High flux solar simulators for solar thermal and thermochemical

Reference	Lamp type & Quantity	Type of reflector	Average flux, kW/m^2
[147]	10 x 15kW Xenon arc	Truncated ellipsoidal	6800
[148]	1 x 7kW xenon arc	Truncated ellipsoidal	3583
[149]	7 x 1.5kW metal halide	Conical	45
[150]	30 x 6 kW metal halide	Ellipsoidal	Varies
[151]*	12 x 7kW	Paraboloid	1 lamp was tested
[152]	1 x 20kW xenon arc	Ellipsoidal	612.24
[153]	7 x6.5kW xenon arc	Truncated ellipsoidal	3200
[154]	12 x 7kW xenon arc	Silicon – on-glass Fresnel lenses	151.54
[155]	7 x 6kW xenon arc	Truncated ellipsoidal	3500
[156]	1 x 75 kW Argon	Ellipsoidal	2380/4250

** The simulator was designed for 12 x7kW lamps but only one lamp was tested experimentally.*

Also commercial simulators are available from different manufacturers such as OAI Trisol 1800 nm solar simulator and I-V systems, Oriel 1000W continuous simulator, etc. Due to the cost of the commercial simulators, some in-house design were reported like a prototype simulator based on light emitting diode (LED) for measurement of current and voltage of amorphous silicon solar cell and light soaking. It is reported that the simulator meet class AAA requirements within 400 to 750nm for illuminated area of 18 x 18cm [157].

Dennis *et al.,* 2014 ([158] presented a solar simulator designed by using a high – power super continuum fisher laser for measuring the efficiency of crystalline and amorphous silicon and thin solar cells. A prism-based spectral shaper was coupled to the system for spectral correction to meet the required standard. Also a large area continuous solar simulator was designed and fabricated by [7] at the Heriot-Watt University, UK for indoor testing of PV cells using nine 1200W metal halide lamps. Maximum intensity of 851 W/m^2 was obtained for illumination area of 750 x 750mm, non-uniformity of 8.5% and maximum rays' collimation of 7.6^o.

From the brief literature survey, it can be seen that various solar simulators exist for indoor testing of solar systems manufactured either by commercial companies or fabricated in house by research institutions to test their research facilities. Some were manufactured completely from scratch while others utilized off – the - shelf materials for their systems due to some reasons like time and budget constraints.

As part of this research, a continuous solar simulator is designed, fabricated and tested based on the ASTM (E927) for testing solar concentrating systems in the University of Birmingham. The processes involved in the development of this simulator for this work is explained in the next section of this chapter.

4.5. Design of a continuous solar simulator for testing solar systems

4.5.1. Basic Design considerations

The following are some of the basic design parameters considered in designing a solar simulator:

- ❖ Selection of the light source with spectral distributions matching or close to that of the sun
- ❖ Provision of intensity variation as required for some locations of the ongoing researches in the school
- ❖ Uniform distribution of the light over the illuminated area
- ❖ Collimation of the rays
- ❖ Temporal instability of the irradiance
- ❖ Selection and optimization of the reflector to meet the required collimation and uniformity

4.5.1.1. Light source

It is very difficult to obtain light spectrum equivalent to that of the sun by using any light source. Various lamps were used as light source for solar simulator such as xenon arc, metal halide, tungsten filament, argon, high pressure sodium vapour lamps, halogen, etc. Several factors are considered when choosing lamp for solar simulator for a particular application such as wavelength (spectrum), stability, intensity, life expectancy, cost, etc.

Xenon arc lamps have advantages over all the lamps because it has spectrum closest to the terrestrial sunlight and are available in single high power bulb. But they are about 10 times the cost/watt of commodity lights and more vulnerable to explosion when used in an array because they are highly pressurized [150] and they require extensive maintenance. Although the spectrum emission of metal halide is not as close to that of the sun as the xenon, it is safer than xenon [150], having longer life span and durable [7] and cheaper compared to xenon [149].

The spectral mismatch of the lamp used in solar simulators can be reduced by either using a spectrum filter to adjust its spectrum (which adds to the cost of the simulator) or by using many lamps of the same grade or a combination of different grades.

4.5.1.2. Collimated rays and reflector shape

Collimated rays refers to the light rays that are parallel and do not disperse as they propagate through a distance. This is a requirement for the simulator to be able to test some systems like some concentrated PV and multijunction cells. Collimating lens are often used to achieve this requirement but they are expensive especially for large beam area. The reflector which houses the lamp plays important role in achieving collimated rays and homogeneous intensity on the target surface. Different shapes have been used as reflectors for solar simulator depending on the application intended. Table 4.4 gives details of the different shapes reported in literature. Usually, optical software like Monte Carlos, Optisworks © and Optics lab © are used in studying the performance and optimization of different reflectors for use in solar simulator.

4.5.2. Design approach of the present continuous solar simulator

The aim is to design a continuous solar simulator with varying intensities to be achieved by adjusting the distance between the simulator and the test facility. It is intended to be used for testing concentrating solar systems manufactured in this thesis. But the study is to be used for fabricating a large area simulator for testing different solar systems. The design approach includes among other things; lamp selection, investigation of the performance of different reflector shapes, studying the uniformity and stability of the flux as well as the collimation of the rays, fabrication and testing of the system.

4.5.2.1. Lamp selection

Due to the advantages of metal halide stated in 4.5.1.1 and the fact that their setbacks are not detrimental to some solar systems, they are widely used in applications such as sport lightings [149]. Metal halide is selected for this work based on these advantages and literature survey has shown that it is suitable for continuous solar simulator and relatively cheap. Two different metal halide lamp of 1200W (HMI 1200 from Osram) and 400W (from Meridian lighting - CED) were used in the optical studies of the different shapes of reflectors. The geometry of the Osram 1200W lamp is shown in Figure 4.2. Comparison of spectrum of the HMI1200 with 1.5G (standard solar) is presented in Figure 4.3 and its technical data is shown in Table 4.5 [7] .

Table 4.5 Technical data of Osram HMI 1200W

Parameter	Value
Rated wattage	1200 [W]
Colour temperature	6000 [K]
Luminous flux	110,000 [Im]
Ignition voltage	5 [kV]
Arc length	10 [mm]
Average life span	1000 [h]

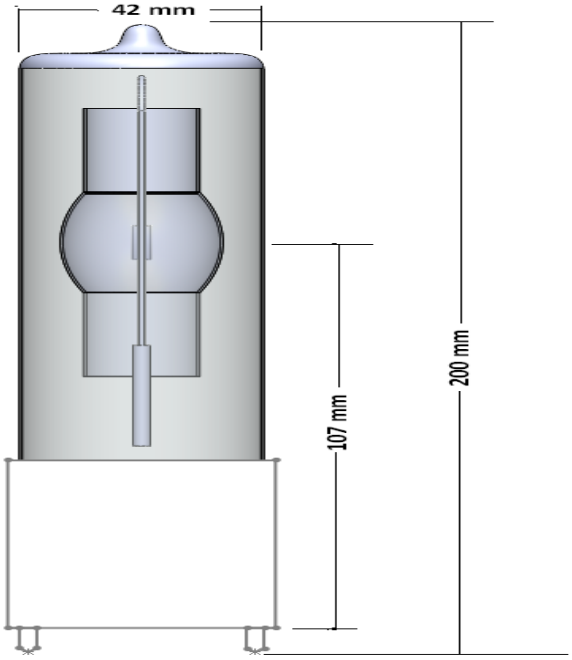

Figure 4.2 Dimensions of Osram HMI 1200W lamp geometry

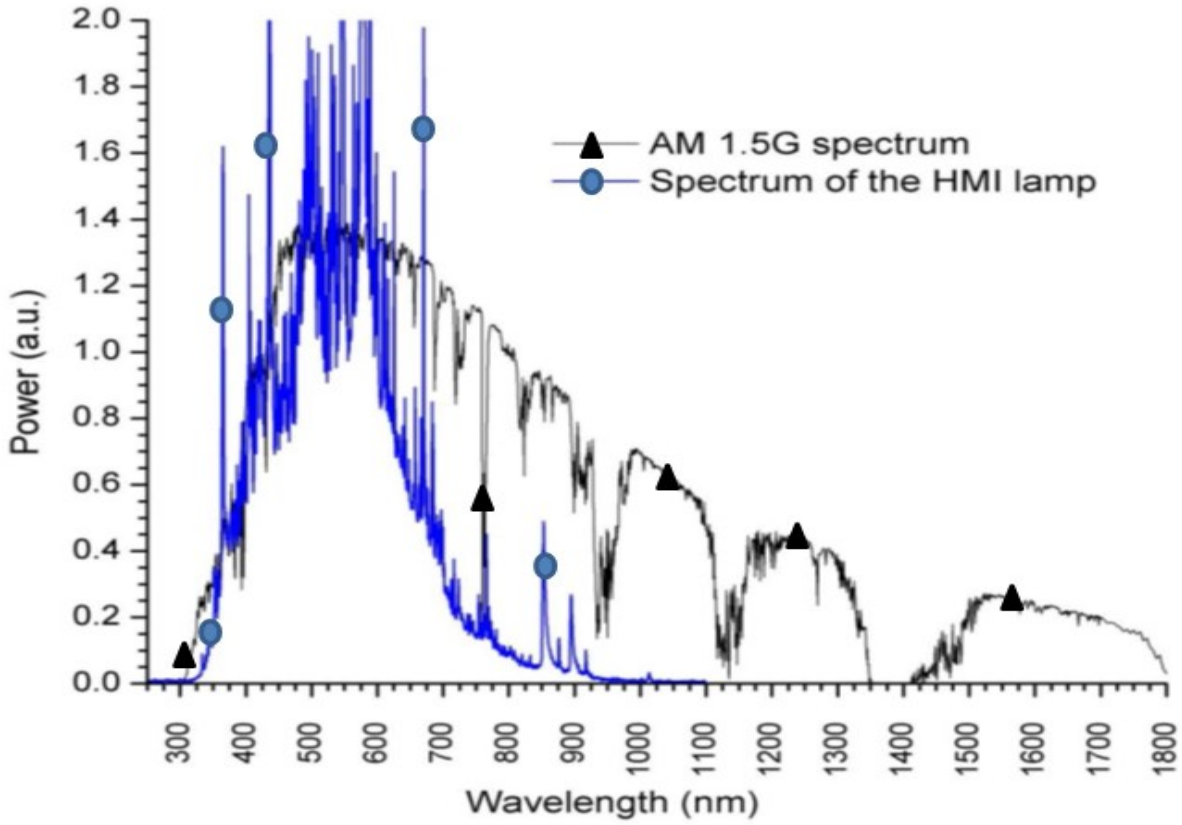

Figure 4.3 Spectrum of HMI 1200W lamp [7]

4.5.2.2. Reflector design

Selection of the right reflector is very important in achieving collimated rays and good uniformity. Several different configurations of three shapes; cone, ellipse and parabola were considered in this work. Different combinations of the aperture diameter, depth and position of the lamps were simulated using Optisworks® ray tracing software and Figure 4.4 shows samples of the reflectors simulated. Figure 4.5 shows detailed geometric characteristics of ellipsoid reflector with two foci (F1 and F2). The study was carried out at different distances (ranging from 50mm to 1500mm) between the illuminated area and the source of the light.

The optical simulation set-up involves defining the light source in terms of power, spectrum, temperature, number of rays, etc. based on the lamp specifications shown in Table 4.5. While for the reflector, the reflectivity of the surface is defined and a 1point – 2 lines radiometric illuminance detector type was defined at the aperture to measure the irradiance passing out from it. A 1000mm x 1000mm receiver was used as the target and its surface was defined as 100% absorbing with also an illuminance radiometric detector defined to read the received irradiance.

The three shapes each having different combinations of aperture diameters such as 120, 150, 170, 200mm and depth of 60, 80 and120mm were simulated with the illumination area at 1,000 and 1500mm distance from the source. The lamp was positioned at 10, 55, 80, 90, 100 and 110mm from the aperture of the reflector (depending on the depth of the reflector), and in each case the aperture and receiver fluxes and power were determined. The selection of the lamp positions were made with the consideration of the focal points of the shapes considered. Figures 4.6, 4.7 and 4.8 show the performance of the three shapes, each with a depth of 120mm at different lamp positions with the receiver placed 1000mm away.

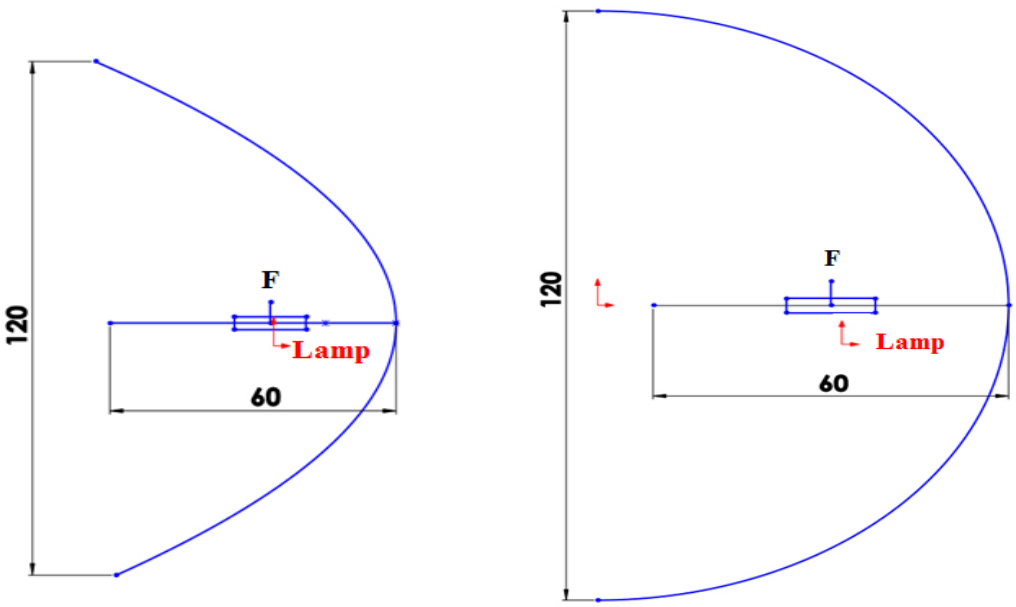

(a) (b)

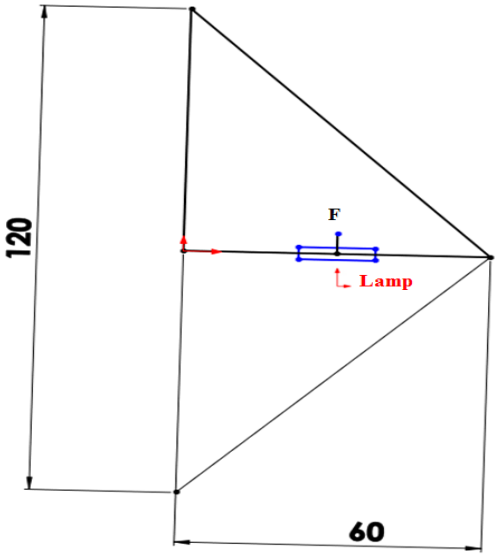

(c) **All dimensions are in mm**

Figure 4.4 2D sketches of (a) parabolic (b) ellipsoidal and (c) conical shape reflectors

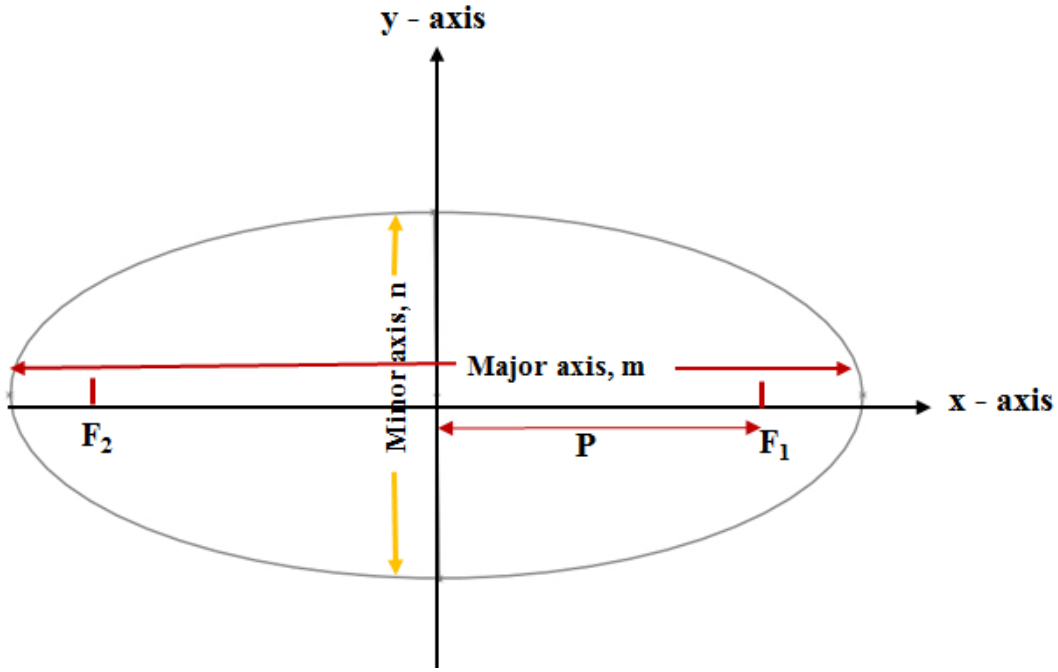

Figure 4.5 Ellipsoid geometric properties

It can be seen from Figures 4.6, 4.7 and 4.8 that the lamp position and the shape of the reflector affect the amount of the power to be received at the target. For conical shape reflector, the power received increases as the lamp is moved inside the reflector and reached maximum (265.6W) around 20mm away from the middle (i.e. around 80mm), then it starts decreasing.

Elliptical and parabolic reflectors show similar patterns to conical but reached maximum at 90mm (743.9W) and 60mm (797.3W) respectively. Although conical reflector gives the lowest power outputs compared with parabolic and ellipsoidal reflectors, but it is capable of delivering power above 200W for all the lamp positions simulated except at 10mm. These results showed that the position of lamp in the reflector and reflector's shape and size affects the amount of irradiance received on the target.

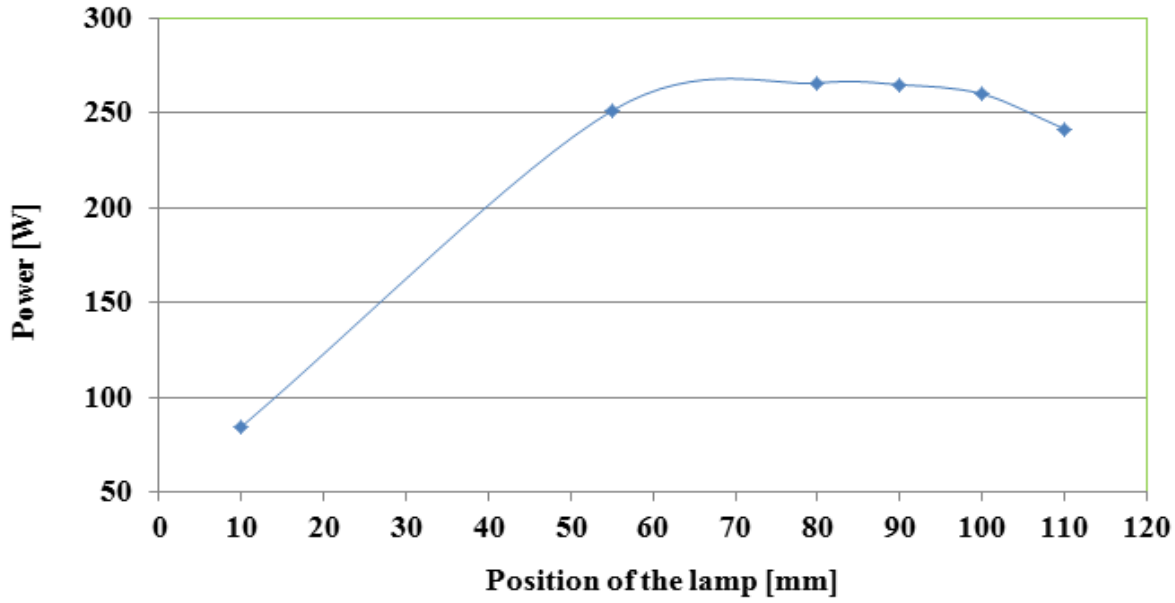

Figure 4.6 Variation of the power received with various lamp positions across the central axis (Conical)

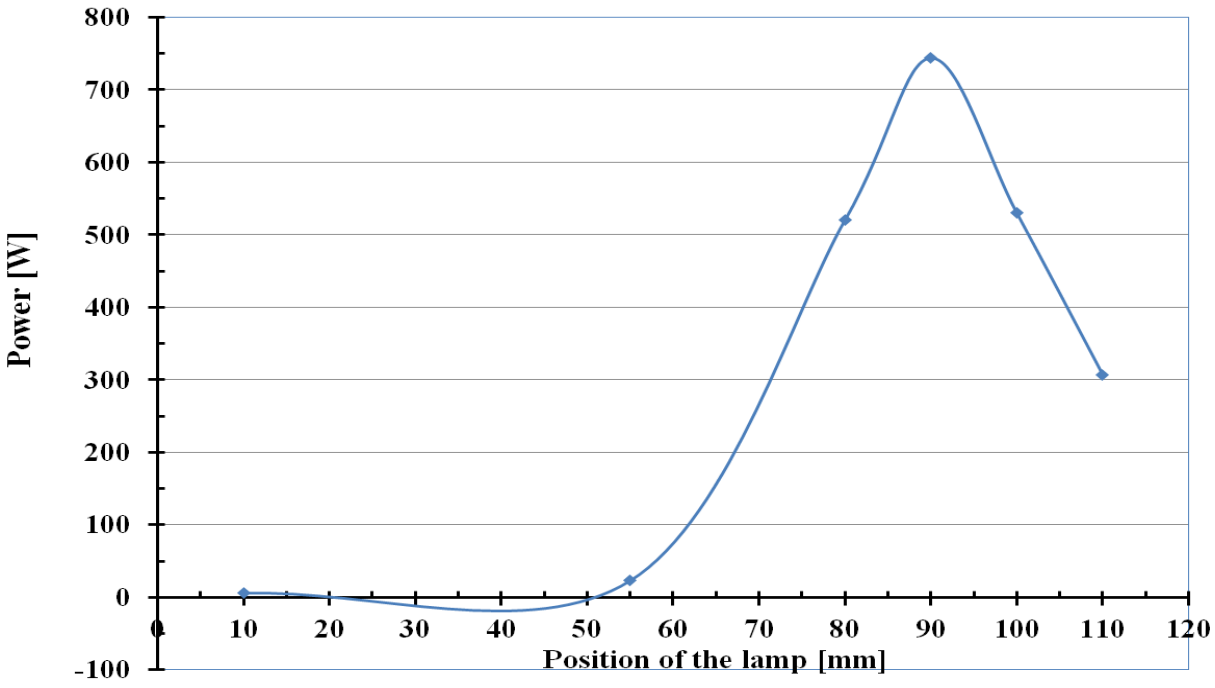

Figure 4.7 Variation of the power received with various lamp positions across the central axis (Ellipsoidal)

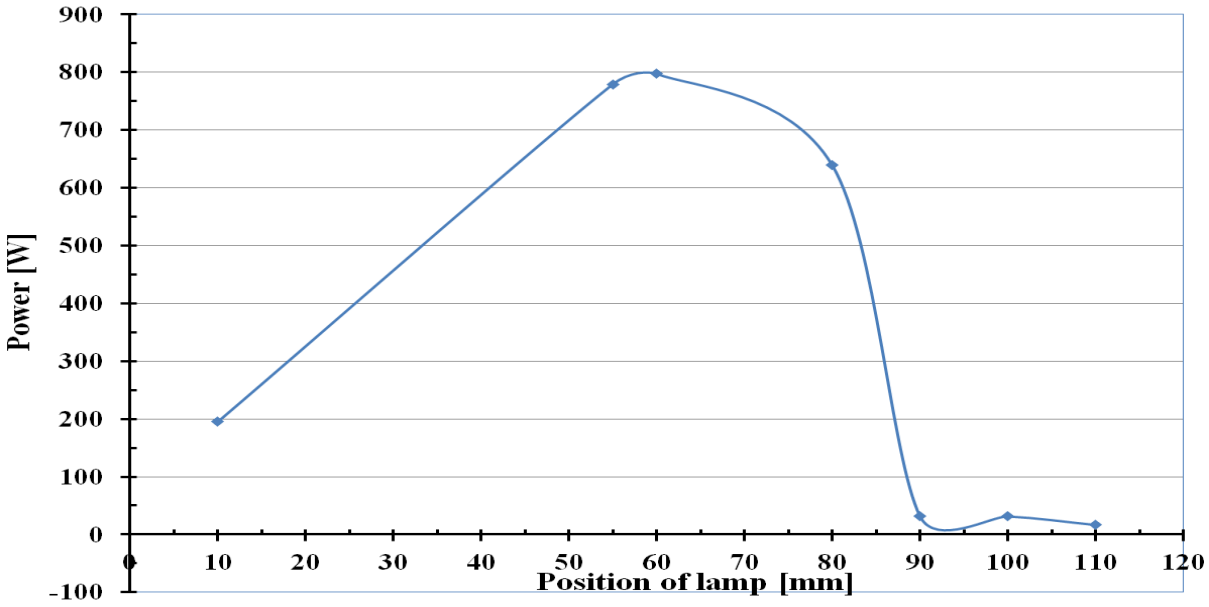

Figure 4.8 Variation of the power received with various lamp positions across the central axis (Parabolic)

Figure 4.9 (a, b and c) show the rays and the irradiance received at a distance of 1000mm from the light source for the three reflector shapes when the lamp is positioned at best location for each shape. It can be seen that the best collimation is obtained from the parabolic shape followed by ellipsoidal. The incident rays in the parabolic reflector's case are concentrated within small area compared to the other two shapes; hence giving highest irradiance. This is due to the fact that rays from a source of light placed at the focal point of a parabola propagate parallel to the axis of symmetry. For ellipsoidal reflector shape, more rays can be captured if the receiver is placed closer to the aperture around the other focus, because all rays originating from one of the foci pass through the other after one specular reflection as shown in Figure 4.9c. The percentages of nonuniformity of the flux on the receiver for the three reflectors are 46, 58.3 and 58% for the parabolic, conic and ellipsoidal respectively. This is due to the decrease of the intensity for areas away from the centre of the lamp. This shows

that for better uniformity more than on lamp is required in solar simulator where region with better uniformity can be detected.

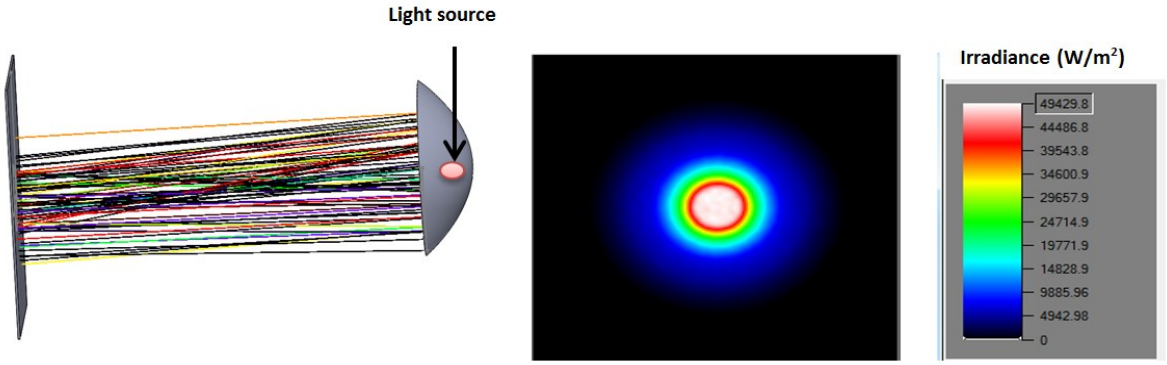

(a) Parabolic

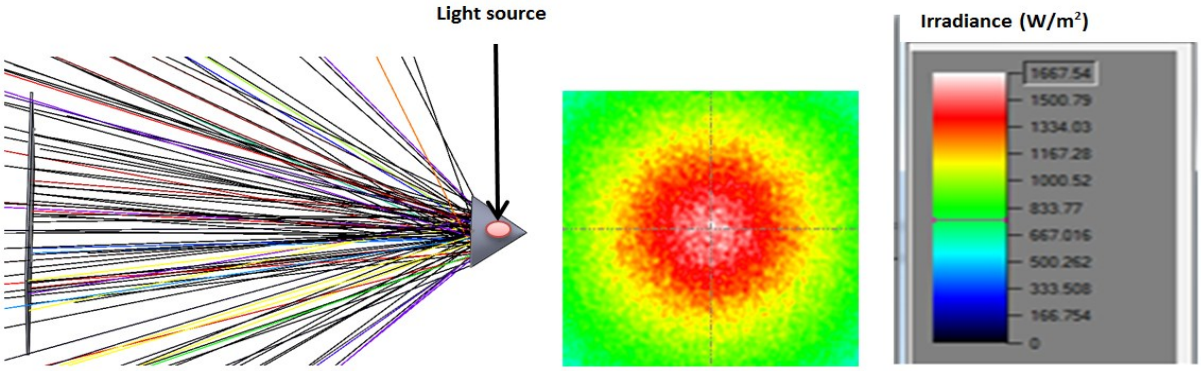

(b) **Conical**

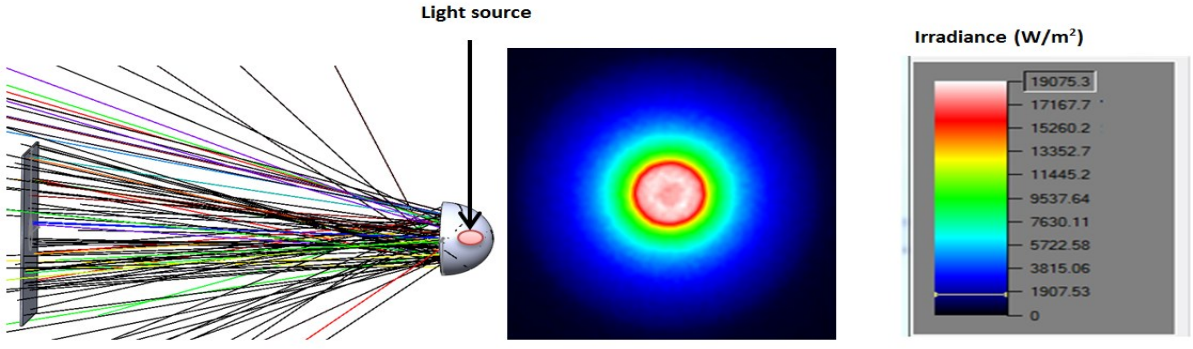

(c) Ellipsoidal

Figure 4.9 Rays and rate of irradiance received at 1000mm distance from each of the three reflectors when the lamps are placed at their best positions

Although parabolic reflector showed best collimation and highest intensity, but ellipsoidal also tends to be a good options especially when the design allows changes of the distance between the solar simulator and the receiver. As a first stage of developing large area solar simulator for the School, an off – the - shelf 400W metal halide lamp enclosed in an elliptical reflector is selected for this work. This is due to the availability, cost, saving of time and labour. Optical simulations, construction, assembling, experimental works and detailed simulation of this lamp are presented in the next section.

4.5.3. Design of continuous simulator for testing solar collectors

Both experimental and simulation studies were conducted on the selected light source to enable design of this simulator for testing the CPC developed in this work and the process is presented in this section.

4.5.3.1. Experimental performance of the light source

An off- the - shelf 400W halide lamp used in the construction of this simulator was purchased from Meridian lighting/CED and its technical data is shown in Table 4.6. The reflector is elliptical shape aluminium (reflectivity of 55%) with aperture and depth of 485 and 285mm respectively. The reflectivities of all the surfaces were measured using a Perkin – Elmer UV-Vis – NIR spectrometer shown in Figure 4.10.

The irradiance was measured using high sensitivity 5 x 5mm radiant flux sensors from Captec Enterprise® which gives out voltage signals. Table 4.7 gives the calibration/sensitivities of the sensors used as obtained from the manufacturer. To determine the irradiance received at diffferent distance from the source and fully characterize the lamp, experimental radiation mapping was carried out using the setup shown in Figures 4.11. Figure 4.12 shows the photograph of the sensor used in the mapping.

Table 4.6 Technical data of 400W metal halide (MBI) and fittings

Properties	Value
Rated lamp wattage	400 [W]
Voltage	240V AC 50Hz
Type	Elliptical mercury Ballast
Control gear ratings	240V – 50Hz 3.50A

The sensor's signal is sent to the DT85 data taker where the sensitivity defined in the scaling of the logger converted the signal to W/m^2. Due to the high sensitivity of the sensors used, they are firmly held by the holder and covered to avoid vibration (Figure 4.11).

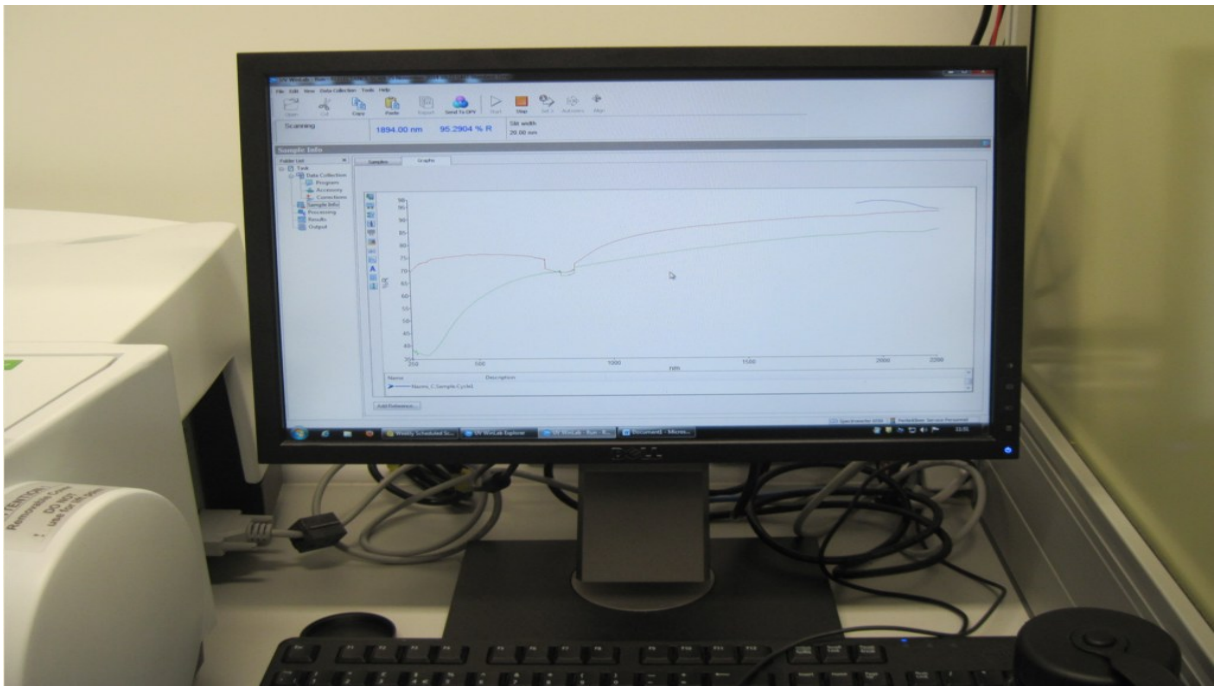

Figure 4.10 Reflectivity measurements on progress

Table 4.7 Calibration of the radiant flux sensors used in the irradiance measurements

Sensor	Sensitivity, μV (W/m^2)
1	0.111
2	0.114
3	0.0994
4	0.0834
5	0.089
6	0.114

The sensors were placed in a plastic holder with covers which were produced using 3D printer to hold them firm in position. Figure 4.13 shows the photograph of the sensor holder and radiation mapping setup. A rotating stand and metal bar were used for the angular movement of the sensors to measure the radiation at different points and axis as shown in Figure 4.13. The holder attached with the sensors was inserted into the metal bar which is screwed on the rotating stand. Also by using the adjustable stand (Figure 4.13), the irradiance was measured at different distance between the receiver and the source and at different axes by rotating the horizontal rod in 90, 180, 270 and 360^o. Figure 4.14 shows the schematic diagram of the radiation measurement procedure. The results of the experimental measurements of the irradiance for 200, 400 and 500mm distance from the source are compared with simulation in the next section (4.5.3.2).

(a) Adjustable stand and base

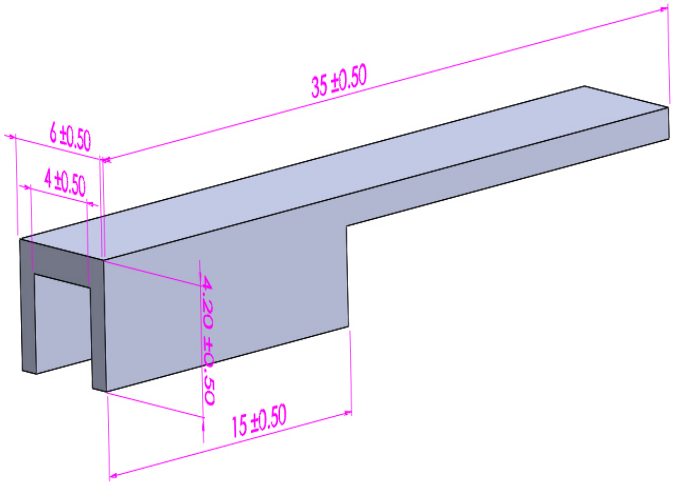

(b) Radiant sensor cover

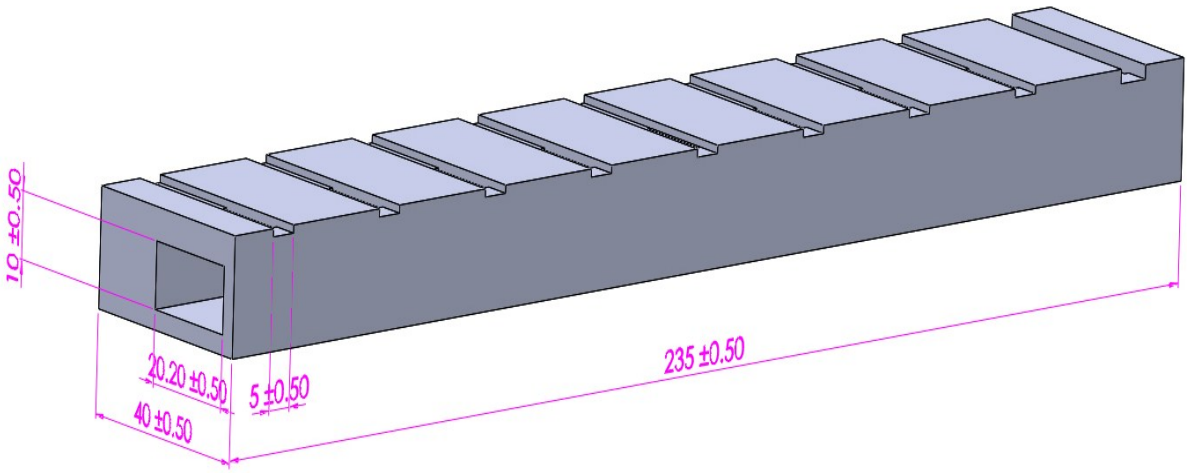

(c) Radiant sensor holder (for nine sensors)

All dimensions are in millimetres

Figure 4.11 3D CAD drawing of the radiation mapping setup

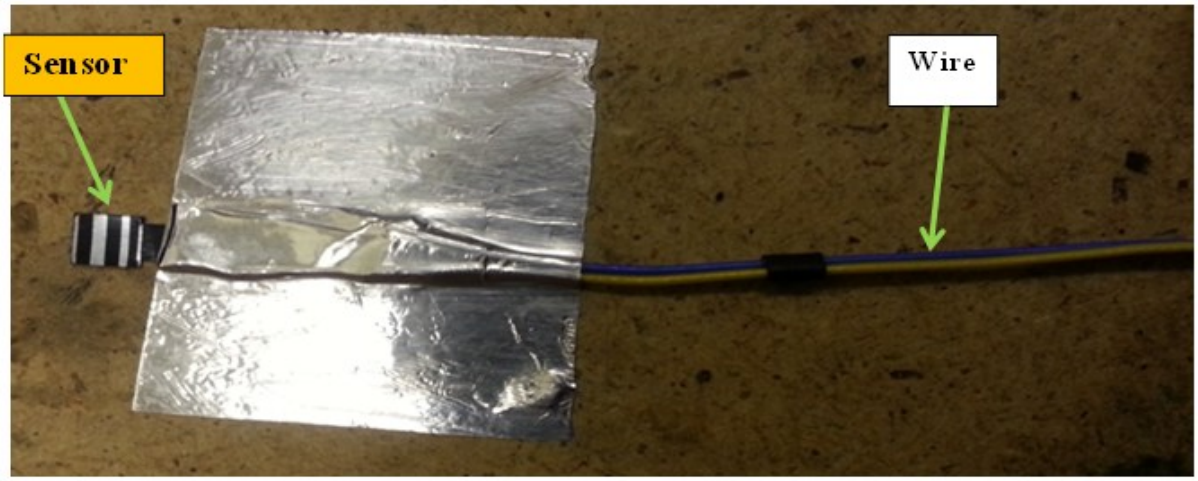

Figure 4.12 A photograph of 5 X 5 Radiant flux sensor

4.5.3.2. Optical simulation

Optical simulation was carried out using one set of the lamps based on the setup explained in section 4.4.2 and validated using the experimental results in 4.4.3.1. Once validated, the simulations will allow a wide range of investigations on the lamp's performance to be carried out.

The irradiance was measured at different distances in accordance to the experiments conducted in section 4.5.3.1 and the average values on the receiver are presented in Figure 4.15. Figure 4.15 compares the surface average predicted irradiances received at difference distances from the simulator with the experimental results. It can be seen that the irradiance reduces as the distance between the source and the receiver increases in both cases and the two approaches show good agreement with average deviation of ±11%. Figure 4.16 shows the trajectory of the rays and the irradiance distributions on a $1m^2$ receiver.

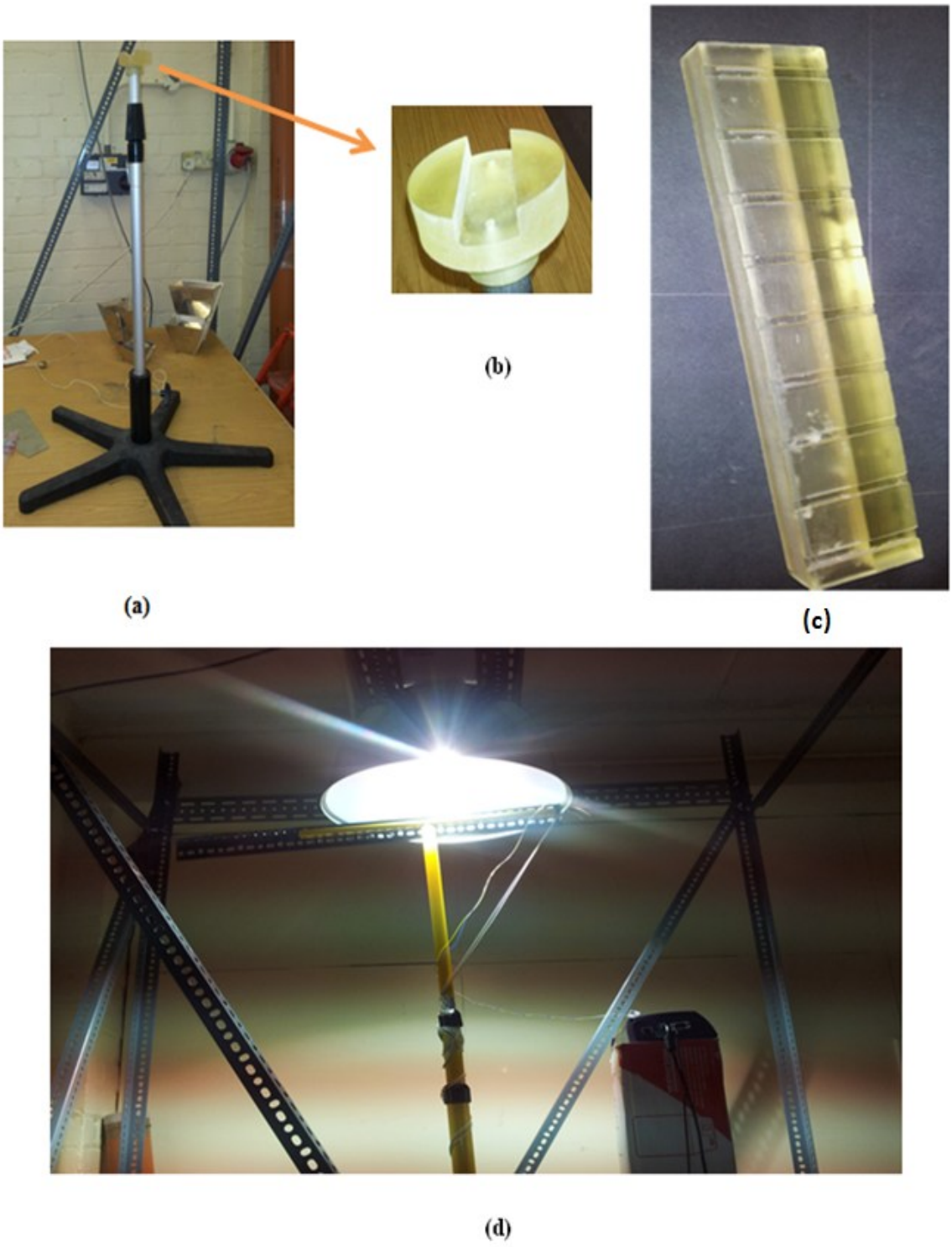

Figure 4.13 Photograph of: (a) rotating adjustable stand; (b) top metal bar holder; (c) sensor holder; (d) radiation mapping at the aperture of the reflector

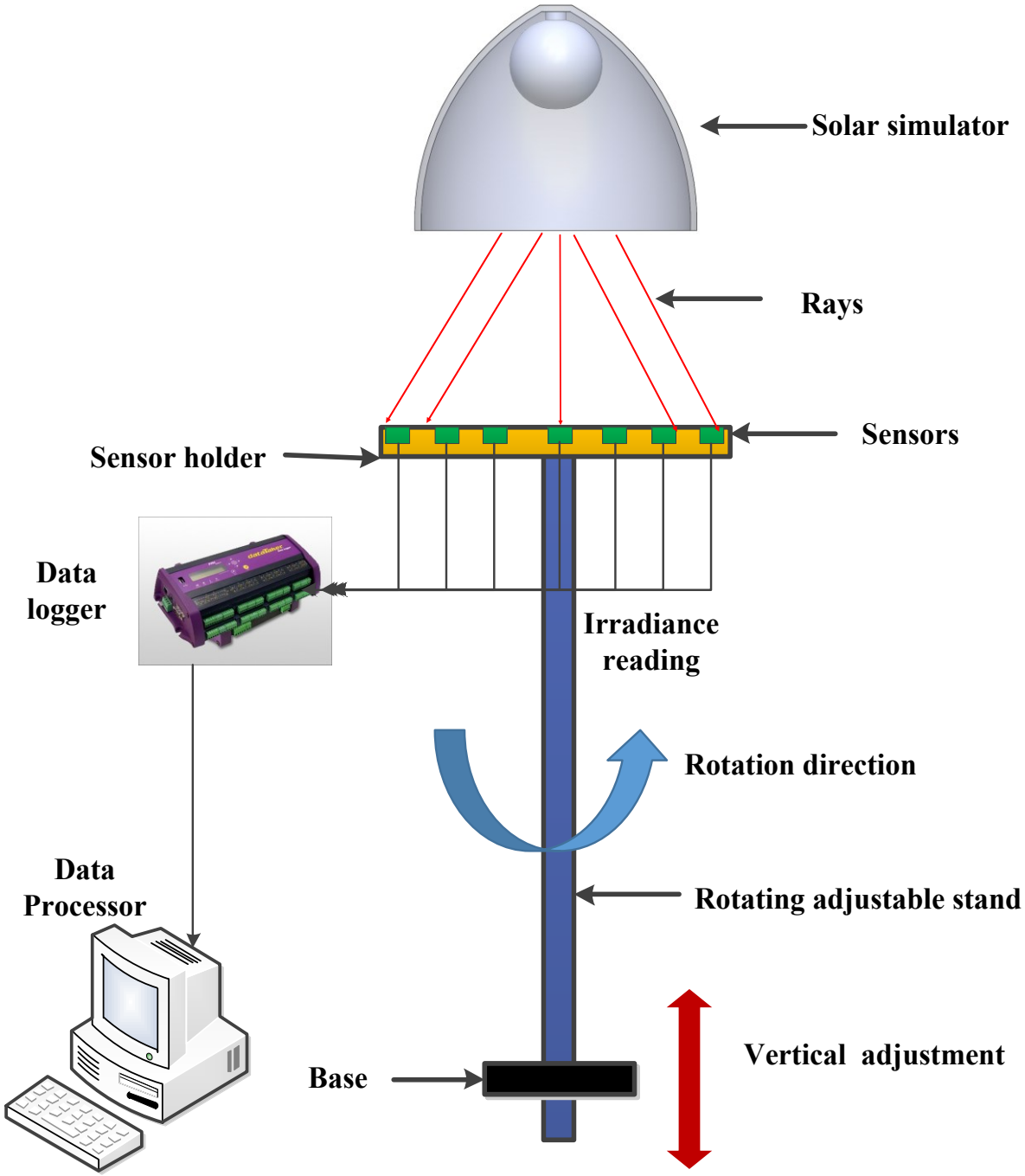

Figure 4.14 Schematic diagram of the radiation measurement procedure

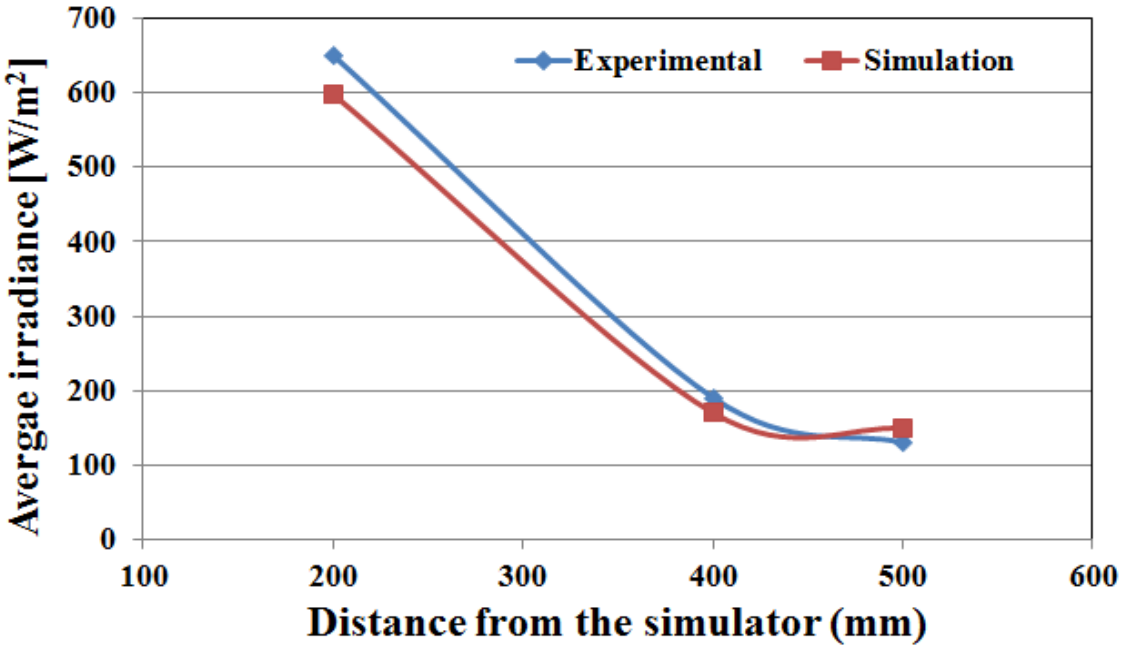

Figure 4.15 Comparison of the experimental average surface irradiance with the simulation at different distances

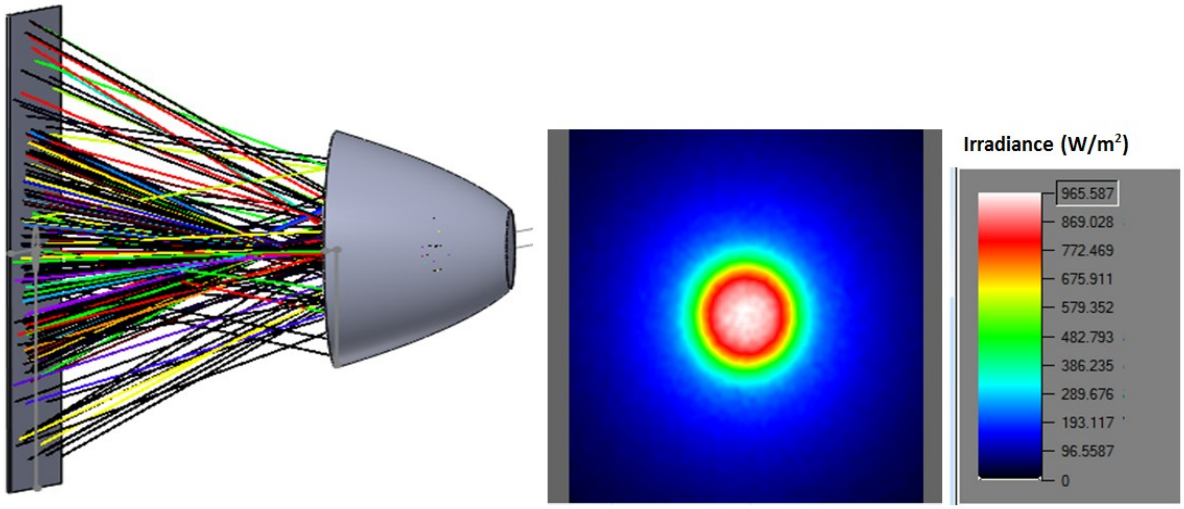

Figure 4.16 Rays and irradiance distributions on a receiver at 400m distance

Figure 4.16 shows the rays and irradiance on the receiver at a distance of 400mm away from the source. It can be seen that there is concentration of rays and higher flux at the centre

which reduces with the distance away from the centre. Also most of the rays converged at the second focal point of such ellipse, and then radiated again to hit the target, which proves that elliptical shape is also good for applications that require high flux concentration.

The reduction in the intensity with the distance is due to the ray's losses (as shown in Figure 4.17) and the increase in the length of the rays' path before reaching the target.

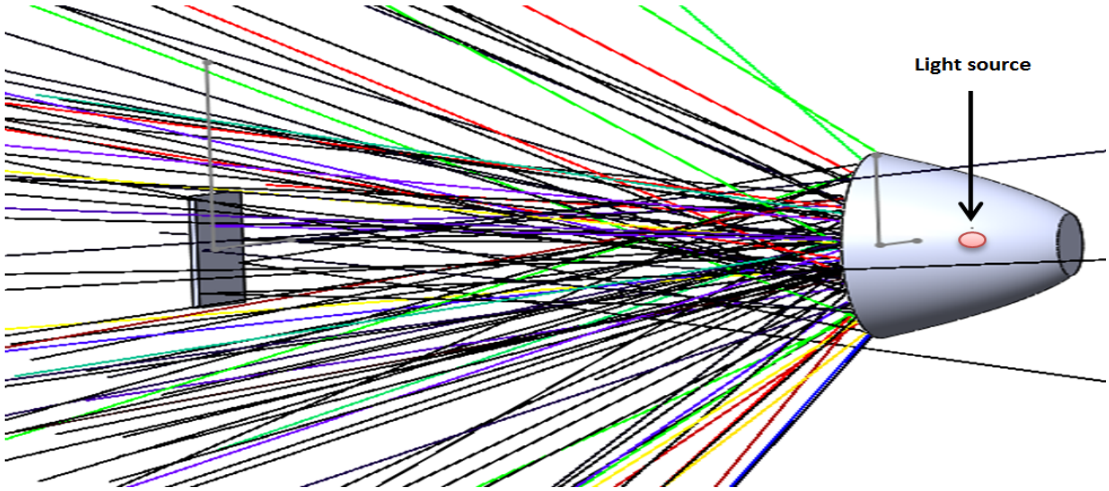

Figure 4.17 Trajectory of rays from the lamp showing received and loss rays

The validated model was used to study the effects of the reflectivity of the reflector. It is shown that the received irradiance can be enhanced if the reflectivity of the reflector is increase as seen in Figure 4.18, where it increased by 26 and 13% when the reflectivity is 65% and 60% respectively compared to 55%. It can also be seen from Figure 4.18 that the effect of the reflectivity is very large at small distance from the source and reduces at large distance.

The mapping and simulation results showed that more lamps are needed to get higher irradiance especially due to the low reflectivity of the reflector (55%) used in this work. Hence, optical simulation was carried out using two lamps at distance of 400 and 500 mm

away from the source and the irradiance are presented in Figure 4.19. There is increase of 84% in the received irradiance compared to one lamp at the two distances.

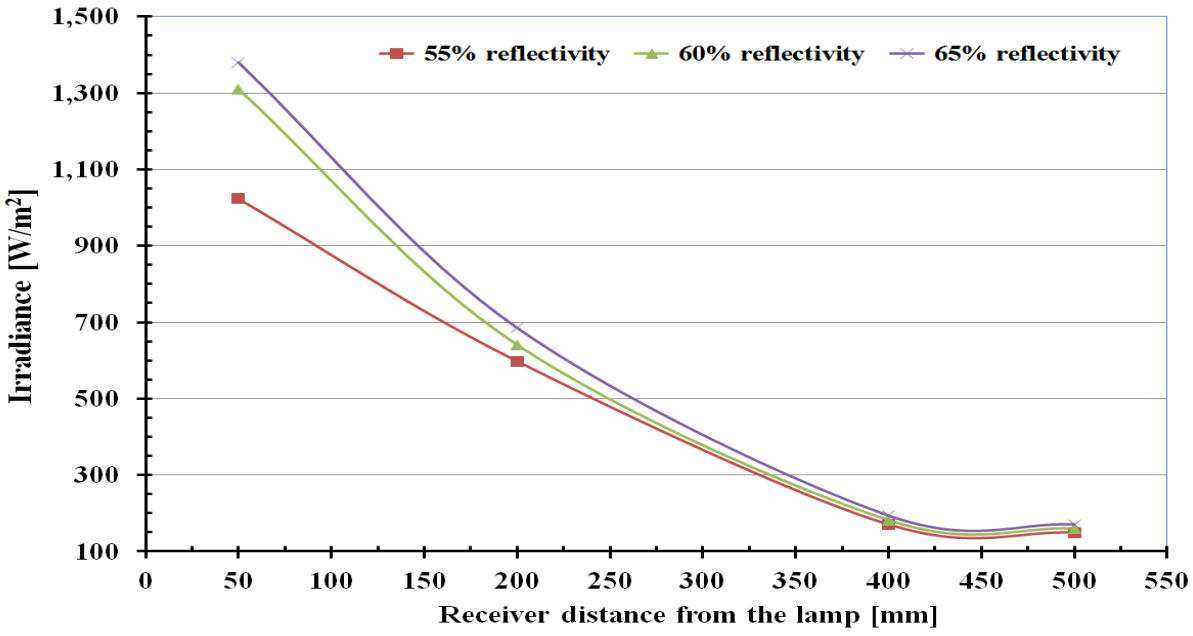

Figure 4.18 Variation of surface average irradiance with distance for different reflectivity

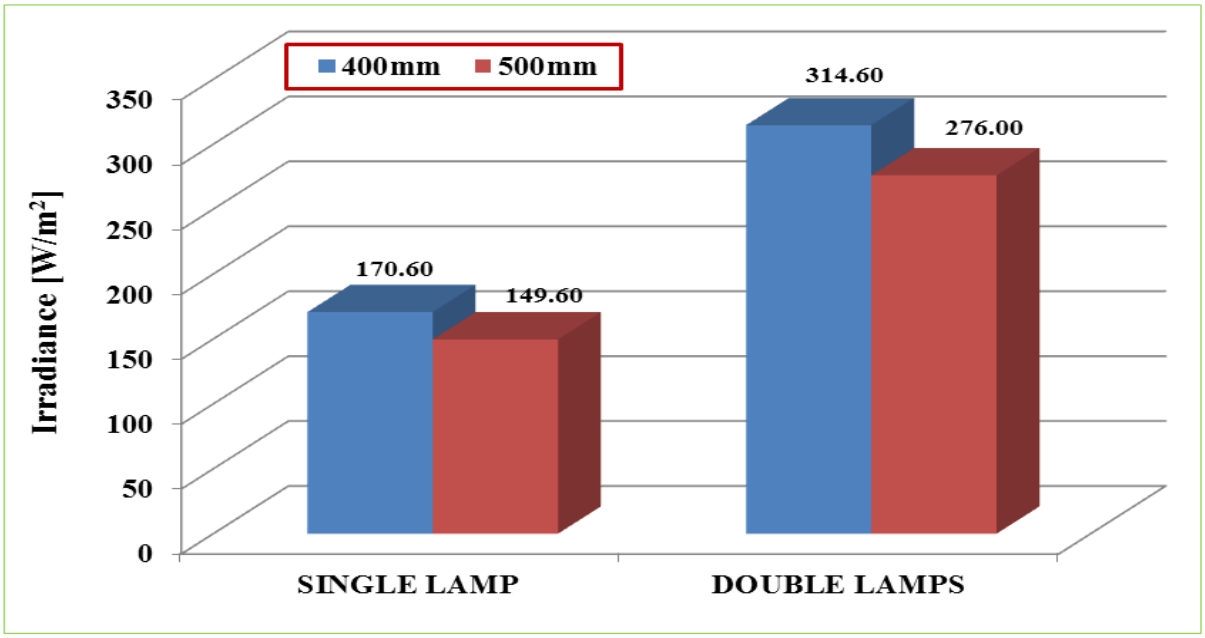

Figure 4.19 Comparison of the irradiance received by $1m^2$ receiver for single and double lamps at 400 and 500 mm distance away from the source

4.6. Construction of two lamp solar simulator

The simulator consists of the electric power supply, structure for holding the lamps, adjustable stand and installation of the lamp.

4.6.1. Simulator assembly

Figure 4.20 shows a schematic diagram of the two lamp solar simulator used in testing the CPC in this thesis. A 1500 x 1050 x 72mm table was used as the base for placing the test rig and steel bar 3050 mm long were mounted vertically at each edge of the table. Metal bars were used to connect the four vertical bars while other bars were screwed longitudinally to strengthen the vertical bars. Two other metal bars were placed horizontally on the top of the horizontal bars for holding the lamp and its accessories. Electrical wiring provisions of seven lamps were made for possible expansion and each lamp has a separate switch which provides flexibility in utilizing the number of lamps required for a certain test. The lamp control box is placed on these horizontal bars and the reflectors were screwed to the bar.

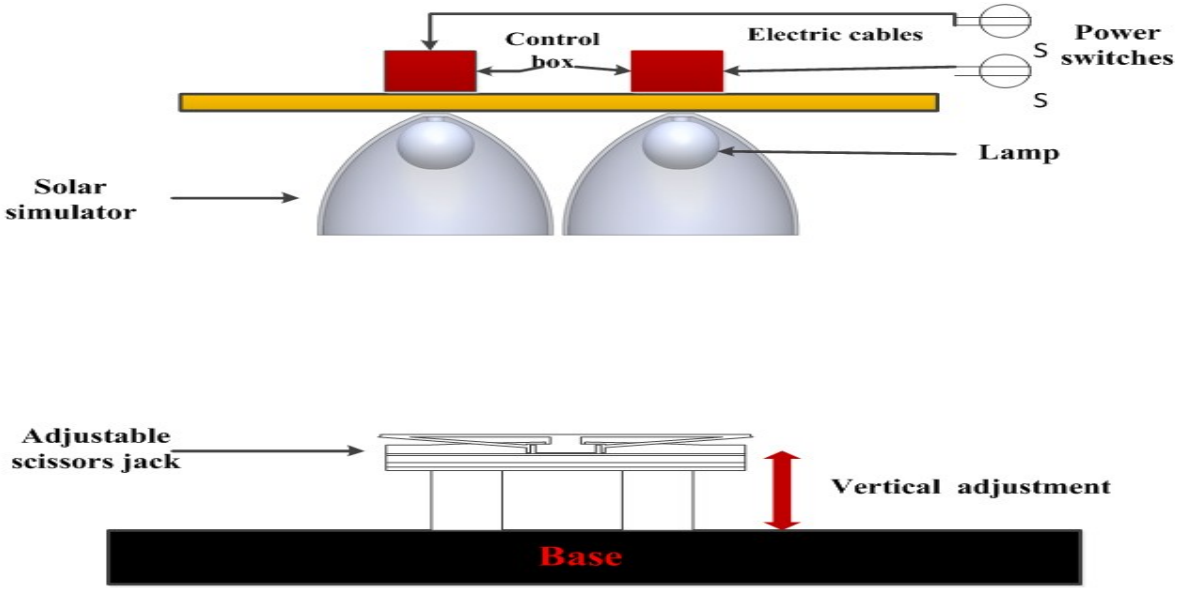

Figure 4.20 A schematic diagram of the two lamp solar simulator and its accessories

The edges of the two reflectors are made to touch one another as simulation results of the two lamps showed that the area between the two lamps has better uniformity (nonuniformity of 10.5% and 21% for vertical and horizontal orientations respectively) as shown in Figures 4.21 and 4.22. These figures show the irradiance distributions along x and y axes measured from the centre of the meeting points of the edges of the two lamps. However, high irradiance can also be obtained when the test facility is placed at the centre of one lamp at a distance close to the simulator.

The test facilities are to be placed on an adjustable scissor jack for changing its distance from the simulator to achieve the required irradiance (Figures 4.20 and 4.23). This adjustable scissor jack (MCPLI) manufactured by Draper tools limited, has minimum and maximum height of 85 and 340mm respectively and maximum capacity of 450kg. The distance can be adjusted to achieve the required irradiance for the intended tests.

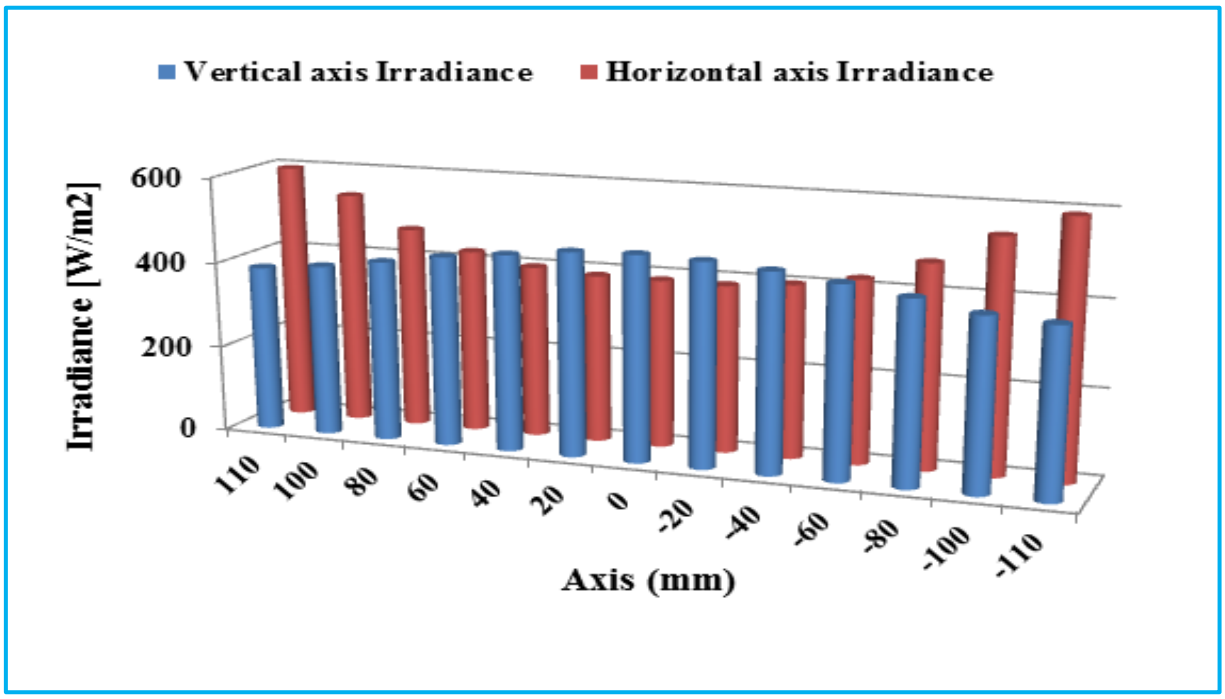

Figure 4.21 Irradiance distributions within the area (220 x 220mm) under the meeting point of the two edges of the reflectors

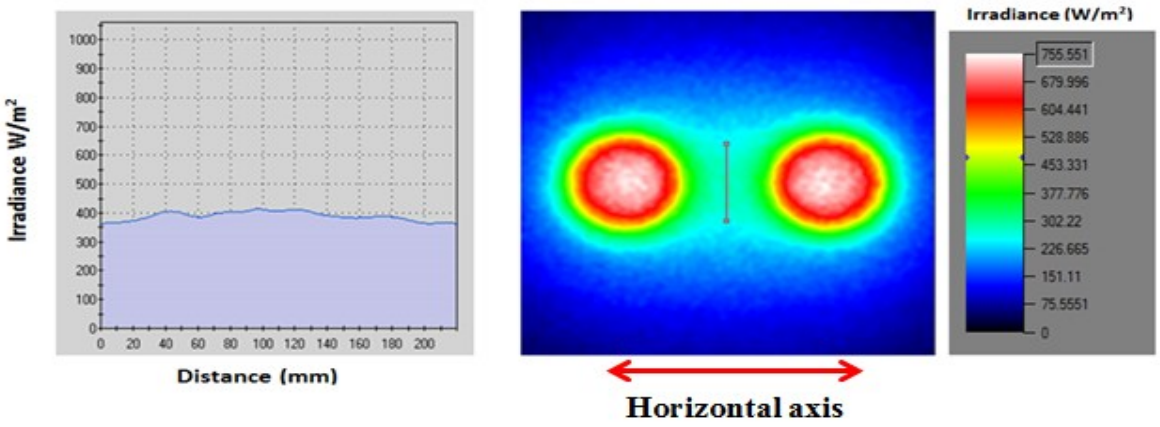

Figure 4.22 Contours of flux within the area (220 x 220mm) under the meeting edges of the two reflectors (Horizontal axis)

Figure 4.23 (a and b) shows the 3D CAD drawing of the two lamp configuration and the photograph of the complete set up of the simulator. Also Figure 4.23a shows the simulator consisting of two lamps and their accessories, table as testing space, adjustable scissor jack, electrical supply and controls, etc.

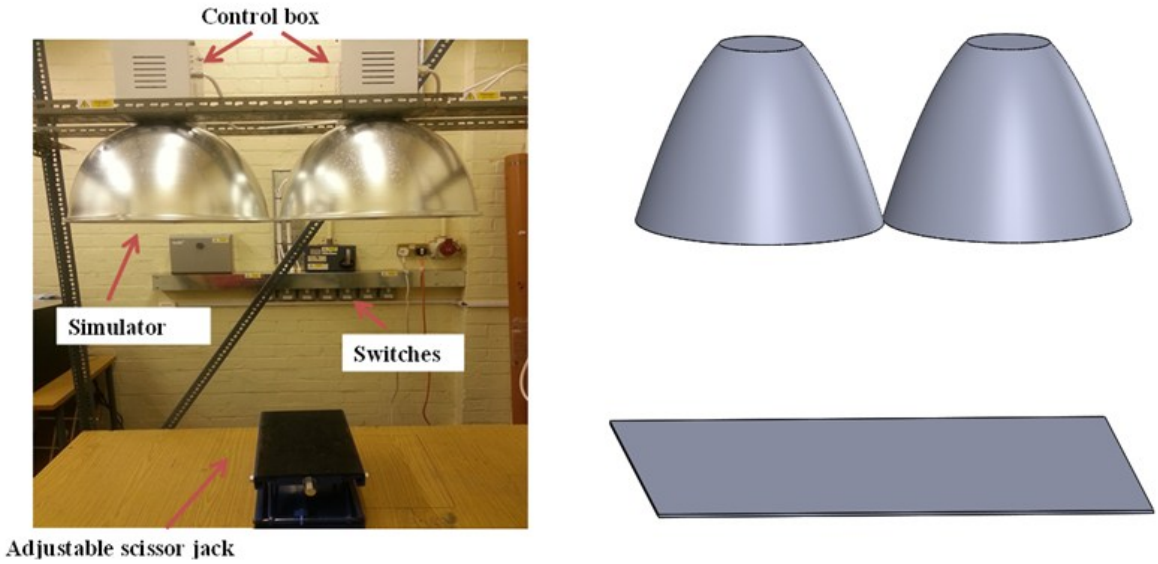

Figure 4.23 (a) Photograph of the two lamp configuration (b) 3D CAD drawing of the simulator

4.7. Characterization of the two lamp simulator

Based on the standards explained in section 4.2.1.2 and 4.2.1.3, the ASTM standard was used to determine the temporal instability and nonuniformity of this simulator. Mapping approach was utilized in determining the irradiance within the area under the meeting edge of the two reflectors. Sixty four (64) boxes were marked (50 x 50mm each) on cardboard paper and sensors were placed at the middle of each box to measure the irradiance falling on such area. Figure 4.24 shows the mapping points considered with green colour (1 to 64 points) and red colour (36 points) representing 400 x 400 mm^2 and 300 x300 mm^2 areas respectively. The simulator was switched on for one hour and allowed to stabilize before taking any readings. Figure 4.25 shows the test setup during the characterization process. Four areas were considered; 400 x 400, 300 x 300, 200 x 250 and 200 x 200mm^2 to measure the percentage non-uniformity within such areas. Figure 4.26 shows the irradiance distribution obtained for 200 x 200 mm^2 areas.

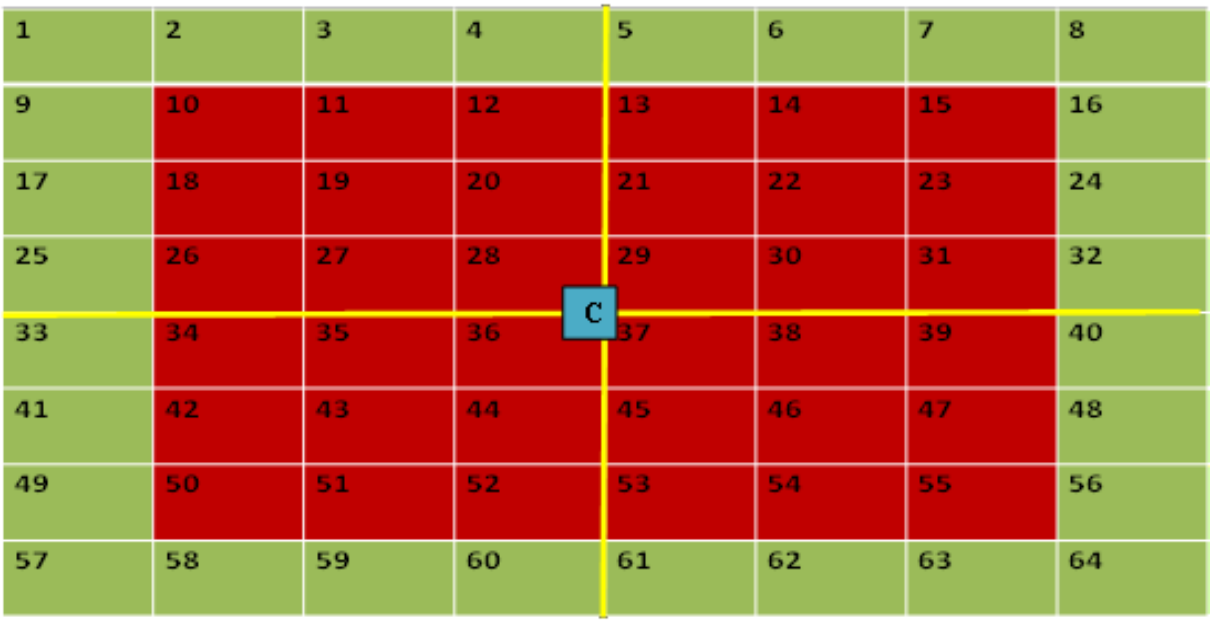

Figure 4.24 Radiation mapping areas

Figure 4.25 Photograph of the simulator characterization

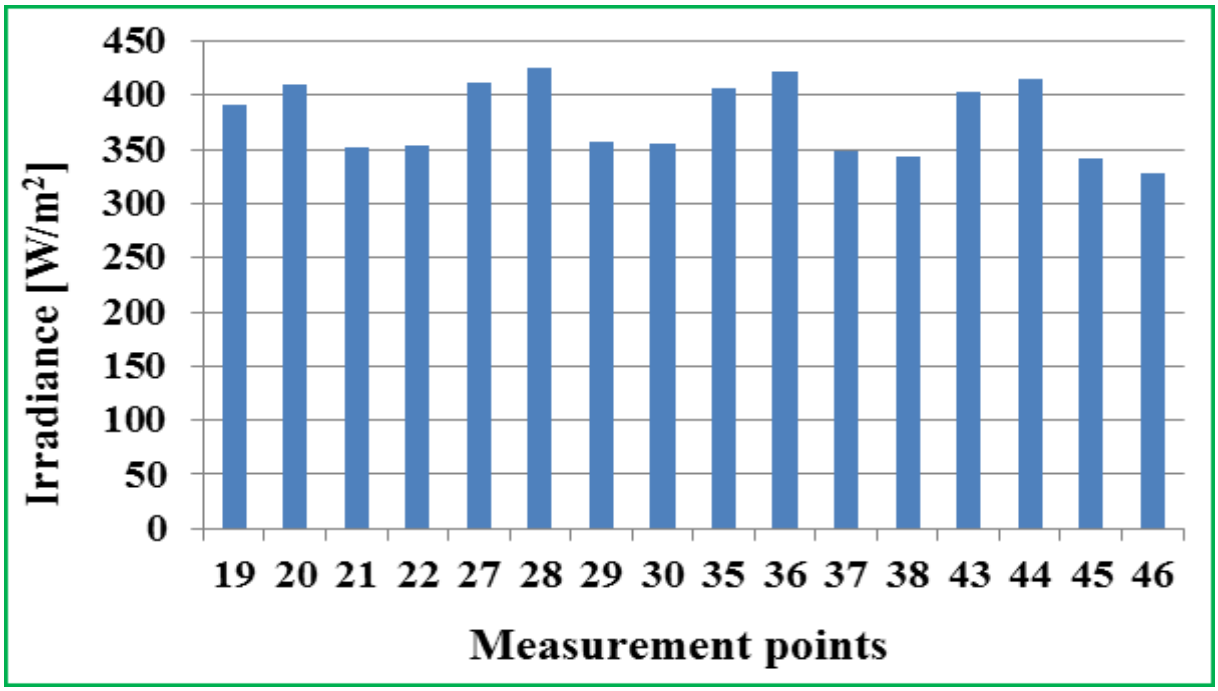

Figure 4.26 Irradiance distributions on 200 x 200 mm^2

Using equation 4.2, the percentage non-uniformity was calculated for the areas considered and the results are presented in Figure 4.27. Figure 4.27 compares the percentage

nonuniformity of the irradiance with the ASTM standard. It can be seen from the figure that the nonuniformity increases on moving away from the area under the meeting point of the two reflectors. This simulator almost meets the allowable tolerance of ASTM within 200 x 250 mm^2 and 200 x 200 mm^2 areas. This shows that for best uniformity, the test facility should be placed within 200 x 200mm^2.

To determine the percentage temporal instability, irradiance was recorded at the 64 points marked at the rate of 1 reading/second for 30 minutes and equation 4.1 was used to calculate the percentage temporal instability for different illumination areas. Figure 4.28 shows the percentage temporal instability for 300 x 300 mm^2, 200 x 250 mm^2 and 200 x 200 mm^2. It can be seen from such figure that the rays from this simulator is stable and meet the class C requirement of ASTM standard for all these areas.

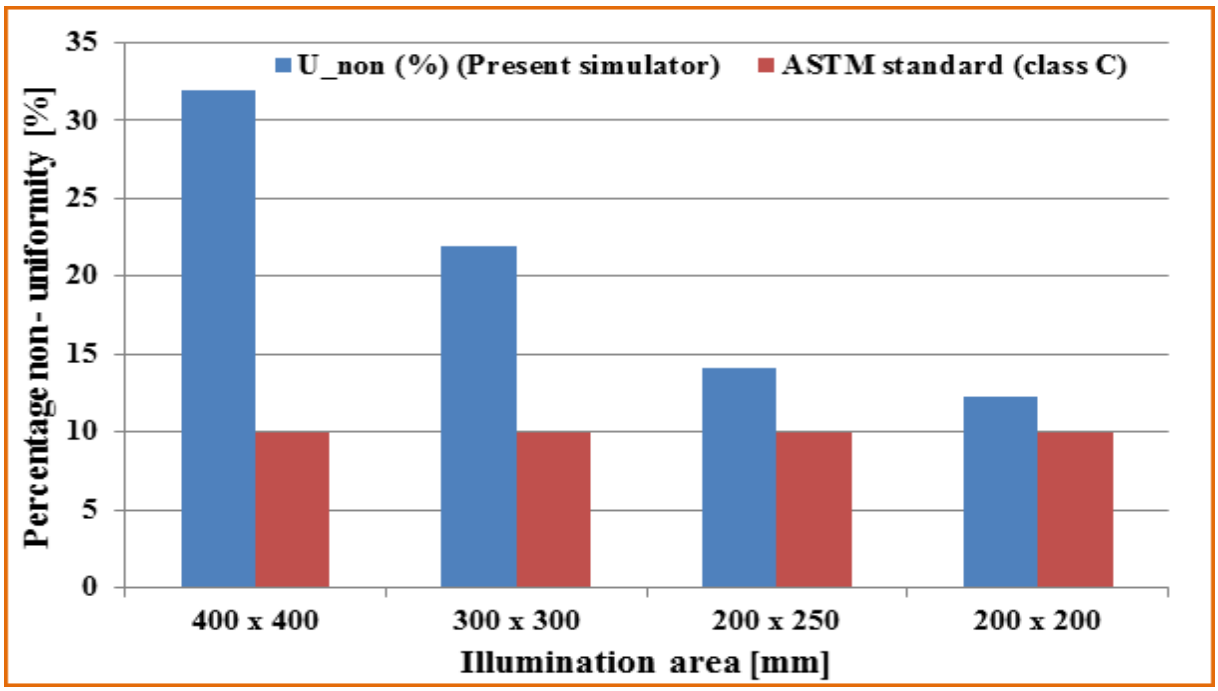

Figure 4.27 Comparison of the percentage nonuniformity of the present simulator with ASTM standard

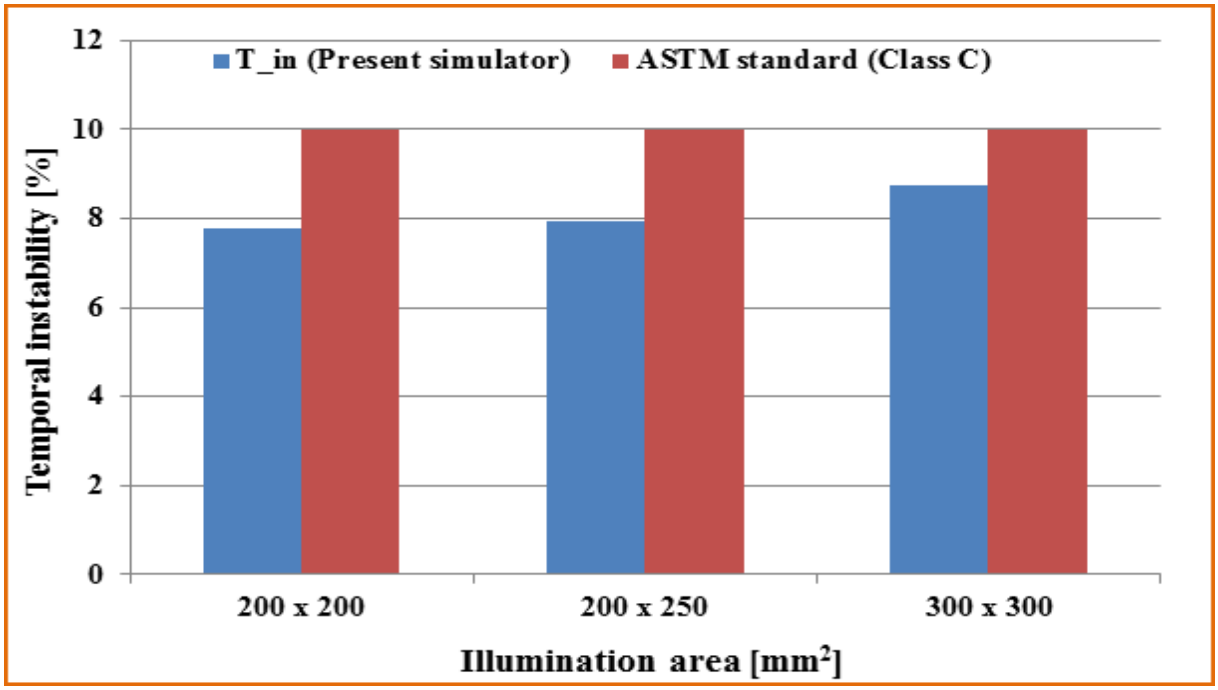

Figure 4.28 Comparison of the percentage temporal instability of the present simulator with ASTM standard

4.8. Summary

Solar simulators are used for indoor testing of solar systems because they accelerate research in solar technology since the test can be done at any time of the day and year. Also the irradiance level and other atmospheric conditions of temperature, wind, etc. can be controlled. Building a solar simulator involves selection of the lamp, reflector, electrical fittings and controls. In order to select a reflector for building a solar simulator for this work, detailed optical simulation was carried out on three different shapes; conical, elliptical and parabolic and their performance was evaluated based on the rays distributions and irradiance received on the target surface. The study was conducted on different parameters such as aperture width, reflector depth, position of the lamp in the reflector and distance between the light source and the receiver.

Results showed that the position of lamp in the reflector and the shape of the reflector are vital in determining the rays' collimation and the amount of irradiance to be received on the target surface. It was shown that the irradiance received on a receiver at a distance away from the source increases as the lamp is moved deep inside the reflector for all the shapes but reaches peak at different positions depending on the shape.

Parabolic shape reflector has shown the best performance in terms of collimation and amount of power received when the lamp is placed at its focal point. Although parabola tends to be the best, elliptical reflector is also a good option especially for concentrating thermal systems where concentrating of flux is required. This is due to its property that rays from a lamp placed at one of its focus will converge at the other focus before radiating out. Hence a receiver placed at such position will receive high level of radiation.

Two an off – the - shelf 400W metal halide lamps enclosed in elliptical reflectors were used in constructing a continuous solar simulator for testing of the CPC collector developed in this work. Various tests were conducted on the constructed simulator and ASTM standard was used in its characterization. The percentage of non-uniformity (ranging from 12 to 21%) was obtained depending on the size of the illumination area considered. Also it was found that the temporal instability of this simulator is 7.78, 7.96 and 8.76% for illumination areas of 200 x 200, 200 x 250 and 300 x 300 mm^2 respectively. This shows that this simulator met the temporal instability requirement of ASTM of class C (which $\leq$ 10%). The detailed studies conducted on the different reflector shapes will enable the continuation of the process of building a large area simulator for wide range of research work.

CHAPTER FIVE

5. Geometric and Optical Characterization and Optimization of heat pipe based CPC – Ray tracing

5.1. Introduction

This chapter presents a detailed investigation of the geometric and optical characteristics of the low concentration (2 – 5X) heat pipe based Compound Parabolic Collector (HPCPC). Two different tools were developed and used in the characterization and optimization. A model was developed in Microsoft Excel (called HPCPCGeometric) which generates the concentrator profile and characterizes it in terms of height, aperture width, concentration ratio, height to aperture ratio, etc. Then ray tracing technique was extensively used to optically characterize and optimize the performance of the HPCPC using advanced ray tracing software Optisworks®. A novel approach of using double receiver in a CPC is also presented and papers were published from this work.

5.2. Heat pipe based CPC

As shown in Table 2.1 in chapter 2, CPC with concentration ratios less than 5 were considered as stationary and can produce output temperature ranging from 60 to 240^{o}C. The reasons for the selection of CPCs with concentration ratio between 2 and 5 in this work are:

- The selected range of concentration ratio can meet most of the domestic and even some industrial needs for heating, cooling, drying, etc.; hence it is enough for the intended applications of this work.

- CPC within this range of concentration ratio can operate either at temperature above that of flat plate or at the same temperature outputs as flat plate (but at lower cost).

The CPC in this work uses tubular shape thermosyphon heat pipe as receiver to enhance the heat transfer and reduces losses hence the name HPCPC. The reader is referred to section 2.2.1 for general introduction on the CPC and section 6.2 for information on heat pipe.

5.2.1. HPCPC Geometry

In generating the HPCPC for this work, acceptance angle and radius of the receiver are considered as the inputs. Acceptance angles ($2\theta_a$) ranging from 20^o to 60^o and receiver radii (r) of 0.011, 0.0125, 0.0225 and 0.025 were used in this study. The selection of the acceptance angle is based on the target concentration ratios and the receiver radii are based on the commercially available pipe sizes and the intended applications. These two parameters were used in generating the geometries and define other factors related to the collector such as the concentration ratio, average number of reflection of the rays and the geometry size (collector height, aperture width and height to aperture ratio).

The following equations [159] were used in generating the geometries of the symmetric CPC of this work:

For involute section;

$$\begin{aligned} x &= r(\pm\varphi\cos\varphi \pm \sin\varphi) \\ y &= r(-\cos\varphi - \varphi\sin\varphi) \end{aligned} \tag{5.1}$$

$$\text{Where} -\left(\frac{\pi}{2}+\theta_a\right) \subseteq \varphi \subseteq 0$$

And for macrofocal parabola section;

$$x = \frac{r}{Cos\varphi - 1}\begin{bmatrix} \pm Cos\theta_a \pm Cos(\varphi - \theta_a) \pm \\ (2\pi - \varphi + 2\theta_a)Sin(\varphi - \theta_a) \end{bmatrix}$$
$$y = \frac{r}{Cos\varphi - 1}\begin{bmatrix} (-2\pi + \varphi - 2\theta_a)Cos(\varphi - \theta_a) \\ -Sin(\varphi - \theta_a) - Sin\theta_a \end{bmatrix} \quad (5.2)$$

Where $2\theta_a \subseteq \varphi \subseteq \pi$

The geometric concentration ratio is related to the half acceptance angle as [18]:

$$C = 1 \diagup \sin\theta_a \quad (5.3)$$

The average number of reflections for full and truncated CPC is calculated as [19]:

$$n_i = \max\left[C\frac{A_{RT}}{4a_T} - \frac{x^2 - \cos_2\theta}{2(1+\sin\theta)}, 1 - 1 \diagup C \right] \quad (5.4)$$

$$x = \left(\frac{1+\sin\theta}{Cos\theta}\right)\left(-\sin\theta + \left(1 + \frac{h_t}{h}\cot^2\theta\right)^{1/2}\right) \quad (5.5)$$

Where A_{RT} is the reflector area per unit depth of the truncated CPC and C is the concentration ratio.

5.2.2. HPCPC Profile model (HPCPCGeometric)

A computer program was developed in Excel spreadsheet using equations 5.1 to 5.5 for generating and characterizing the HPCPC within the stated concentration ratios. The HPCPC formed from this model is made up of four segments; positive and negative involute as well as positive and negative macrofocal, joined together as shown in Figure 5.1a. Each segment is generated by x and y coordinates based on equations 5.1 and 5.2, using the receiver radius and the range of the φ (which depends on the acceptance angle). Figure 5.1b shows a flow chart summarizing the procedure of the model.

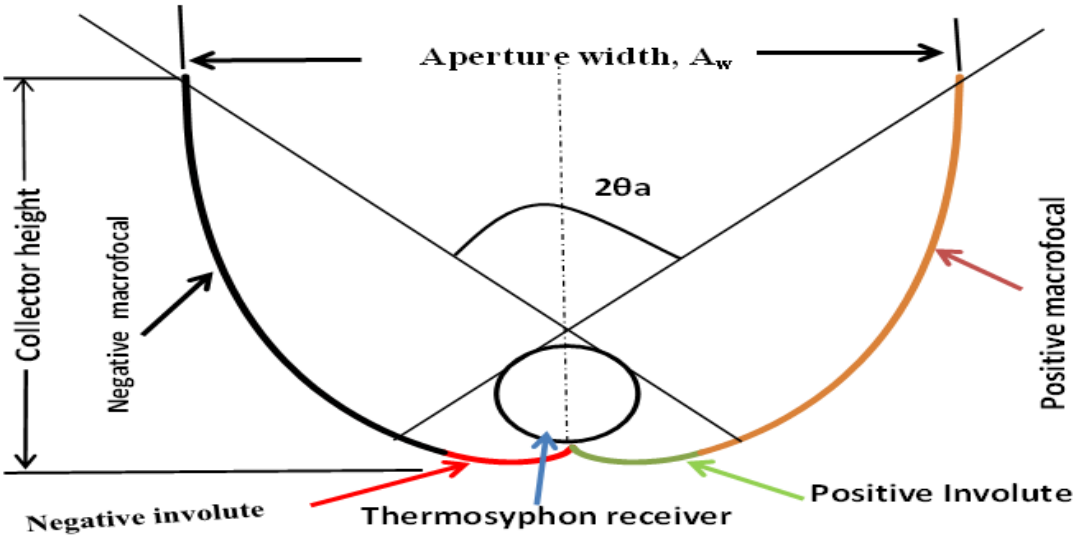

Figure 5.1(a) 2-D view of the HPCPC

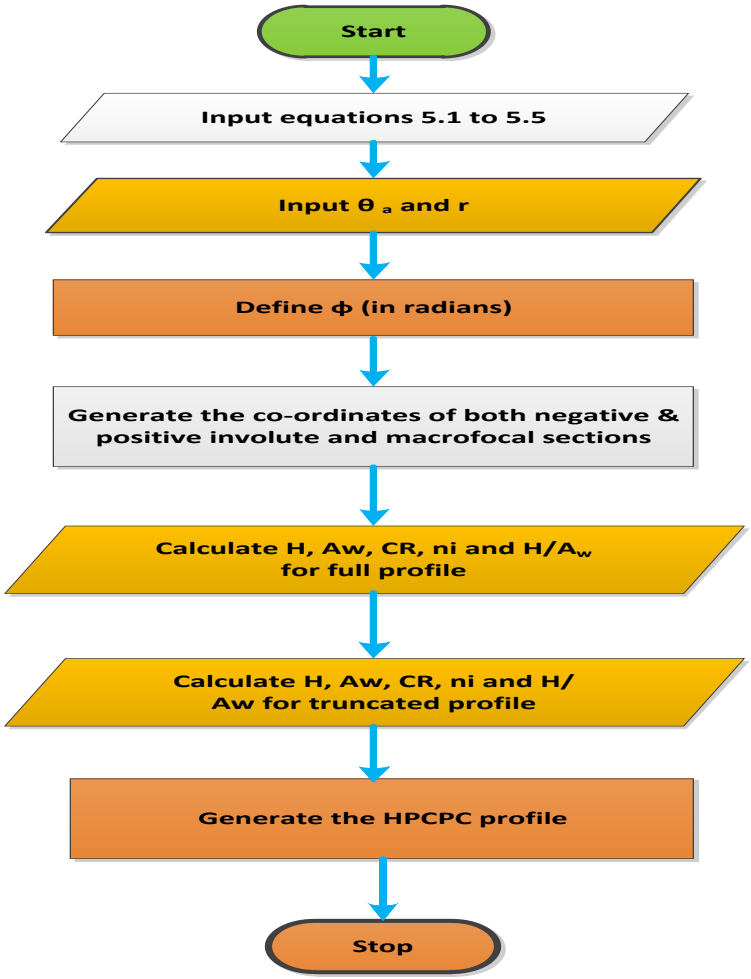

Figure 5.1(b) Flow chart of the HPCPC geometric model

The generated coordinates are plotted using scatter chart type to obtain the geometry, and once the receiver radius is changed for a particular acceptance angle, the values in the coordinates and the generated HPCPC are updated to give a new shape and dimensions. Other outputs obtained are the concentration ratio, collector height, aperture width, height-to-aperture ratio and average number of reflections.

5.2.3. Effects of CPC acceptance angle and receiver radius on HPCPC geometry

Using the model developed in 5.2.2 and the acceptance angles and receiver radii stated in section 5.2.1, the geometry of different HPCPCs were generated and characterized based on the collector height, aperture width, CR, height to aperture ratio, etc. Figure 5.2 shows two dimensional views of the HPCPCs generated from this model at different acceptance angles and 12.5mm receiver radius. Also to verify the geometric parameters of the generated HPCPC obtained from this model, the parametric equations 5.1 and 5.2 were coded in the Solidworks® software and twenty different geometries were generated and characterized. Figure 5.3 shows 3D view of one of such geometry obtained from solidworks. The results from the two approaches were found to be the same and the characteristics of some of these geometries are shown in Table 5.1

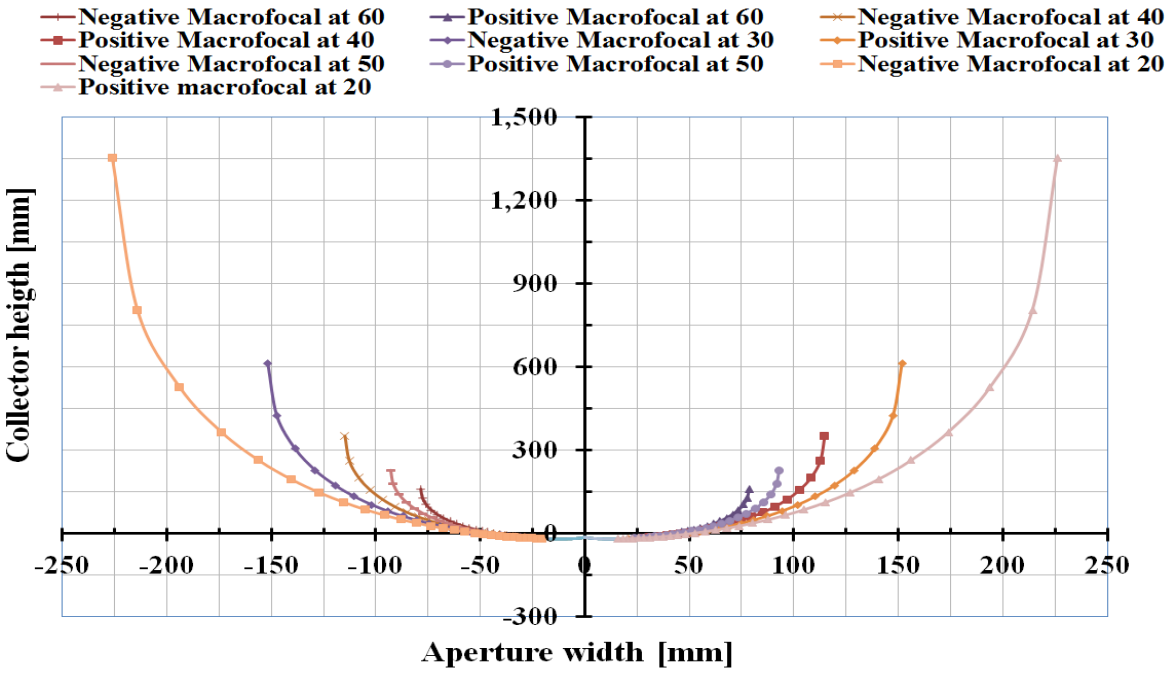

Figure 5.2 Two dimensional views of the generated CPCs at different acceptance angles and receiver radius of 12.5mm

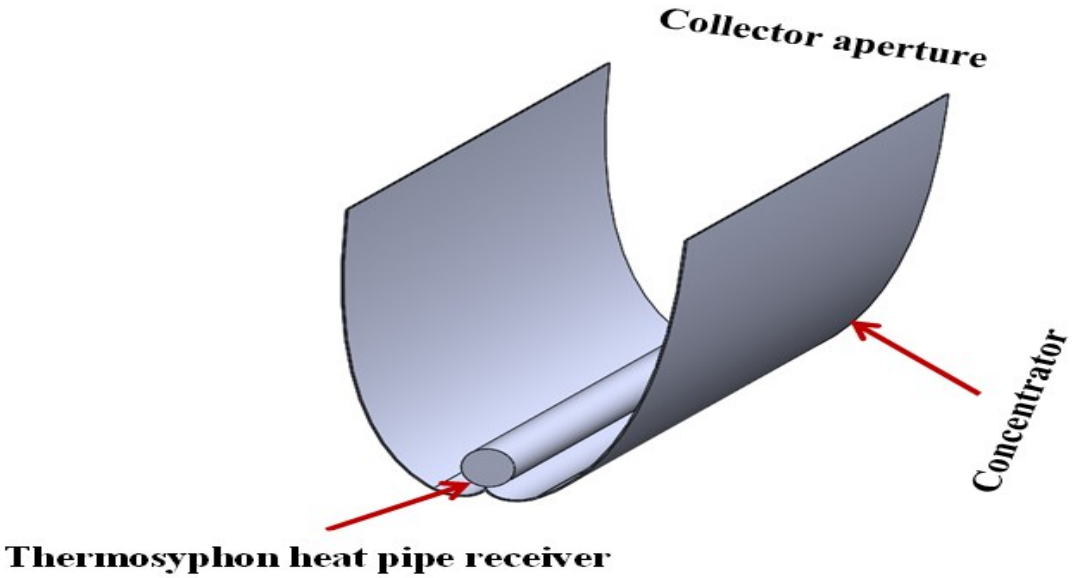

Figure 5.3 3D view of the HPCPC generated from solidworks

Table 5.1 Characteristics of some of the CPCs generated from this model

s/n	Receiver radius (mm)	Geometric Parameters	Acceptance angle		
			60^o	40^o	30^o
1	12.5	Collector height (mm)	180.66	371.617	634.171
		Aperture width (mm)	157.08	229.64	303.45
		Concentration ratio	2	2.92	3.86
		Height to aperture ratio	1.15	1.62	2.09
2	22.5	Collector height (mm)	325.796	668.91	1141.51
		Aperture width (mm)	282.74	413.34	546.22
		Concentration ratio	2	2.92	3.86
		Height to aperture ratio	1.15	1.62	2.09
3	25.0	Collector height (mm)	361.329	743.234	1268.34
		Aperture width (mm)	314.16	459.27	606.91
		Concentration ratio	2	2.92	3.86
		Height to aperture ratio	1.15	1.62	2.09

Table 5.1 and Figure 5.4, show the effects of the CPC acceptance angle and the receiver radius on its geometry. The height of the collector decreases as the acceptance angle increases when the receiver radius is kept constant, thus 60^o acceptance has the shortest concentrator for each receiver size. Figure 5.5 shows the effects of the acceptance angle and receiver radius on the aperture width of the HPCPC. It can be seen from such figure that the aperture width increases as the acceptance angle decreases for any receiver size.

Also, it can be deduced from Table 5.1 and Figures 5.4 and 5.5 that both the collector height and the aperture width increase as the receiver radius increases. Furthermore, as the

acceptance angle decreases both the collector height, aperture width and the concentration ratio increase.

Hence a full CPC with small acceptance angle and large receiver tends to be bigger and have higher concentration ratio compared to its counterpart of large acceptance angle and small receiver size. Such results were used to derive the following simple correlations for a low concentrating symmetric CPC:

$$H = r \Big/ 0.0645(2\theta_a)^{1.8494} \tag{5.6}$$

$$A_w = r \Big/ 0.0766(2\theta_a)^{0.964} \tag{5.7}$$

Where H, r, A_w and $2\theta_a$ are the collector full height, receiver radius, aperture width and acceptance angle (in radian) respectively. These correlations can easily give the dimensions of a symmetric CPC for a particular acceptance angle and receiver radius.

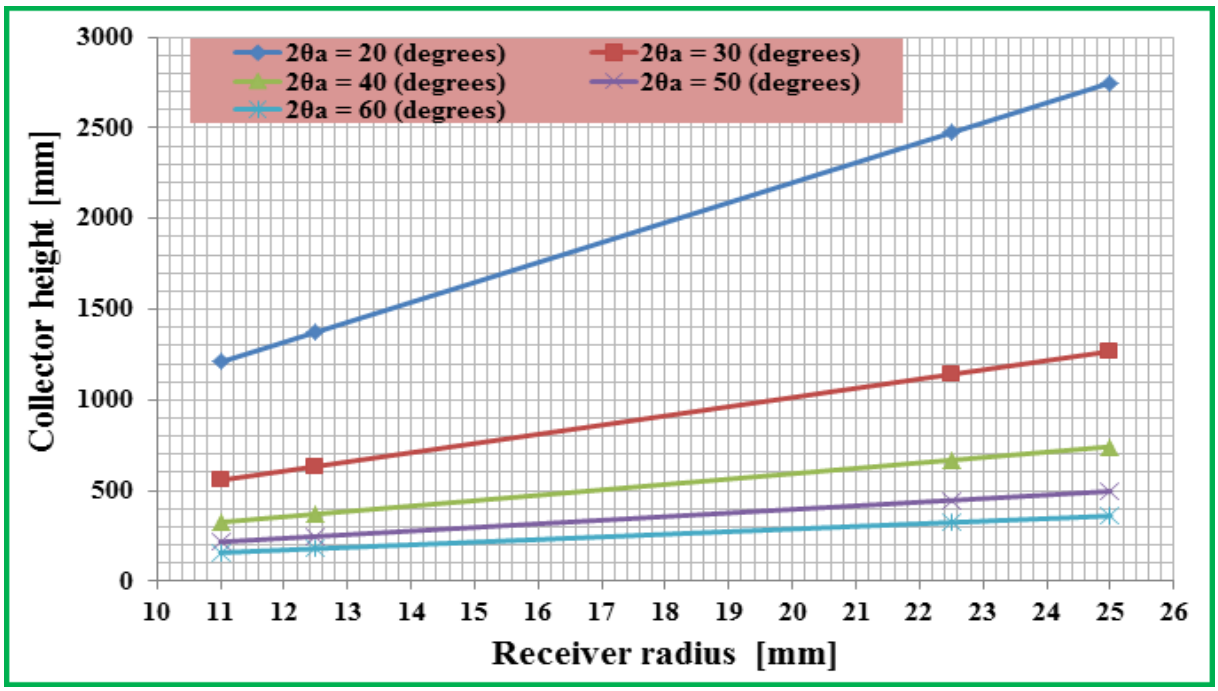

Figure 5.4 Variation of the CPC height with the receiver radius at different acceptance angles

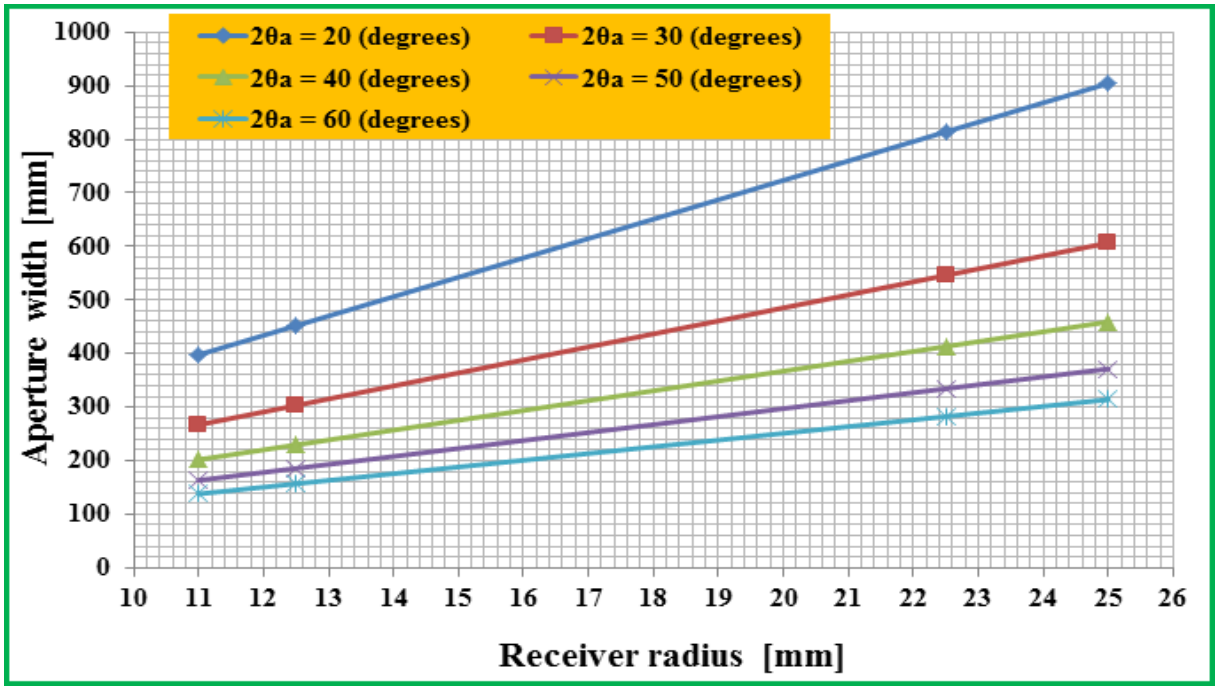

Figure 5.5 Variation of the CPC aperture width with receiver radius at different acceptance angles

It can also be seen from Table 5.1 that height-to-aperture ratio and the geometric concentration ratio increase with the decrease in the acceptance angle but they are independent of the receiver radius. This shows that the increase in height due to the increase in the receiver size is proportional to the increase in the aperture width, thus by combining equations 5.6 and 5.7, the height can be expressed as:

$$H = {1.19A_w}/{(2\theta_a)^{0.8854}} \tag{5.8}$$

It is shown from the foregoing results that the acceptance angle of the HPCPC is very important in defining the geometric characteristics and concentration ability of a CPC solar collector.

5.2.4. Effects of truncation on the HPCPC geometry

Although large acceptance angle results in small size geometry with low concentration ratio,

but generally, the reflector of the CPC tends to be very large. The upper part tends to be parallel to the central plane of symmetry of the concentrator, hence it contributes little to the radiation reaching the absorber, so such part can be removed without any significant effect on the performance of the collector [18]. This process of reducing the height of the solar collector is called ***truncation***. Hence CPC is truncated to reduce its height which results in saving materials, space and cost with little sacrifice in performance. The height of the full collector (H) is usually cut to (h) and this causes changes in the aperture width and half acceptance angle as shown in Figure 5.6.

To ease reference to several configurations of HPCPC studied in this thesis, a nomenclature of HPCPC***x***R***y*** is used throughout which stands for *"heat pipe based compound parabolic collector with* ***x*** *acceptance angle and* ***y*** *receiver radius"*.

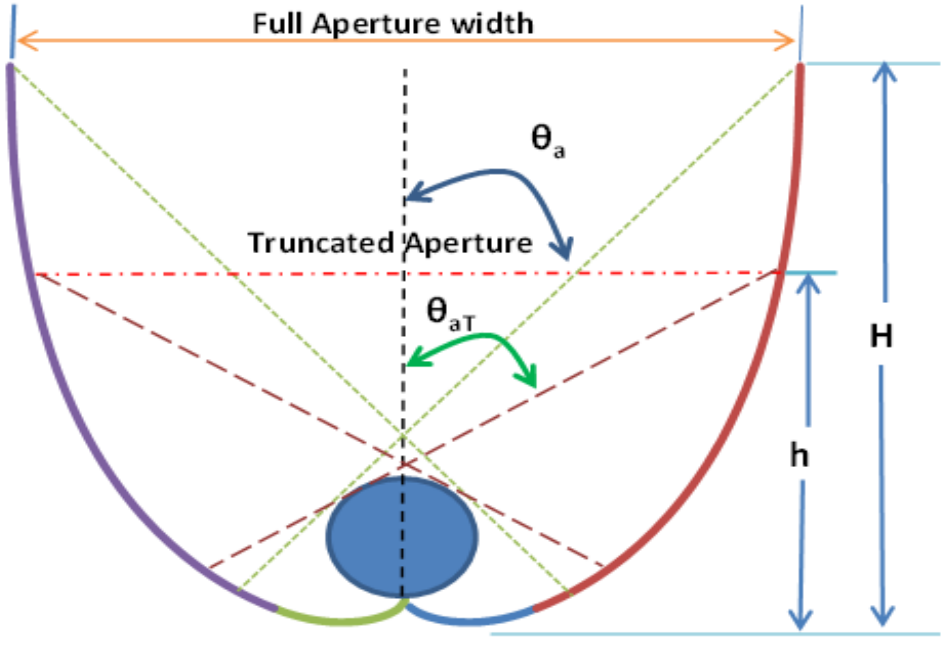

Figure 5.6 Full and Truncated HPCPC

To study the effects of the truncation on the geometry of HPCPC, the heights of the HPCPC60, HPCPC40 and HPCPC30 with receiver radii of 12.5 and 25mm were truncated by

10, 30, 50 and 70% and Figure 5.7 shows samples of the generated profiles. Table 5.2 (a, b and c) show the geometric characteristics of HPCPC60R12.5, HPCPC40R12.5 and HPCPC30R12.5 at different percentage of truncation (referred to as *truncation level*).

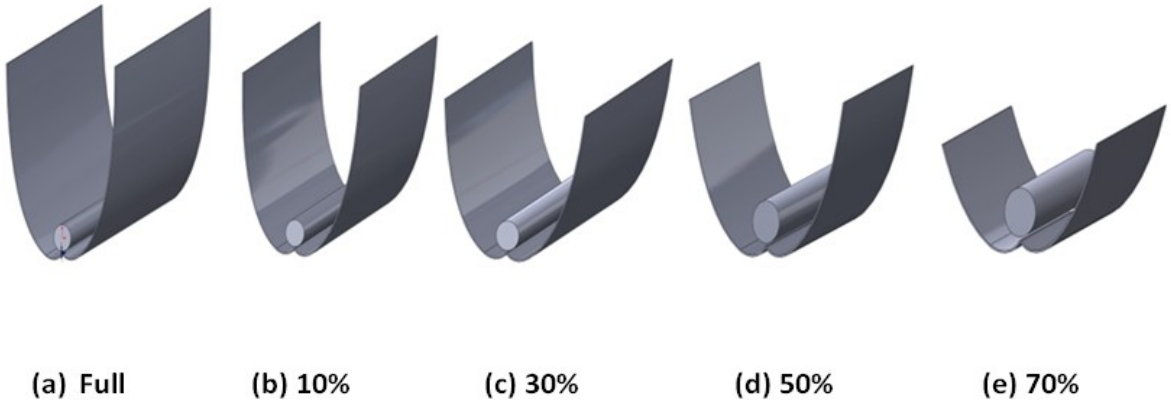

Figure 5.7 Configurations of HPCPC60R12.5 at different truncation levels

It can be seen from these tables that as the truncation level increases, the collector height, aperture width, average number of reflection and height-to-aperture ratio decrease while the acceptance angle increases.

Table 5.2(a) Geometric characteristics of HPCPC60R12.5 at different truncation levels

Percentage truncated (%)	**Collector Height (mm)**	**Aperture Width (mm)**	**Height-to-Aperture ratio**	**Concentration ratio**	**Half Acceptance Angle/^{o}**	**Average number of reflection**
0	180.65	157.08	1.15	2.00	30.00	0.500
10	162.58	156.60	1.04	1.99	30.17	0.497
30	126.45	152.30	0.83	1.94	31.00	0.485
50	90.33	141.99	0.64	1.81	33.50	0.448
70	54.20	122.14	0.44	1.56	39.87	0.359

Table 5.2(b) Geometric characteristics of HPCPC40R12.5 at different truncation levels

Percentage truncated (%)	Collector Height (mm)	Aperture Width (mm)	Height-to-Aperture ratio	Concentration ratio	Half Acceptance Angle/^{o}	Average number of reflection
0	371.6	229.60	1.62	2.92	20.00	0.66
10	334.44	228.96	1.46	2.92	20.06	0.66
30	260.12	222.88	1.17	2.84	20.63	0.65
50	185.8	208.14	0.89	2.65	22.17	0.62
70	111.48	179.17	0.62	2.28	26.00	0.56

Table 5.2 (c) Geometric characteristics of HPCPC30R12.5 at different truncation levels

Percentage truncated (%)	Collector Height (mm)	Aperture Width (mm)	Height-to-Aperture ratio	Concentration ratio	Half Acceptance Angle/^{o}	Average number of reflection
0	634.20	303.50	2.09	3.86	15.00	0.74
10	570.78	302.59	1.89	3.85	15.04	0.74
30	443.94	294.73	1.51	3.75	15.45	0.73
50	317.10	275.55	1.15	3.51	16.56	0.71
70	190.26	237.57	0.80	3.02	19.30	0.67

The concentration ratio of the HPCPC decreases as the truncation level increases as shown in Figure 5.8 and this is due to the increase in the acceptance angle. Also the average number of reflection decreases with the increase in the truncation level as showed in Figure 5.9 and this is due to the decrease in the concentration ratio and these trends are found to be the same for HPCPC40 and HPCPC30 (Table 5.2b and c). From these results it is shown that truncated HPCPC have wider acceptance angle, lower concentration and low number of reflection. Hence it can accept more radiation than full profile and have fewer losses due to reflection.

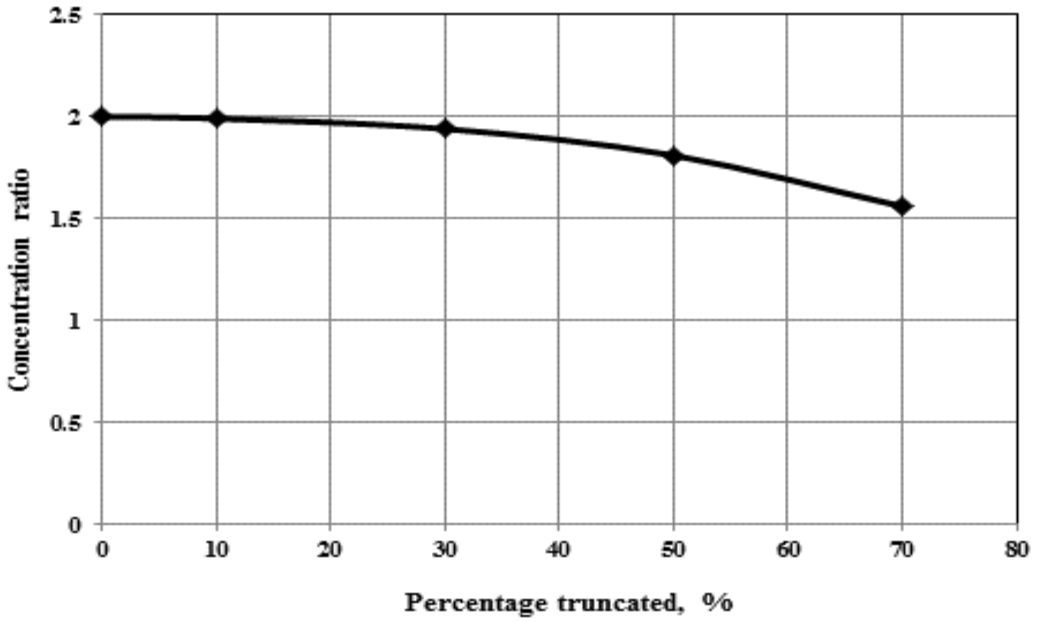

Figure 5.8 Variation of concentration ratio with truncation level for HPCPC60R12.5

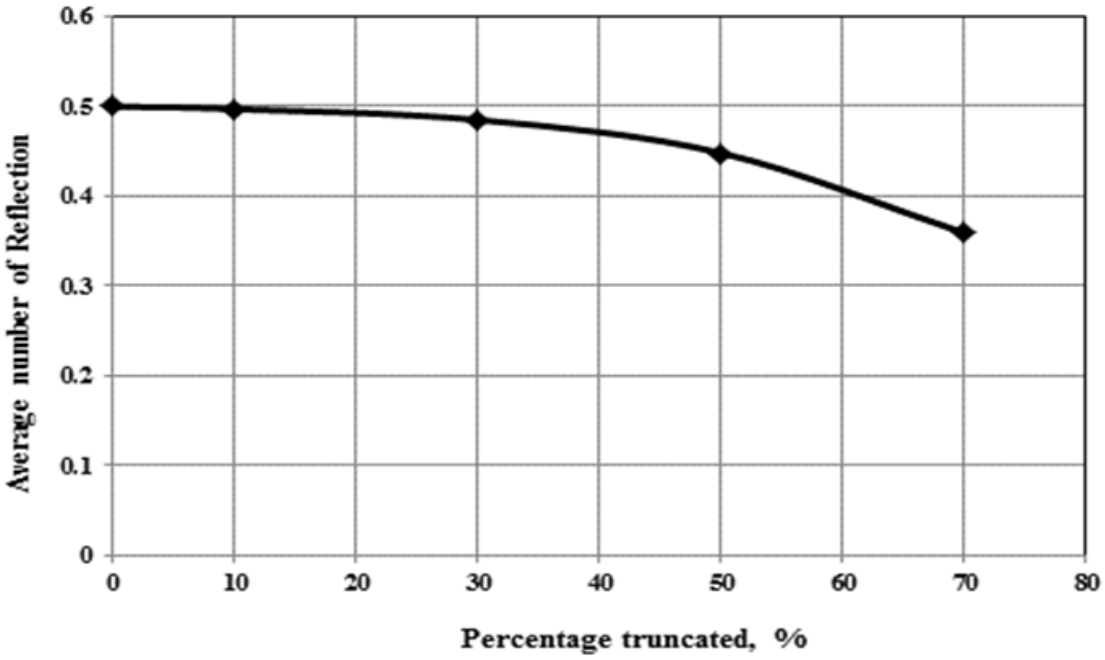

Figure 5.9 Variation of average number of reflection with truncation levels

5.3. Optical performance prediction of the HPCPC – Ray tracing Technique

Ray tracing technique is employed in the analysis of concentrating collectors to determine the intensity and distribution of the rays on the receiver of the collector. It is used to determine the optical performance of solar systems both thermal [160] and PV [115, 161] systems. The method employs vectors for determining the direction and point of intersection of incident rays with the reflecting surface, and then the direction of the reflected rays which follow the law of reflection (Figure 5.10).

Snell's law describes the behaviour of the refracting surfaces by defining the relationship between the angles of incidence and refraction for rays striking a surface between two media of different refractive indices. The laws of reflection and refraction are applied to the trace rays in solar systems and can be expressed in vector form as [161]:

$$\vec{r}_{ref} = \vec{i} - 2\left(\vec{i}.n\right)n \tag{5.9}$$

$$n_r \vec{r}_{ref} = n_i \vec{i} + \left(n_r \vec{r}_{ref}.n - n_i \vec{i}.n\right)n \tag{5.10}$$

Where $\vec{i}$ and $\vec{r}_{ref}$ are the directions of incident and reflected rays respectively. While n is the direction of the normal of the reflector surface. The incident, reflected and normal all lie on the same plane and it is assumed that the incident and reflected rays make equal angles with normal (specular) as shown in Figure 5.10.

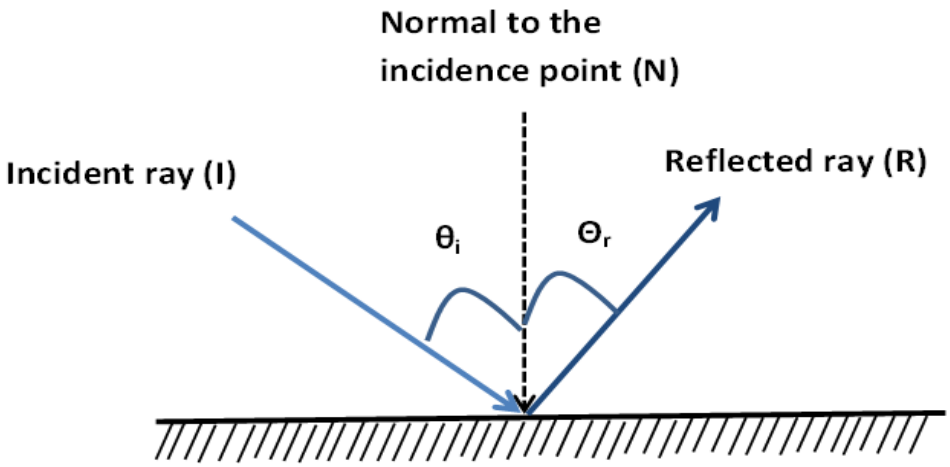

Figure 5.10 Law of Reflection

Figure 5.11 shows the behaviour of rays entering a CPC at different incident angles. Rays incident at angles less than half acceptance angle are reflected onto the receiver either directly or after undergoing a number of reflection(s). But rays with incident angles greater than the half acceptance angle are reflected back through the aperture without hitting the receiver as lost rays.

If the CPC aperture is covered with glass, the rays striking the aperture may be reflected back, absorbed or transmitted through the glass. The direction of the transmitted rays is defined by Snell's law. Some of the rays striking the reflector are reflected back whereas some are absorbed causing loss of energy depending on the reflectivity of its surface. The assumptions of ray tracing analysis can be summarized as follows [161]:

i. All rays obey Fermat law which states that rays follow shortest distance and take minimum time when travelling from one point to another
ii. All rays are specular (i.e. angle of incident equals to angle of reflection)
iii. The incident solar radiation is made up of parallel rays carrying equal amount of energy

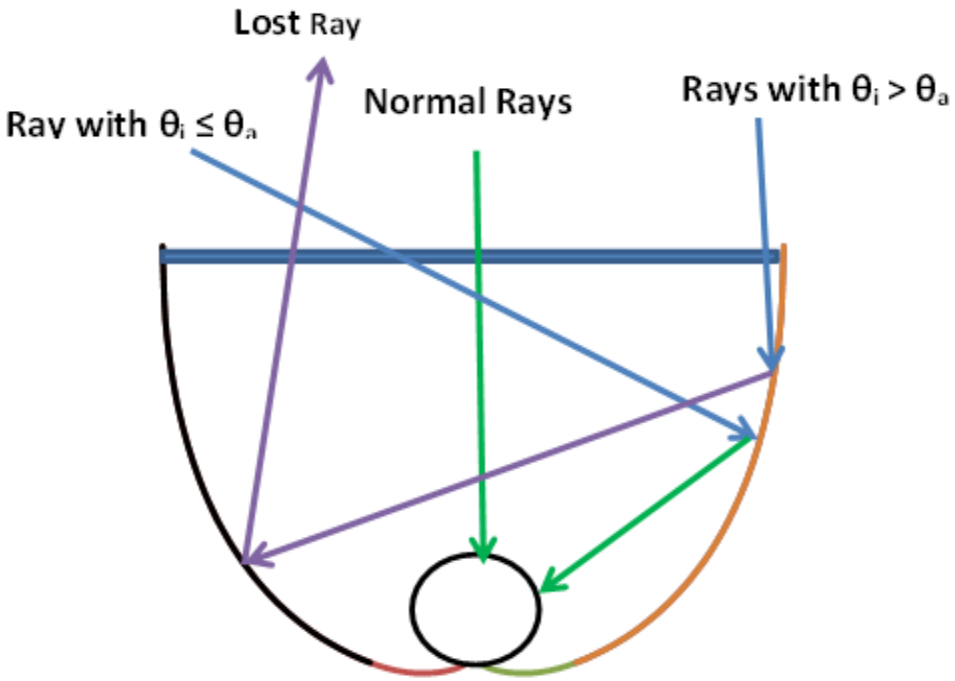

Figure 5.11 Behaviour of rays in CPC

5.3.1. Optical simulation set – up

An advanced ray tracing software (Optisworks®) was used throughout this thesis for optical performance simulations. The package is capable of simulating the performance of solar systems at various solar hour angles (or incident angle), irradiance, material properties and different configurations of collector, etc. The technique is capable of simulating the sun intensity at different sun hour angles, to show irradiance, power and flux distributions on the collector aperture and on the receiver surface.

The use of this software for ray tracing and simulation of the HPCPC involves five major stages (shown in Figure 5.12) including generating the HPCPC profiles, modelling the source (sun), defining material properties, defining the incoming and receiver detectors and running the ray tracing and simulation. Due to the shape of the receiver of this work (cylindrical),

eight detectors were used to identify the flux distribution on the top, bottom and two sides of the receiver.

The source can be modelled to represent the real sun or a light source like lamp in a solar simulator. Its definition involves defining the power (W), emittance type (uniform or variable), intensity type (Lambertian, Cos or Gaussian), spectrum (Monochromatic or blackbody), temperature, ray tracing (true or false colour) and the number of rays. The boundary conditions applied include the irradiance in the source, reflectivity of the concentrator, absorptivity of the receiver and limited half angle.

A simulation was carried out according to the process outlined in Figure 5.12 using the average radiation of the mean day of November (700 W/m^2, as obtained from the model in chapter 3) at tilt angle equal to the latitude of Kano. In this simulation, the source was set to generate 10 Mega Watts rays and the shape of the source was defined as planar and its size was made larger than the aperture area of the collector, so that the rays emitted cover the entire HPCPC aperture. The intensity type used was "Lambertian" and limited half angle of 0^o was set for the source. The simulation was run at different solar hour angles with zero taken as the zenith position. The modelled sun moves in the E-W orientation along the length of the collector as shown in Figure 5.13.

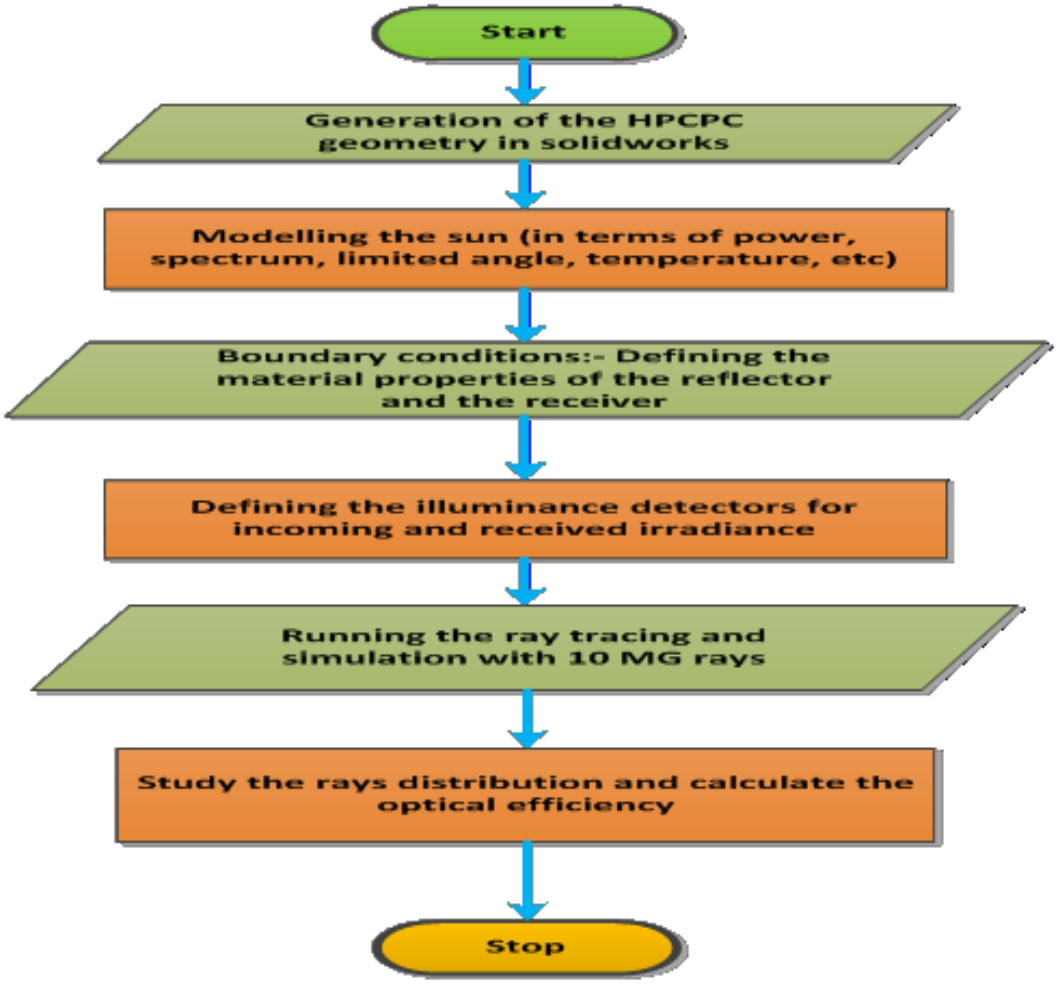

Figure 5.12 Flow chart of the modelling process of HPCPC using ray tracing technique

Figure 5.13 shows the distributions of rays within the CPC, irradiance on the aperture and irradiance on the bottom of the thermosyphon receiver for sun hour angles of 0^o, 30^o, 45^o and 75^o, where 0^o is the zenith. It shows that as the sun angle increases (i.e. moving away from the zenith), the amount of rays inside the collector is reduced and more rays are lost. Also, the irradiance on the aperture decreases as the sun moves from 0^o (700 W/m^2) to 75^o (228 W/m^2). Figure 5.13 also shows non-uniform irradiance distributions at the bottom of the receiver with high concentration at some points on its surface.

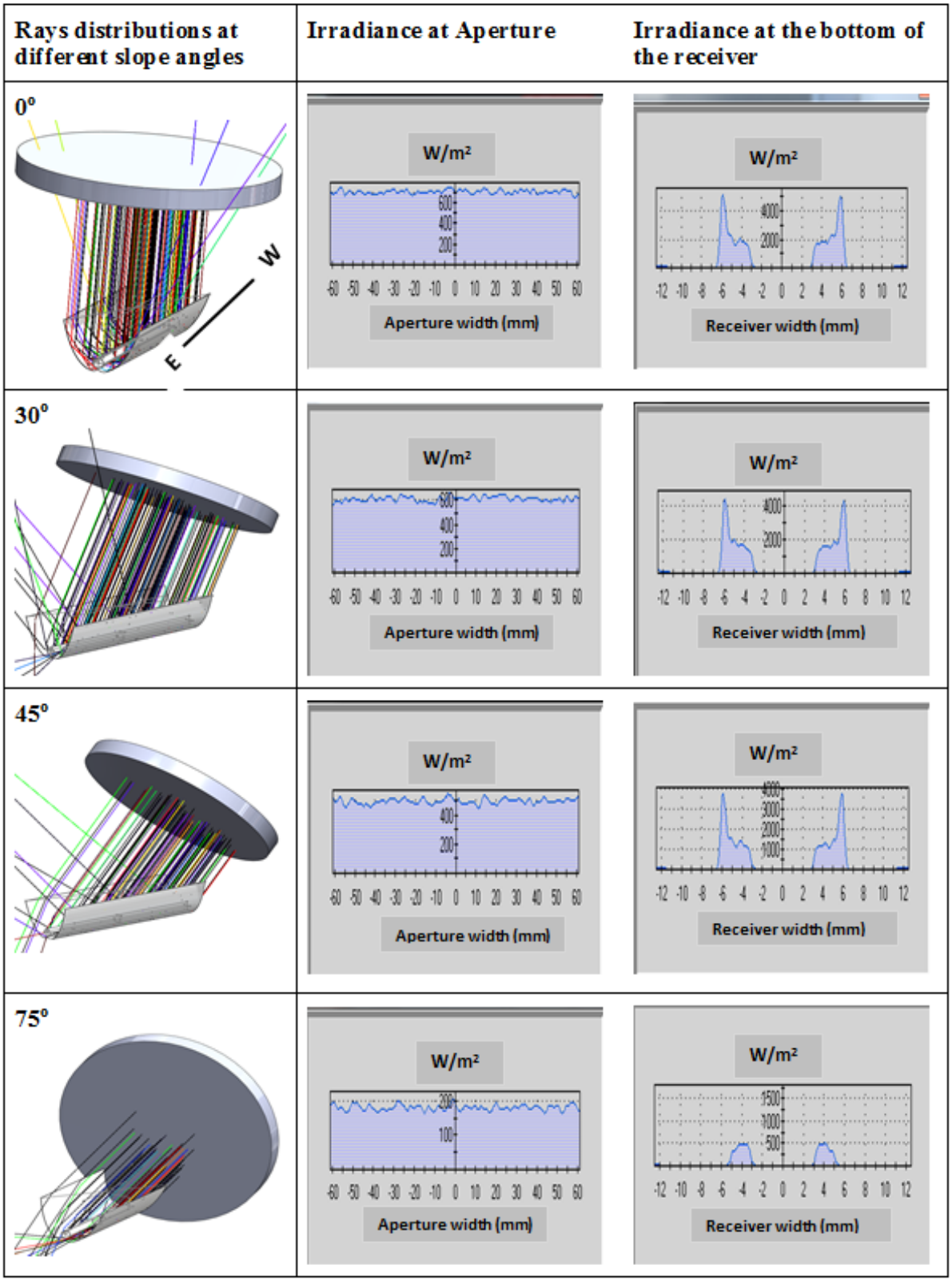

Figure 5.13 Rays distribution, irradiance at the aperture and the bottom of the receiver at different sun hour angle

Concentration of the irradiance at such regions creates hot spots on the receiver. These hot spots cause thermal losses due to the large temperature difference between the region and the ambient. The effects of the hot spot on the collector can be reduced by either locally changing the geometry of the receiver (creating cavity) or altering the surface quality at the hot spots. Such results highlight the advantage of using ray tracing technique in the analysis and design of CPC collectors where hot spot regions can be identified and appropriate solutions can be developed.

5.4. Optical performance of HPCPC

5.4.1. Optical performance of HPCPC60R11

The modelling procedure of the advanced ray tracing technique to be used in this thesis for the prediction of the optical performance of HPCPC was first validated with experimental results.

Two geometries of HPCPC60R11; with reflectivity of 60% (HPCPCR60) and 80% (HPCPCR80) truncated by 60% (Figure 5.14) whose characteristics are given in Table 5.3 were fabricated using electric discharge machining (EDM) process in the school of Mechanical Engineering, University of Birmingham, UK. EDM is a machining process of cutting a work piece to the desired shape by using an electrical spark as cutting tool. The surface of one the concentrator and the side plates were polished and reflectivity of 60% was achieved which was measured using a Perkin – Elmer UV – Vis –NIR spectrometer shown in Figure 4.8 at the University of Exeter, UK. Figure 5.15 shows the reflectivity test results for the concentrator. The concentrator surface of the other geometry was lined with reflective film material (reflectivity = 80%).

Table 5.3 Geometric characteristics of full and truncated HPCPC60R11

Parameter	**Full profile**	**Truncated profile**
Acceptance angle (^{o})	60	67.5
Collector height (mm)	158.99	64
Receiver radius (mm)	11	11
Aperture width (mm)	138.23	116.16
Collector length	200	200
Aperture area (mm^2)	27646	23232
Receiver area (mm^2)	13823.01	13823.01
Concentration ratio	2	1.8
Reflectivity of the concentrator	60% and 80%	60% and 80%

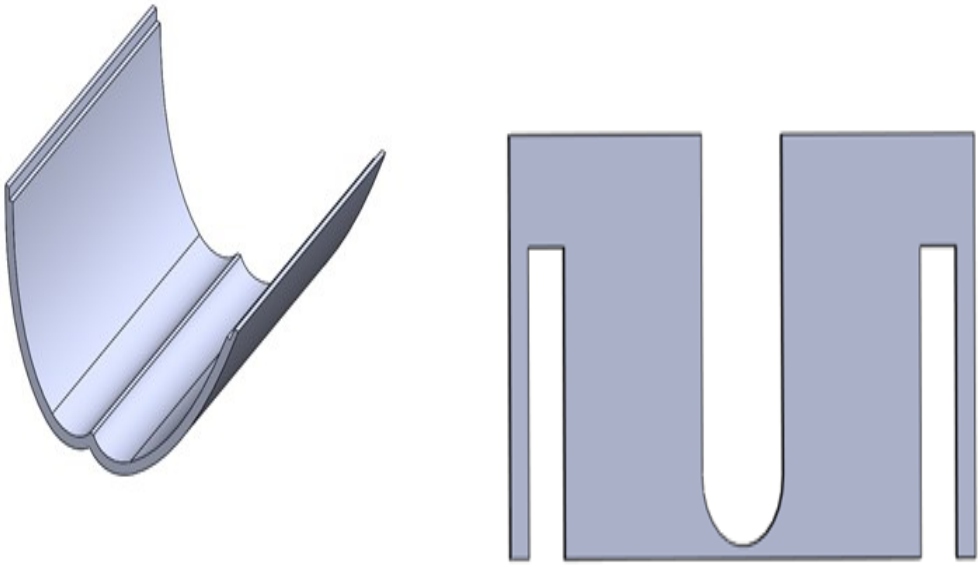

a. Concentrator **b. Side cover**

Figure 5.14 Truncated HPCPC60R11

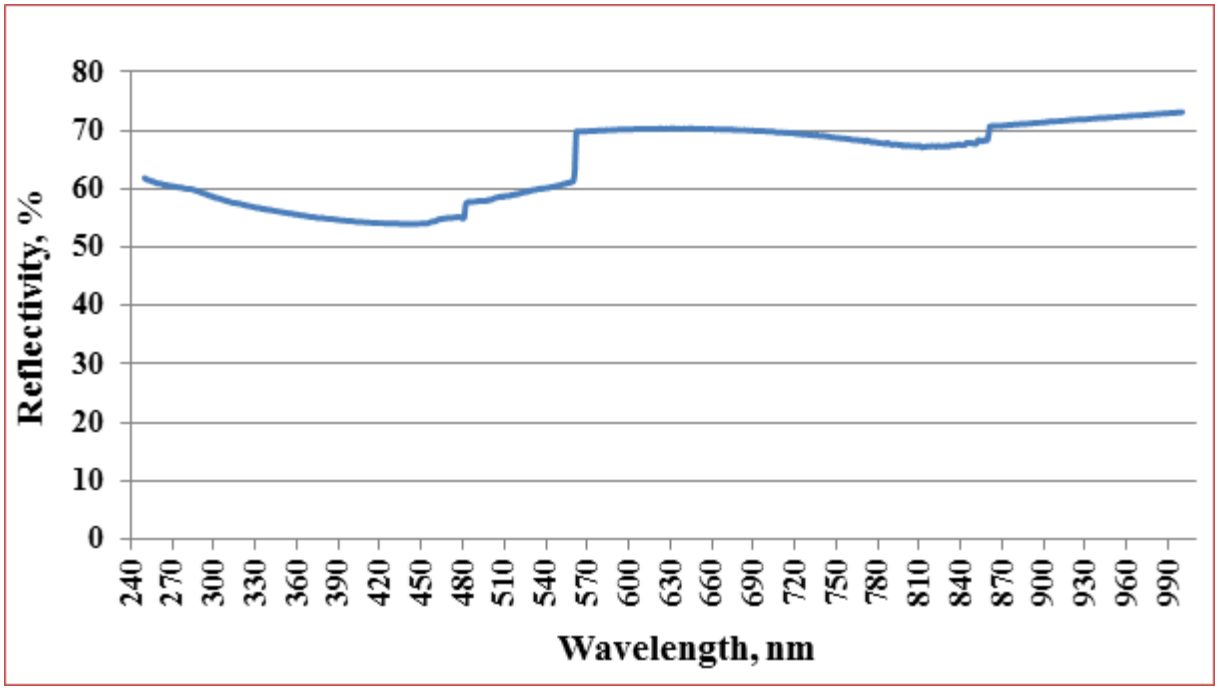

Figure 5.15 Relectivity measurement for the concentrator

5.4.1.1. Experimental set – up

The experimental test rig for the validation of the optical simulation consists of the HPCPC60R11, 400mm long thermosyphon heat pipe, radiant flux sensor, angular adjustment frame, DT85 data taker and other instrumentations. The source of the light is the continuous solar simulator designed for testing the HPCPC in this thesis and discussed in chapter 4. Figures 5.16 and 5.17 show the schematic diagram and photograph of the experimental test facility respectively used for optical and thermal tests.

The incoming and received irradiance were measured using high sensitivity 5 x 5mm flux radiant sensors placed on the aperture and the receiver at various positions. The sensors were purchased from Captec Enterprise® and their technical informations were given in section 4.4.3.1.

The optical experiment was run at different inclination of the collector to the horizontal which represent the solar hour angles and the performance was evaluated based on the optical

efficiency of the collector. Horizontal position is taken as zenith (represented by zero degrees) and the test was conducted between +45^{o} and -45^{o} solar hour angles. At the beginning of the experiment, the simulator was switched on and allowed to reach steady state which takes at least one hour (as discussed in chapter 4). The irradiance at the collector aperture and on the receiver is read by mapping process for each angle and optical efficiencies were evaluated based on equation 5.11.

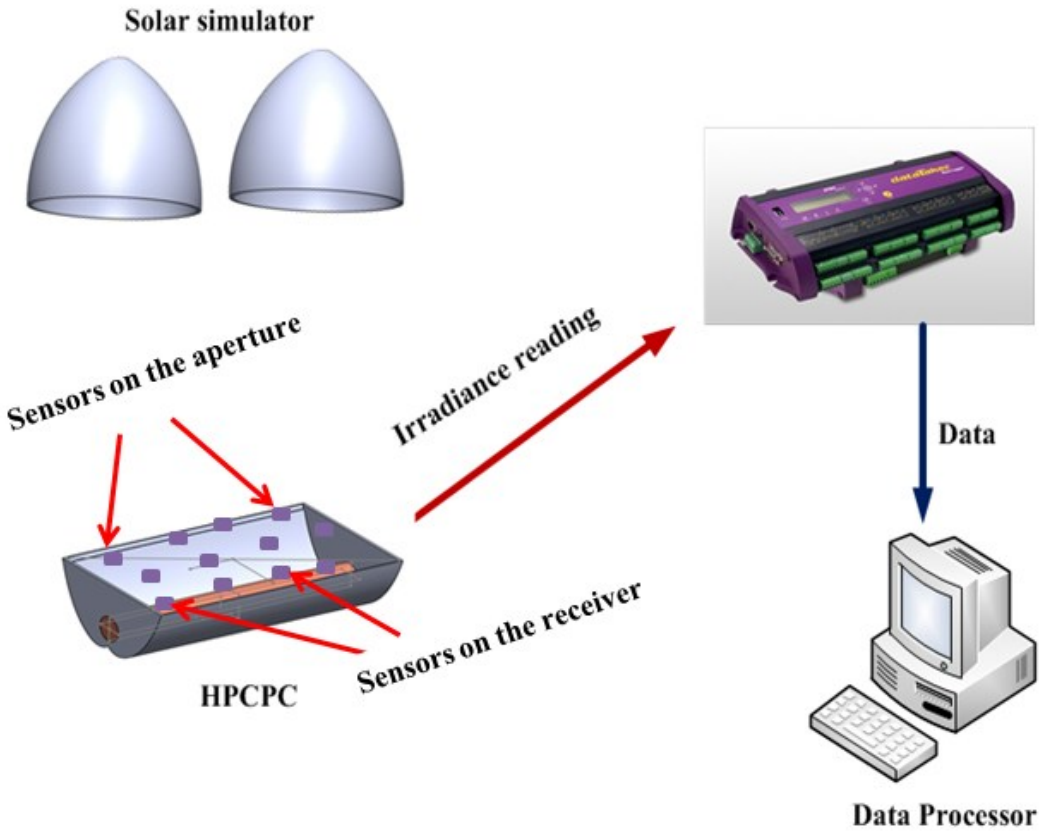

Figure 5.16 Schematic diagram of the test rig

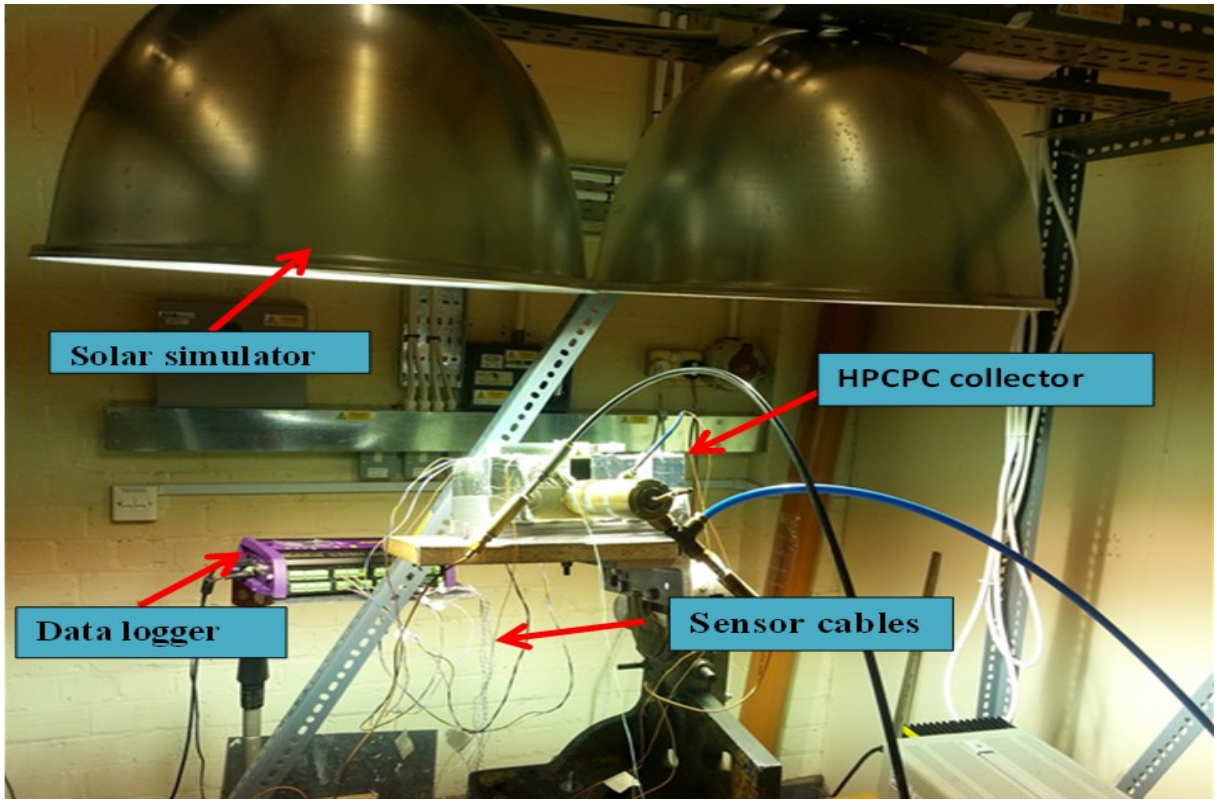

Figure 5.17 Photograph of the experimental set – up

5.4.1.2. Ray tracing analysis for truncated HPCPC60R11 and Validation

Ray tracing analysis was carried out on a HPCPC60R11 whose characteristics is shown in Table 5.3 and experimentally tested in section 5.4.1.1. The simulation set – up was made based on the procedure illustrated in Figure 5.12 and the simulator described in chapter 4 and used in section 5.3.1 was modelled as the source. The simulation was run between solar hour angles of $+45^{o}$ and -45^{o} and the incoming and received irradiance were obtained and optical efficiency evaluated. Figure 5.18 (a and b) shows rays from the simulator at different solar hour angles. The experimental and the simulation results were compared and they showed good agreement within ±4.5% deviation as shown in Figure 5.19. However, the optical efficiency is low in this case due to the low reflectivity of the concentrator.

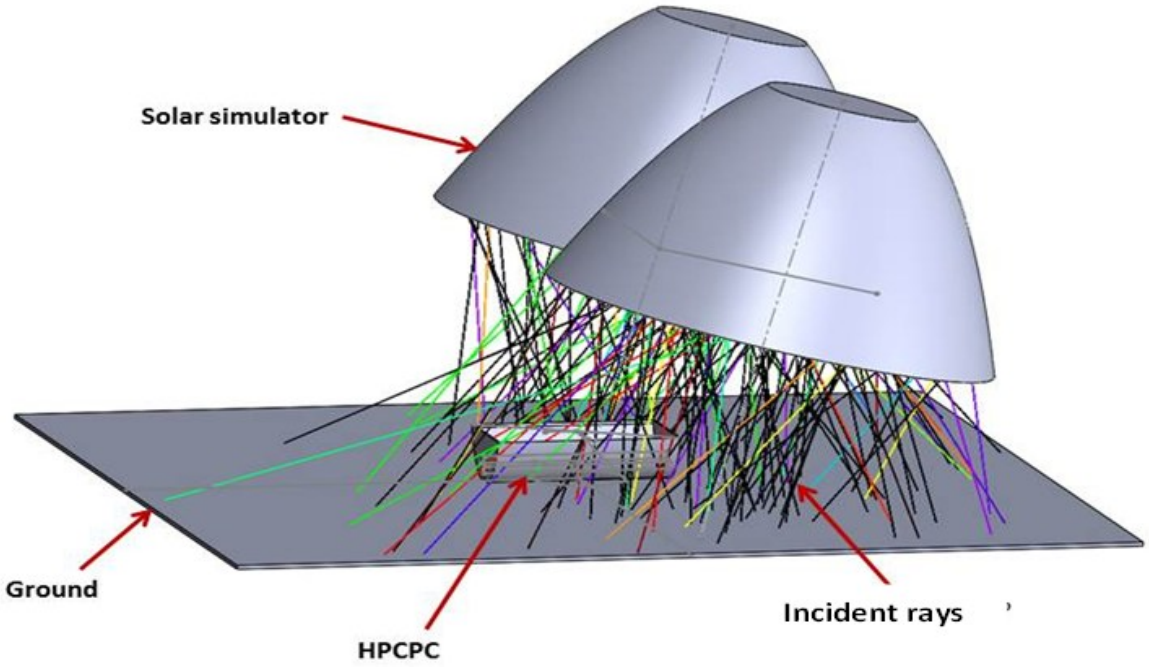

(a) Rays trajectory

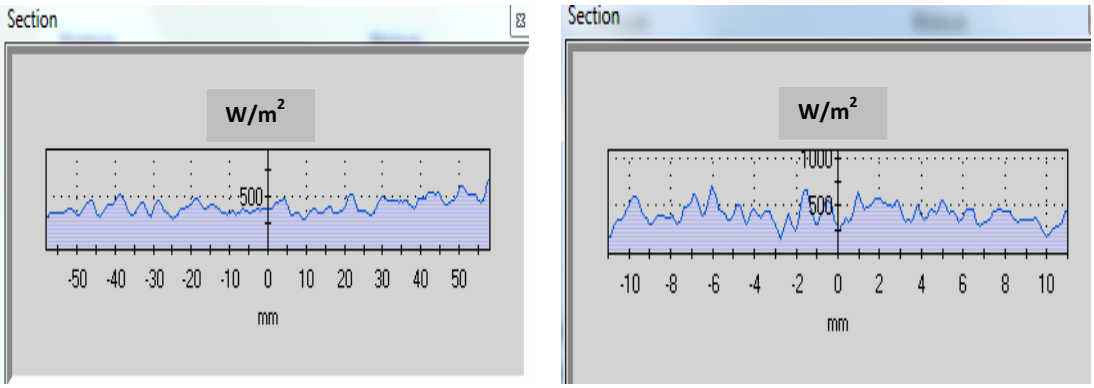

(b) Incoming irradiance **(c)** Top irradiance

Figure 5.18 Incident rays, incoming and received irradiance at 15° solar hour angle

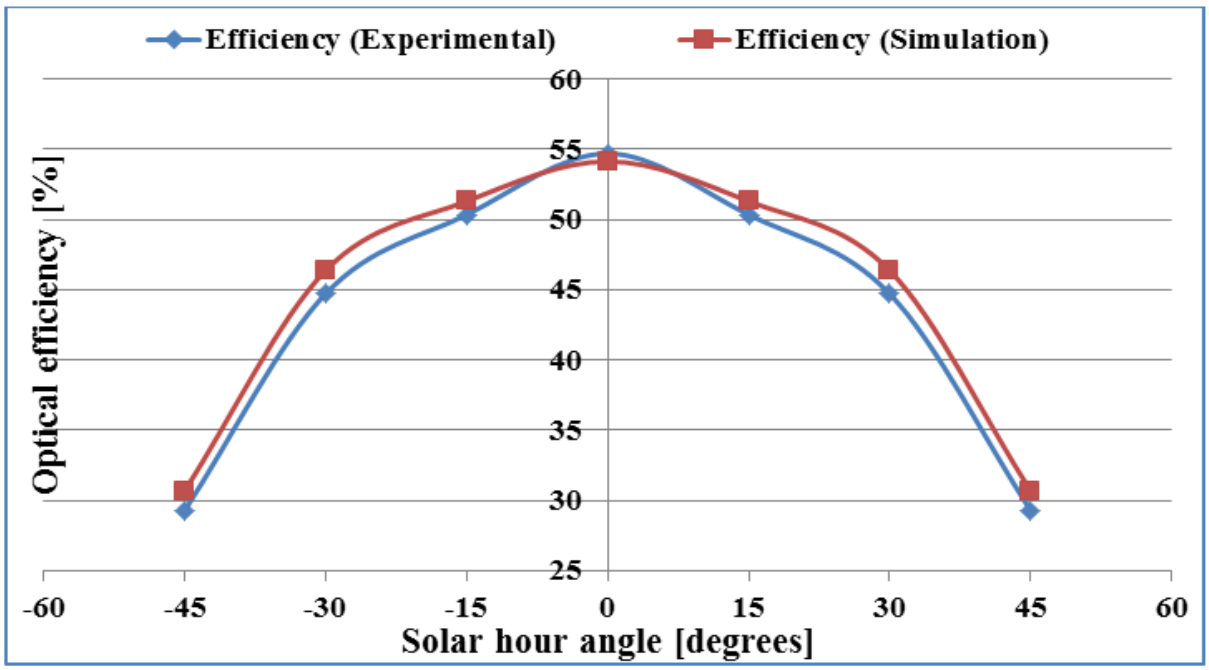

Figure 5.19 Optical efficiency of the HPCPC60R11 at different solar hour angles (simulation and experimental)

5.4.2. Optimization of HPCPC (2 – 5X) using ray tracing technique

Having validated the ray tracing optical simulation approach in 5.4.1.2, this modelling technique is used in investigating and optimizing the performance of different configurations of the HPCPCs characterized in 5.2.1 (concentration ratio between 2 and 5). In this thesis, the performance of the HPCPC's geometries are presented either at different solar hour angles or solar time which represent the incident angles of the rays as defined in Table 5.4.

The simulations were set based on the procedure in Figure 5.12, but the source is modelled to represent the real sun as shown in Figure 5.20. Figure 5.20 shows how the incident rays on the HPCPC aperture and receiver behave as the sun incident angle changes. To generalize this modelling approach, standard irradiance of 1000 W/m^2 was used in most of the investigations. However, in some cases that are more of applicable to particular location, the radiation modelled in chapter 3 is used as inputs to the model. The performance was compared based

on the flux received, hours of operation and optical efficiencies of the different geometries at different solar hour angle. The optical efficiency is calculated as [162]:

$$\eta_{opt.} = \frac{\text{Average Power On The Receiver}}{\text{Average Power On The Aperture}} \tag{5.11}$$

Table 5.4 Solar parameters used in the performance analysis of HPCPC

Solar time, t	Solar hour angle [degrees]	Watch time
5 hours before solar noon (-5)	-75	07:00 AM
4 hours before solar noon (-4)	-60	08:00 AM
3 hours before solar noon (-3)	-45	09:00 AM
2 hours before solar noon (-2)	-30	10:00 AM
1 hour before solar noon (-1)	-15	11:00 AM
Solar noon	0	12.00 noon
1 hour after solar noon (1)	15	1:00 PM
2 hours after solar noon (2)	30	2:00 PM
3 hours after solar noon (3)	45	3:00 PM
4 hours after solar noon (4)	60	4:00 PM
5 hours after solar noon (5)	75	5:00 PM

It can be seen from Figure 5.20 (a) that at zenith almost all the incident rays are reflected on the receiver either directly or after one or more reflection. This is because at such position all the rays are incident with angle less than the acceptance angle of the HPCPC. But as the sun moves away from the zenith some rays will be lost due to their incident angle being greater than the acceptance angle (Figure 5.20b).

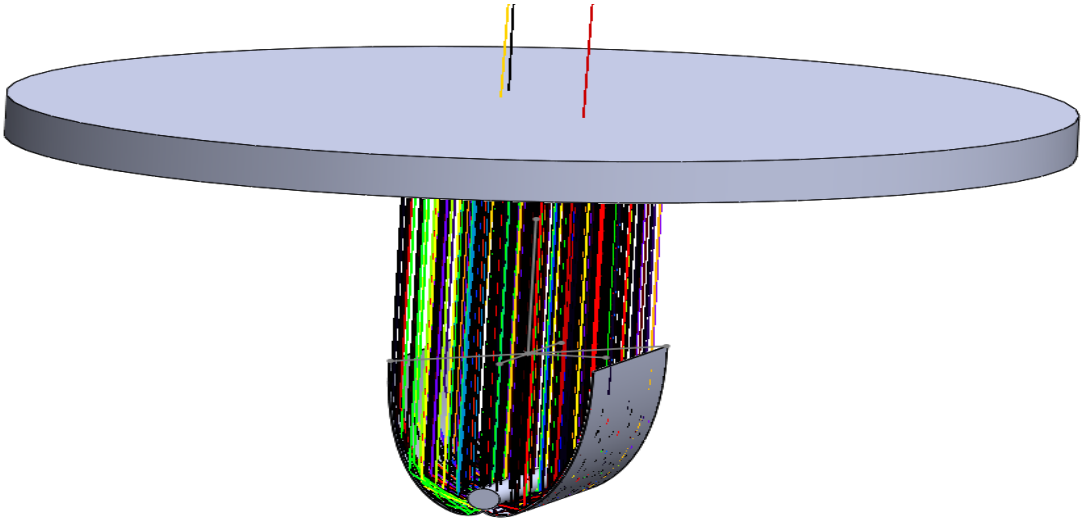

(a) Rays at 0^o (zenith)

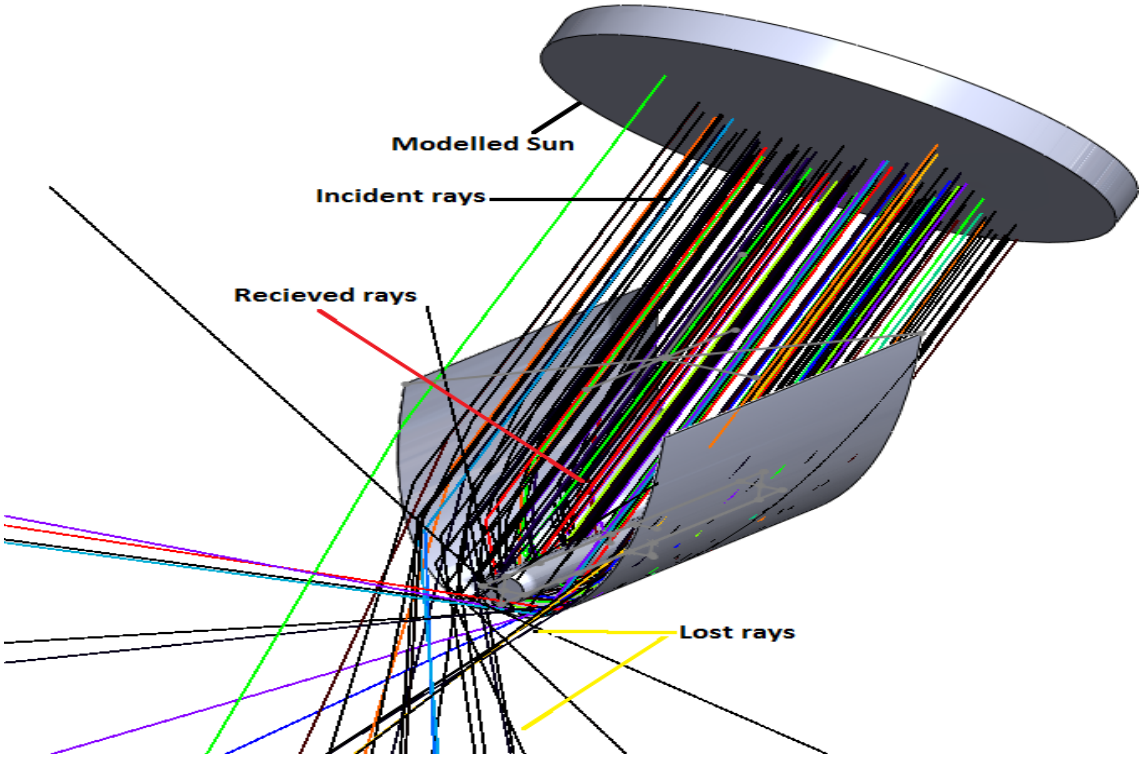

(b) Ray at 45^o

Figure 5.20 Trajectories of the rays incident on HPCPC at different solar hour angles

5.4.2.1. Effects of acceptance angle and receiver radius on the optical performance of HPCPC

The effects of acceptance angle and receiver radius on the HPCPC's geometric characteristics were shown in section 5.1.3. Ray tracing technique is employed to study their effects on the optical performance of the nine configurations of the HPCPCs shown in Table 5.1. Irradiance of 1000 W/m^2 was used in setting up the source and the geometries were simulated in static condition while their performances were evaluated at different solar hour angles. Table 5.5 gives the geometric and optical properties employed in this simulation.

Table 5.5 Geometric and optical properties employed in ray tracing analysis of the various configurations simulated

Parameter	**HPCPC60**	**HPCPC40**	**HPCPC30**
Acceptance angle (^{o})	60	40	30
Receiver radius (mm)	12.5, 22.5 and 25	12.5, 22.5 and 25	12.5, 22.5 and 25
Reflectivity of the concentrator (%)	90	90	90
Receiver absorptivity (%)	100	100	100
Range of solar hour angle (^{o})	-75 to 75	-75 to 75	-75 to 75
Collector length (mm)	200	200	200

Figures 5.21 and 5.22 show the optical efficiencies and irradiance distributions of the configurations in Table 5.5 at different solar hour angles. From these figures, the followings can be observed:

i. For each acceptance angle, the optical efficiency decreases as the receiver radius increases. This is due to the increase in the reflector height with the receiver size and the upper part (which contributes less in focusing the radiation to the receiver) may shade the rays from reaching the receiver.

ii. The optical efficiency increases with the increase in the acceptance angle due to the increase in the rays' acceptance.

iii. The HPCPC with wide acceptance angle operates with reasonable efficiencies for many hours in static position because all rays within the half acceptance angle are concentrated on the receiver.

iv. HPCPC60R12.5 tends to have best performance in terms of optical efficiency and hours of operations but have the least geometric and flux concentration ratios compared to the rest.

v. The optical efficiency of the HPCPC decreases with the increase in the concentration ratio. Hence, the configurations with narrow acceptance angle provide high concentration at the expense of the optical efficiency and operating hours.

vi. The incoming irradiance reduces as the source moves away from 0^{o} (zenith) and also the distributions of the flux on the receiver changes as shown in Figure 5.22. There is high concentration of flux at some areas on the receiver at lower incident angles which creates hot spots as shown in Figure 5.13.

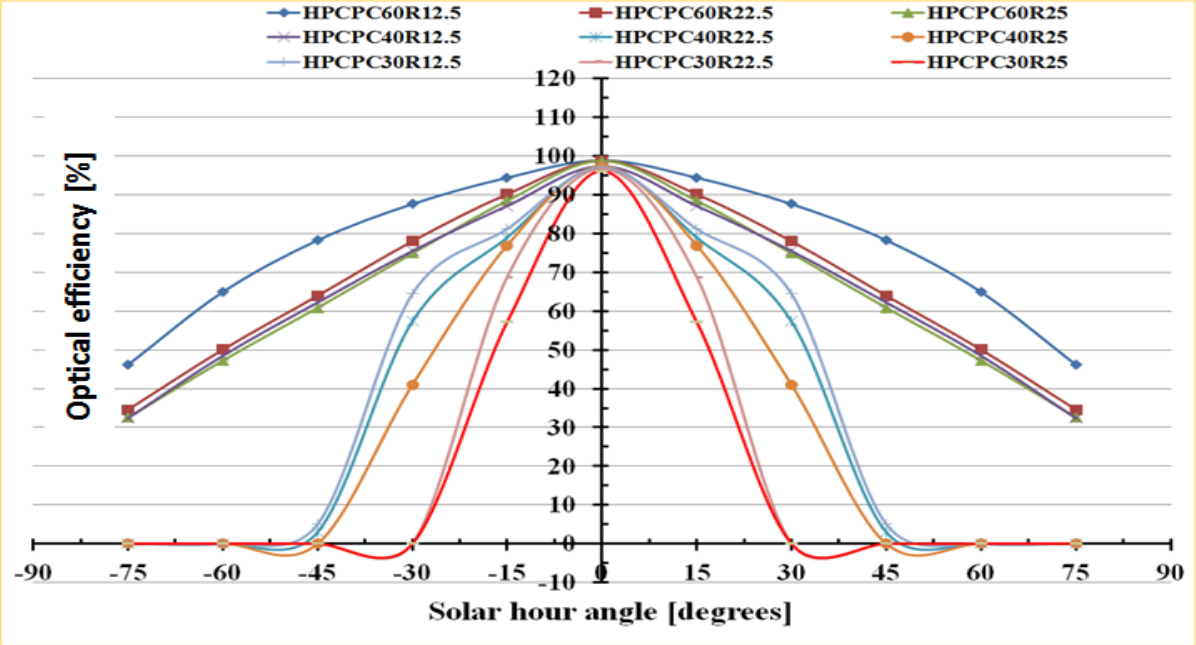

Figure 5.21 Optical performances of HPCPC configurations at different incident angles

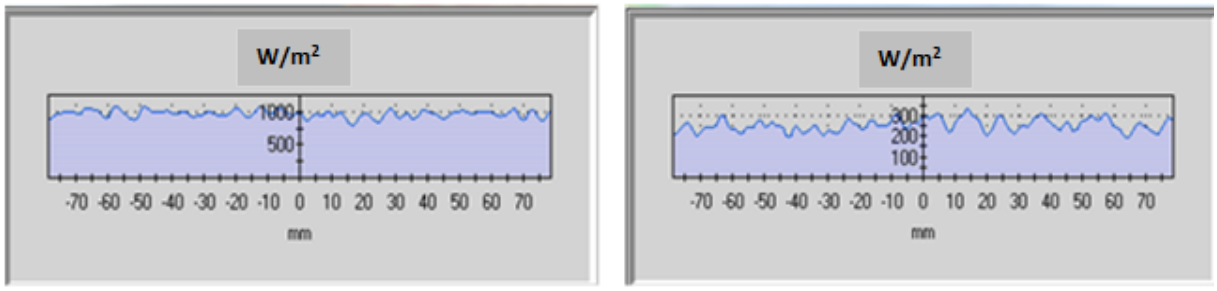

(a) Incoming irradiance at 0° (b) Incoming irradiance at 75°

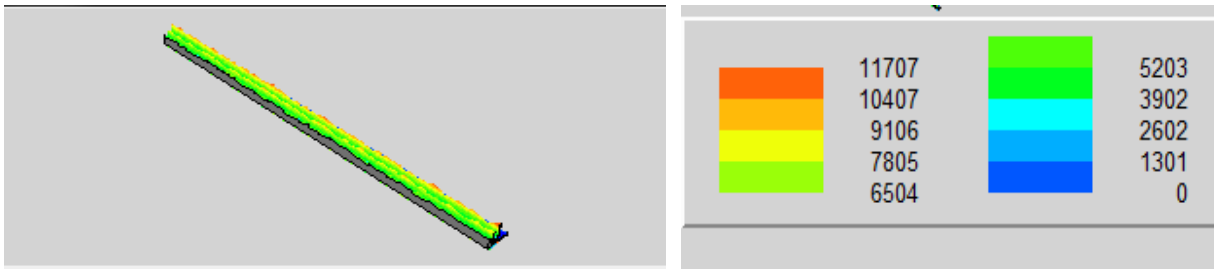

(c) Receiver bottom irradiance at 0°

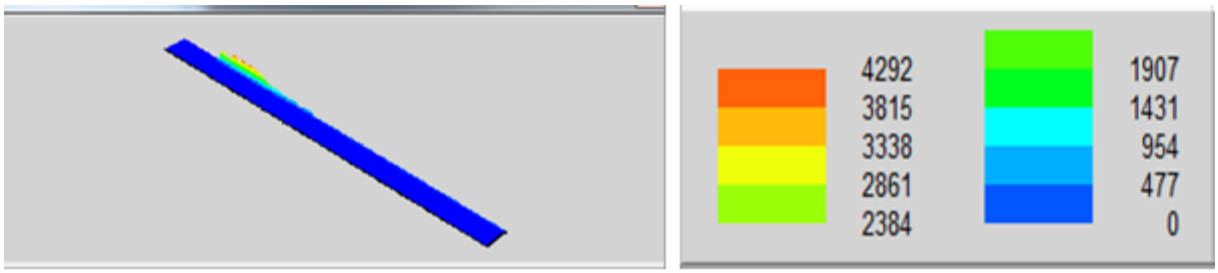

(d) Receiver bottom irradiance at 75°

Figure 5.22 Irradiance distributions at different solar hour angles

5.4.2.2. Effects of gap between the receiver and the concentrator

The parametric equations in 5.1 and 5.2 require that the receiver touch the reflector as shown in Figure 5.3 which may cause thermal losses, hence usually gap is left between them. However, such gap if not minimized can cause rays loss as shown in Figure 5.23. In order to investigate the effects of this gap, the HPCPC60R12.5 was simulated using ray tracing method with 0, 1, 1.5, 2 and 2.56mm gap. This is the range that can be achieved without changing the position of the receiver. It is clear from Figure 5.23 that the gap causes loss of

rays which leads to drop in optical efficiency as the gap dimension increases as shown in Figure 5.24.

Although very small gap dimensions were considered but still the results of the simulation showed that the optical efficiency decreased with the increase in the gap (Figure 5.24). This reduction is due to the loss of rays through the gap and loss due to the reflection of some rays before hitting the receiver. The maximum reduction in optical efficiency is 2.1% when the gap is 2.5mm and hence a gap of 2mm (with 1.3% reduction) is adopted in this work for easy assembling of the parts.

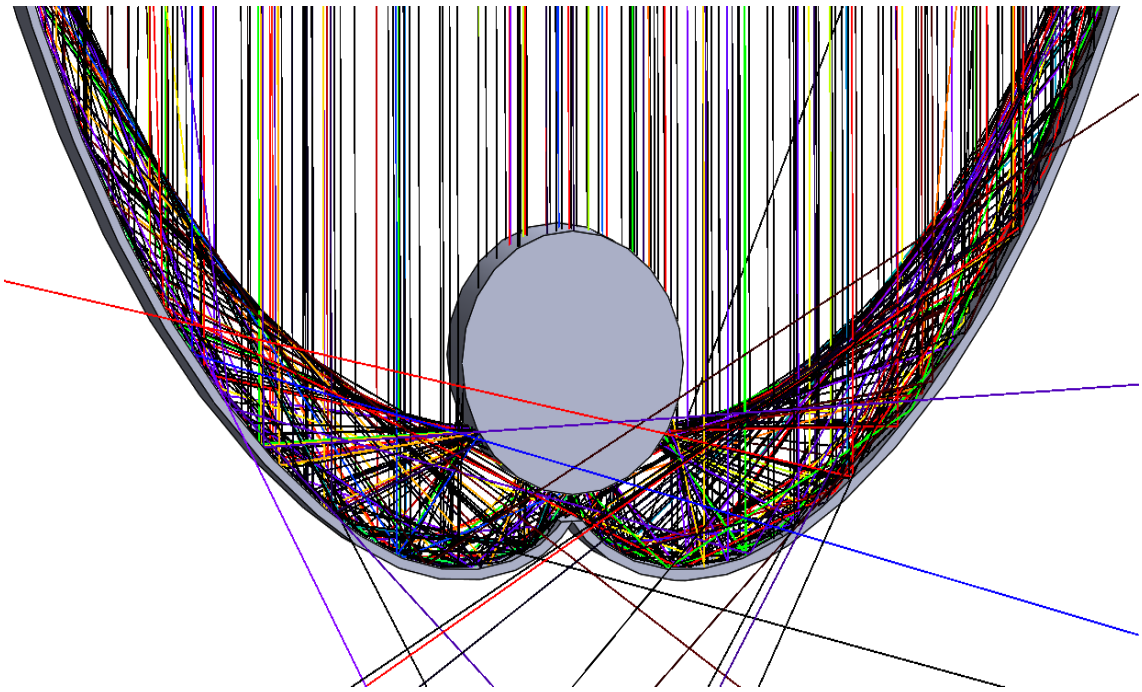

Figure 5.23 Rays loss due to gap between receiver and reflector

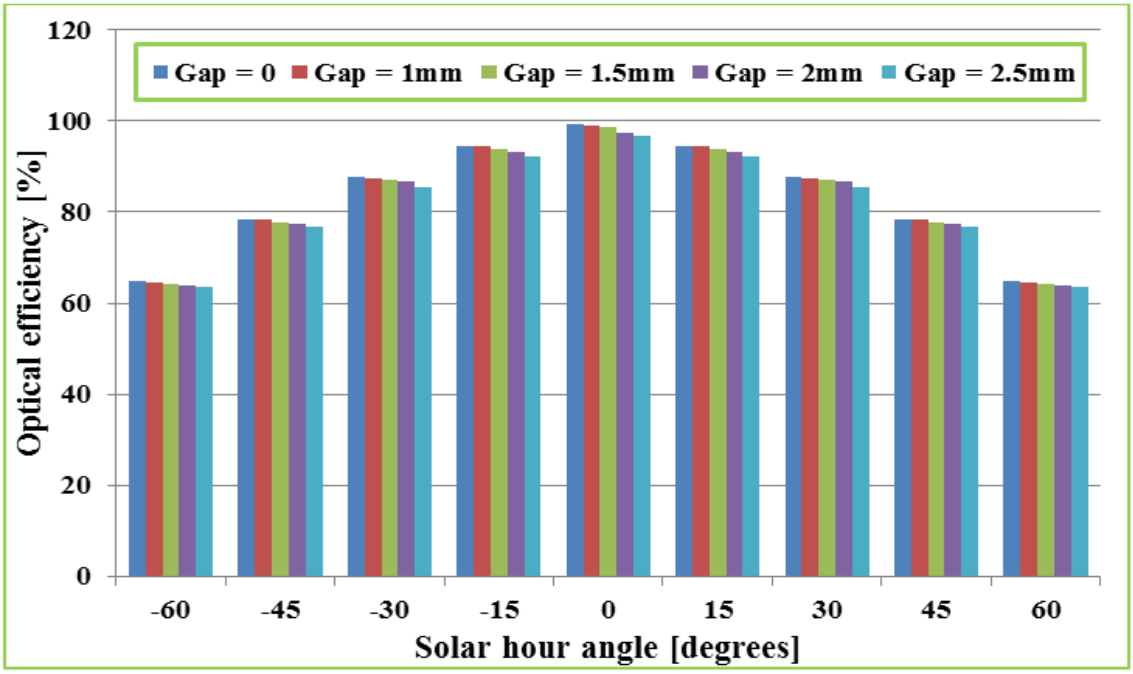

Figure 5.24 Variation of optical efficiency of HPCPC60R12.5 with incident angle at different gap dimensions

5.4.2.3. Effects of collector length and orientation

The HPCPC60R12.5 with gap of 2mm between the receiver and reflector was used in investigating the effects of the collector length and orientation on the amount of the irradiance concentrated on the receiver and the optical efficiency. Figures 5.25 and 5.26 show the variation of the optical efficiency and the power concentrated on the receiver respectively with the solar time. The figures show performance enhancement as the length of the collector increases.

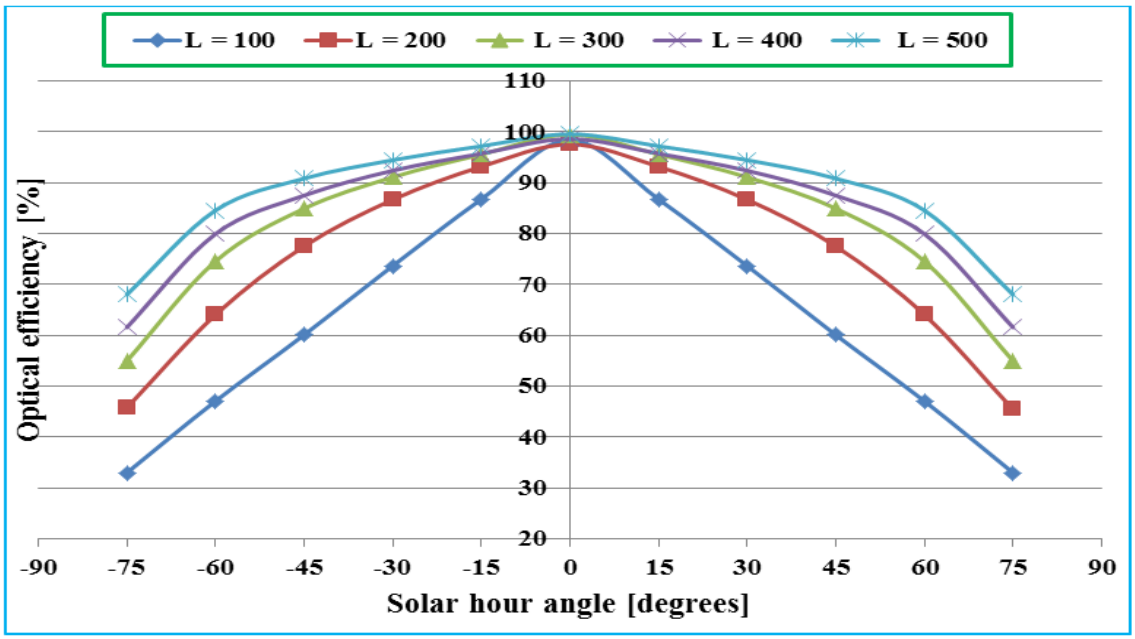

Figure 5.25 Variation of optical efficiency with the incident angle for different collector lengths

There is 38.6% increase in daily average optical efficiency with 500mm long HPCPC compared to 100mm, but there is only 4% increase when compared 400mm and 500mm long collectors, hence 500mm is reasonable length for this work.

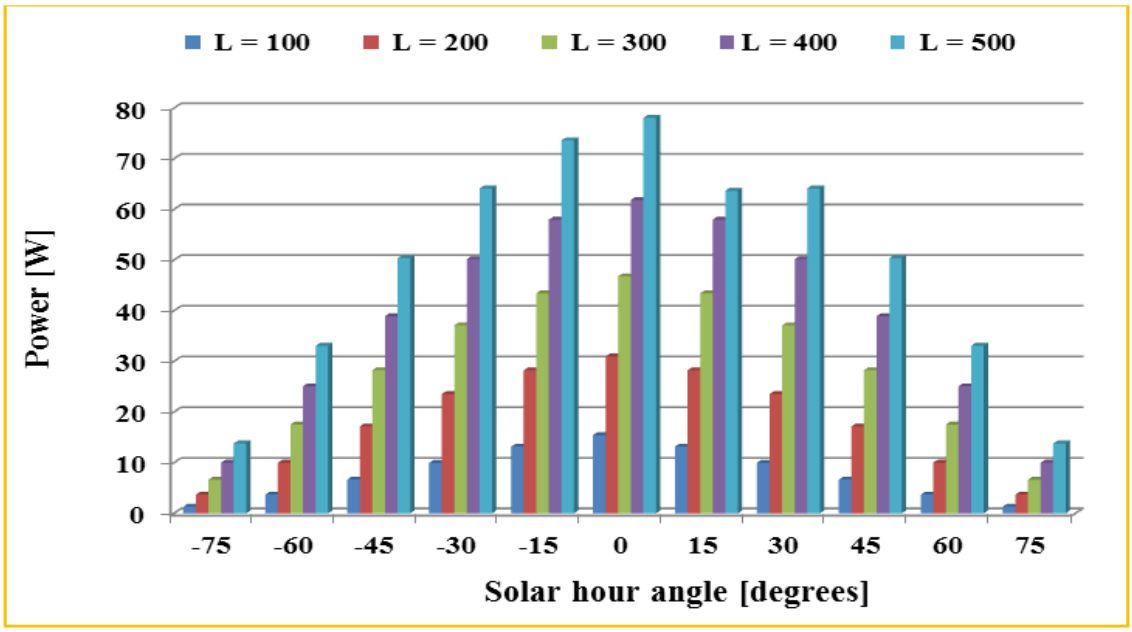

Figure 5.26 Power concentrated on the receiver at different incident angle for different collector lengths

The performance of the HPCPC60R12.5 with overall length of 500mm was simulated in North – South (N – S) and East - West (E – W) orientations under static condition. It can be seen from Figure 5.27 that the collector oriented E – W outperformed the one in N – S direction. It is clear that when oriented in N – S direction (surface azimuth equals to 90^{o}), it must track the sun continuously for it to work for many hours and this is achieved by turning its axis to face the sun. But if stationary, as simulated in Figure 5.27, it only receives radiation during the hours when the sun is within its acceptance angle.

When the collector was oriented with its long axis along E –W direction (i.e. surface azimuth equals to zero); it can receive radiation for longer hours through its wide acceptance angle along its length. This highlights the advantage of having reasonable length of collector and wide acceptance angle because their combined effects can greatly affect the HPCPC's performance. In practice wide acceptance angle also accepts reasonable amount of diffuse radiation but this is at the expense of concentration ratio.

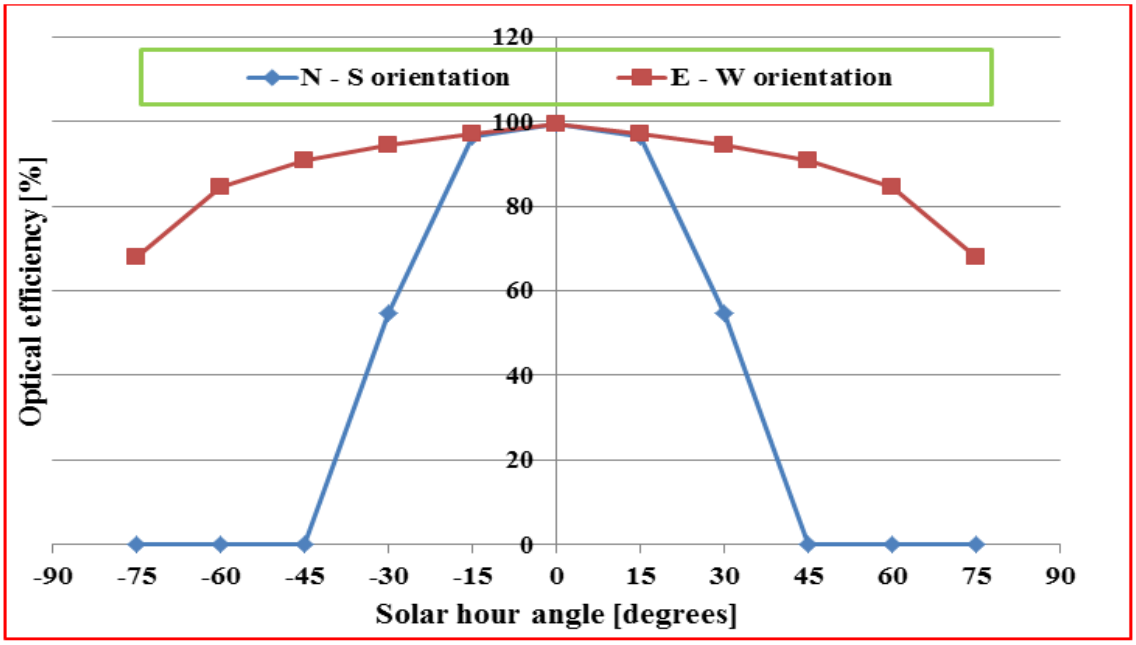

Figure 5.27 Variation of Optical efficiency of HPCPC with incident angle for different orientations

5.4.2.4. Effects of truncation on the optical performance of HPCPC

The effects of truncation on the geometrical characteristics of HPCPC were discussed in section 5.1.4. As seen in the literature review, truncation of up to 50% was recommended from previous works, but detailed study is required for the purpose of optimization. Also considering the fact that two important parameters; optical efficiency and concentration ratio give an opposite effect when truncation level increases, it will of paramount importance to study this parameter in detail.

Intensive optical simulations were carried out using various configurations of HPCPCs with acceptance angles of 30^o, 40^o and 60^o and two different receiver radii of 12.5 and 25mm. Each profile was truncated by 10, 30, 50 and 70% and their optical efficiencies were predicted at different solar hour angles. Figures 5.28 (a, b and c) show the optical efficiency versus the sun angle at different truncation levels for three out of the six configurations. The Figures show similar pattern of increasing optical efficiency as the truncation level increased. This is due to the increase in acceptance angle and decrease in the average number of reflections.

It can also be seen from the figures that the number of hours that HPCPC30R12.5 receives radiation increases with the truncation compared to the full profile as shown in Figure 5.28 (c). Table 5.6 shows the effects of truncation on the other configurations with receiver radii of 25mm. As shown in Figure 5.28, the optical efficiency increases due to the increase in acceptance angles and decrease in average number of reflections. Also the concentration ratio decreases with the increase in truncation level due to the increase in acceptance angle.

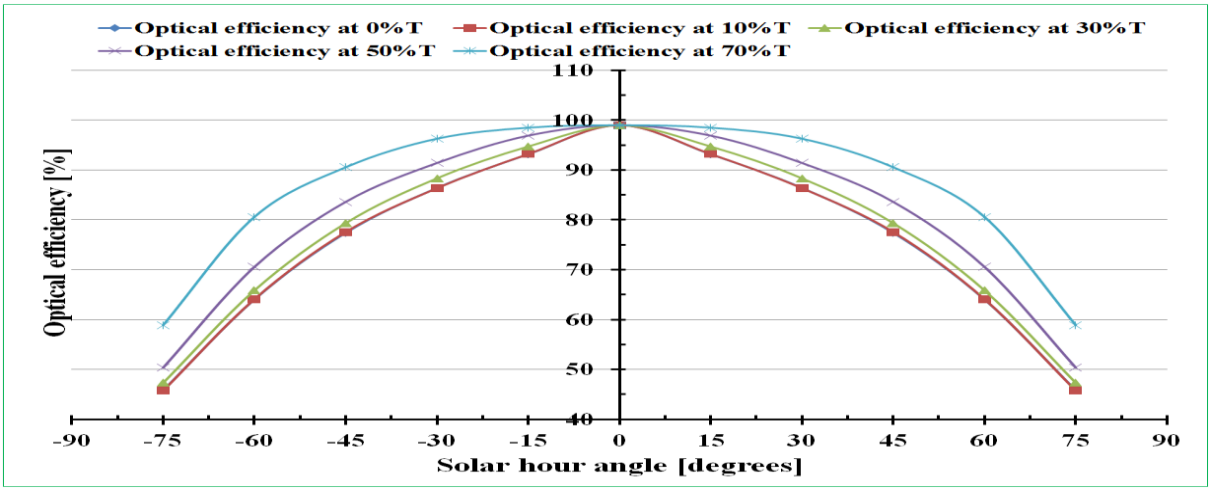

(a). HPCPC60R12.5

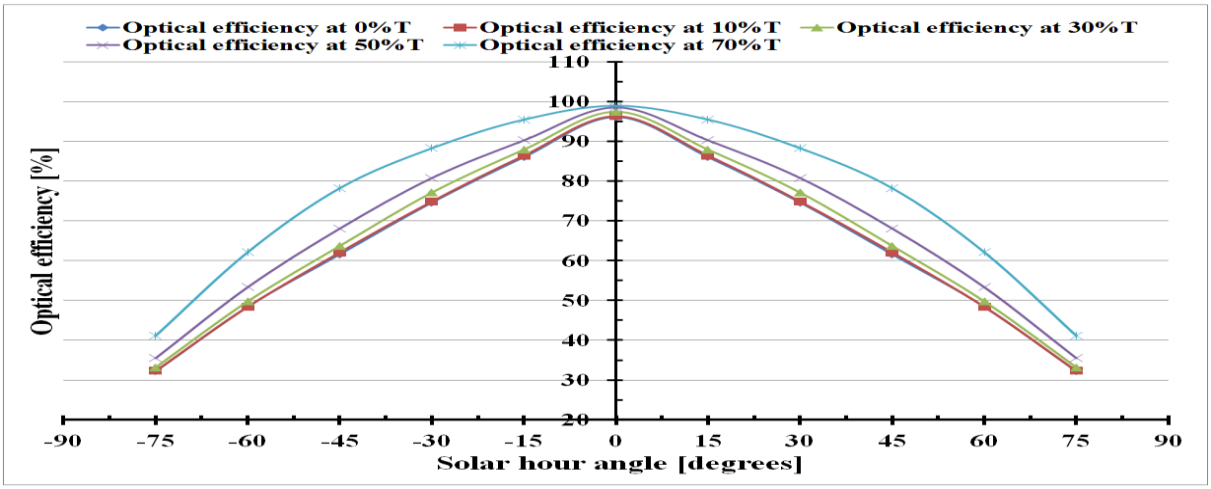

(b). HPCPC40R12.5

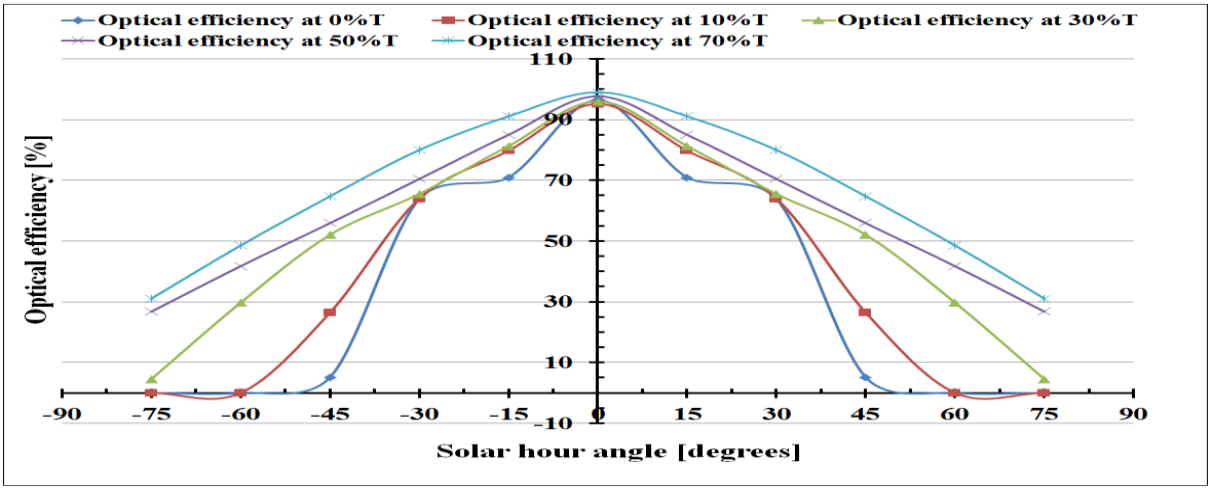

(c). HPCPC30R12.5

Figure 5.28 Optical performances of different configurations of HPCPC at various truncation levels

Table 5.6 Summary of the truncation effects on the other geometries simulated

Truncation level, %	Parameter	HPCPC60R25	HPCPC40R25	HPCPC30R25
0	Daily average optical efficiency	64.3	30.3	19
	Acceptance angle	60	40	30
	Average number of reflection	0.5	0.66	0.74
	Concentration ratio	2	2.92	3.86
10	Daily average optical efficiency	64.5	33.4	20.7
	Acceptance angle	60.2	40.12	30.1
	Average number of reflection	0.49	0.66	0.74
	Concentration ratio	1.99	2.91	3.85
30	Daily average optical efficiency	65.9	42.3	22.5
	Acceptance angle	62.06	41.27	30.91
	Average number of reflection	0.48	0.65	0.73
	Concentration ratio	1.94	2.84	3.75
50	Daily average optical efficiency	69.2	55.9	32.4
	Acceptance angle	67.1	44.34	33.12
	Average number of reflection	0.45	0.62	0.71
	Concentration ratio	1.81	2.65	3.51
70	Daily average optical efficiency	75.9	62.2	52.5
	Acceptance angle	80.2	52	38.61
	Average number of reflection	0.36	0.56	0.67
	Concentration ratio	1.56	2.28	3.02

However, since truncation causes increase in acceptance angle, then the concentration ratio decreases with the increase in truncation level, hence the two effects are compared in Figure 5.29. Figures 5.29 (a, b and c) show the variation of the daily average optical efficiencies and concentration ratios with truncation level. Since the optical efficiency and concentration ratio tend to have opposite effects on the HPCPC performance, it will be beneficial if they are plotted in the same graph to obtain the best combination of these two parameters at any truncation level as shown in Figure 5.29.

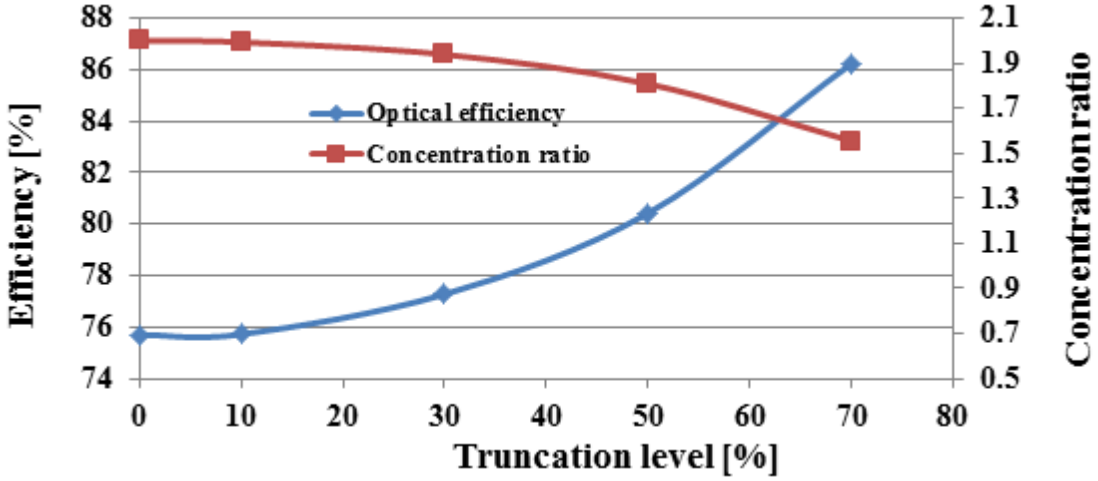

(a) HPCPC60R12.5

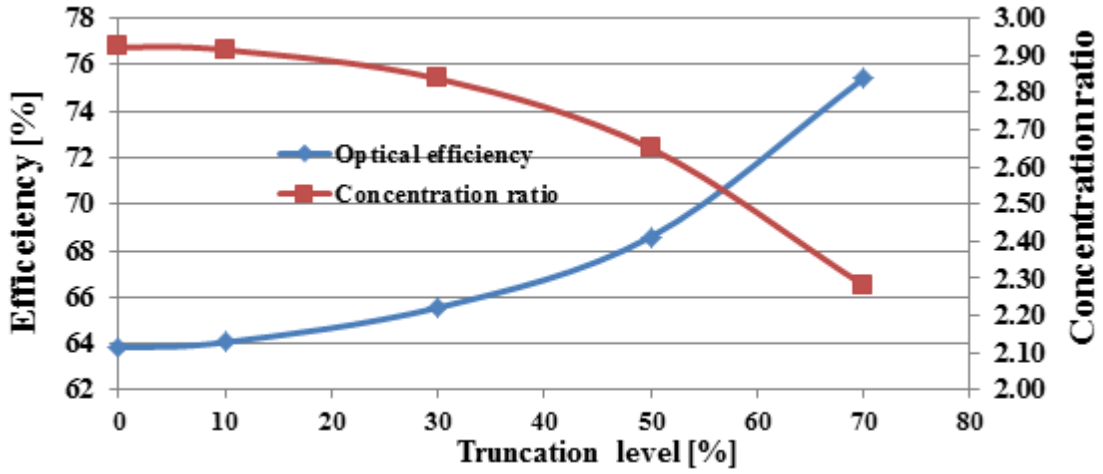

(b) HPCPC40R12.5

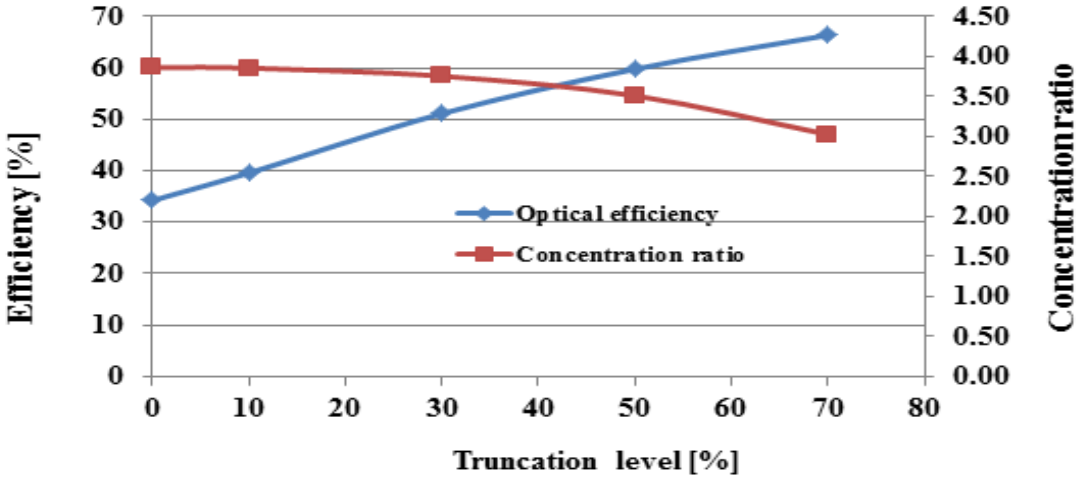

(c) HPCPC30R12.5

Figure 5.29 Variation of Average daily optical efficiency and Concentration ratio with truncation level

The curves in Figure 5.29 meet at different coordinates for the three configurations presented. At the intersection points; the HPCPC60R12.5, HPCPC40R12.5 and HPCPC30R12.5 can be truncated respectively by 62%, 55% and 43% to achieve optical efficiencies/concentration ratios of 84%/1.65, 71%/2.55 and 55%/3.5 respectively. Using the charts in Figure 5.29, an informed decision can be made for choosing the level of truncation with the least sacrifice to in concentration ratio.

5.4.2.5. Effects of receiver size on Optical efficiency of truncated HPCPC

It has been seen that the receiver radius affects the characteristics of full HPCPC geometry according to equations 5.1, 5.2, 5.4 and 5.5. In this section, ray tracing technique is used to study the effects of receiver size and shape on the optical performance of HPCPC60 truncated by 62% (i.e. the configuration that gives the highest daily average optical efficiency as shown in 5.4.2.4). Four different receiver radii 6, 11, 22.5 and 25 mm were simulated for nine hours (i.e. between 8am and 4pm) using the annual average radiation of Kano (540 W/m^2) when the collector is tilted at an angle equal to the latitude and the results are shown in Figure 5.30. It can be deduced from such figure that the optical efficiency increased with the increase in the receiver size for all the hours of the day. The low efficiency of the small receiver is due to the increase in the average number of reflections, as many rays had to hit the concentrator and lose some of their energy (depending on the reflectivity of the surface) before reaching the receiver. Also the concentration ratio decreased with the increase in the receiver size and this also account for the increase in the optical efficiency.

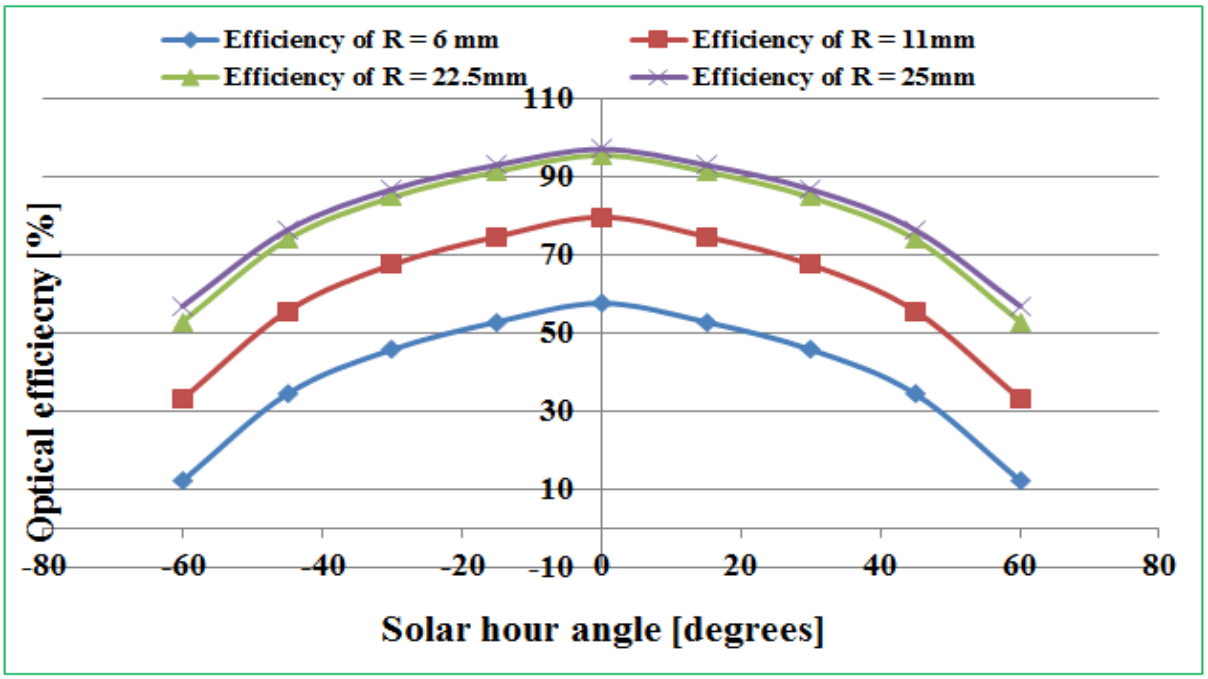

Figure 5.30 Variation of optical efficiency with solar hour angle for different receiver radii

Therefore it can be concluded that from the optical point of view that the larger the area of the receiver, the better its optical performance provided the collector height remain constant. This is due to the ability of large volume receiver to accept most of the rays directly without hitting the reflector, hence reducing the average number of reflection.

5.4.2.6. Optical performance of double receiver HPCPC

It has been shown that a large receiver performs better than small ones optically, but thermally it has large area for heat transfer to the ambient. But if two receivers are used in one concentrator, the optical gain can be achieved and the area for heat transfer to the ambient is also minimized compared to large single receiver. Based on these findings, a novel idea of using two receivers aligned horizontally and vertically in single CPC was investigated for performance enhancement and economic reasons. Also the potential of elliptical receiver with its major axis aligned horizontally and vertically were investigated.

The optical performance of HPCPC60, HPCPC40 and HPCPC30 was simulated using a concentrator length of 200mm. The receivers used are single tubular with diameter of 25mm, two tubular receivers each of 25mm diameter aligned horizontally and vertically and a single elliptical receiver with major axis ranging from 45mm to 60mm and minor axis ranging from 20mm to 30mm aligned horizontally. Figure 5.31 shows the rays distributions on the receivers at sun hour angle of 0^{o} (zenith) for the various receivers used.

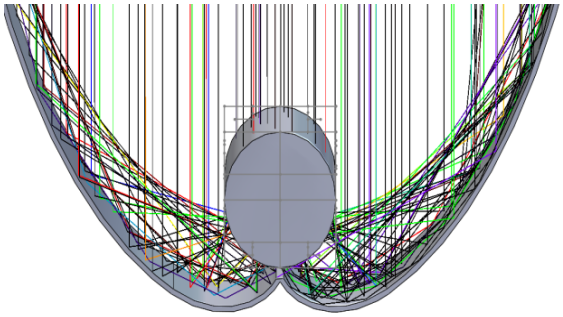

(a) Single cylindrical

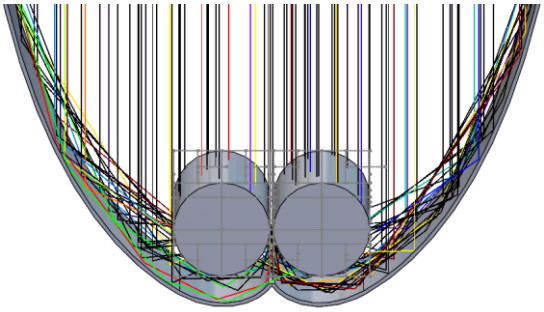

(b) Double horizontally aligned cylindrical tubes

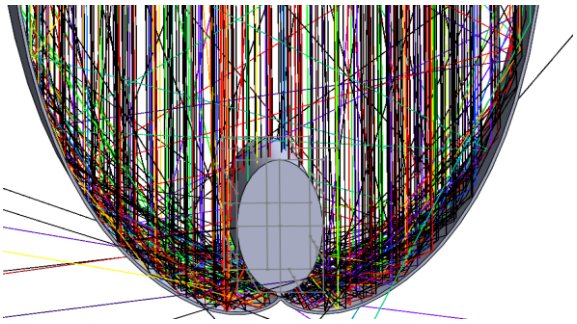

(c) Elliptical with its major axis vertically aligned

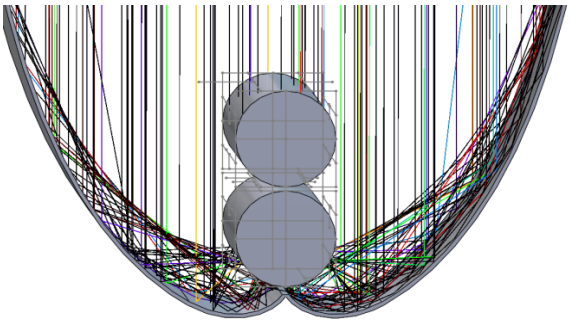

(d) Double vertically aligned cylindrical tubes

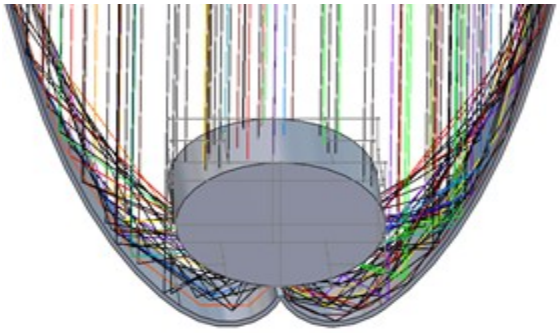

(e) Elliptical with horizontally aligned major axis

Figure 5.31 Rays distributions on different HPCPC receiver configurations

From this Figure, it can be seen that rays hit the tubes either directly or after one or multiple reflections and this is defined by the receiver configurations. Also the average number of reflections is significantly reduced when an elliptical tube or horizontally aligned double tubes are used compared to single and vertically aligned double or elliptical tubes.

Figure 5.32 (a and b) shows the variation of the power received and optical efficiency with solar time for the three CPCs; HPCPC30, HPCPC40 and HPCPC60 where each Figure compares three receiver configurations; single tube, double tubes aligned horizontally and double tubes aligned vertically. It can be shown from these Figures that the double tubes aligned horizontally outperformed the other configurations with an increase in the average daily optical efficiency of 14, 14.8 and 15% compared to the single tube for HPCPC60, HPCPC40 and HPCPC30 respectively. This means that some rays that ought to hit the reflector before reaching the single receiver tube may be directly absorbed by either of the tubes in horizontal tube configuration.

The vertically aligned double tubes showed the same performance as the single in all the cases. This can be explained using the ray's distributions shown in Figure 5.31, as the top tube receives flux only on the top side while the bottom one receives flux on the bottom and the two sides. This result shows the advantage of using two tubular receivers aligned horizontally. However, Figure 5.31 (b) shows that the inner adjacent surfaces between the two tubes received little radiation; therefore an elliptical configuration which surrounds the two tubes may provide an improvement. Hence the performances of elliptical receivers with the major axis of 50mm and minor axis of 25mm aligned horizontally i.e. E(50:25) and vertically i.e. E(25:50) were compared as shown in Figure 5.33. It is clear from this figure that the horizontally aligned elliptical receiver gives higher optical efficiency (10%) than the vertical

one. This is also due to the lower average number of reflections in horizontal alignment as seen in Figure 5.31 (c and e)

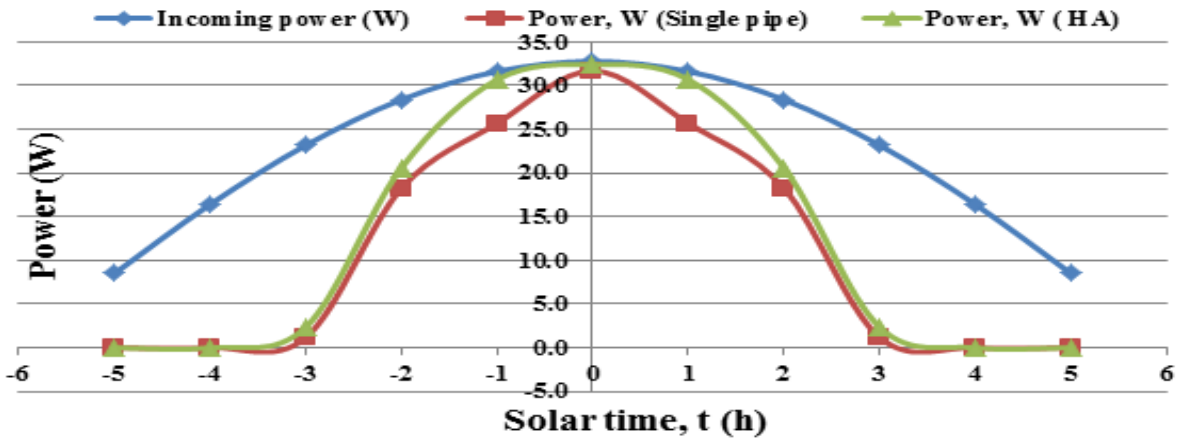

(i) HPCPC30

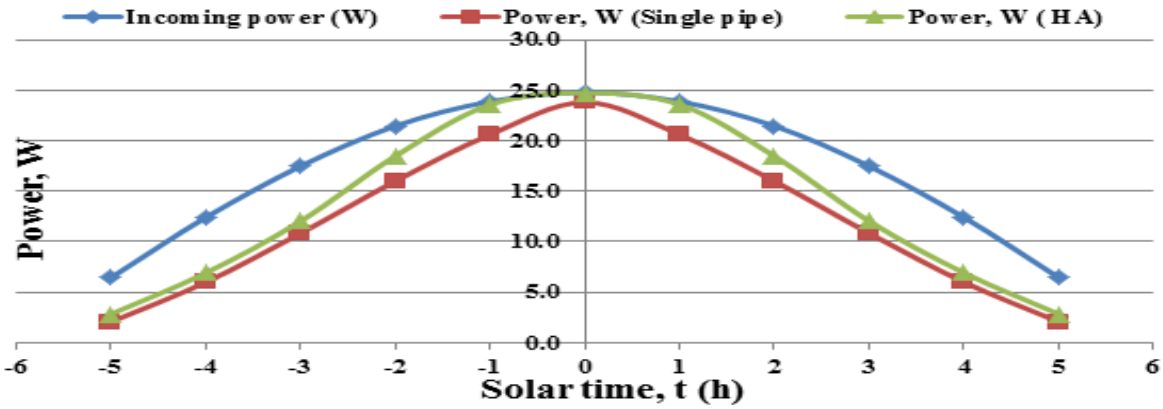

(ii) HPCPC40

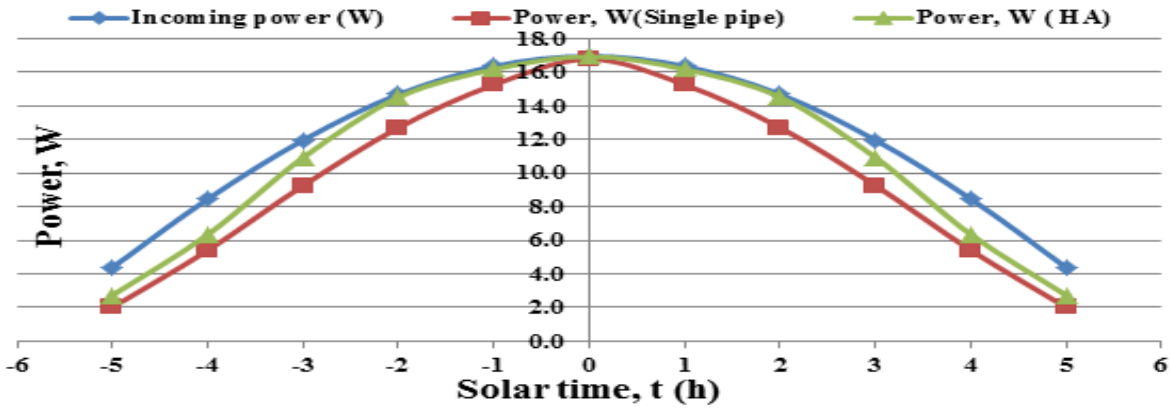

(iii) HPCPC60

Figure 5.32a Power received by different HPCPC configurations

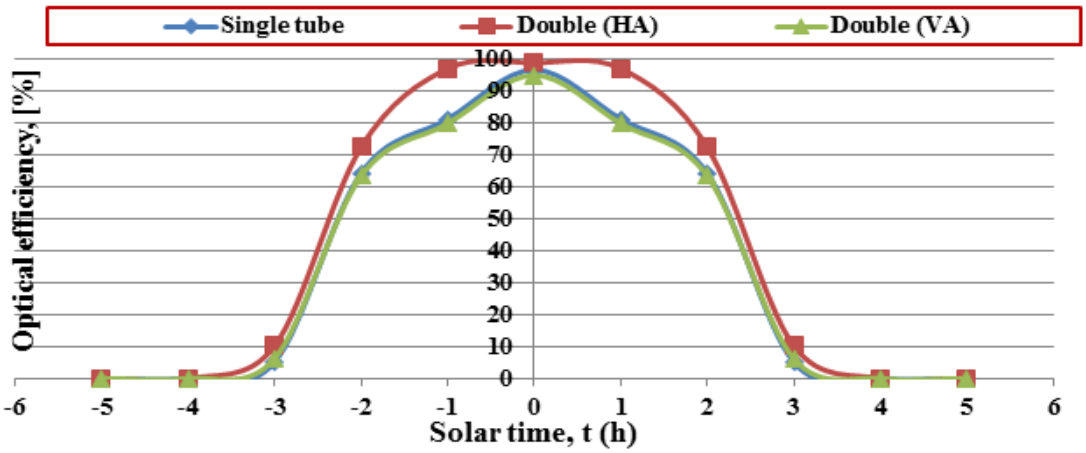

(i) HPCPC30

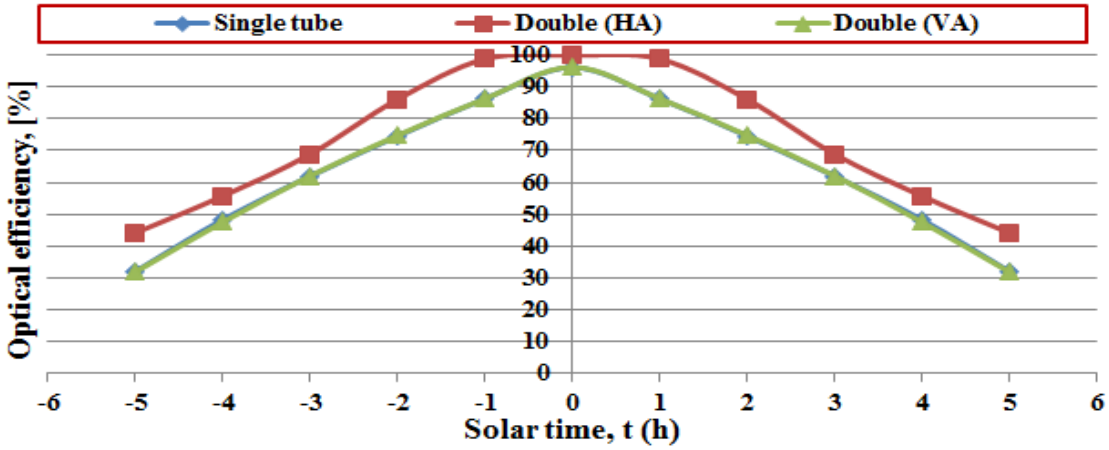

(ii) HPCPC40

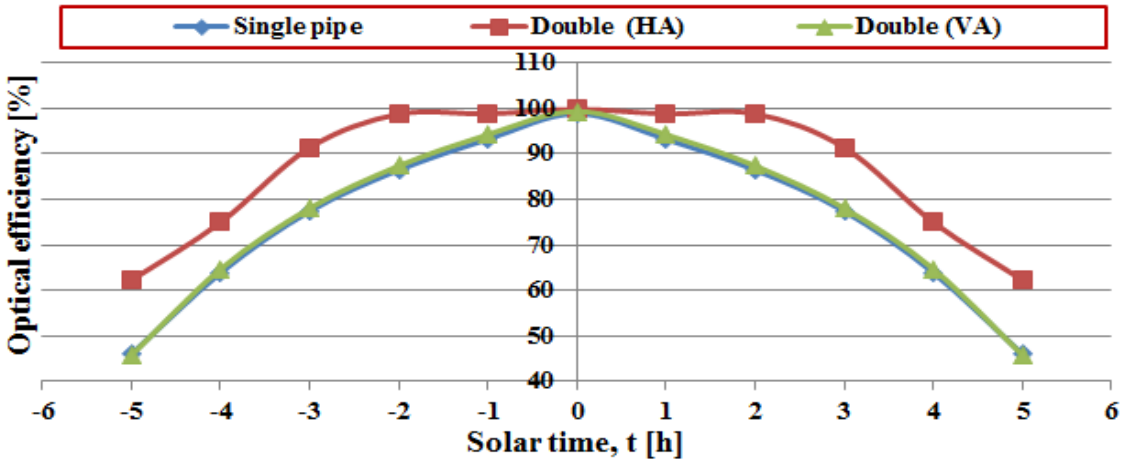

(iii) HPCPC60

Figure 5.32b Optical performances of different configurations of HPCPC

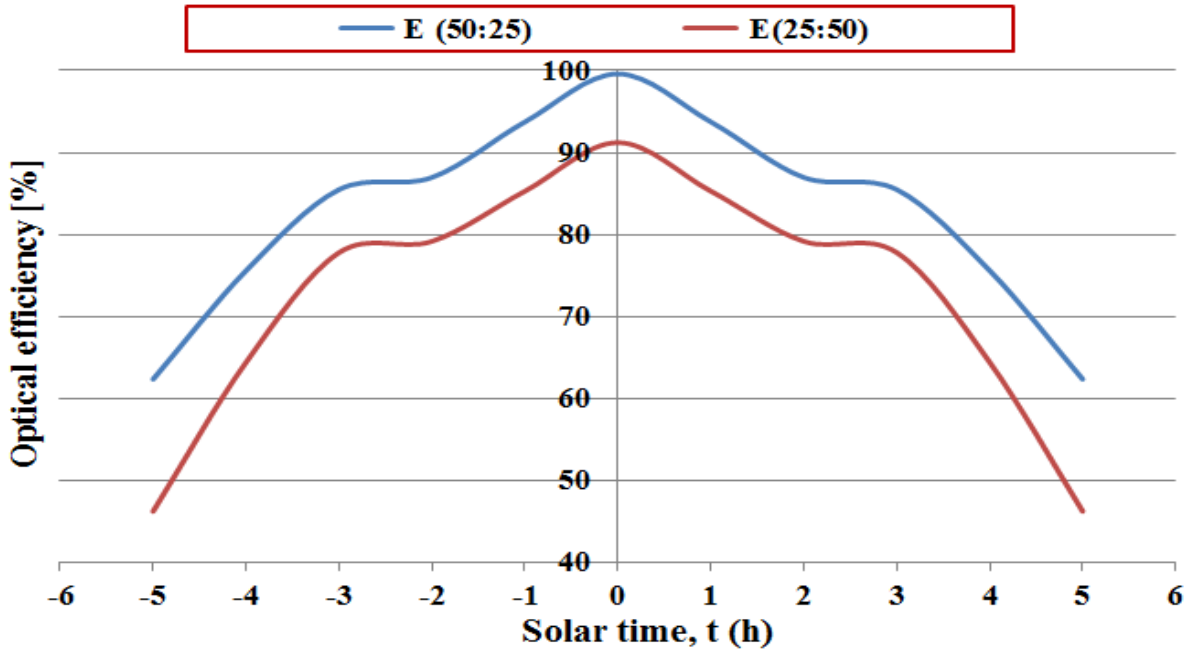

Figure 5.33 Optical performance of elliptical receiver at different solar time for different alignments

Since aligning major axis horizontally gives better results, different combinations of the elliptical receiver with the major axis aligned horizontally were simulated and results are presented in Figure 5.34. It can be deduced from the figure that the larger the receiver the higher the optical efficiency for the same reason of less number of reflections.

Figure 5.35 compares the optical performance of the elliptical receiver E(60:30), two tubular receivers and the single tubular receiver in the horizontal configuration. It can be seen that configuration E (60:30) gives 17% increase in the daily average optical efficiency compared to the conventional single tubular receiver of 25mm diameter, but have almost the same performance with the double receiver configuration.

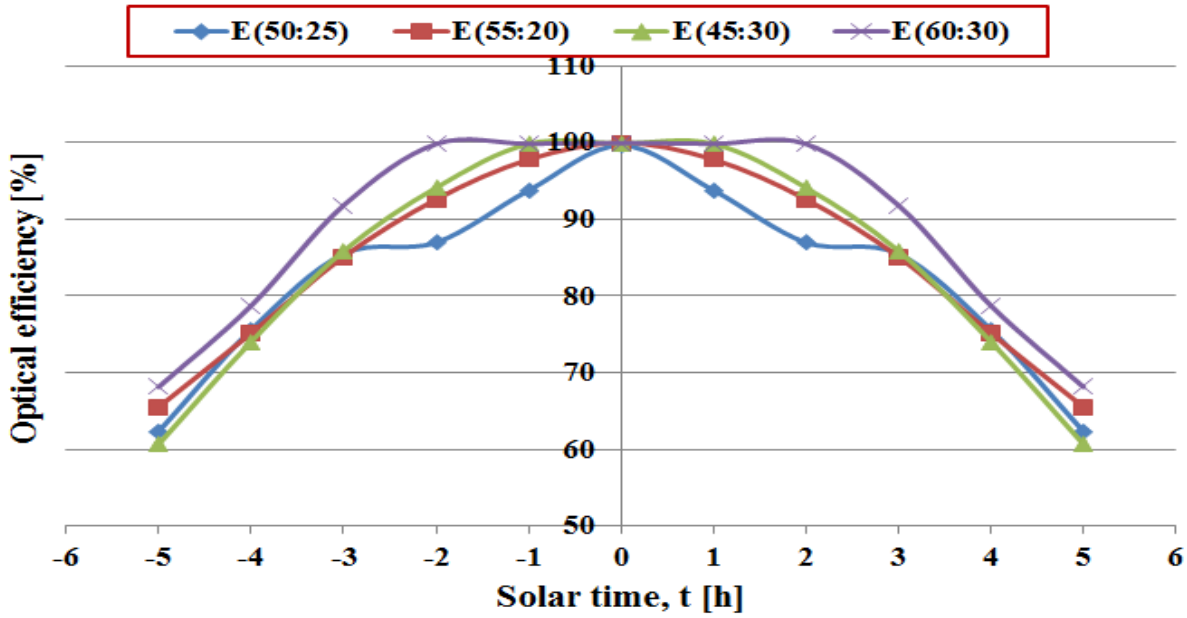

Figure 5.34 Optical performances of different elliptical receiver configurations for horizontal alignments

It can also be observed in Figure 5.35 that the E(60:30) shows some improvement over double horizontal receivers in the early and late hours of the day because of its ability to capture more rays without reflection due to its large size.

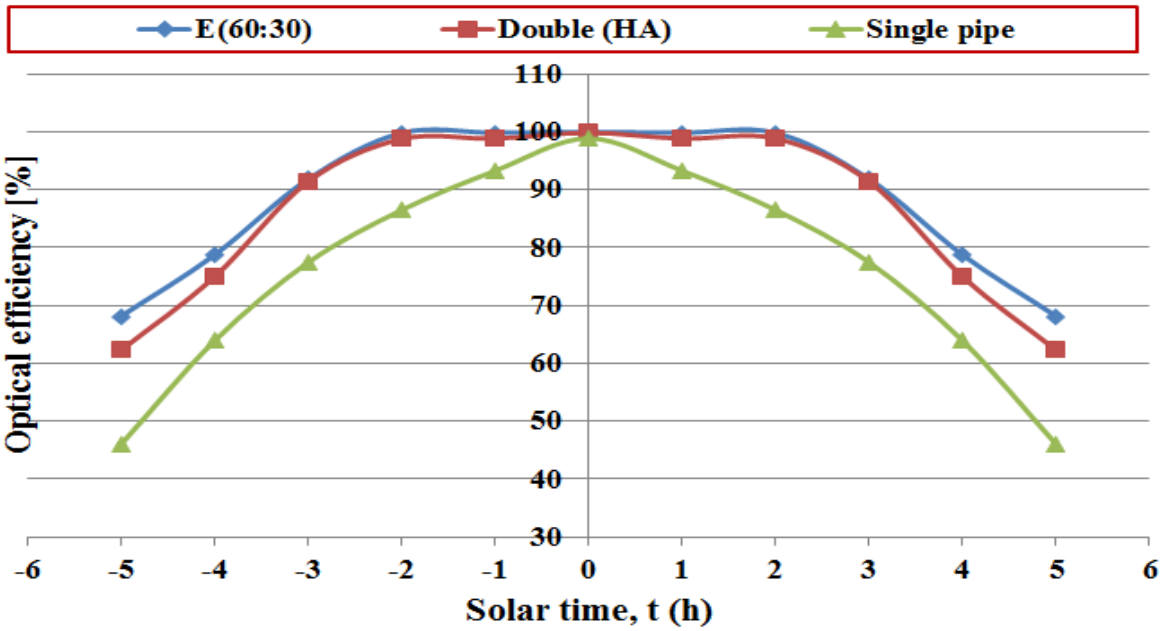

Figure 5.35 Performance comparisons of elliptical, single and double receiver configurations

The E(60:30) is made larger than the double tubular receiver so as to cover the gap between them, but the E(60:30) has larger area liable to losses compared to double receiver configuration.

5.5. Summary

Detailed analysis of the characteristics of HPCPC (2 -5X) was carried out by developing a computer program in Microsoft Excel spreadsheet. The program used parametric equations to determine the HPCPC geometric parameters like height, aperture width, height-to-aperture ratio, truncation effects, concentration ratio and average number of reflections. It also generated the HPCPC profile for various inputs of acceptance angles and receiver radii. Results have shown that acceptance angle of the HPCPC is the most important parameter in determining its geometric characteristics because it affects the collector height and aperture, concentration ratio, average number of reflections, etc. New correlations relating collector height, aperture width and acceptance angles were generated using the data obtained from such model. Truncating HPCPC60, HPCPC40 and HPCPC30 by 70% increases the acceptance angle by 28.7, 30 and 33.4% respectively leading to corresponding decrease in concentration ratios of 21.7, 22 and 22.24% respectively.

Extensive optical simulation was carried out on HPCPC configurations (2 - 5X) geometrically characterized in section 5.1.2 with different combinations of acceptance angles, receiver radii, collector length and orientation, material properties, etc. Optimization was carried out based on the receiver shape, size and alignment, truncation level, gap between receiver and reflector, etc. Full profile of HPCPC60R12.5 was found to have the highest optical efficiency (76.5% daily average) and number of operating hours (11 hours), but it has the least concentration (2X). The closest competitive with different acceptance angle is HPCPC40R12.5 with daily

average optical efficiency, operating hours and concentration ratio of 64.4%, 11 and 2.92 respectively.

Results showed that truncation increased the optical efficiencies of all the configurations simulated giving average daily optical efficiencies of 86.2, 75.4 and 66.3% for HPCPC60R12.5, HPCP40R12.5 and HPCPC30R12.5 respectively and corresponding concentration ratios of 1.56, 2.28 and 3.02 at 70% truncation level. But the intersection points of the optical efficiency and concentration ratio is the best choice because they give reasonable values for the two parameters. At the intersection points; the HPCPC60R12.5, HPCPC40R12.5 and HPCPC30R12.5 can be truncated respectively by 62%, 55% and 43% to achieve optical efficiencies/concentration ratios of 84%/1.65, 71%/2.55 and 55%/3.5 respectively.

Novel approach of using two receivers in single CPC was introduced for optical performance enhancement, economic and other logistic reasons. Conventional solar compound parabolic concentrators are fitted with one tubular receiver situated along the axis of the two parabolas. Advanced ray tracing technique was used to investigate the potentials of using two tubes in a single compound parabolic concentrator and that of using elliptical to improve the optical efficiency. Results from ray tracing simulation showed that two tubular receivers aligned horizontally improved the HPCPC daily average optical efficiency by up to 15% compared to the single tubular receiver with the same diameter. As for the vertically aligned two tubes configuration, no improvement in the optical efficiency was predicted. Elliptically shaped single receiver with 60mm and 30mm major and minor axes respectively has shown an increase in the daily average optical efficiency of about 17% compared to single tube with 25mm diameter. The ray tracing technique employed in this chapter was experimentally validated and the results showed good agreement within ±4.5% deviation.

CHAPTER SIX

6. Performance Characterization of a two – phase closed thermosyphon – CFD and Experiment

6.1. Introduction

The type of receiver used in a concentrating solar thermal collector plays a vital role in the overall performance of the collector. Using tubular receiver configuration has been shown to offer some advantages of minimum back losses and low cost. Thermosyphon heat pipes are selected for this work as receiver in the HPCPC to maximize the thermal performance of the collector and minimize losses. Performance characterization of a two – phase closed thermosyphon heat pipe (TPCT) was carried out both experimentally and numerically in this chapter.

Literature review presented in chapter two showed that various parameters affects the performance of thermosyphon heat pipe, hence investigating some of these parameters experimentally is important for enhancing its performance for use as a receiver in a solar collector. These parameters includes working fluid, fill factor, aspect ratio, heat input, inclination angles, cooling water flow rates, etc. There are conflicting results reported on the effects of some parameters such as the inclination angle [82, 85, 86, 163, 164]. Due to these conflicting results and the fact that large number of factors contribute to the performance of thermosyphon, it is important to investigate its performance characteristics in consideration with the intended application. Since the thermosyphon for this work is to be used in a CPC solar collector for domestic use, it is important to characterize it based on such application.

This chapter presents a brief overview of the heat pipe technology including their advantages, operations and applications. An experimental test facility was constructed to study the effects of heat inputs, cooling water flow rate and the pipe inclination on the performance of thermosyphon. Design, set up, commissioning and detailed description of the test facility are presented in this chapter. Also detailed descriptions of the thermosyphon tested are given together with instrumentation and their calibrations. Methods followed in the data reduction and uncertainty estimation are also fully described.

Since experimental work is cost and time intensive, numerical study is an alternative for wide range of investigations on the performance of thermosyphon under different conditions. Literature presented in chapter 2 showed that several numerical studies were presented on the effects of heat input, fill ratio, grooves on the surface, etc. but some aspects are left such as the effects of inclination, flow rate and condensation enhancement which creates a gap especially for solar thermal applications and some are addressed in this work.

6.2. Heat pipe technology

Heat pipe is a two phase heat transfer device involving simultaneous evaporation and condensation processes. In terms of heat transfer, heat pipes are better than the best conductor, hence they are often referred to as “superconductors”. The idea of heat pipe was first initiated by Gaugler in 1942, but it was not until 1962 when Grover invented the first unit, its remarkable properties were realized and its development began [165].

Heat pipes transfer heat from the evaporator section to the condenser by simultaneous evaporation and condensation in a sealed container with minimum losses. Some heat pipes have adiabatic section to separate these two regions by a distance determined by the application. They consist of sealed container usually made from copper or aluminium with or

without wick material lined on the inner wall and working fluid charged under a vacuum. The condensate returns to the evaporator by capillary effects in case of wicked heat pipe and by gravity in case of wickless heat pipe (thermosyphon). Hence for thermosyphon, the condenser must be above the evaporator while for the wicked heat pipe, the capillary forces in the wick ensure the condensate returns to the evaporator regardless of the position as shown in Figures 6.1.

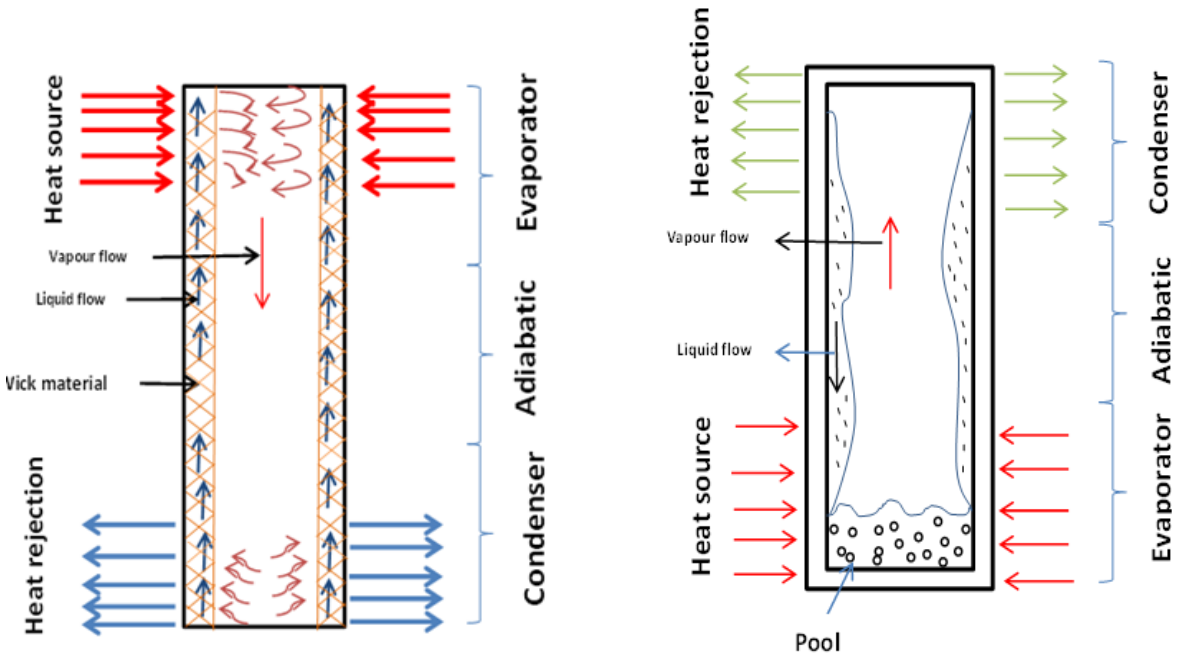

(a) (b)

Figure 6.1 Operations of (a) wick and (b) wickless (thermosyphon heat pipes) [166]

Heat pipes have numerous advantages over other types of pipes in terms of high heat conduction, light weight, efficient heat transfer and design flexibility. Due to these advantages, the technology undergone rapid development in the past decades [167] and also their applications are found in spacecraft thermal control [165], heat exchangers [168], solar energy systems [78, 169], electronic cooling [170, 171], etc.

There are different types of heat pipes and classified based on [172]:

I. Nature of fluid circulation: capillary driven, flat plate, two- phase close thermosyphon, rotating heat pipes, etc.
II. Control of heat transfer: heat pipes in this category are called “controlled heat pipe”, which includes variable- conductive, thermal switch and thermal diode
III. Electrostatic – driven heat pipes such as electro hydrodynamic heat pipe
IV. Osmotic driven heat pipe like osmotic heat pipe
V. Others include inverse, micro, reciprocating, cryogenic, capillary pumped loop heat pipes, etc.

The rate of heat transfer in capillary driven heat pipes is governed by five operating limits; vapour pressure, sonic, circulation, boiling and entrainment. In designing a heat pipe, three basic components are considered; the container, working fluid and the wick material. All these materials are required to have properties that will make the pipe operate effectively and readers are referred to heat pipe text books for further details such as [165, 167].

6.3. Thermosyphon heat pipe

In addition to the general advantages of heat pipes, thermosyphon type is found to be highly durable, reliable and cost effective what make them useful for various applications such as solar heating of building [81], cooling of turbine blades, transformer, electronics, internal combustion engines and nuclear reactor [173-175]. This is due to their ability to dissipate and transfer large amount of energy from small area without significant loss. Some applications of thermosyphon require that the pipe be inclined to an angle from the horizontal to increase the exposure of the system to the maximum solar radiation [78-81].

Apart from the material of the thermosyphon, another important parameter is the quantity of the liquid charged in relation to the volume of the evaporator, called fill ratio, FR or liquid ratio. It is defined as the volume of the working fluid in an unheated pipe, V_{liq} to the volume of the evaporator, V_e as:

$$FR = {V_{liq}}/{V_e} = \frac{4V_{liq}}{\pi D^2 l_e} \tag{6.1}$$

Proper choice of fill ratio is very important, as insufficient amount of fluid causes dry out while excessive amount reduces performance and increases the cost of the pipe. FR of a thermosyphon should be between 40% and 60% for vertical pipes and between 60 and 80% for inclined pipes [172, 176].

Thermosyphon is proved to be a good choice as a receiver for solar concentration systems due to the advantages stated. But to derive the best benefits of these advantages, proper choice and characterization of the pipe is of paramount importance. The pipe dimensions selected for this work (400mm long and 22mm external diameter) and other considerations are based on the intended application and the characteristics of the concentrator to be used as discussed in chapter five of this thesis. In the next section of this chapter, details of the experiment and numerical (CFD) characterization of the chosen thermosyphon is presented.

6.4. Description of the experimental test rig

Figure 6.2 shows a schematic diagram of the experimental test rig used in the characterization of the thermosyphon used in both vertical and inclined positions. It consists of a two – phase closed thermosyphon heat pipe, heating coil, water jacket and instrumentations as shown in Figure 6.3. The thermosyphon used in this work is a closed copper tube of 22mm outer

diameter. 0.9mm thickness and 400mm long manufactured by S & P coil products limited. The evaporator and condenser are each 200mm long; hence there is no adiabatic section. The pipe was charged with water as the working fluid and the fill ratio of 0.65 was used throughout the experiment which is appropriate for this application [172, 176].

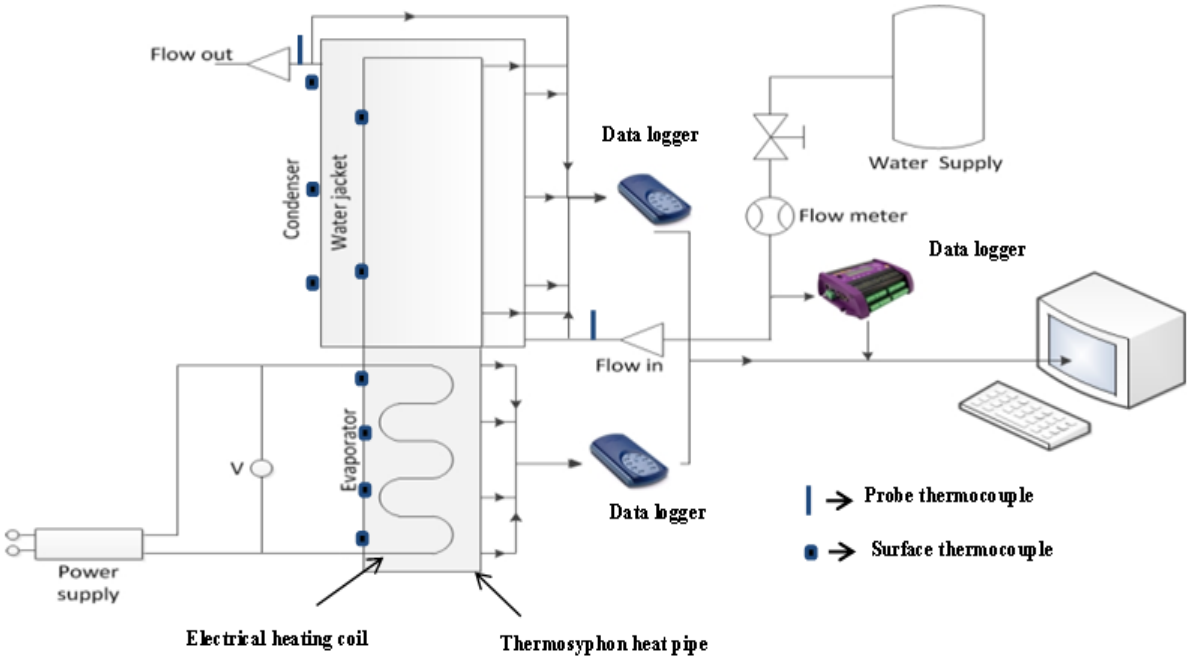

Figure 6.2 Schematic diagram of the experimental rig

The evaporator section is wrapped evenly with electric wire and electric energy is supplied and controlled by TSx1820P Programmable DC PSU 18V/20A power regulator to provide the heating requirement for boiling the fluid. The voltage input was measured using a multimeter connected close to the pipe to account for the voltage drop while the current was read from the power regulator. The evaporator section is also insulated with 25mm thick pipe insulator to reduce the heat loss to the ambient (Figure 6.3). Twelve surface thermocouples were placed at different locations on the test pipe; four on the evaporator wall (at 0.02, 0.07, 0.12, and 0.17

m from the tip of the evaporator) and two on the condenser wall at 0.25 and 0.35m as shown in Figure 6.2. The electric wires were wrapped in such way that they are not directly on the thermocouples so as they do not affect their readings. Two probe thermocouples were installed at the inlet and outlet of the manifold to measure the temperatures of the cooling water. Three other thermocouples were used on the water jacket and one on the insulator to measure the effectiveness of the insulation and the jacket. All the readings were sent to Pico TC - 08 data loggers connected to a PC.

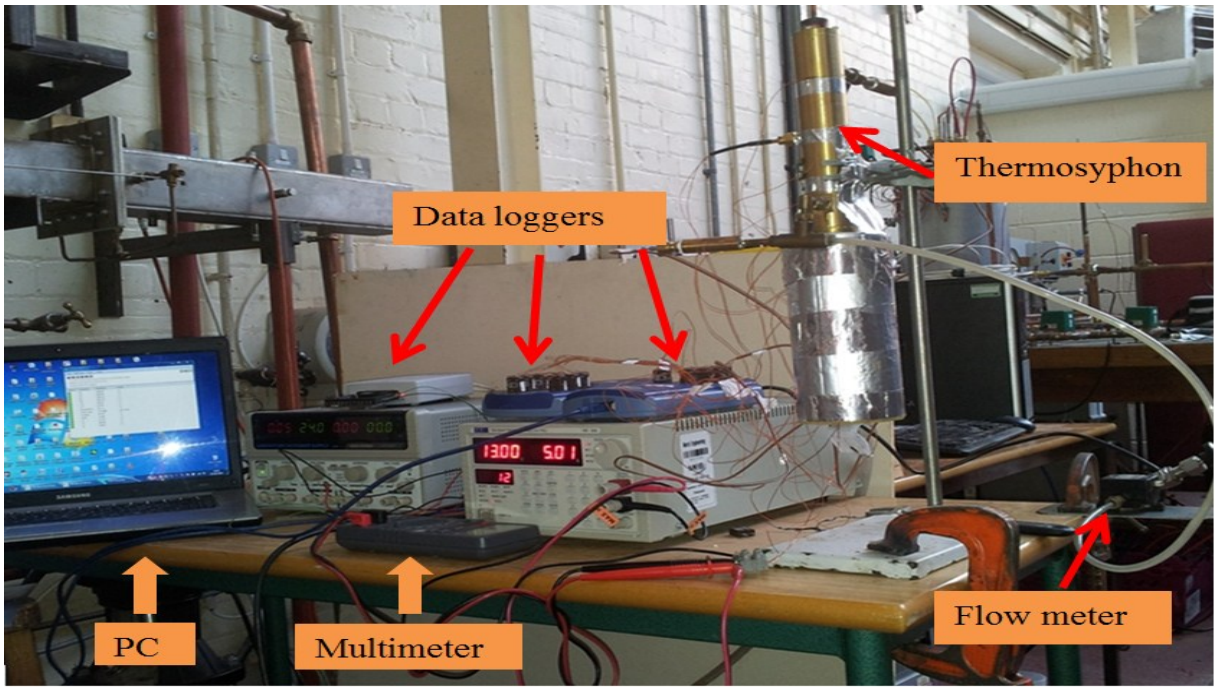

Figure 6.3 Picture of the heat transfer characterization of thermosyphon test rig

The condenser section was cooled by using a double pipe concentric water jacket through which cooling water flows. The flow rate of the cooling water was controlled by a valve and measured by an Omega FLR1009ST-I flow meter (50 – 500 mL/min range). The selection of this flow meter is based on preliminary calculations of the expected range of the rate of heat transfer to the cooling water for this work. Using the maximum flow rate obtainable from the flow

meter, and velocity of 1 m/s, the minimum internal diameter, d_i of the annulus will be 0.0222m. Based on these calculations a standard size pipe of outer diameter of 1 inch by 20 BWG with internal diameter of 23.62mm was found to be desirable for the jacket with the dimension as shown in Figure 6.4. Based on the selected flow meter, the dimensions of the manifold were obtained using flow in annulus equations:

$$\dot{m}_w = \rho A V$$

$$= \rho \pi/4 \left(d_{iann}^{\ 2} - D_o^{\ 2}\right) V \tag{6.2}$$

$$d_i = \sqrt{D_o^{\ 2} + 4m_w/\rho \pi V} \tag{6.3}$$

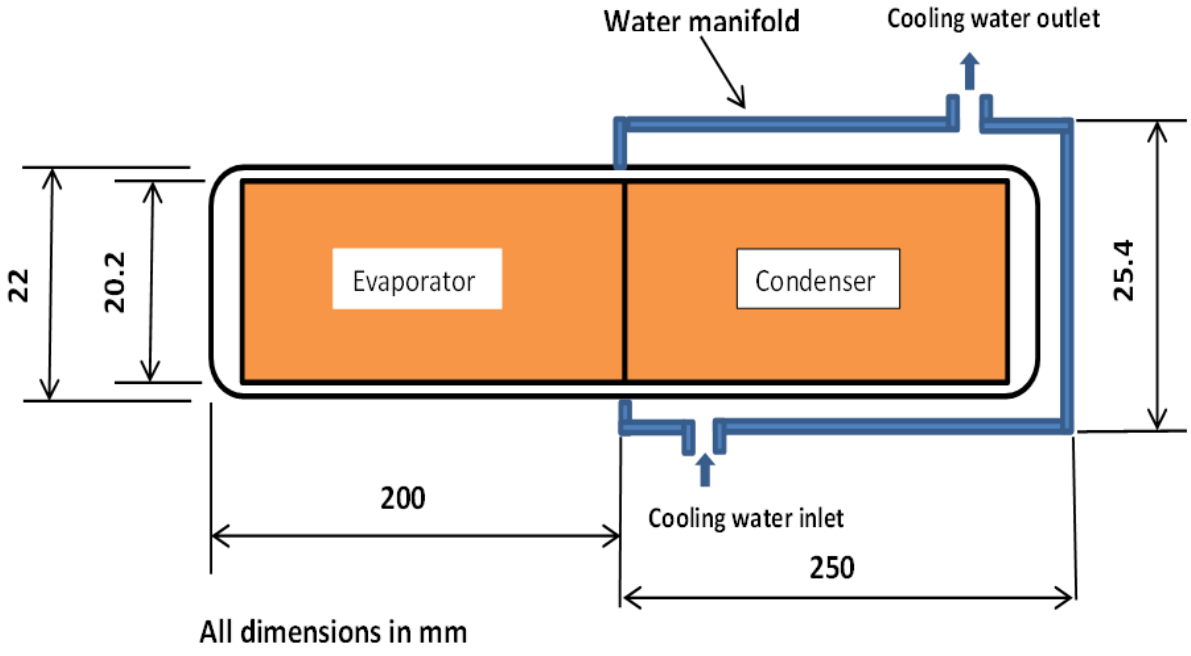

Figure 6.4 Dimensions of the thermosyphon and water manifold

The water in the evaporator gain energy from the pipe wall, vaporise and rise up to the condenser section where it gives out the latent heat of condensation to the cooling water and condense back to liquid that flows to the evaporator by the gravity effect and the cycle continues. The heat gained increases the temperature of the cooling water and the inlet and the outlet temperatures are recorded using two probe thermocouples.

6.4.1. Instrumentation

The test rig was instrumented with measuring devices of temperature, flow rate, power and angular orientation to enable investigating the flow and heat transfer characteristics of the selected thermosyphon.

6.4.1.1. Thermocouples

T – type thermocouples were used in all the temperature measurements in this work. Omega STC-TT-TI-36-1M thermocouples were used for measuring the wall temperature and their specifications are given in Table 6.1 as obtained from the database of the manufacturer.

Table 6.1 Specification of surface thermocouple

Specification	Code	Interpretation
Insulation	TT	PFA
Type	T	T- type thermocouple
Wire gauge	36	36 AWG
Length	1M	1m

For the measurement of the cooling water temperatures, probe thermocouple model TJC100 – CPSS – M 050G from Omega was used and their specifications are given in Table 6.2 [177].

Table 6.2 Specification of Probe thermocouple

Specification	Code	Meaning
Length of lead wire	100	
Type of thermocouple	CP	T – thermocouple
Casing (sheath) material	SS	Stainless steel
Casing diameter	M050	0.50mm
Junction type	G	Grounded
Length of the probe	100	100mm

6.4.1.2. Flow meter

An Omega FLR1009ST-I flow meter (50 – 500 mL/min range) was used for measuring the flow rate of the cooling water flow rates. The output signal from this flow meter is 4 – 20mA. In order to receive a voltage signal output, 100 ohms resistor was connected to the terminal 2 of the logger board where the signal cable from the meter is connected.

Figure 6.5 shows the wiring diagram of the flow meter to the logger and the power supply. The meter was excited with 0.005A and a voltage of 24V from Skytronic adjustable DC power supply. Excitation current was supplied to the flow meter by an adjustable power supply with maximum deviation of ±1% + 2 digits from Skytronic (model 650.682).

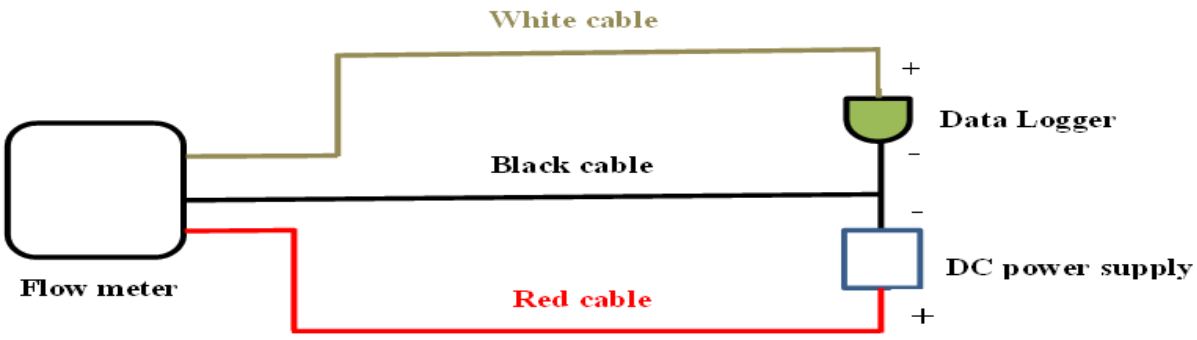

Figure 6.5 Electric wiring of the flow meter [177]

6.4.1.3. Power supply

The power to the heating wire is supplied and controlled by TSx1820P Programmable DC PSU 18V/20A power regulator with accuracy of ± (0.1% +1 digit) and ± (0.5% + 1 digit) for voltage and current respectively. The DC current was read from the digital reading on the power regulator while those of the voltage were read from a digital multimeter connected to the two terminals of the wire close to the pipe to account for voltage drop.

6.4.1.4. Data logging

The flow meter readings were sent to Pico 1012 data logger attached with an electric board for converting current signal from the meter to voltage. The thermocouples readings were sent to Pico TC – 08 data loggers through a connection plug. Due to the number of the thermocouples, two Pico TC – 08 data loggers (each having eight ports), were used for the temperature readings. All the data loggers are connected to a Personal Computer (PC) for receiving the readings as shown in Figures 6.2 and 6.3. The DC voltage and current readings were manually read and recorded.

6.4.1.5. Angular measurement

The orientation of the thermosyphon relative to the horizontal was measured using a high precision protractor from TLC, the true angle finder (TLC 7004) with accuracy of ± 0.5^{o}.

6.4.2. Calibration of the instruments

Different instruments have been used in this experiment for measuring temperature, flow rate, voltage and current. The readings were used for determining the effects of parameters like heat input, flow rate, inclination angle, etc. on the performance of the thermosyphon. All the instruments were calibrated and the uncertainties of their measurements were evaluated.

6.4.2.1. Calibration of water flow meter

The water flow meter was calibrated using a standard 500ml graduated cylinder. The flow to the flow meter is controlled by a valve and the time taken to fill the cylinder is recorded for a particular opening while the voltage signal from the meter is sent to a data logger and PC. Five different runs at increasing of valve openings were carried out and the flow rates were obtained by dividing the 500ml by the time taken in minutes for each run. A curve of the flow rate (in ml/min) against the voltage signal was generated and related R –squared value and equation were obtained as shown in Figure 6.6. The uncertainties due to the volume collecting method and curve fittings are ±8.7mL/min and 5.84mL/min respectively. Details of the uncertainty calculations are shown in Appendix B.

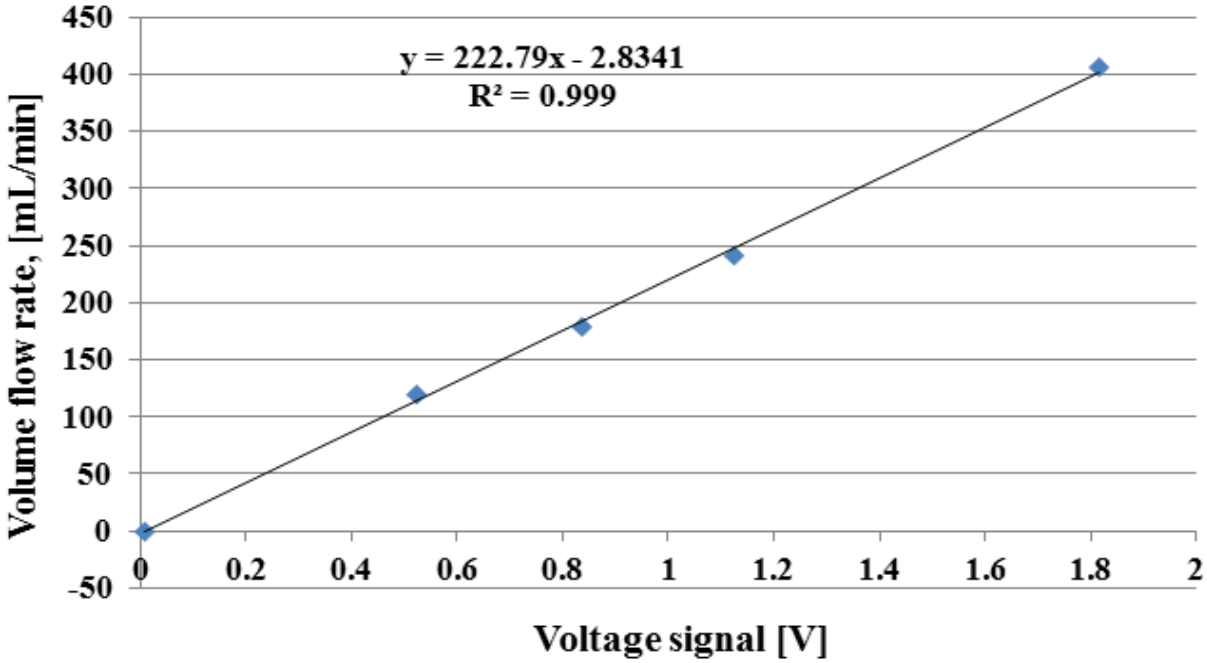

Figure 6.6 Calibration of the water flow meter (Omega FLR1009)

6.4.2.2. Calibration of thermocouples

The thermocouples used in this work were calibrated against a Resistance Temperature Detector (RTD). All the thermocouples and the RTD were immersed in a water bath at the same level and the heat supplied to the water was controlled by a thermostat. The readings of the thermocouples and the RTD were sent to a data logger and retrieved in a PC after reaching steady state. All the surface thermocouples show similar readings for all the heat inputs and calibration curve of the surface-one (i.e. one placed at the 0.02m) is presented in Figure 6.7. While the calibration curves for the inlet and outlet probes thermocouples are shown in Figure 6.8 and 6.9.

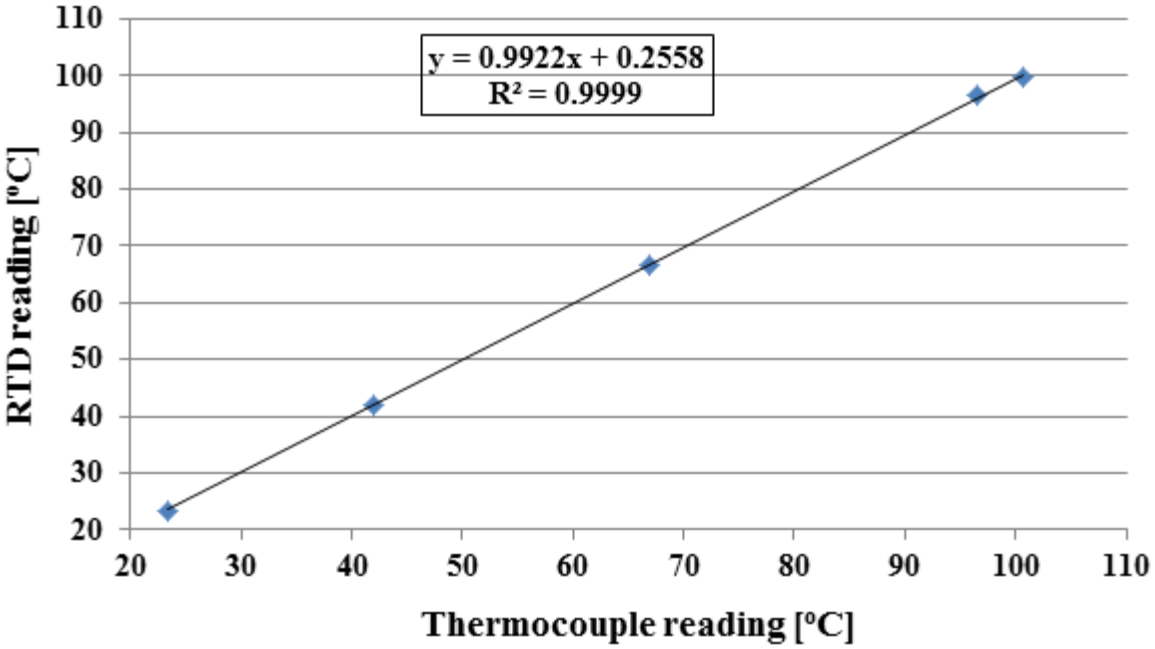

Figure 6.7 Calibration curve of the surface-one thermocouple

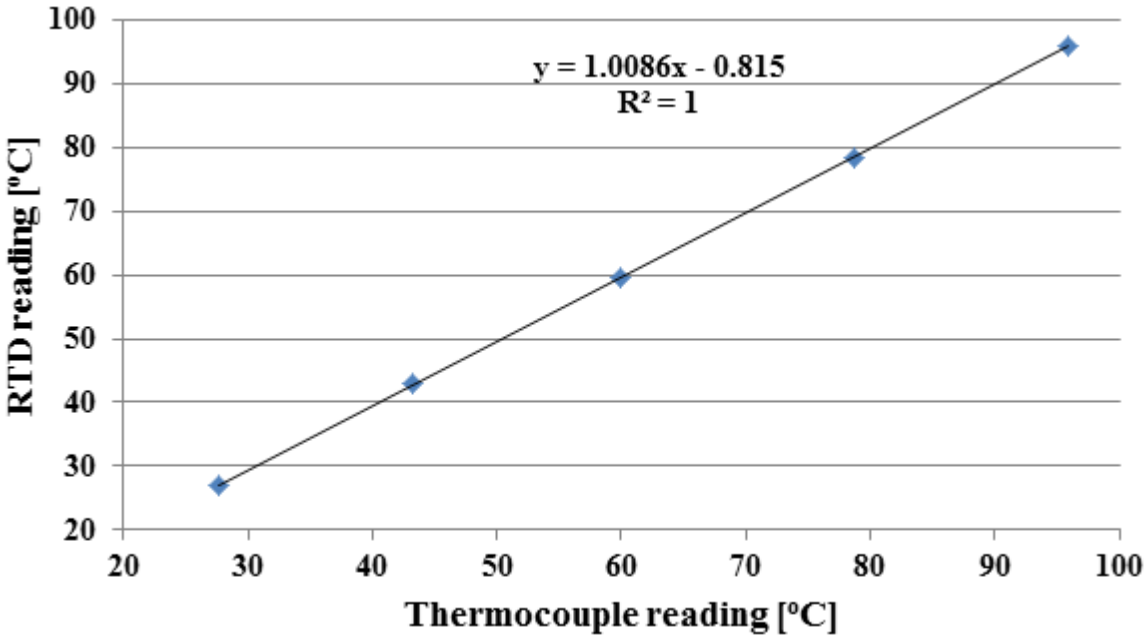

Figure 6.8 Calibration curve of the inlet water probe thermocouple

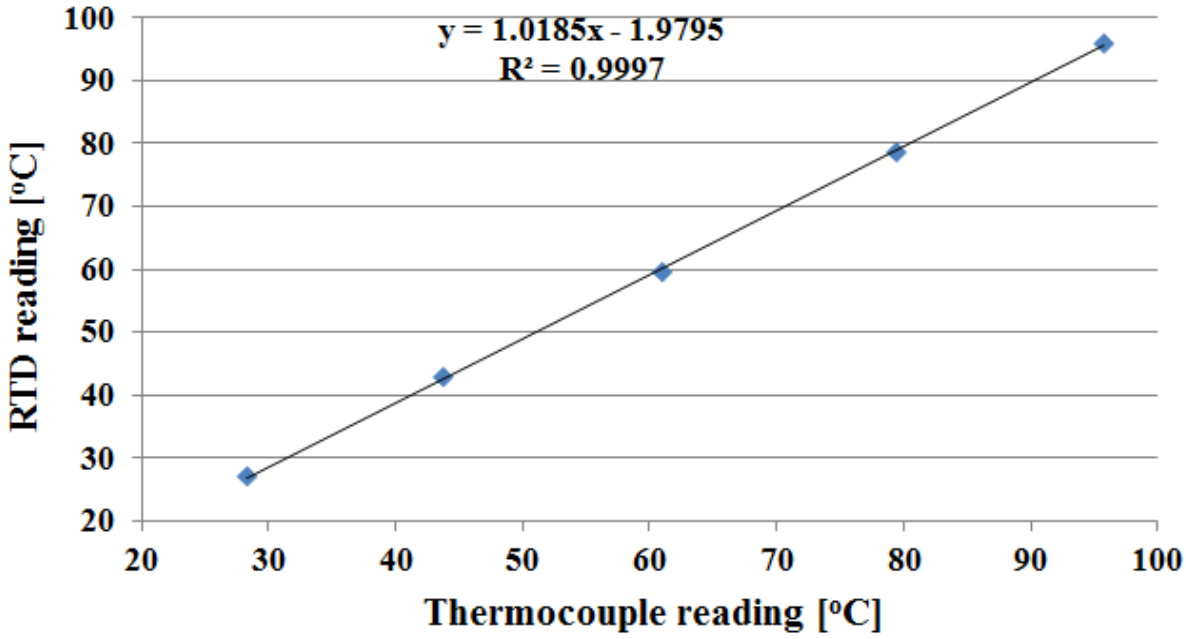

Figure 6.9 Calibration curve of the outlet water probe thermocouple

6.5. Experimental procedure

The test facility was completed when all the parts were connected and water circulation system was checked for possible leakages. The operating conditions were set based on the type of the investigation to be carried out. But in all the cases, the system is allowed to run and stabilize before readings were taken. Preliminary tests show that the system reaches steady state at least after half hour. Ninety samples of readings were taken for each input at the interval of 10 seconds. The data taken includes the temperatures, flow rates, voltage and current. Various investigations were carried out on the effects of heat inputs, cooling water flow rate, inclination effects of the pipe. Detailed procedure for each case and the results obtained are presented in section 6.6.

6.5.1. Measurement accuracy

Errors are usually encountered in engineering measurements due to human and measuring devices which are considered to be either systematic or random. While systematic error is fixed for each reading, random is not the same. Proper calibration can correct systematic error while random error can be removed by uncertainty analysis.

The overall uncertainty can be estimated by using Root Square Sum (RSS) of the systematic and random errors [177]:

$$U_{overll} = \pm\sqrt{U^2{}_{systematic} + U^2{}_{random}} \tag{6.4}$$

The systematic error includes calibration, data acquisition and hysteresis errors and could be determined as:

$$U_{systematic} = \sqrt{\sum_{i=1}^{M} U^2{}_{i,systematic}} \tag{6.5}$$

M is the number of the systematic error origin and could be determined from the laboratory calibration or manufacturers' data.

The random error is statistical and can be estimated as:

$$U_{random} = t_{N-1,95\%} S_{\bar{x}} \tag{6.6a}$$

Where $S_{\bar{x}}$ is the student deviation of the mean given by [177]:

$$S_{\bar{x}} = \frac{1}{\sqrt{N}} \sqrt{\frac{\sum_{i=1}^{N} \left(X_i - \overline{X}\right)^2}{N-1}} \tag{6.6b}$$

$t_{N-1,95\%}$ is the student distribution factor for degree of freedom N -1 (N is the number of sample data).

6.5.2. Uncertainty propagation

Uncertainty propagation was carried out to evaluate the probable random errors in the measured and derived values. This is carried out for the power, temperature and flow rates measurements. The uncertainty of a particular parameter, P can be represented as a function of independent variables, *V1*, *V2,V3,……Vi* as P = P (*V1*, *V2, V3…….Vi*) and with their individual uncertainties estimated as Δ*V1*, Δ*V2,* Δ*V3…….* Δ*Vi*, the uncertainty of P will be the combination effects of the uncertainties of the entire variable as :

$$\Delta P = \pm\sqrt{\left(\partial P/\partial V_1\,\Delta V_1\right)^2 + \left(\partial P/\partial V_2\,\Delta V_2\right)^2 + \left(\partial P/\partial V_3\,\Delta V_3\right)^3 + ... + \left(\partial P/\partial V_i\,\Delta V_i\right)^2} \qquad (6.7)$$

The uncertainty associated with various measurements and the derived quantities are presented in the next sections and the details calculations procedure is explained in appendix B.

6.5.3. Uncertainty in flow rate measurement

An Omega FLR1009ST-I flow meter (50 – 500 mL/min range) was connected to the cooling water circuit and the flow rate was controlled by a globe valve. The output signal from this flow meter is 4 – 20mA. In order to receive a voltage signal output, 100 ohms resistor was connected to the terminal 2 of the logger board where the signal cable from the meter is connected. The uncertainty of the flow meter was found to be ±2.09%FS. The uncertainties due to the volume collecting method and curve fittings are ±8.7mL/min and 5.84mL/min respectively. The overall uncertainty due to the flow rate measurement for full scale is 10.48mL/min. Detailed calculations of the flow rate uncertainty are shown in Appendix B.

6.5.4. Uncertainty in Temperature measurement

Six Omega STC-TT-TI-36-1M thermocouples were fixed on the wall of the pipe used for measuring the surface temperature, while two probe thermocouples (model TJC100 – CPSS – M 050G) from Omega were connected at the inlet and outlet of the cooling water channel. The thermocouples were calibrated with RTD thermocouples with accuracy of ±0.03. The average overall uncertainties of surface and probe thermocouples are ±0.38 and ±0.45 K respectively. Detailed calculations of these uncertainties are shown in Appendix B.

6.5.5. Uncertainty in electrical power measurement

The electrical power used to heat up the evaporator was determined as the product of voltage and current. The uncertainty in the electric power Q_{in} is calculated by:

$$U_{Q_{in}} = \sqrt{\left\langle \left(\partial Q_{in} / \partial I \right) . \Delta I \right\rangle^2 + \left\langle \left(\partial Q_{in} / \partial V \right) \Delta V \right\rangle^2} \tag{6.8}$$

$$= \sqrt{(V \Delta I)^2 + (I \Delta V)^2}$$

Solving equation 6.8 in Engineering equation solver together with the manufacturer's datasheet, the uncertainties of the voltage and current were found to be ±0.018 V and 0.1A respectively leading to the overall uncertainty for the power measurement at the maximum power (110.6W) used in the experiment was found to be ±1.65W. Detailed calculations of the power uncertainties are shown in Appendix B.

6.6. Experimental results

6.6.1. Effects of heat input

The effect of heat input on the performance of thermosyphon was investigated. The flow rate was fixed at the start of the experiment and the heat supply was set at the required value and the system was allowed to run and stabilize. The experiment was repeated for each heat input using the same procedure to confirm repeatability.

Seven different heat input values of 20.43, 39.52, 51.6, 60.18, 81.69, 101.55 and 109W were used with an average flow rate of 0.00224 kg/s for the thermosyphon at the vertical orientation. These heat inputs were obtained from optical simulations on different geometries of compound parabolic concentrators described in chapter five. The temperature, flow rate, voltage and current readings were all recorded.

The power input, P_{in} (W) to the evaporator is calculated from the product of the current, I (A) and voltage, V (V) thus:

$$P_{in} = VI \tag{6.9}$$

The effectiveness of thermosyphon heat pipe is determined by its overall thermal resistance, R_{th} given by [94]:

$$R_{th} = \frac{T_{ae} - T_{ac}}{Q_{in}} \tag{6.10}$$

Where T_{ae} and T_{ac} are the average temperatures on the evaporator and the condenser surfaces respectively.

The performance of the thermosyphon can also be evaluated in terms of the ratio of rate of heat output to the heat input as [178]:

$$\eta = Q_{out} / P_{in} \tag{6.11}$$

The rate of heat transfer to the cooling water (output) can be determined by:

$$Q_{out} = \dot{m} C_p (T_{out} - T_{in}) \tag{6.12}$$

Where $\dot{m}$ is the water mass flow rate, kg/s and C_p is the specific heat capacity of water, kJ/kg-K, while T_{in} and T_{out} are the average inlet and outlet cooling water temperatures respectively.

Figure 6.10 shows the temperature distribution on the wall of the thermosyphon heat pipe at vertical orientation. There is almost uniform temperature distribution for each heat input and this is due to the constant temperature phase change processes taking place in the evaporator and condenser sections. However, there is significant drop in the temperature between the evaporator and the condenser sections due to the water flowing in the condenser section. It can also be deduced from the figure that there is gradual increase in the wall temperature as the heat input increased from 20.43W to 109.51W. But it decreased with further heat input increase from 101W to 109W, indicating that the thermosyphon reached it maximum operation limit at such conditions of heat inputs and flow rate of cooling water. It can also be deduced from the figure that for all the heat inputs considered, there is rise in the temperature at the top of the condenser. This is due to the rise of the saturated steam to the top of the tube and the thin film layer of the liquid due to the type of the condensation taking place [88]. The thickness of the condensate liquid layer increases downward (as it is found in filmwise condensation) hence creating more resistance which lead to the low wall temperature compared to the top of the pipe.

Figure 6.11 shows the variation of the experimental thermal resistance with heat input. It can be seen from the figure that the thermal resistance decreases as the heat input increases. This is because at low heat input, the effective thermal resistance increases, because the resistance due to the boiling in the evaporator increases at higher rate than that in the condenser. As the heat input increases the overall thermal resistance is governed by the resistance to the flow in the evaporator and condenser where an increase in the generation of vapour from the evaporator to the condenser sections (contribute to the trend) leaves small layer of the liquid on the pipe wall which causes low thermal resistance. So the thermosyphon can perform better at high heat inputs provided it does not exceed its operation limits.

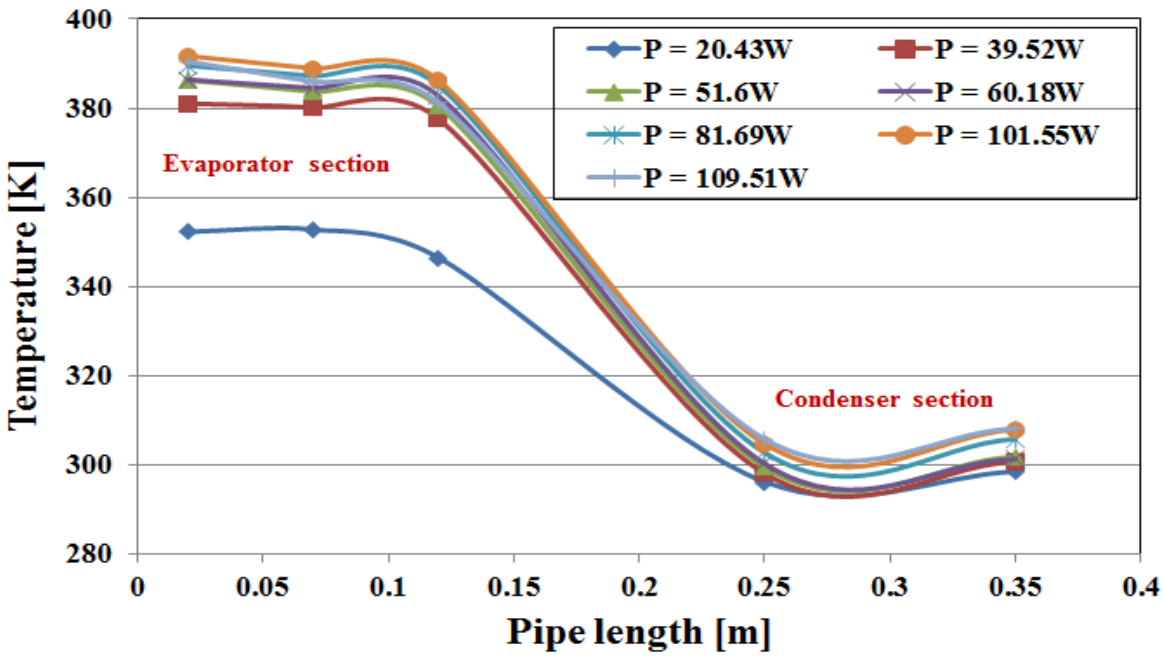

Figure 6.10 Temperature profile on the thermosyphon wall for different power inputs

The variation of the thermosyphon performance with the heat input is shown in Figure 6.12. It can be seen from such figure that the performance of the pipe increases as the heat input increases from 20 to 81.69W, but it tends to decrease as more heat is supplied showing the limit of this pipe which depends on the operating conditions like cooling water flow rate.

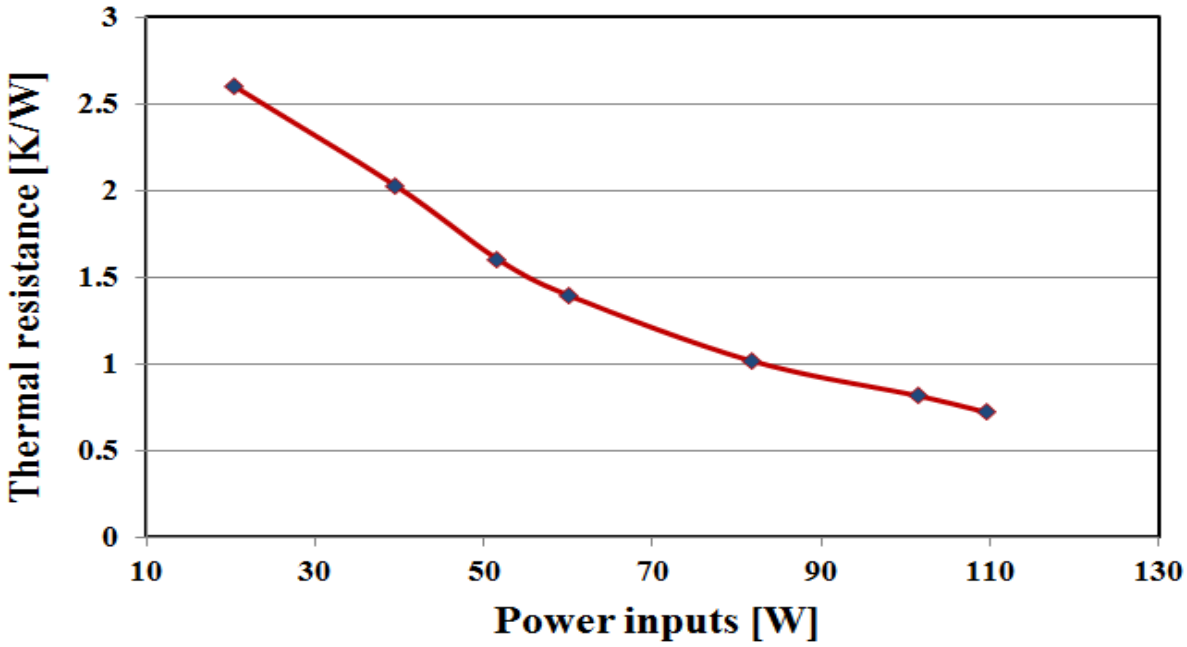

Figure 6.11 Variation of the overall thermal resistance with power inputs

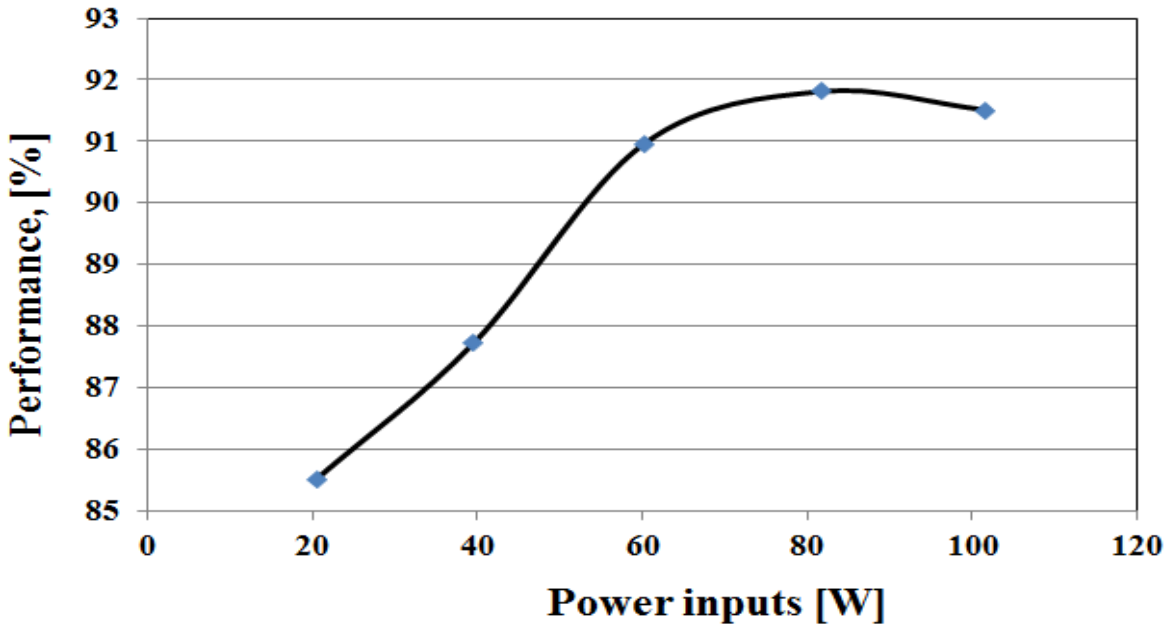

Figure 6.12 Performance of thermosyphon at different power inputs

The reason for this behaviour can be explained based on the heat transfer mechanism at the condenser section which depends on the magnitude of the heat input supplied to the

evaporator section. At low heat input, the vapour generated from the evaporator section is small, so there will be significant dry areas in the condenser section; in such situation heat transfer is largely by free convection. But as the heat is gradually increased, more vapour will rise to the condenser section, there will be high condensation rate on the condenser wall and the dominant heat transfer mechanism will be condensation. At certain high heat input, thick layer of liquid can be formed on the wall of the pipe causing high thermal resistance and hence lower the heat transfer to the cooling water. This limit depends on various other factors like cooling water flow rate, fill ratio, pipe geometry, etc.

6.6.2. Effects of cooling water flow rate

The effect of varying the cooling water flow rate at constant heat input was investigated on the performance of thermosyphon heat pipe. The heat input was fixed at 101W while five different flow rates ranging from 0.00156 to 0.00611 kg/s were investigated. Temperature and the flow rate readings were recorded for each run and the effects were evaluated based on the overall thermal resistance, rate of heat transfer to the cooling water, outlet temperature of cooling water, performance of the thermosyphon, etc. The performance of the pipe in terms of heat transfer to the cooling water increases with the flow rate as shown in Figure 6.13. This is due to the mass flow of the cooling water which results in the enhancement of the rate of heat transfer from the pipe wall to the cooling water and subsequent increase in the efficiency. The convective heat transfer coefficient on the cooling water side was determined from [94]:

$$h_c = \frac{Q_{out}}{\pi D L_c (T_c - T_{cw})} \tag{6.13}$$

Where T_c and T_{cw} are the temperatures of the condenser wall and cooling water respectively. The convective heat transfer coefficient on the condenser section increased significantly with

the increase in the flow rate as shown in Figure 6.14. This increase is due to the increase in the rate of heat transfer to the cooling water and the decrease in the condenser wall temperatures.

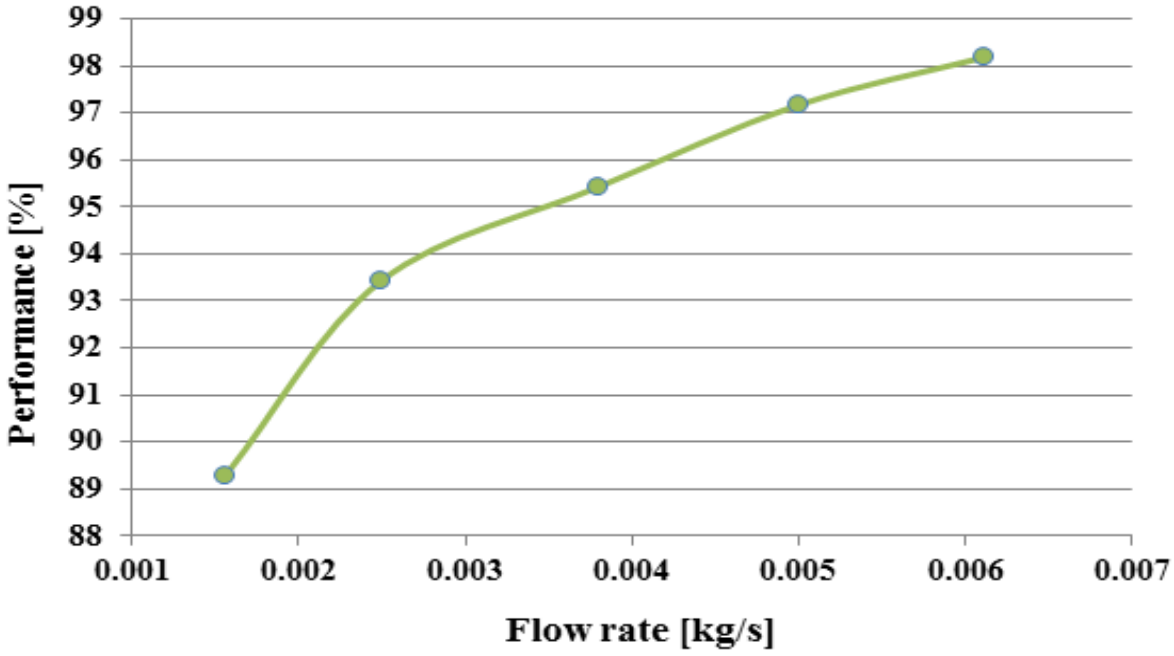

Figure 6.13 Performance of the thermosyphon at different cooling water flow rates

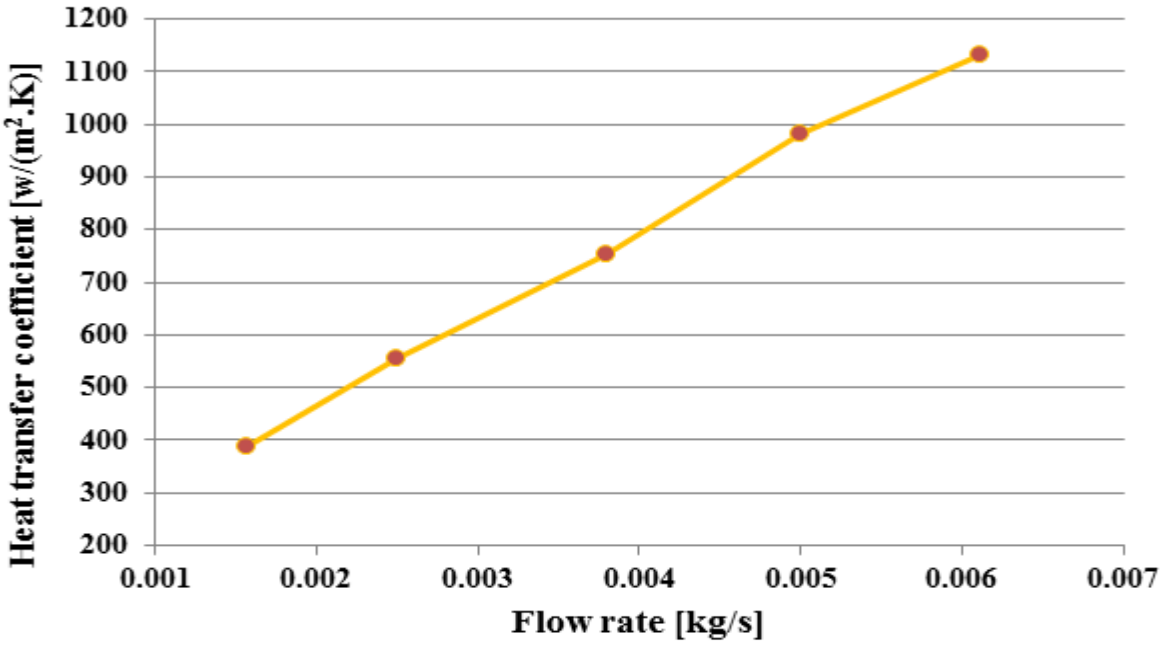

Figure 6.14 Variation of convective heat transfer coefficient with water flow rates

Figure 6.15 shows the variation of the cooling water outlet temperature with the flow rates. It can be seen from the figure that increasing the flow rate of the cooling water decreases the temperature at which it leaves the system. This is due to the increase in the mass flow of the water as the flow rate increases. Comparing Figures 6.13 and 6.15, an inform decision can be taken on the choice between the heat transfer rate and the temperature at which the water will be delivered and this will be dictated by the intended application. The two parameters can be read and compared at a particular water flow rate within the range tested by using Figure 6.16. The two curves met at approximately 301.5 K, 93.5% efficiency and 0.0026 kg/s at average water inlet temperature of 291.4 K. Thus above such point, there is increase in the performance but decrease in the outlet temperature of the cooling water.

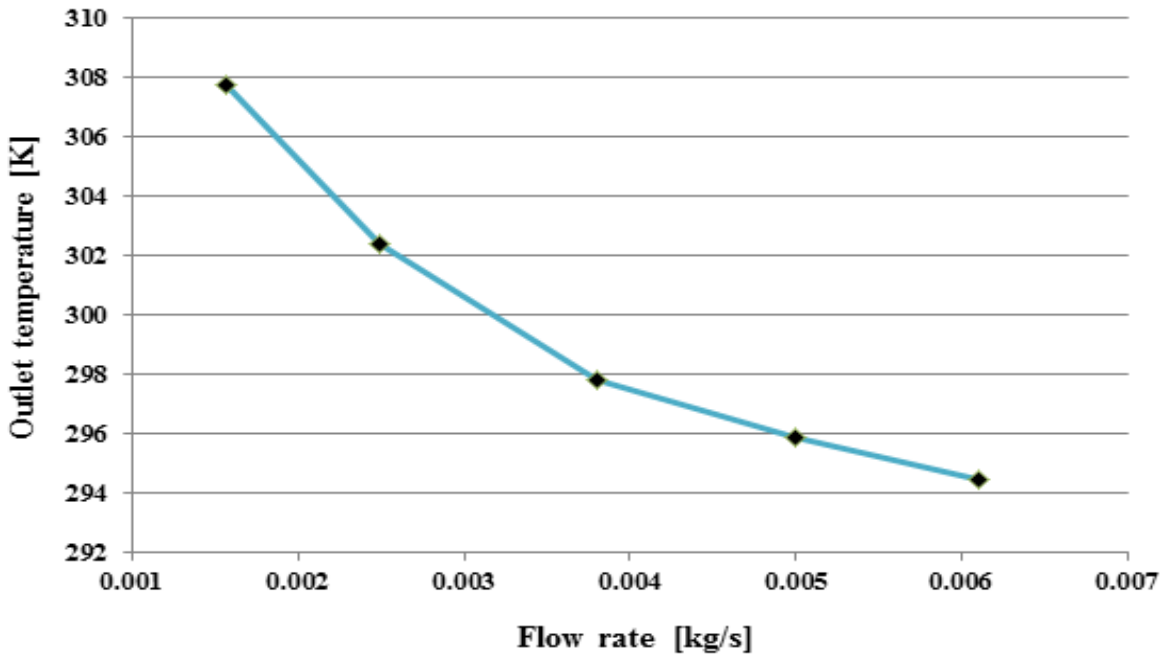

Figure 6.15 Variation of the cooling water outlet temperature with flow rate

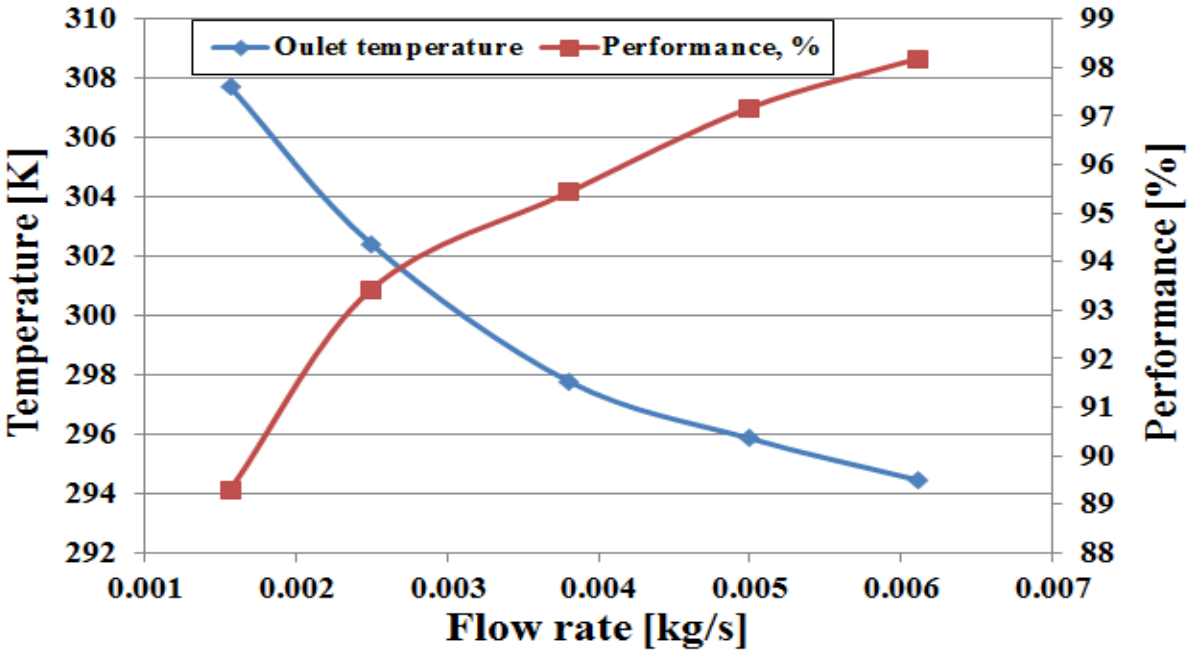

Figure 6.16 Variation of the cooling water temperature and thermosyphon efficiency with water flow rate

6.6.3. Effects of inclination angle

As explained earlier the operation of thermosyphon depends on the gravity effect, hence the condenser has to be above the evaporator for the condensate to return to the evaporator for the cycle to continue. Inclining the pipe to an angle from the horizontal affects its performance depending on the operating conditions and the pipe geometry. In this work, the effect of the inclination angles from 10 to 90^{o} on the convective heat transfer coefficient, thermal resistance and efficiency of the pipe were investigated.

Three different heat inputs; 31.18, 51.70 and 109.63 W (equivalent to 2255.90, 3735.22 and 7922.16 W/m^2) at constant average cooling water flow rate of 0.0021 kg/s were used in investigating the effect of inclining thermosyphon relative to the horizontal. Figure 6.17

shows the variation of the performance of the thermosyphon with the inclination angle at three different heat inputs. It can be deduced from the figure that the heat transfer to the cooling water increases with the increase in the inclination in all the cases making 90^{o} been the best. But the effects is more pronounced at small heat input giving enhancement from 10^{o} to 90^{o} of 17.8%, 13.9% and 3.4% for 31.18W, 51.7W and 109W respectively. Also there is sharp difference in the range 40^{o} to 50^{o} angle in all the cases. The effect of the inclination angles on the thermosyphon performance is due to the change in the flow patterns, increase in convective heat transfer coefficient, effects of gravitational force on the return of the condensate to the evaporator, etc.

The data in Figure 6.17 clarifies the contradictory reports in the literature on the effects of inclination angle that the effects is more significant at certain heat inputs but insignificant at higher inputs especially when the operation limit of the pipe is approached.

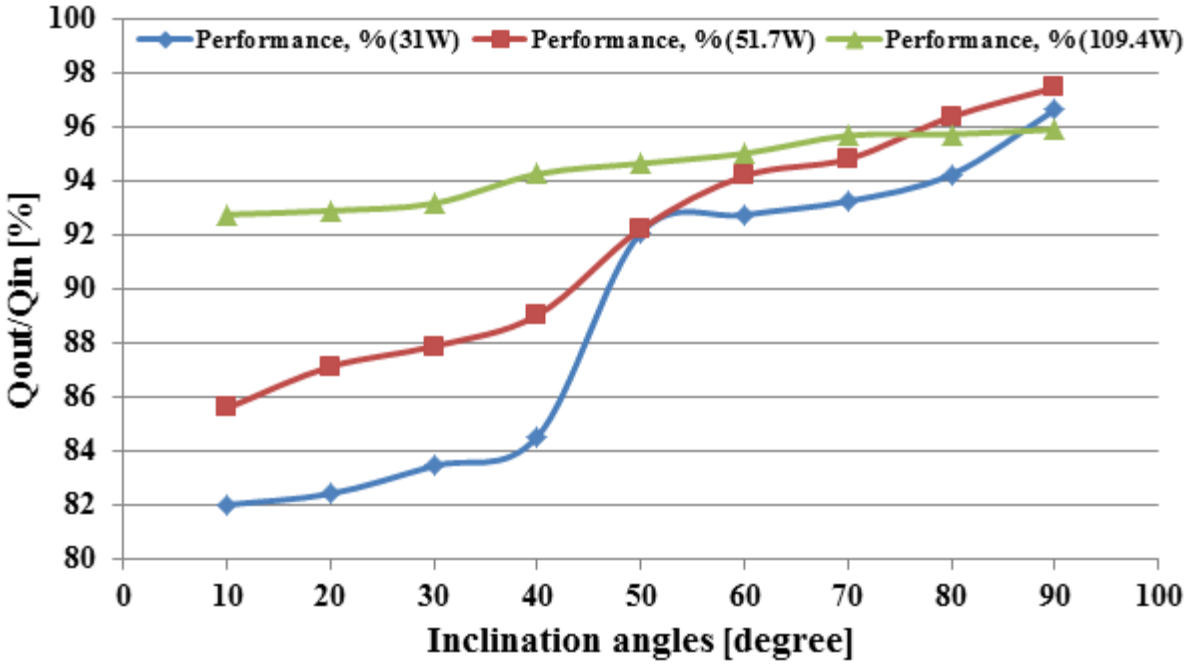

Figure 6.17 Variation of the performance of thermosyphon with inclination angle at different power inputs

6.7. Numerical study of the performance of thermosyphon

As stated earlier, many parameters affect the performance of thermosyphon heat pipe and investigating them experimentally will be cost intensive and time consuming. Numerical modelling like Computational Fluid Dynamic analysis (CFD) is an alternative, where many of those parameters can be studied. In CFD, a set of discretised equations are solved with the help of computer to get an approximate solution [179]. In this section, a CFD analysis was carried out on the flow and heat transfer characteristics of a thermosyphon heat pipe in both vertical and inclined orientations. To accomplish this task, a commercial Ansys fluent 15.0 was used to model the evaporation and condensation processes taking place in a thermosyphon heat pipe using volume of fluid (VOF) approach.

6.7.1. Theory

Multiphase flow is a flow involving mixture of phases of fluid (either of the same or different substances) at macroscopic level with identified boundary between them. One of the phases is considered as continuous (primary) and the other as dispersed within the continuous (secondary). Examples of multiphase flow include bubbly flow, droplet, slug, stratified flows, fluidized bed, etc. as shown in Figure 6.18. Two approaches exist for the mathematical calculations of multiphase flows; Euler – Euler and Euler – Lagrange approaches. In Euler – Euler approach, the phases are considered to be penetrating each other continuously. But the Euler-Lagrange approach treats the fluid phase as continuous and solved by Navier - Stoke equation while the diffuse phase is solved by tracking huge number of its particles.

Four different multiphase modelling techniques are available in Fluent and the choice depends on the type of flow and the stoke number (ratio of dispersed phase time to that of continuous phase).

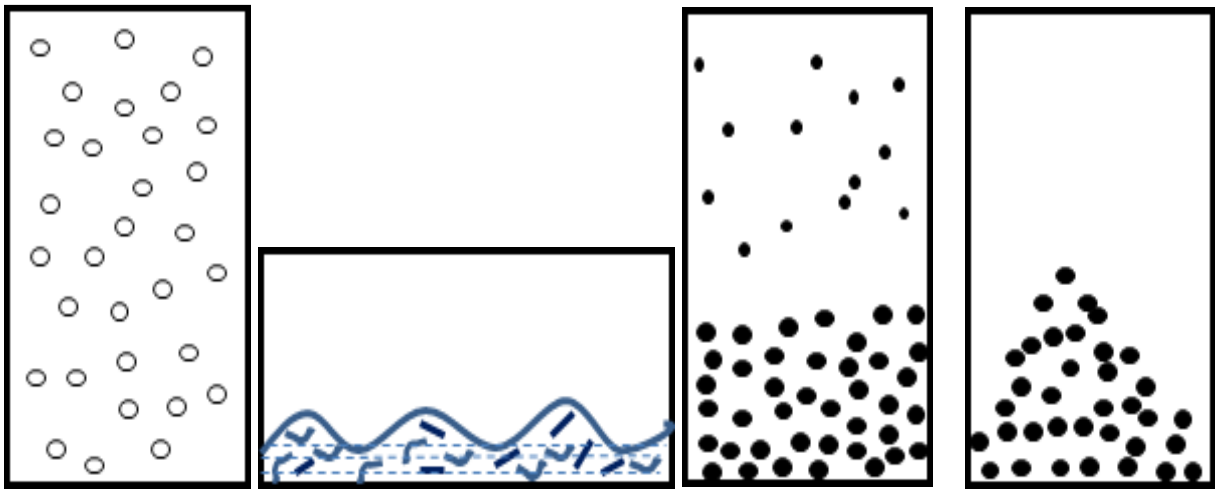

(a) (b) (c) (d)

Figure 6.18 Types of flow: (a) Bubbly, droplet or particle laden (b) Stratified/free flow (c) Sedimentation (d) Fluidized bed [180]

These approaches are [180]:

i. Discrete phase model (DPM)

ii. Eulerian model

iii. Mixture model and

iv. Volume of Fluid model (VOF)

All these models except DPM are based on Euler- Euler approach available in Ansys Fluent. Mixture model is aimed at two or more fluid or particulate phases, where mixture momentum equation is solved for continuous phase while relative velocity is determined for the dispersed phases. Sedimentation, particle – laden, bubble flows, etc. can be modelled using mixture model approach. A set of "n" number of momentum and continuity equations are solved for each phase and the coupling is done through pressure and interphase exchange in Eulerian model. Eulerian model can be used in bubble columns, fluidized bed, particle suspension, etc. VOF is used for modelling two or more immiscible fluids by solving a single set of momentum equations and tracking the volume fraction of each fluid in the computational cell

all over the domain. It is applied to steady/transient tracking of liquid/gas interface, free surface and stratified flows, etc.

6.7.2. Governing equations used in building this model

The motion of the working fluid inside a thermosyphon is described by continuity, momentum and energy equations. The continuity equation of the VOF for the secondary phase (*l*) is described as [180]:

$$\nabla.\left(\alpha_l \rho_l \vec{u}\right) = -\partial/\partial t\left(\alpha_l \rho_l\right) + S_m \tag{6.13}$$

S_m is the source term, used in the calculation of the mass transfer during evaporation and condensation and α is the volume fraction of the fluid. But for the primary phase, the continuity equation can be solved based on the constraint below [180]:

$$\sum_{l=1}^{n} \alpha_l = 1 \tag{6.14}$$

The energy equation is shared among the primary and secondary phases and is expressed as [180]:

$$\partial/\partial t\left(\rho E\right) + \nabla.\left[\vec{v}\left(\rho E + p\right)\right] = \nabla.\left(k_{eff} \nabla T\right) + S_E \tag{6.15}$$

S_E is the energy source term for calculating the heat transfer during evaporation and condensation.

The momentum equation for the VOF can be written as [181]:

$$\frac{\partial\left(\rho\vec{v}\right)}{\partial t}+\nabla.\left(\rho\vec{v}\vec{v}\right)=-\nabla p+\nabla\left[\mu\left(\nabla\vec{v}+\nabla\vec{u}-\frac{2}{3}\mu\nabla.\vec{v}\,I\right)\right]+\rho g+F_v \tag{6.16}$$

Where

$$\rho=\alpha_l\rho_l+\alpha_v\rho_v \tag{6.17}$$

$$k=\alpha_l k_l+\alpha_v k_v \tag{6.18}$$

$$\mu=\alpha_l\mu_l+\alpha_v\mu_v \tag{6.19}$$

$$E=\frac{\alpha_l\rho_l E_l+\alpha_v\rho_v E_v}{\alpha_l\rho_l+\alpha_v\rho_v} \tag{6.20}$$

$$E_l=C_{p,l}\left(T-T_{sat}\right) \tag{6.21}$$

$$E_v=C_{p,v}\left(T-T_{sat}\right) \tag{6.22}$$

F_v acts as the source term in the momentum equation given by [181]:

$$F_v=\sigma_{lv}\frac{\alpha_l\rho_l k_v\nabla\alpha_v+\alpha_v\rho_v k_l\nabla\alpha_l}{0.5\left(\rho_l+\rho_v\right)} \tag{6.23}$$

Where σ_{lv}, is the surface tension between the liquid and the vapour and k is the surface curvature. The effect of the surface tension between the two phases is introduced to the model according to the following equation (from steam table) [94] where T is the temperature shared by the phases:

$$\sigma_{lv}=0.09805856-1.845x10^{-5}T-2.3x10^{-7}T^2 \tag{6.24}$$

6.7.3. Model setup

6.7.3.1. Geometry and meshing

A 2D geometry of the 400mm long thermosyphon used in the experiment was developed and meshed in Gambit software to simulate the flow and heat transfer in the pipe. Grid independence test was conducted by generating three different mesh sizes of 23,998, 38,278 and 120,794 cells in Gambit software (Figure 6.19) and their properties are shown in Table 6.3. Temperature distributions along the wall of the pipe were monitored and shown in Figure 6.20 to test the grid independence of the results. The results show almost the same temperature distributions along the wall of the pipe for the mesh sizes of 38,278 and 120,794 cells. Figure 6.21 shows the vapour volume fraction in the evaporator section showing gradual generation of bubbles generated at different computational time. The top section (red colour) shows the presence of only vapour with a volume fraction of 1. Under such region there is mix of vapour and liquid with blue colour indicating the liquid which has vapour volume fraction of zero. The flow patterns and the vapour generation in the pipe change with the heat input. Also the thickness of the condensate on the wall of the pipe changes with the heat applied and other boundary conditions like cooling water flow rate as discussed earlier.

Table 6.3 Mesh information

Mesh information	**Run 2**	**Run 7**	**Run 8**
Cells	23,988	38,278	120,794
Faces	47,463	75,716	235,893
Nodes	23,474	37,437	115,098
Cell zone	4	4	4
Face zone	14	14	14

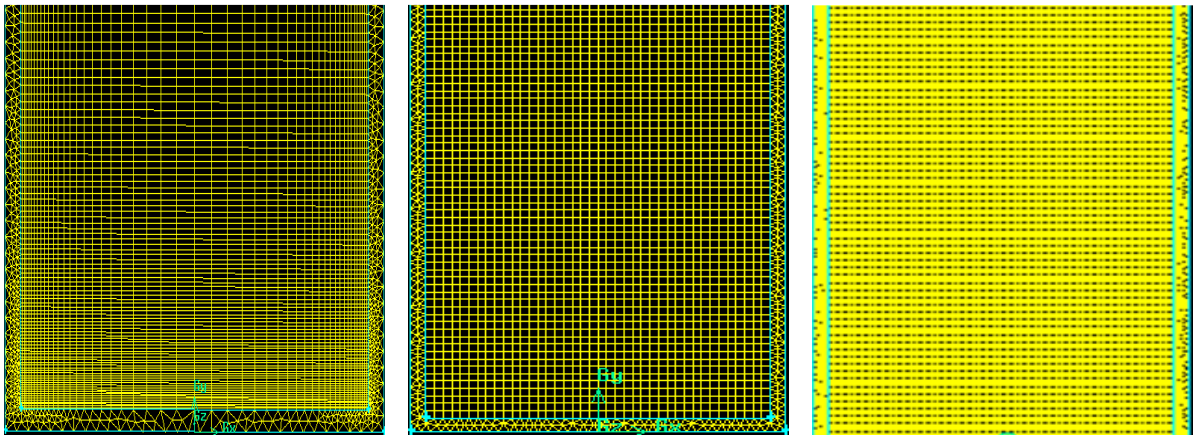

23,988 **38,278** **120,794**

Figure 6.19 Sections of the computational mesh

To reduce the computational time, the mesh size of 38,278 Quad, Map cells was used in the simulation of this work since it gives the same results with 120,794 cells (Figure 6.20).

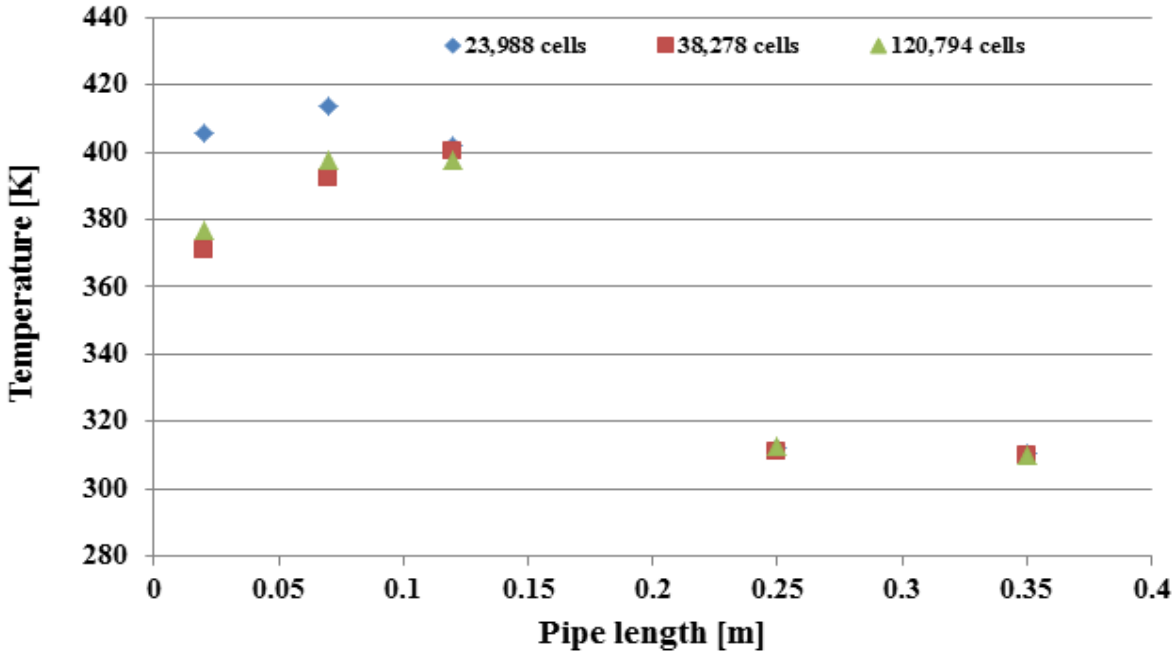

Figure 6.20 Temperature distributions along the axial length of the pipe for different mesh sizes

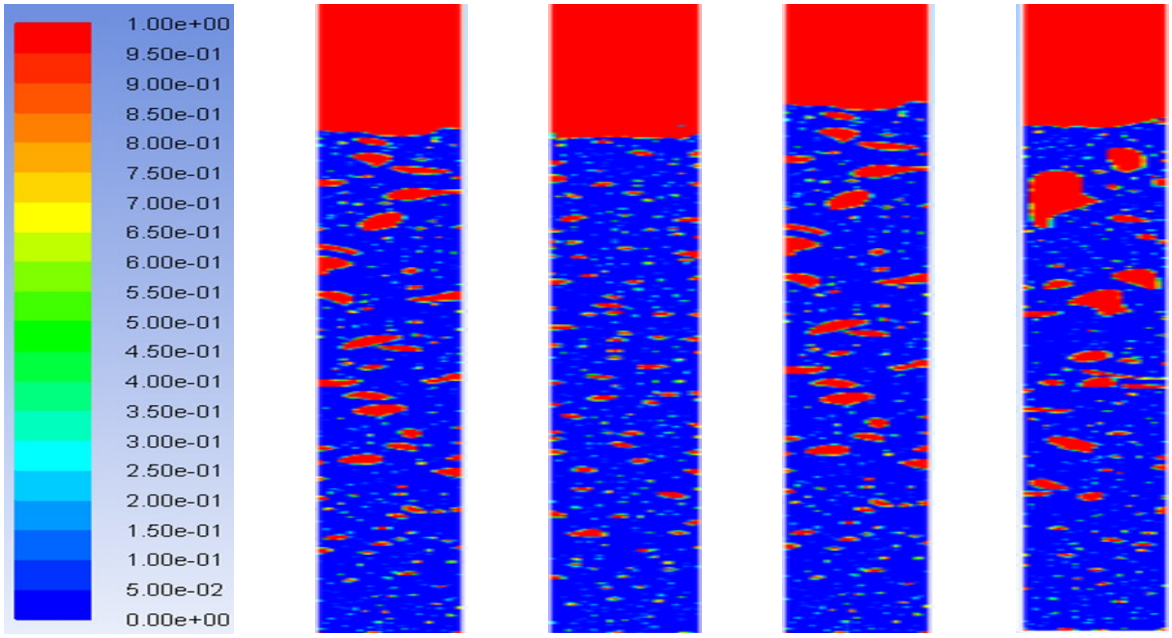

Figure 6.21 Contours of vapour volume fraction at different computational time.

6.7.3.2. Modelling of the heat and mass transfer during the simultaneous evaporation and condensation processes

Since FLUENT (VOF approach) alone cannot simulate the evaporation and condensation in the thermosyphon, a user-defined function (UDF) was developed to customize the VOF to meet the requirement of this work. An interpreted type UDF was developed for calculating the mass and heat transfer between the liquid and vapour. Mass, S_m and energy source, S_E terms in the continuity and energy equations respectively are defined in the UDF and linked to the FLUENT governing equations. Both evaporation and condensation processes require two mass source terms for the liquid and vapour phases while heat transfer requires only one source term for the phases during evaporation and condensation. Correlations proposed by De

Schepper *et al.,* [93] for source terms are used in this work to calculate the mass and energy transfer as shown in Table 6.4.

The UDF codes for this work were written by using equations in Table 6.4 and are linked to the fluent using the saturation temperature for each case.

6.7.3.3. Boundary conditions and the thermophysical properties of the materials

According to the experiment, five different values of heat fluxes of 2,858.65, 4,353.32, 5,910.002, 7,346.37 and 7,922.16 W/m^2 (equivalent to 39.5152, 60.1759, 81.69405, 101.5538 and 109.508 W) were applied to the evaporator section as energy input for the thermosyphon at vertical orientation. Each heat input was applied under the same condition of constant average flow rate of 0.00227 kg/s. While for inclination cases, a constant average heat flux of 51.7 and 109.7W were used for the inclination angles of 50^o to 90^o and average flow rate of 0.0022 kg/s.

Convective thermal condition was applied to the condenser section by specifying the heat transfer coefficient, h_c W/m^2-K of the cooling water according to the equation 6.13

All the parameters in equation 6.13 are obtained from the experiment and used to calculate the convective heat transfer coefficient for each case and used in the Ansys fluent as input. As part of the boundary condition, the inner walls of the tube are considered as stationary and non – slip.

Water-vapour and water-liquid are considered as primary and secondary phases respectively and phase interaction is defined in the surface tension force modelling using polynomial profile in terms of temperature with the coefficients of 0.09805856, -1.84 x 10^{-5} and -2.3 x 10 $^{-7}$ (equation 6.24). Water is considered as the working fluid with fill ratio of 0.65 and its

density was activated using polynomial profile with the coefficients of 859.0083, 1.252209 and -0.0026429 according to the equation derived from steam table as [94]:

$$\rho_l = 859.0083 + 1.252209T - 0.0026429T^2 \quad (6.31)$$

Table 6.4 Correlations for mass and energy source terms [93]**.**

Energy	**Phase change**	**Temperature**	**State**	**Correlation**
Mass	Evaporation	$T_m > T_{sat}$	Liquid	$S_m = -0.1\rho_l\alpha_l \frac{T_m - T_{sat}}{T_{sat}}$ (6.24)
			Vapour	$S_m = 0.1\rho_l\alpha_l \frac{T_m - T_{sat}}{T_{sat}}$ (6.25)
	Condensation	$T_m < T_{sat}$	Liquid	$S_m = 0.1\rho_v\alpha_v \frac{T_{sat} - T_m}{T_{sat}}$ (6.26)
			Vapour	$S_m = -0.1\rho_v\alpha_v \frac{T_{sat} - T_m}{T_{sat}}$ (6.27)
Heat transfer	Evaporation	$T_m > T_{sat}$	$S_E = -0.1\rho_l\alpha_l \frac{T_m - T_{sat}}{T_{sat}} LH$ (6.28)	
	Condensation	$T_m < T_{sat}$	$S_E = 0.1\rho_v\alpha_v \frac{T_{sat} - T_m}{T_{sat}} LH$ (6.29)	

Other thermophysical properties defined in the model are listed in Table 6.5 for both the working fluid and the pipe. The phase change was considered to occur at the boiling temperature of 373K. The latent heat of 2455 kJ/kg was used in the UDF and the saturation temperature was taken as the average of the evaporator and condenser temperatures for each case as obtained from the experiment.

Table 6.5 Thermophysical properties of the materials used in the model

Material and Properties		
Pipe	Material	Copper
	Thermal conductivity	387.6 W/m-K
	Density	8978 kg/m^3
Water - liquid	Density	Equation 6.31
	Specific heat capacity	4.182 kJ/kg-K
	Thermal conductivity	0.6 W/m-K
	Molecular weight	18.0152 kg/kgmol
	Viscosity	0.001003 kg/m-s
Water - Vapour	Density	0.5868495 kg/m^3
	Specific heat capacity	2014 kJ/kg-K
	Thermal conductivity	0.0261 W/m-K
	Molecular weight	18.01534 kg/kgmol
	Viscosity	1.34 10^{-5} kg/m-s

6.7.3.4. Solution method and convergences

The calculations were done by using COUPLED scheme for the pressure –velocity coupling, first order upwind for the momentum, volume fraction and energy while first order implicit is used for the transient formulation. The solution is considered to be converged when the residual scales of mass and velocity is below ten to the order of -4 (10^{-4}). The gravity was taken as 9.81 m/s^2 in the y-axis for the vertical orientation cases. For the inclined heat pipe

simulation, the gravitational force was determined on both x and y axes for each angle according to Figure 6.22 and activated in the Ansys fluent.

The Calculations were carried out with the time step size of 0.0005 and number of time step between 120,000 and 180,000 depending on when the solution reaches a steady state (i.e. between 60 and 90S). Due to the small number of the time step, a courant number of 0.25 was used. After initialization of the solution and patching the volume fraction to the evaporator section, the model is run and allowed to reach steady state.

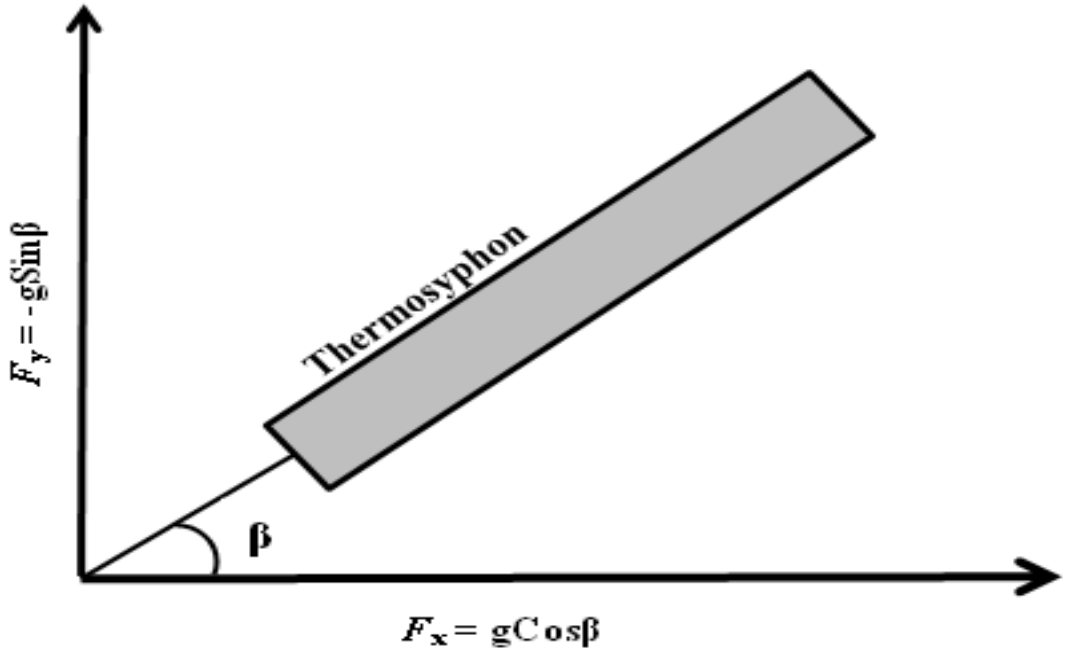

Figure 6.22 Forces on an inclined thermosyphon heat pipe

6.7.4. Modelling results and validation

The temperature distributions on the thermosyphon walls and the overall thermal resistances for different heat inputs obtained from the CFD model is validated with the experimental results for the vertical orientation. Also the CFD results of the inclined cases are validated with the experiment in terms of temperature profile and the thermal resistances. Also the effects of cooling water flow rate and thickness of the evaporator wall were simulated.

6.7.4.1. Temperature profile and the thermosyphon performance at vertical position

The CFD predicted temperature on the thermosyphon wall is compared with the experimental results for five different heat inputs when the pipe is at vertical position (90^o) as shown in Figures 6.23 (a and b). It can be seen that the temperature distributions in the two figures show similar trend. There is reasonable agreement between the simulation and the experimental results for the various heat inputs used as seen in the Figure 6.23. The slight deviation (maximum deviation of 4.2%) may be due to the heat losses that occur in the experiment but not considered in the simulation especially on the condenser side where there is no insulation.

It can also be deduced from the figures that there is gradual increase in the wall temperature as the heat input increase up to certain value when the performance limit of the pipe is reached. This is because at low heat input, the vapour generated from the evaporator section is small, so there will be significant dry areas in the condenser section; in such situation heat transfer is largely by free convection. But as the heat is gradually increased, more vapour will rise to the condenser section, there will be high condensation rate on the condenser wall and the dominant heat transfer mechanism will be condensation. At certain heat input, thick layer of liquid can form on the wall of the pipe causing high thermal resistance and hence low heat transfer.

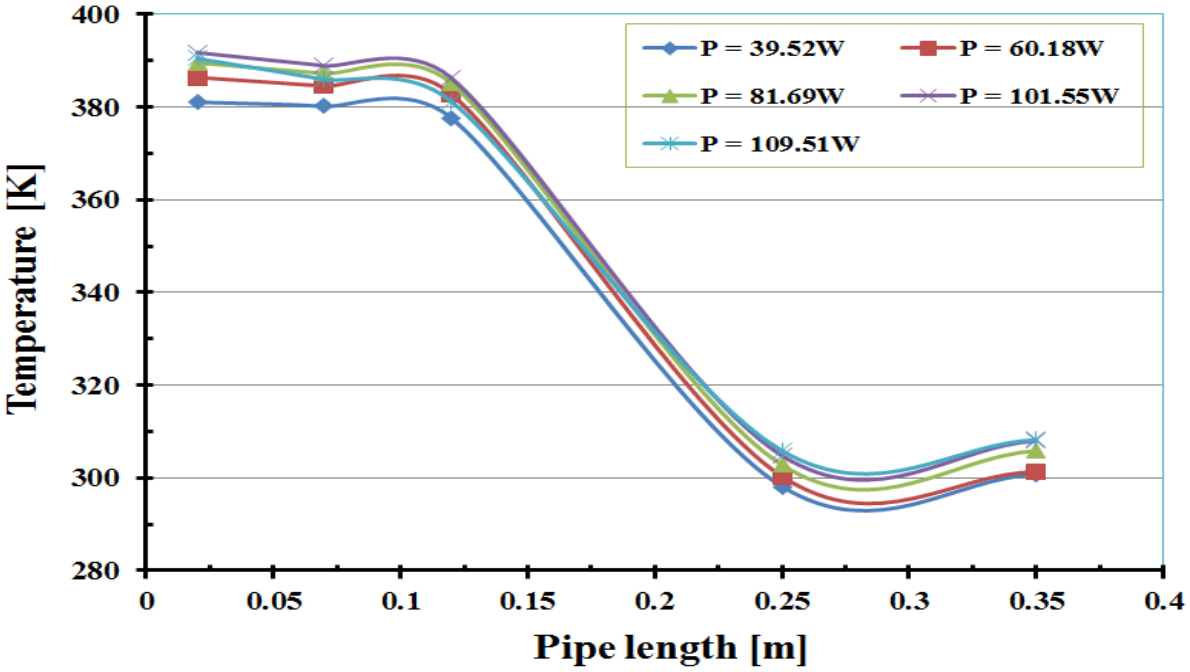

(a) Experiment

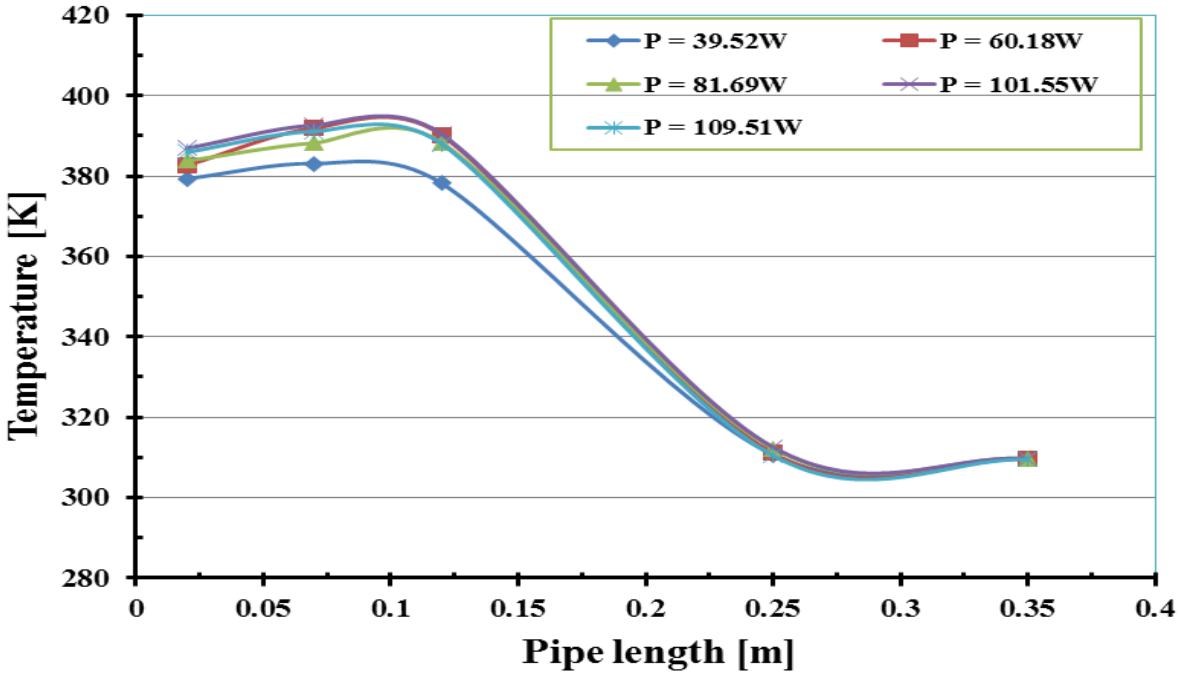

(b) CFD

Figure 6.23 Comparison of temperature distributions between experiment and CFD for different power inputs

Figure 6.24 shows the variation of the thermal resistances with the heat inputs for both CFD and experiment. It can be seen from the figure that the results show a decrease in the thermal resistance as the heat input increases and reasons for such behaviour is explained in 6.5.3.1. There is also increase in the generation of vapour from the evaporator section evaporating to the condenser section leaving small layer of the liquid on the pipe wall which causes low thermal resistance. This will lead to the increase in the performance of the pipe in terms of heat transfer to the working fluid due to the high condensation rate. Reasonable agreement is found between the predicted thermal resistance and the experimental with an average deviation of 5.8%. The deviation can be due to the losses occurring in the experiment especially on the condenser wall (where there is no insulation) but not considered in the simulation. Thus the predicted temperature on the condenser wall is higher than that of the experiment (see Figure 6.23) and this explains why the predicted thermal resistance is lower than that from the experiment.

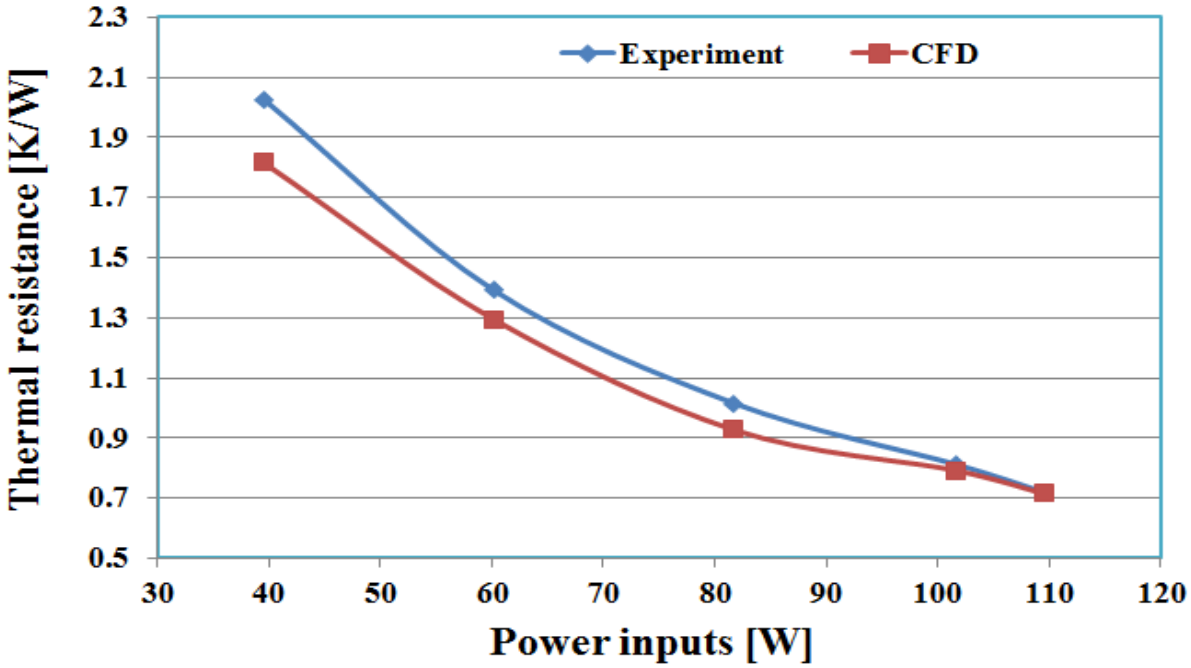

Figure 6.24 Comparison of the predicted overall thermal resistance with experiment

6.7.4.2. Temperature profile and thermal resistance of the thermosyphon at different inclination

For the first time (to my knowledge), the effects of inclination angle is modelled numerically to study the temperature profile on the thermosyphon wall and the overall thermal resistance. In according to the experiment conducted in section 6.5.3.3 the performance of the thermosyphon inclined at five (out of the ten angles experimentally investigated) different angles (50 to 90^{o}) was simulated with a constant average heat inputs of 51.7W and 109.7W and using all other parameters as in the experiment. Figure 6.25a (i and ii) compare the predicted temperature distributions with that of the experimental for two different inclination angles and heat inputs with deviation of ±1.5% and ±1.8% for inclination angles of 50 and 70^{o} respectively when the heat input is 51.7W. For the heat input of 109.7W, the deviation was found to be ±1.2 and ±2.8% for 50 and 80^{o} inclination angles respectively. Figure 6.25b (i and ii) compares the temperature distribution on the wall of the thermosyphon obtained from experiment with the predicted values (CFD) for all the inclination angles investigated.

It can be seen from Figure 6.25 that the temperature on the pipe wall tends to be higher at lower angles compared to the higher ones, this is due to the slope that exposes some parts of the pipe to the heat without contact with fluid, hence causes high temperature rise. At the condenser section, some part of the pipe will be covered with layer of water due to the low angle which can cause high resistance to the heat flow to the cooling water hence higher thermal resistance.

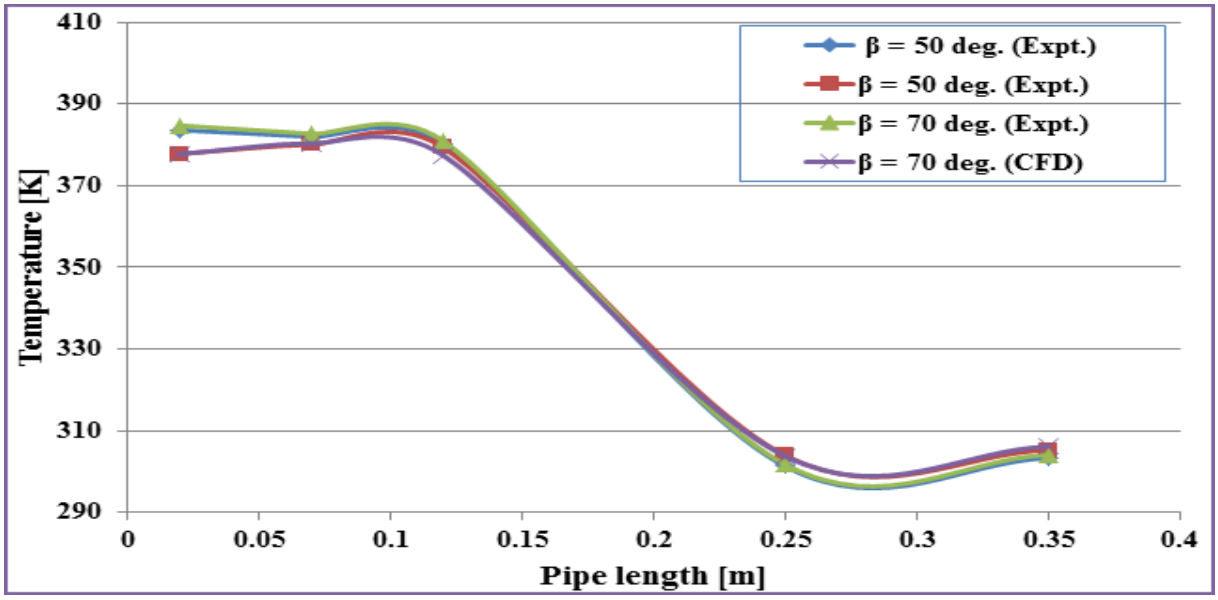

(i) Temperature profile for P = 51.7W

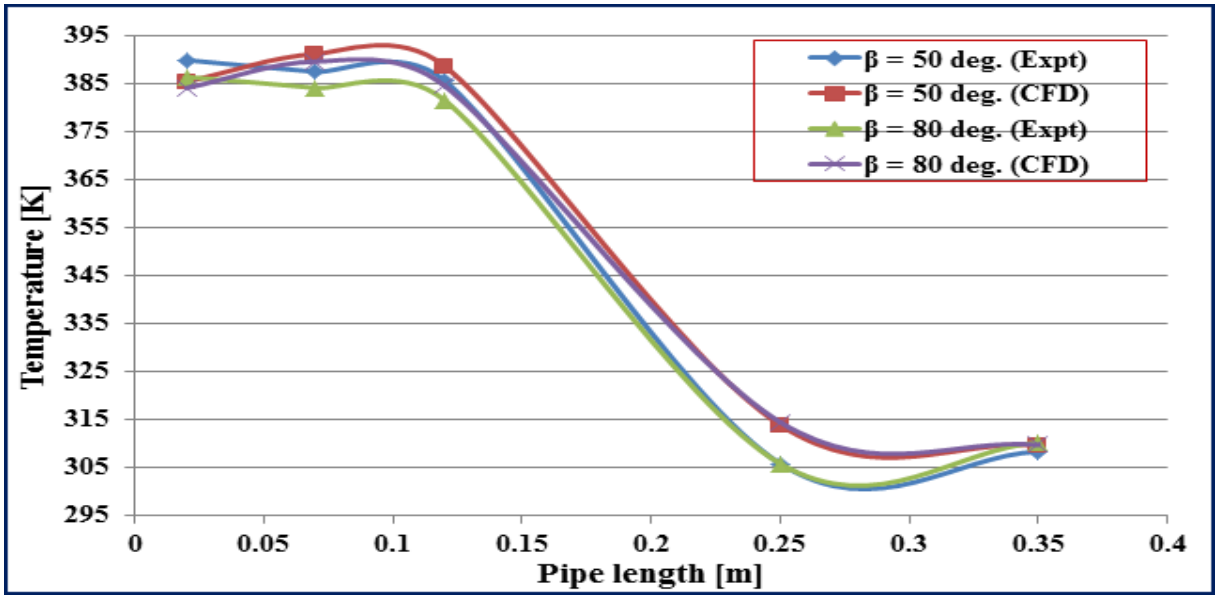

(ii) Temperature profile for P = 109.7W

Figure 6.25a Comparison of temperature distributions between experimental and CFD at different inclination angles for two different power inputs

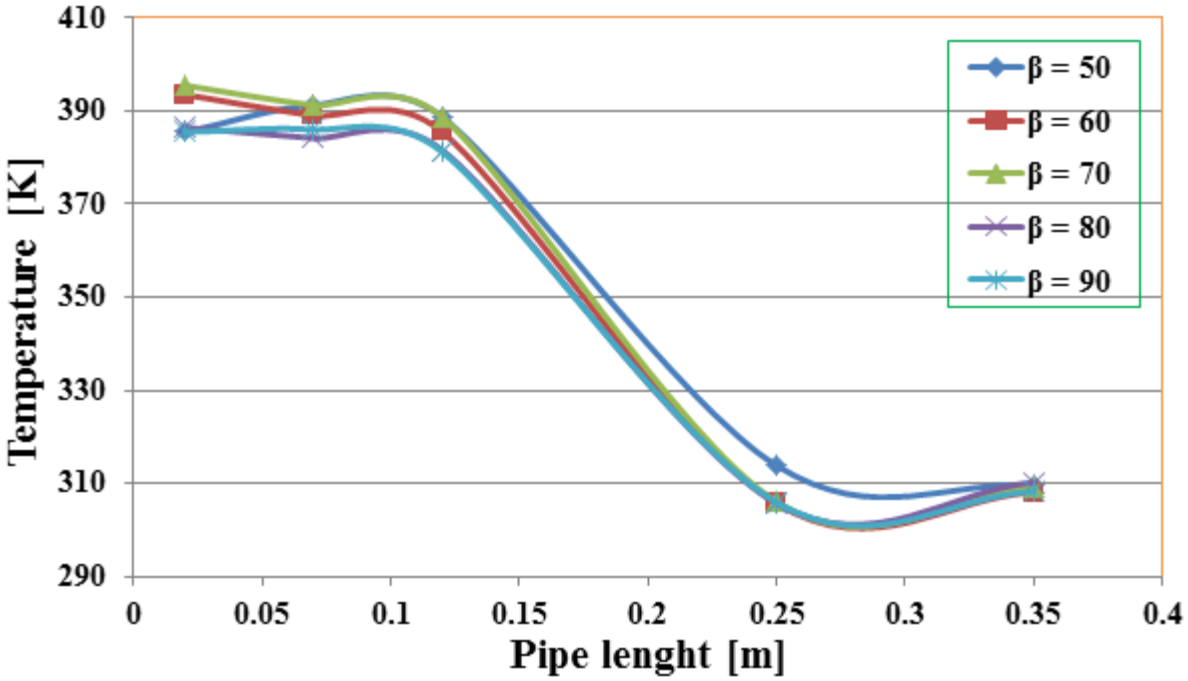

(i) Experiment

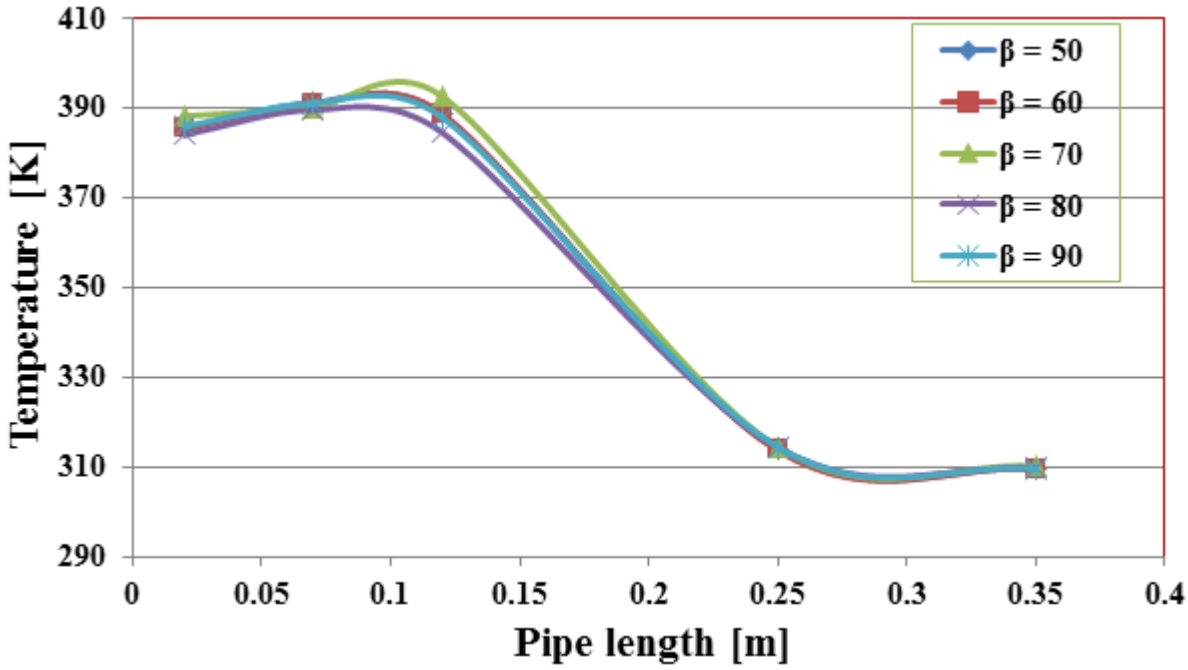

(ii) CFD

Figure 6.25b Comparison of the predicted wall temperature with the experiment at different inclination angles

Figure 6.26 compares the experimental and predicted thermal resistance at different inclination angles when the heat input is 109.7W. It can be seen from such figure that the lowest thermal resistance was obtained at the 80^{o} and 90^{o} inclination angles. Also the predicted thermal resistance at different inclination angles showed good agreement with experiment with maximum deviation of ±5.7%.

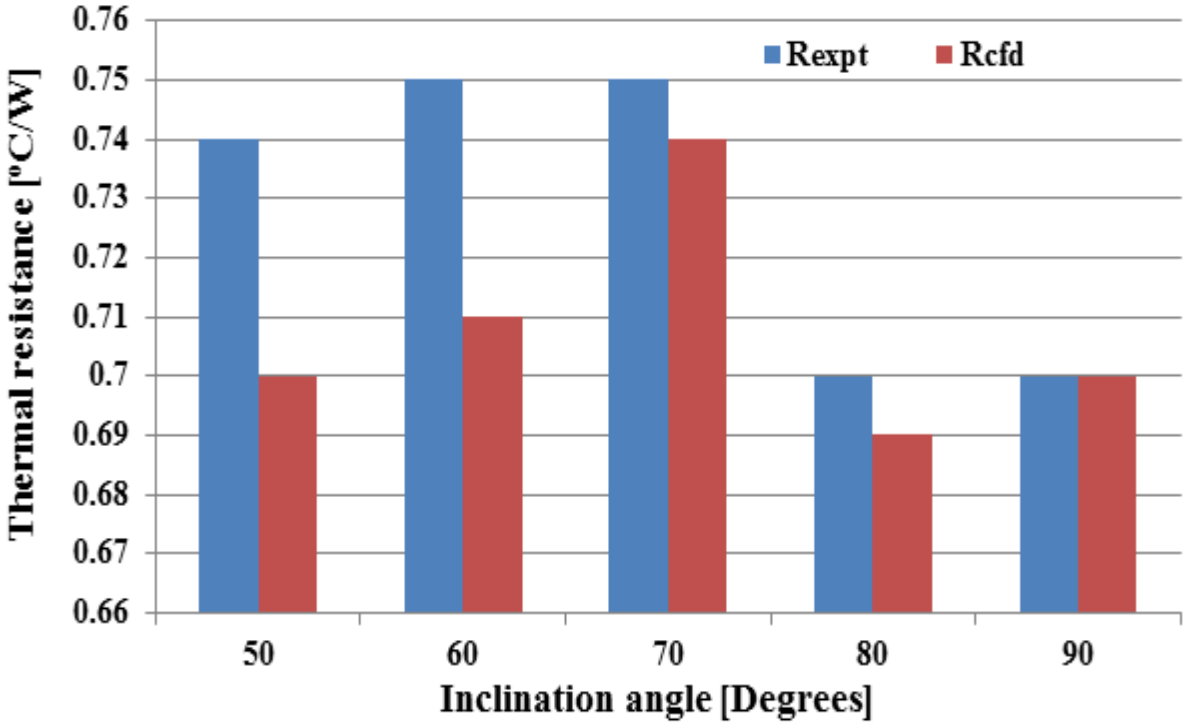

Figure 6.26 Comparison of the predicted overall thermal resistance with experimental at different inclination angles

The numerical results show good agreement with the experiment in terms of the temperature profile and thermal resistance. It can also be seen that the deviation (in terms of temperature distributions) is more on the condenser side which can be attributed to the lack of insulation causing heat losses which are not considered in the model.

6.7.4.3. Comparison of the Performance of the thermosyphon at different flow rates

In order to further validate the model, the effects of the cooling water flow rate in the condenser side was also numerically investigated and compared with the experimental results reported in section 6.5.4 (Figure 6.27). The model was set based on the conditions of the experiments described in section 6.5.4 and the effect of each flow rate was activated by defining its convective heat transfer coefficient as one of the boundary condition.

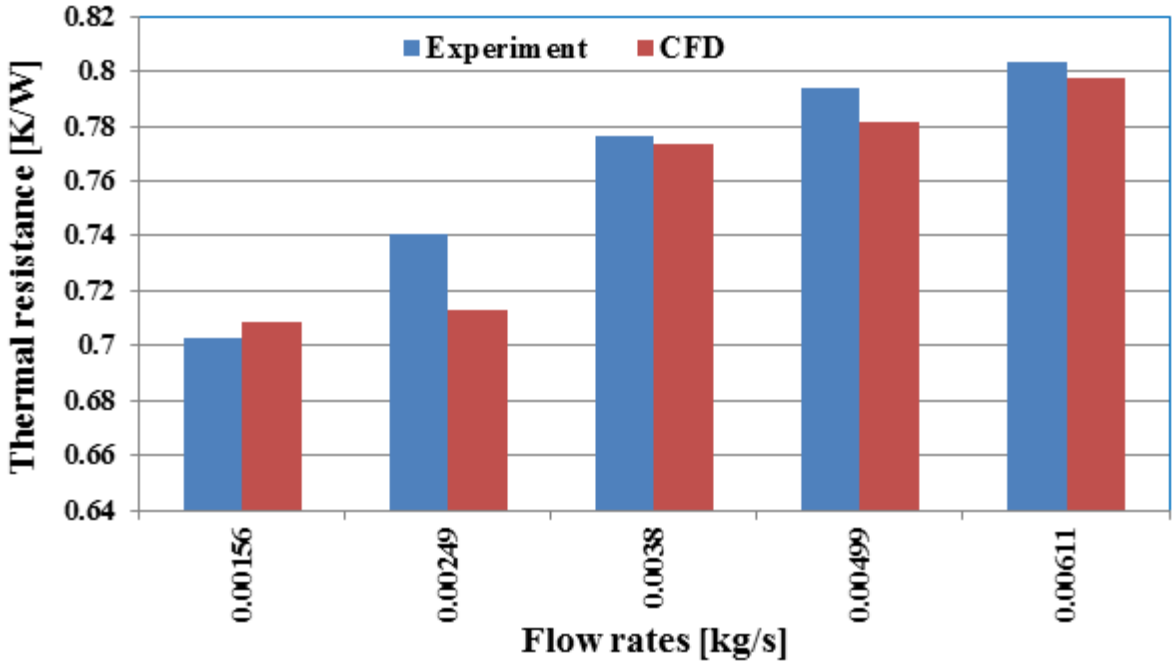

Figure 6.27 Comparison of the predicted overall thermal resistance with experimental at different flow rates

There is slight increase in the overall thermal resistance as the cooling water flow rate increases in both cases (Figure 6.27). This is due to the decrease in the condenser surface temperature as the flow rate increases. While the temperature on the evaporator section almost remains constant and this cause increase in the temperature difference between the evaporator

and condenser and subsequently increase in the thermal resistance (in accordance to the equation 6.10).

6.7.4.4. Effects of evaporator thickness on the performance of the thermosyphon

Upon validating the model, the effects of the thickness of the evaporator wall of the thermosyphon was investigated. The thickness was activated on the evaporator section only because it is the area coated with high absorbing material in real solar applications in order to maximize the energy transfer to the working fluid. Thickness from 0.9mm to 4.5mm was added to the wall boundary conditions of the evaporator in Ansys fluent to simulate the effect. The layers added are assumed to be of the same material with the pipe (copper) and the effect was evaluated based on the overall thermal resistance of the pipe (Figure 6.28).

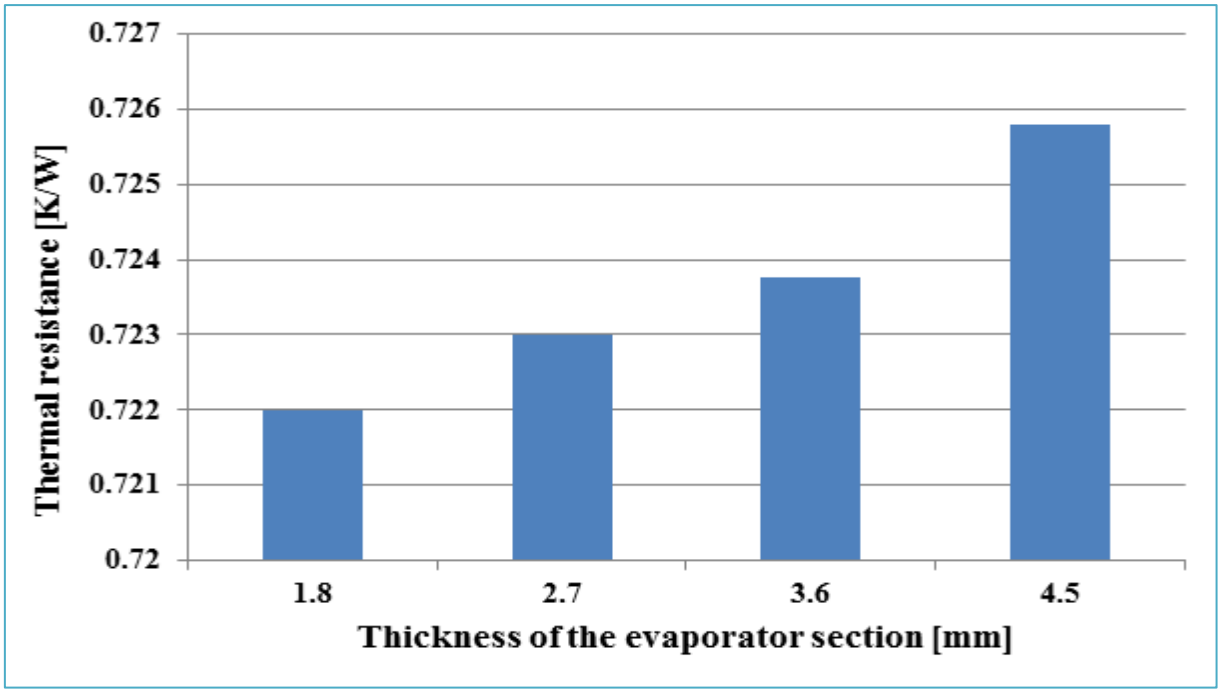

Figure 6.28 Variation of the overall thermal resistance with the evaporator thickness

There is insignificant increase in the overall thermal resistance as the thickness of the evaporator section increases as shown in Figure 6.28. This can be due to the high conductivity of the material of the pipe and due to the range investigated which is narrow.

6.8. Summary

Several parameters affect the operation of thermosyphon such as fill ratio, working fluid, inclination, geometry, heat input, cooling water flow rate, etc. Experimental and numerical (CFD) studies were carried out in this chapter that enable the investigation of the effects of some of these parameters on a 400mm long two-phase closed thermosyphon for use in CPC solar thermal collector. The fluxes and power obtained from the optical simulation in chapter five were used as inputs to the experiment and CFD model. The effects of heat input on the temperature distributions on the wall of the pipe, thermal resistance and overall performance of the pipe at vertical orientation were investigated both experimentally and by CFD. Also for the first time, the effect of inclination angle was successfully added in the fluent. Good agreement was found between the experimental and CFD in all the cases with slight deviation. Wide range of heat input, cooling water flow rates and inclination were investigated to enable reasonable conclusions to be drawn.

The outcomes of this chapter can be summarized as follows:

i. The wall temperature of the thermosyphon increases with heat inputs within the operation limit of the pipe and it tends to be uniform on the evaporator section for each heat input due to the constant temperature phase change. But there is rise of temperature at the top of the condenser due to the rise of the saturated steam to such region and the thin film layer.
ii. The overall thermal resistance decreases with increase in the heat input.

iii. The performance of the thermosyphon in terms of heat transfer to the cooling water increases with the heat input till when the pipe reaches its maximum operation limit.

iv. Increasing the flow rate of the cooling water in the condenser section increases the pipe's performance and convective heat transfer coefficient, but decreases the outlet water and condenser surface temperatures.

v. Inclining thermosyphon to an angle from the horizontal led to the performance enhancement especially at lower heat inputs. Performance enhancement (in terms of heat transfer to the cooling water) of 17.8, 13.9 and 3.4% were achieved for heat inputs of 31.8, 51.7 and 109W respectively. These findings can explain the contradictory reports found in literature on the effects on inclination angle, since this work investigated wide range of angles (10 to 90^{o}) coupled with validated numerical approach (CFD).

vi. VOF model approach in Ansys together with UDF can fully simulate the complex evaporation and condensation processes taking place in thermosyphon for both vertical and inclined orientations.

CHAPTER SEVEN

7. Thermal performance of HPCPC and proposed applications

7.1. Introduction

This chapter presents the experimental thermal performance of the HPCPC developed and optically characterized in chapter five. The HPCPC utilized the thermosyphon heat pipe characterized experimentally and numerically in chapter six, as receiver. It also presents the experimental study of the performance of the HPCPC at different inclination angles of the thermosyphon heat pipe. The thermal performance of the novel double receiver HPCPC is also presented. All the investigations were carried out using the solar simulator developed in chapter four. The chapter also presents the numerical performance predictions of array of HPCPC for possible applications in cooling systems under the weather conditions of Kano using a validated model in Ansys fluent.

7.2. Thermal performance of HPCPC

7.2.1. Experimental test – up

Figures 7.1 and 7.2 show respectively a schematic diagram and photograph of the experimental test facility used for optical and thermal tests. It consists of the two HPCPCs developed in chapter five, 400mm long thermosyphon heat pipe characterized in chapter six, radiant flux sensor, angular adjustment frame, DT85 data taker and other instrumentations

which were discussed in chapter five. It also has the cooling water circulating system used to extract the heat from the condenser section of the thermosyphon heat pipe. Surface thermocouples were installed on the tubes and two probe thermocouples were installed at the inlet and outlet of the cooling water to measure the temperatures on the tube surface and the cooling water. The flow rate of the water is controlled by a valve and measured by a flow meter. The calibration, measurement accuracy and uncertainty propagation of the flow meter, surface and probe thermocouples, TLC protractor and programmable DC power supply were discussed in chapter 6.

The source of the light is the continuous solar simulator designed for testing the HPCPC in this thesis and discussed in chapter 4.

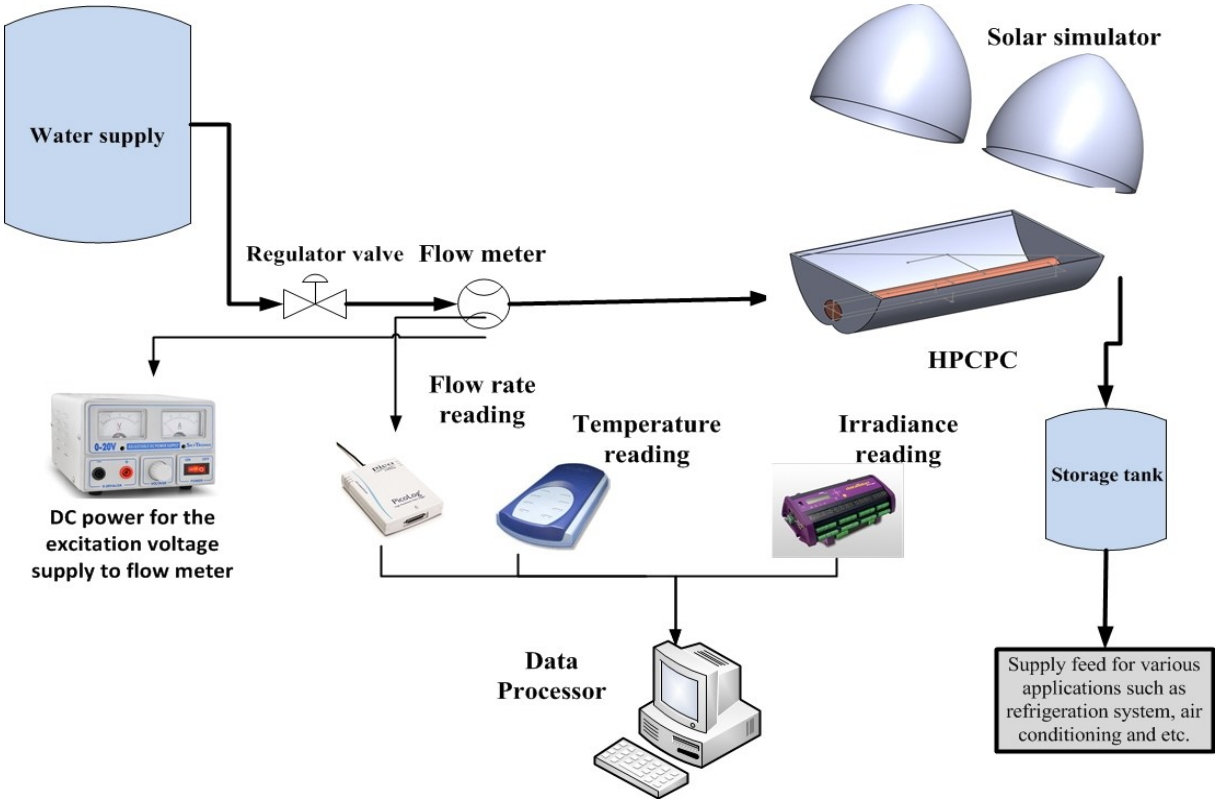

Figure 7.1 Shematic diagram of the test rig for the optical and thermal performance of HPCPC

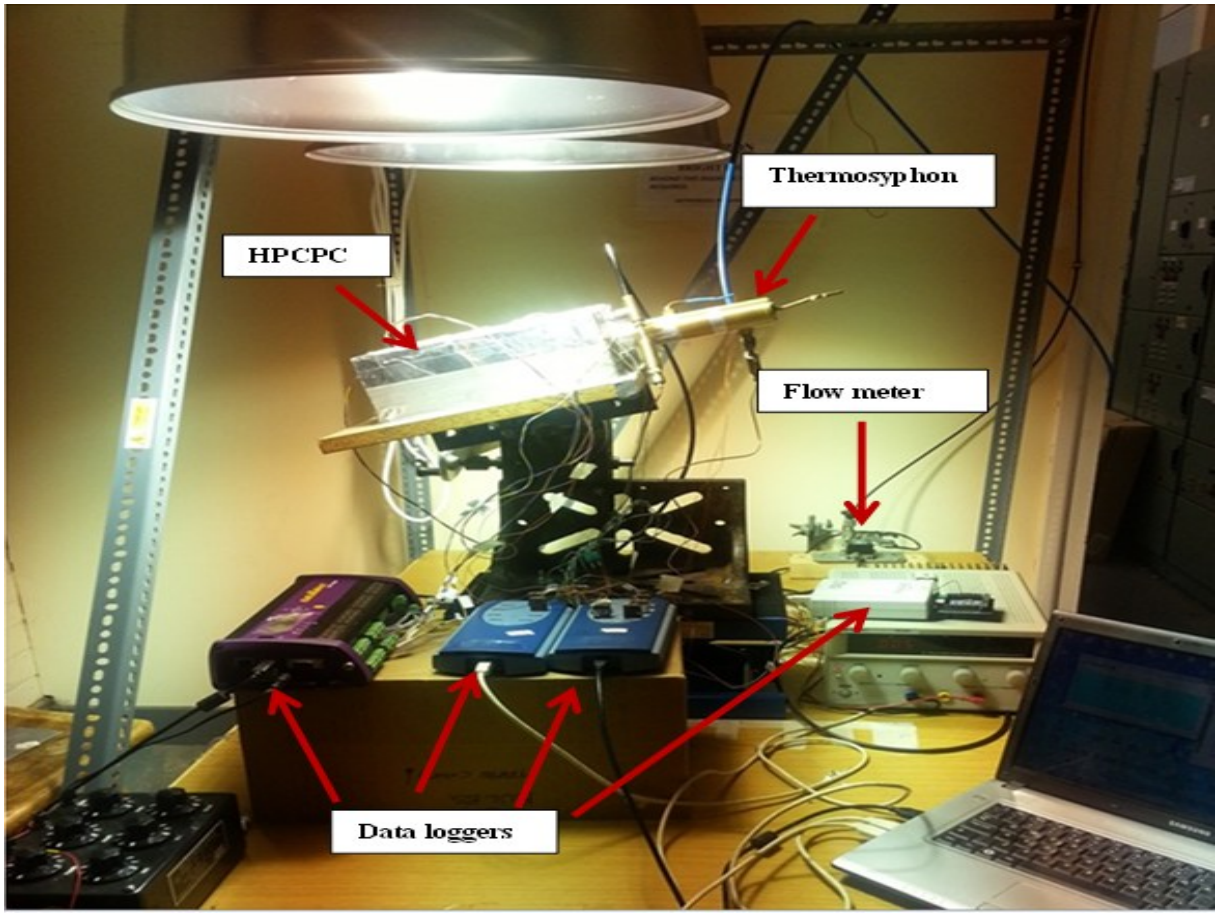

Figure 7.2 Photograph of the experiment on the effects of inclination angle of thermosyphon

7.2.1.1. Experimental procedure

The solar simulator is switched on and allowed to stabilize for one hour and the incoming irradiance was measured by using the radiant flux sensors by mapping the aperture area while the received irradiance was measured on four sides of the tube.

The performance of two HPCPCs; with reflectivity of 60% (HPCPCR60) and 80% (HPCPCR80) developed in chapter five was investigated. Cooling water was circulated at average flow rate of 0.0018 kg/s through the water jacket to remove heat from the condenser section. Reading of the water flow rate, irradiance, ambient, surface, inlet and outlet

temperature were recorded for each run (Figure 7.2). The experiments were repeated to proof repeatability of the measurements.

The test was conducted at different irradiance levels by adjusting the distance between the HPCPC and the solar simulator and at thermosyphon inclination angles of 0, 10, 20, 30, 40 and 50^{o} from the horizontal by using the angular adjustment frame and the average. The average ambient temperature during the test was 19.5^{o}C. The rate of heat transfer to the cooling water was calculated was calculated using equation 6.12. Figures 7.3 shows the received power on the tube and rate of heat transfer to the cooling water at different pipe inclination angles for average irradiance of 2457.72W/m^{2} using HPCPCR60 with the solar simulator perpendicular to the collector. It can be seen that the power concentrated on the thermosyphon increases with the inclination up to 30^{o} compared to the 0^{o}.

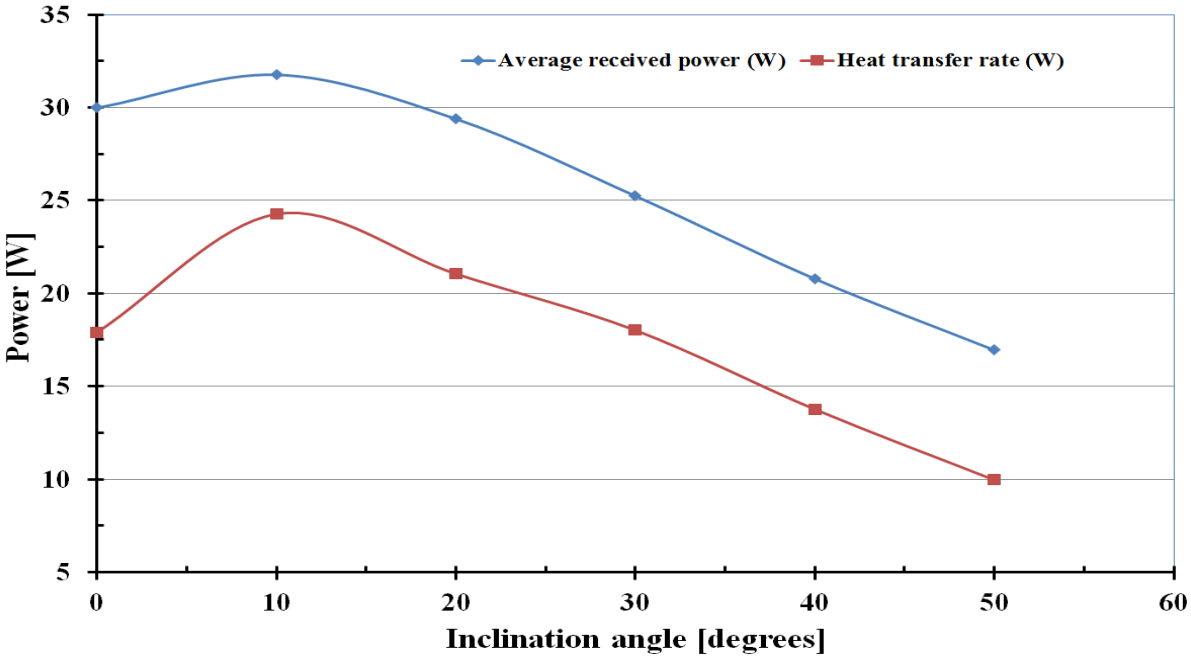

Figure 7.3 Power received by the thermosyphon and heat transferred to the cooling water at different inclination angles

The thermal efficiency of the thermosyphon fitted into the HPCPC was calculated as the ratio of the heat transferred to the cooling water to the power received on the tube. Using the power in Figure 7.3, the thermal efficiency of the thermosyphon is determined at different inclination angle of the pipe fitted into the HPCPC as shown in Figure 7.4. It can be seen from such figure that the HPCPC can function well with inclination angle up to 40^{o} where it gives maximum efficiency at 10^{o} of 76% and for angles between 20 – 30^{o} of 72% and at 45^{o} it has 66% which is higher than that at zero degrees angle (60%).

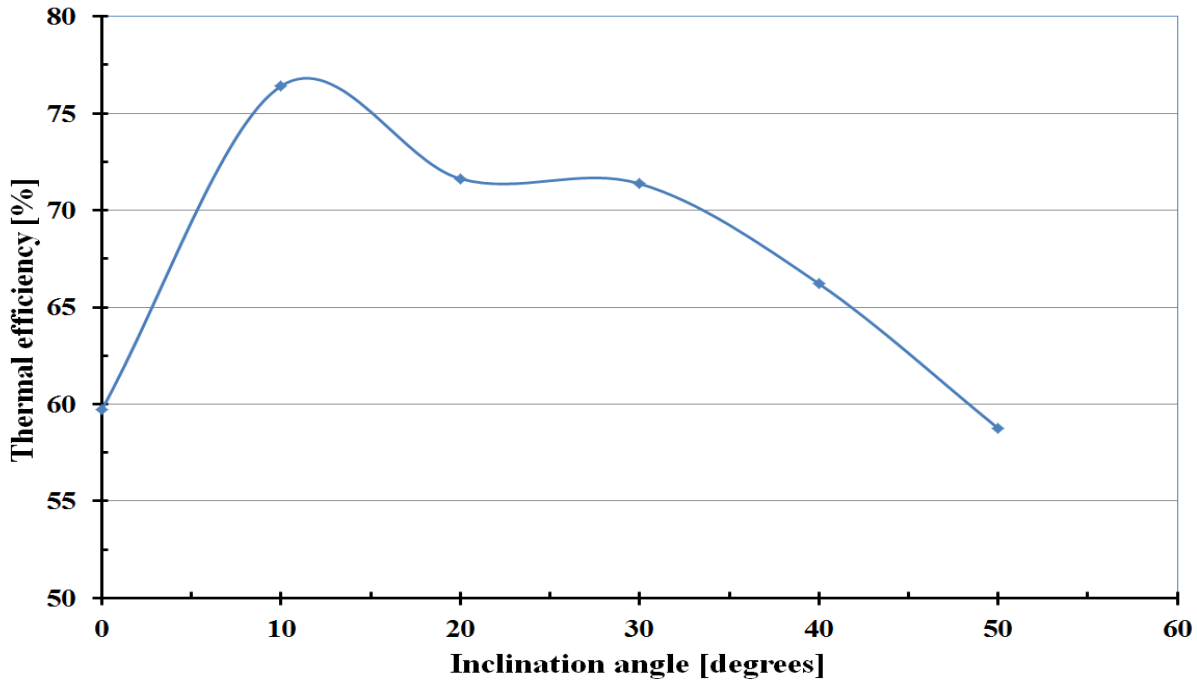

Figure 7.4 Variation of thermal efficiency of the thermosyphon fitted in the HPCPCR60

Experiment was run using the HPCPCR60 and HPCPCR80 to find the effects of the reflectivity of the concentrator. The test was run at irradiance of 1067.71 W/m^2 and the rate of heat transfer to the cooling water at different inclination of the thermosyphon was calculated for the two collectors using equation 6.12 and is presented in Figure 7.5. It can be seen from the figure that maximum improvement of up to 27% in heat transfer is achieved with HPCPCR80 compared to HPCPC60.

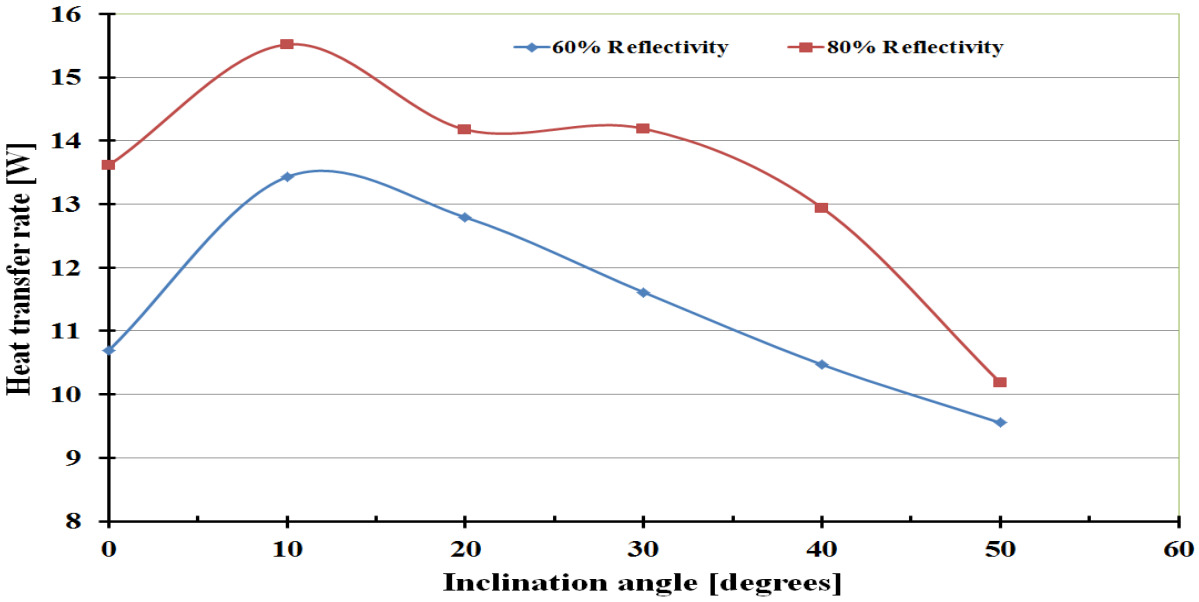

Figure 7.5 Variation of heat transfer rate with the inclination angles of the thermosyphon

Figures 7.6 and 7.7 show the comparison of the percentage change in the heat transfer rate between horizontal (0^o) and inclined orientation at irradiance level of 1067.71 W/m^2. It can be deduced from these figures that 10^o gave maximum heat transfer rate for both collectors.

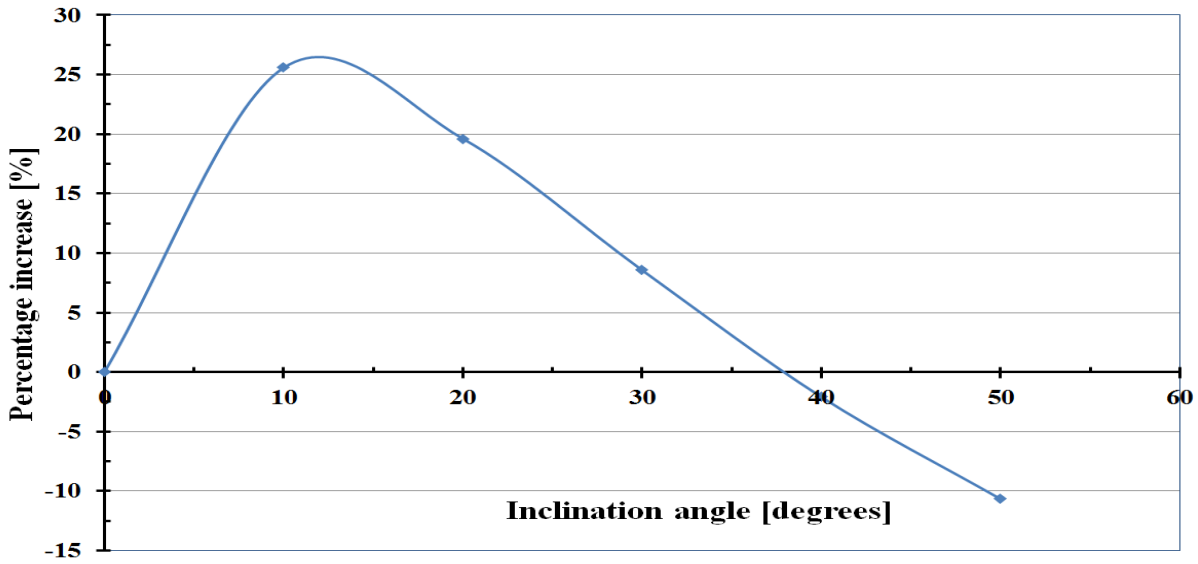

Figure 7.6 Comparison between the heat transfer rates at different inclination angles with horizontal orientation (60% reflectivity)

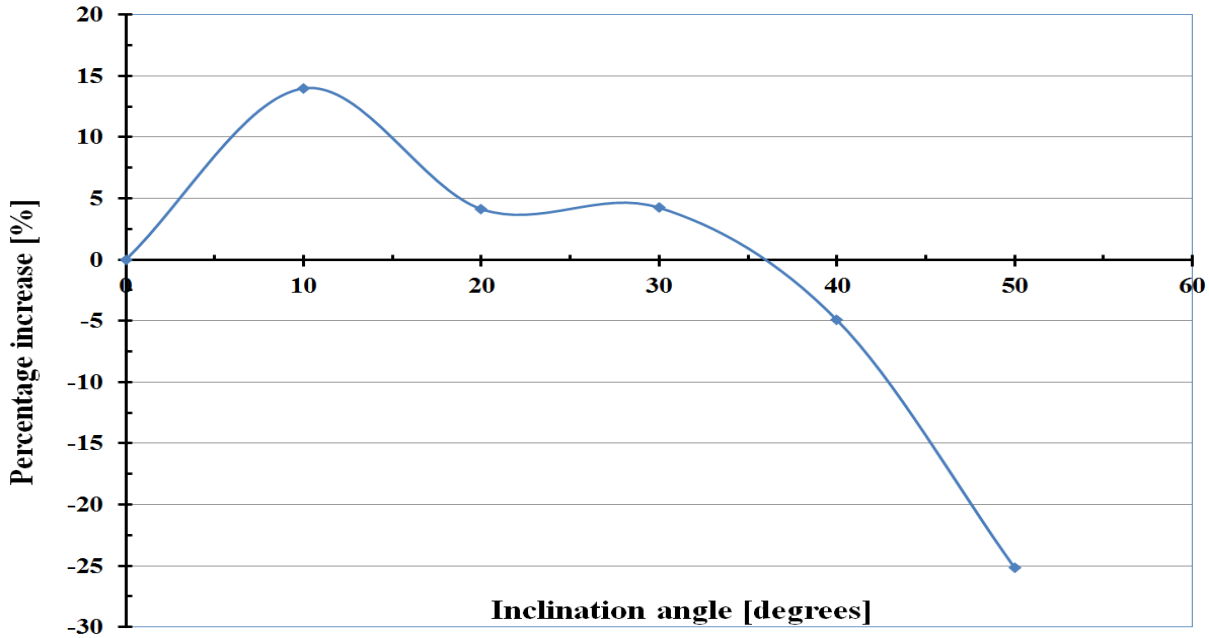

Figure 7.7 Comparison between the heat transfer rates at different inclination angle with horizontal orientation (80% reflectivity)

The performance of the HPCPCR80 was tested at different cooling water flow rate. Figure 7.8 shows that the rate of heat transfer increases with the increase in the cooling water flow rate.

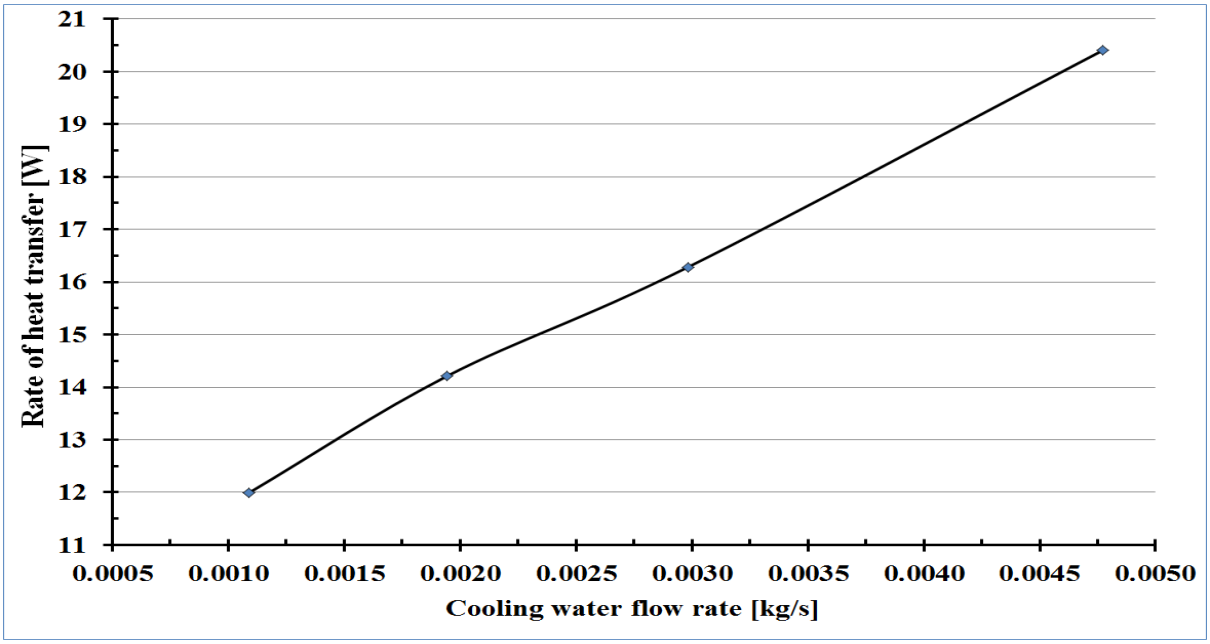

Figure 7.8 Variation of the rate of heat transfer with the cooling water flow rates at 1067.71 W/m^2 and 30^o inclination.

7.3. Thermal performance of double receiver HPCPC

In section 5.4 of chapter 5, the potential of using two receivers in one concentrator was investigated using optical simulations. To further support this novel idea, a study was conducted using the thermosyphon heat pipe characterized experimentally in chapter 6. The study is aimed at comparing the rate of heat transfer to the cooling water by the single and double tube configurations. The power obtained from optical simulation in section 5.4.2.6 for single tube and sum of the power from double tube (Figure 5.32a) were used as input in the heat transfer characterization of thermosyphon test rig in chapter 6 (Figure 6.2 and 6.3). Figure 7.9 compares the rate of heat transfer of the double pipe collector with that of the single pipe collector. It can be seen that the double pipe aligned horizontally outperformed single tube by 21, 19.8 and 17.4% in terms of rate of heat transfer to the cooling water for HPCPC30, HPCPC40 and HPCPC60 respectively for seven hours operations in a day. While for nine hours operations, the percentage increase is 16.7, 18 and 18.3% for HPCPC30, HPCPC40 and HPCPC60 respectively. These results highlight the potential of using more than one tubular receiver in one concentrator

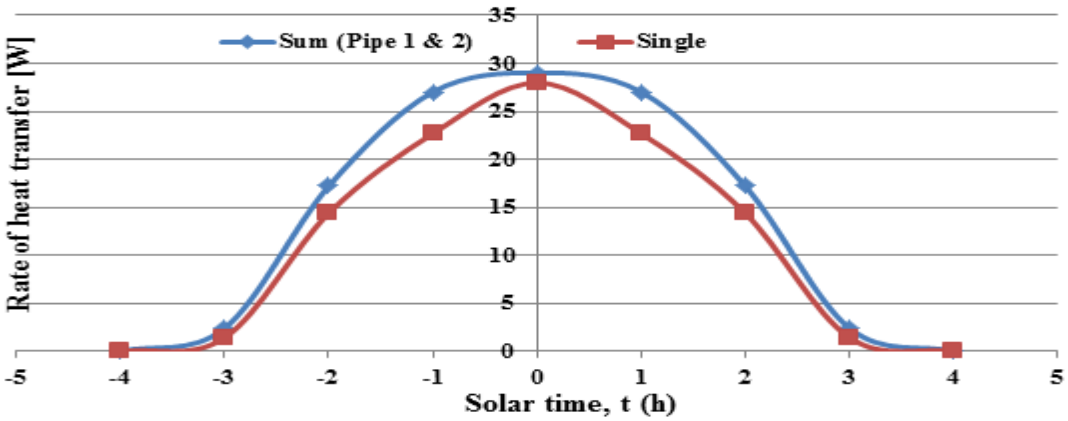

(a) HPCPC30

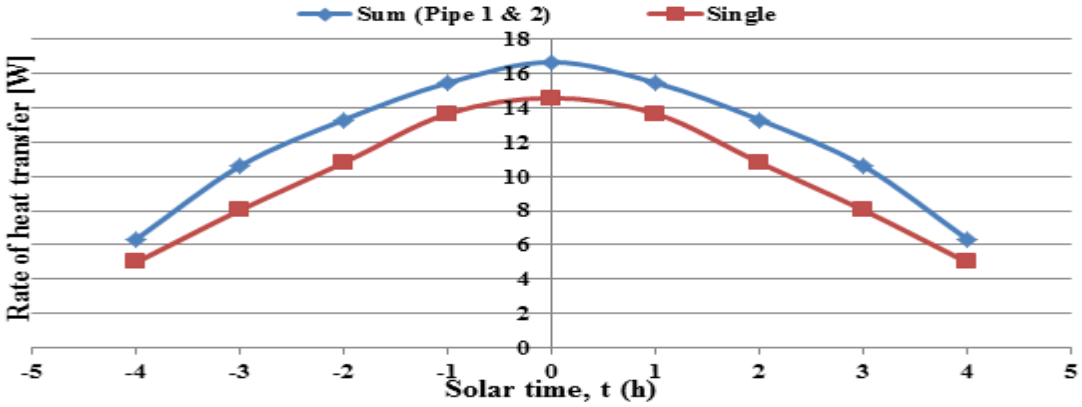

(b) HPCPC40

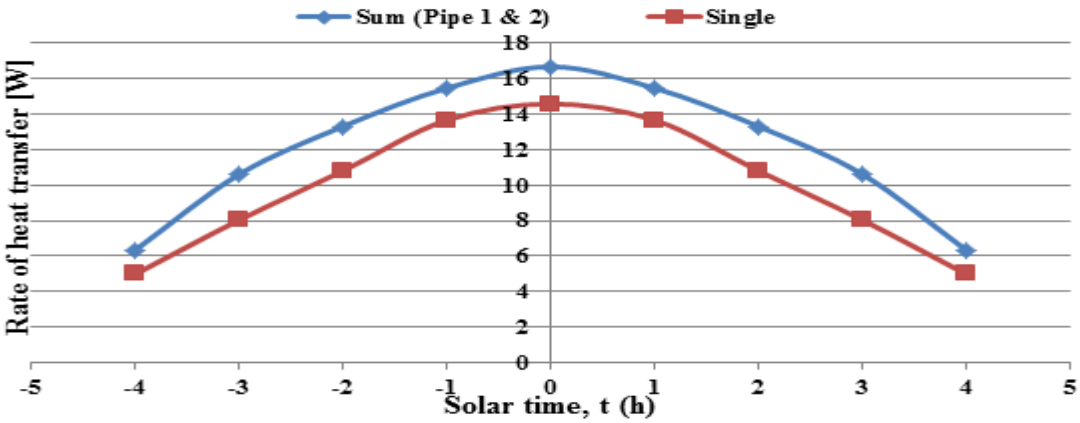

(c) HPCPC60

Figure 7.9 Comparison of experimental heat transfer rate between single and double receiver configurations of HPCPC

7.4. HPCPC for applications in solar cooling system for Kano

In the introduction chapter, the energy issues in Nigeria in general and Kano state in particular were discussed. The radiation modelling of Kano in chapter three has shown that the region has great potential for solar radiation throughout the year. The studies conducted on the major parameters that affect the performance of CPC solar collectors (i.e. solar radiation available, design and orientation) and the optimization carried out, have led to design and performance prediction of solar cooling system for Kano.

Based on the studies carried out in previous chapters, two different configurations of HPCPCs with the best collector gap, truncation, length, and orientation were simulated for powering cooling systems in Kano. The approach includes optical and thermal simulations of array of HPCPCs to predict their performance in terms of outlet temperature and power generation.

7.4.1. Validation of the approach

The thermal modelling to be employed in this design will first be validated while the optical simulation procedure has been validated in sections 5.3.1. The condenser section of the thermal experiments in section 7.2 was modelled in Ansys fluent to simulate the heat transfer to the cooling water as shown in Figure 7.10. A steady state single phase model was set up with mass flow rate inlet and pressure outlet. The model was solved using coupled solver and second order spatial discretization for pressure, momentum and energy.

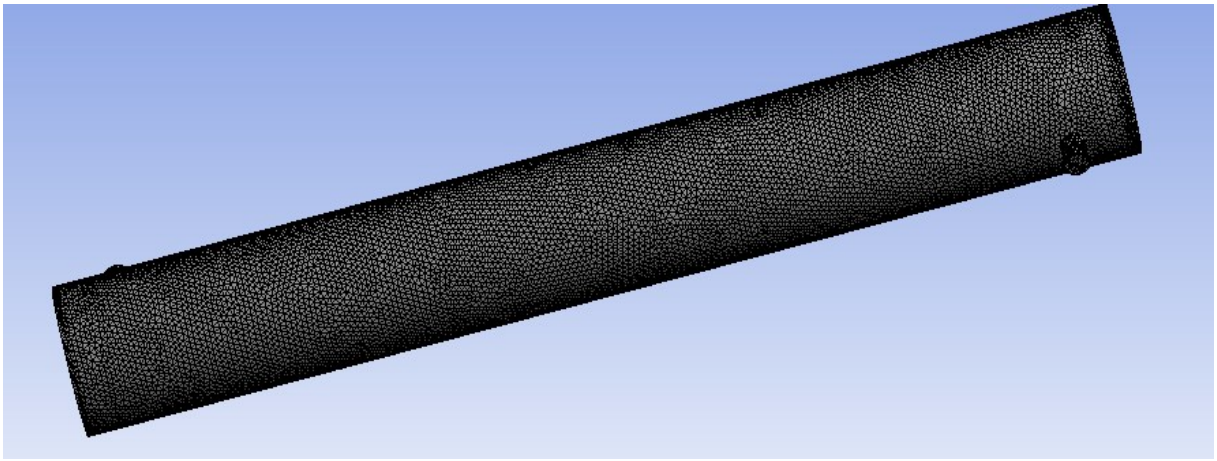

Figure 7.10 Condenser section with cooling water jacket

Two different heat fluxes (878.8 and 1383.56 W/m^2) from section 7.2 were applied to the condenser surface assuming the effectiveness of this thermosyphon as 90% (section 6.5.1). The properties of water such as density, thermal conductivity, viscosity and specific heat were all defined based on the temperature range. Using the mass flow rates and inlet water temperature from the experiment, the model was run till convergence and the simulation results was compared with the experimental results and were in good agreement within ±5% (Figure 7.11). Figure 7.11 shows the water temperature difference between inlet and outlet for the two heat fluxes and Figure 7.12 (a and b) shows the temperature contours of the cooling water for the two cases. It can be seen from this figure that the water temperature increases as it flows over the hot surface of the condenser. Also the density of the water decreases as it gets heated from inlet to the outlet as shown in Figure 7.13. Upon validation, this modelling approach is to be used in the thermal performance prediction of an array of HPCPC in the next section.

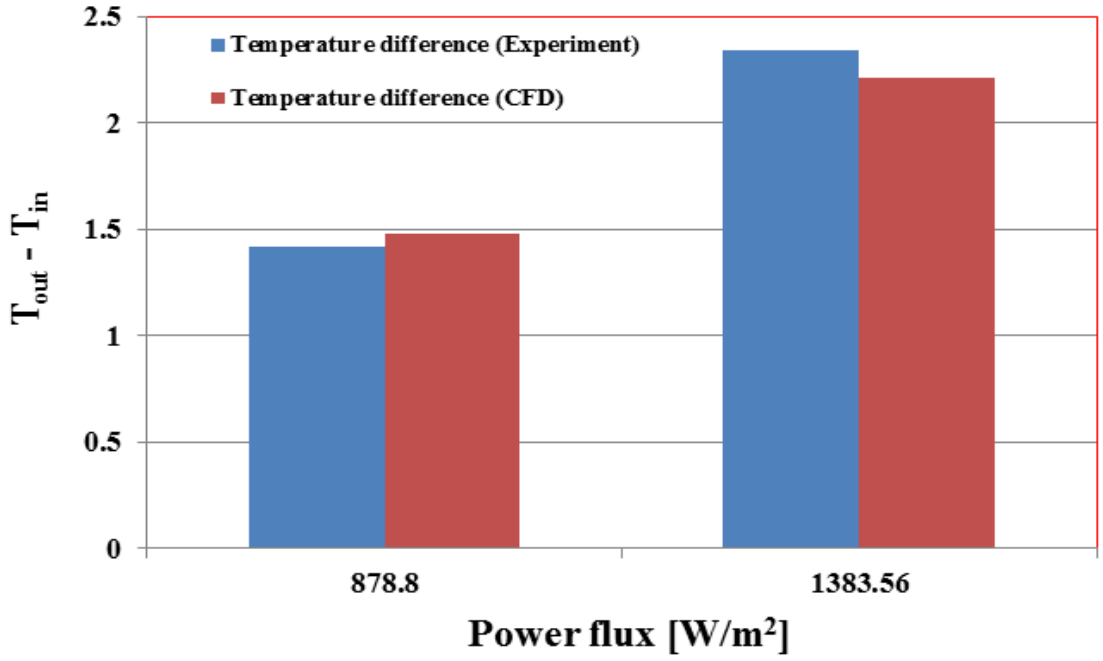

Figure 7.11 Comparison between Experimental and CFD results

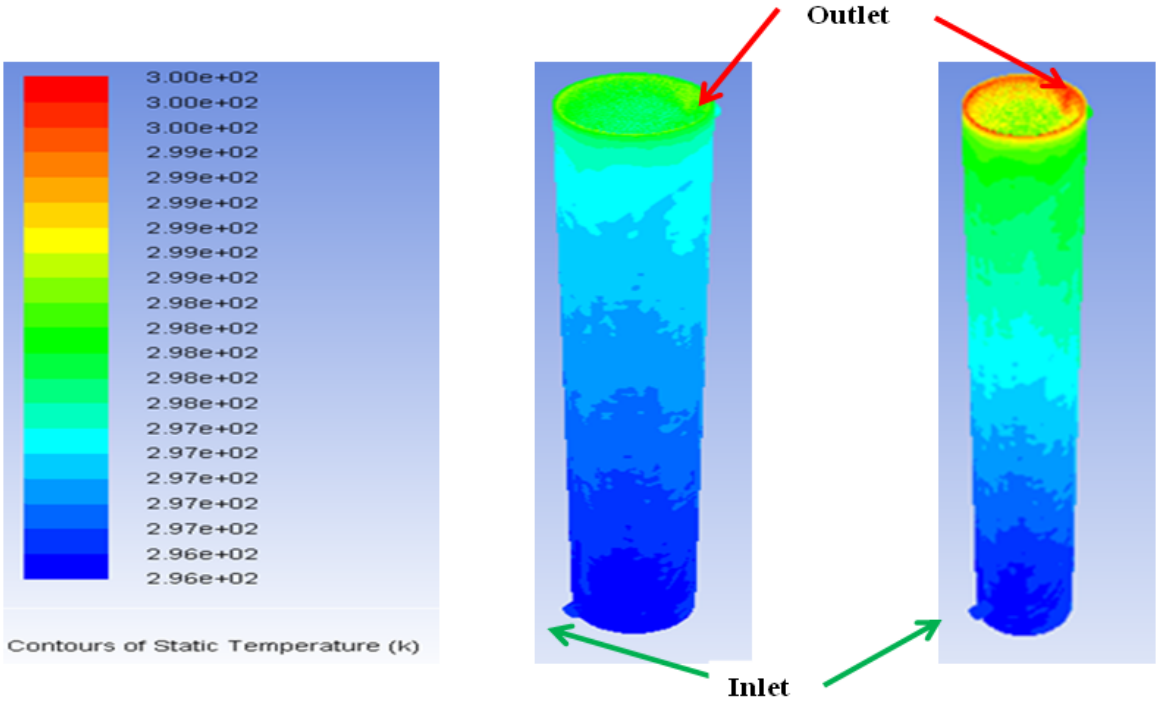

Figure 7.12 Temperature contours of the cooling water

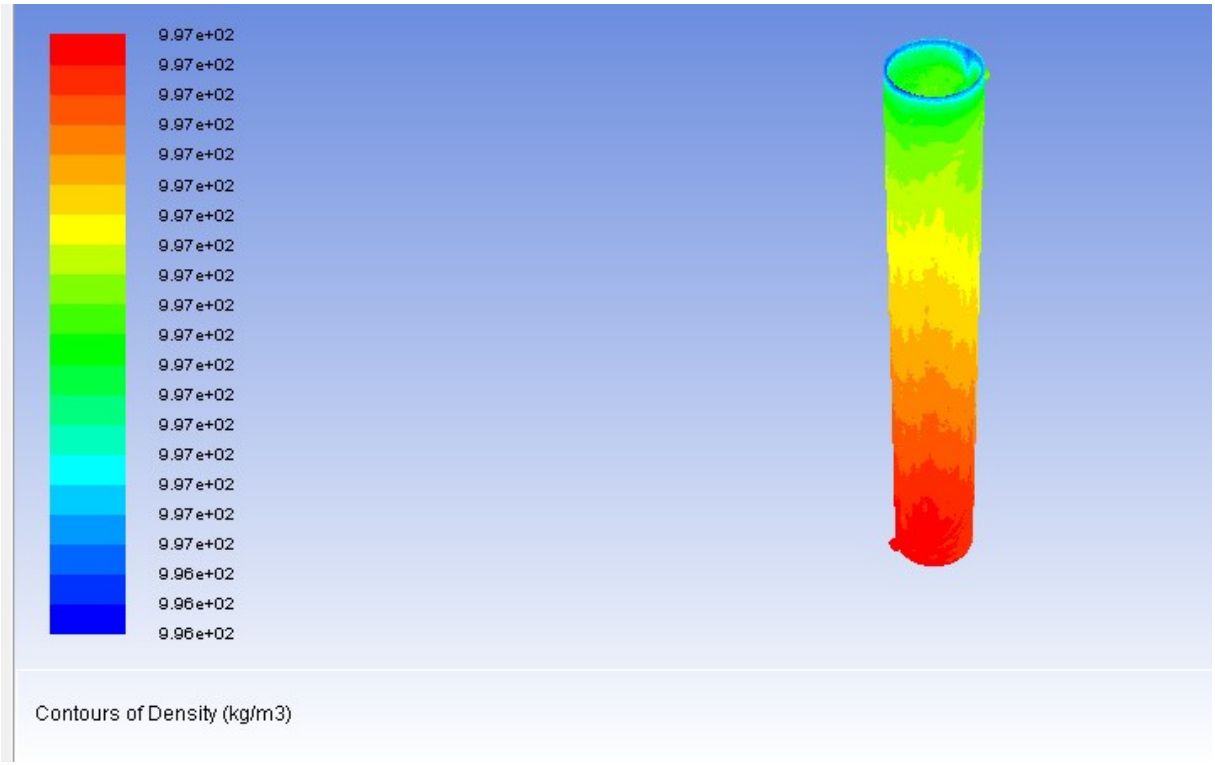

Figure 7.13 Variation of the density of the water from inlet to outlet

7.4.2. Performance of array of HPCPC

Two different configurations of HPCPC (HPCPC60R12.5 and HPCPC30R12.5) were selected based on the studies presented in chapter 5 that showed their best truncation levels (see Figure 5.29), hence are truncated by 62 and 43% respectively. Their geometric characterization at such truncation levels are shown in Table 7.1 and will be referred to as HPCPC60R12.5BT and HPCPC30R12.5BT, where BT stands for best truncation level.

Table 7.1 Geometric parameters of the selected HPCPCs

S/N	Parameters	HPCPC60R12.5BT		HPCPC30R12.5BT	
		Full	Truncated	Full	Truncated
1	Truncation level (%)	0	62	0	43
2	Acceptance angle (^{o})	60	72	30	32
3	Collector height (mm)	180.67	68.65	634.17	361.48
4	Aperture width (mm)	157.08	131.60	303.45	283.88
5	Concentration ratio	2	1.7	3.86	3.63
6	Collector length	-	500	-	500

7.4.2.1. Performance of a single HPCPC

The optical and thermal performance of a single HPCPC was first simulated so that the number of tubes required for a certain application can be estimated. The irradiance was obtained from optical simulation using irradiance of March at optimum angle from chapter three. Weather conditions of Kano such as ambient temperature, water inlet temperature, etc. were applied in the simulation according to the setup in section 7.4.1. March was selected because of the following:

i. It is among the hottest months as shown in Figure 7.14.
ii. The intended application is cooling
iii. It has the highest irradiance on horizontal surface

Figure 7.14 shows the daily ambient average temperature of Kano from 1971 to 2008, as obtained from Nigerian Meteorological Agency [140] where the average ambient temperature of 2008 (For March = 37^{o}C) was used with deviation of ± 5% from the average of the 37 years. The data of 2008 was chosen to be consistent with the radiation data used in chapter three. The water jacket dimensions for the single tube were calculated for 25 mm tube based on the dimensions of the water jacket used in the existing experimental test rig (Figure 6.4) and are shown in Table 7.2.

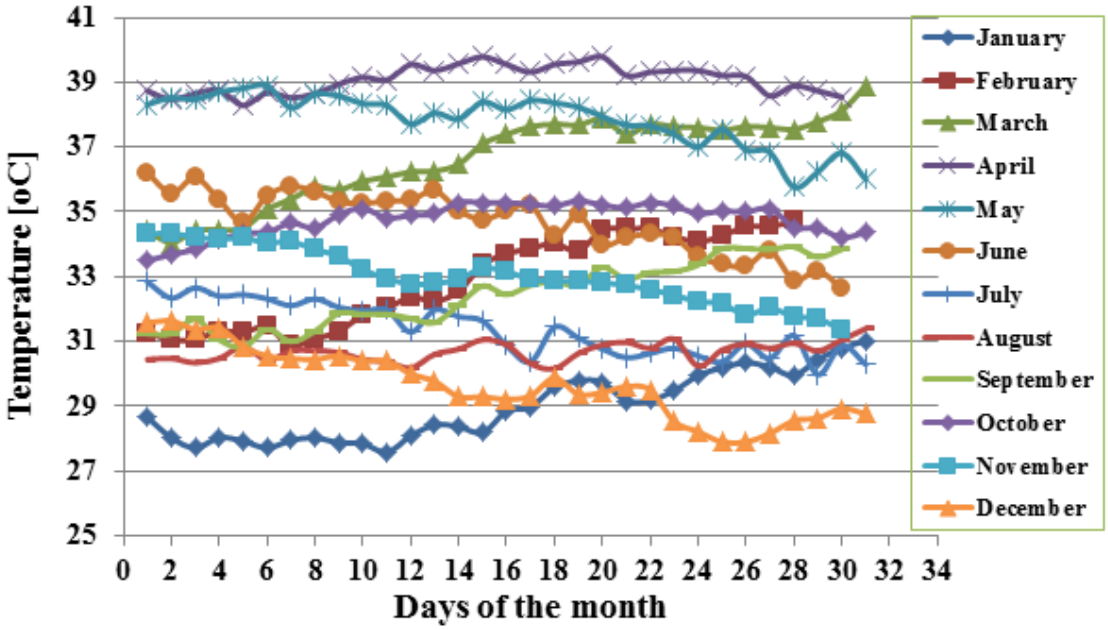

Figure 7.14 Daily average ambient temperature of Kano, Nigeria

Table 7.2 Dimensions of water jacket for single tube

S/N	Description	Dimension (mm)
1	Condenser tube diameter	25
2	Length of the condenser	200
3	Outer diameter of the Jacket	31
4	Inlet and Outlet diameter	8

The heat flux applied on the condenser was obtained from the optical simulation using the HPCPC60R12.5BT whose parameters are shown in Table 7.1. Convection heat transfer coefficient of 20W/(m^2K) [182], free steam temperature of 310K and water inlet temperature was 298K were used in the model.

Using the flow rate of 0.0018 kg/s (section 7.2) and irradiance at noon of March (1094 W/m^2) applied to the tube, the performance was evaluated based on the water outlet temperature and rate of heat transfer to the cooling water. Figure 7.15 shows the temperature gradient of the cooling water. Outlet temperature and rate of heat transfer of 306.32K (i.e. ΔT =8.32) and 62.73W were obtained respectively. This shows that more energy and higher outlet water temperature can be obtained if arrays of 10 tubes are used.

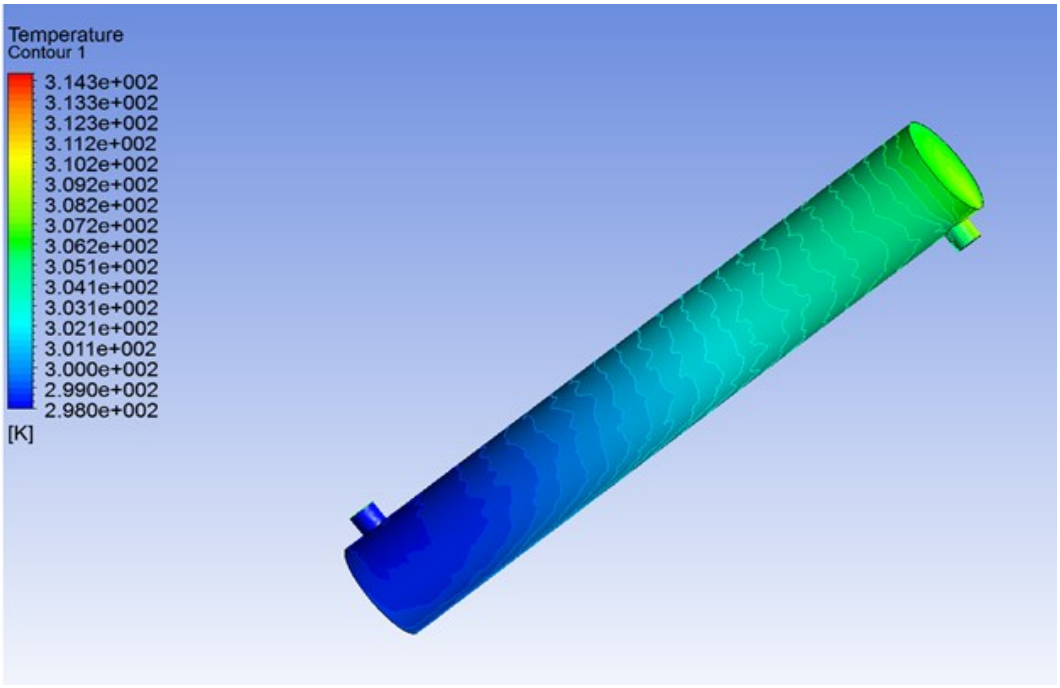

Figure 7.15 Temperature profile of the cooling water

7.4.2.2. Optical and thermal performance of array of 10 tubes

Based on the simulation results in 7.4.2.1, the optical performance of HPCPC60R12.5BT and HPCPC30R12.5BT collector consisting of array of 10 tubes was simulated under climatic condition of Kano for the month of March. Irradiance at different solar hour angles were determined and used as inputs in Ansys fluent to find the thermal output. Some of the geometric characteristics and dimensions of the array were shown in Tables 7.1 and 7.2. Based on such dimensions, the array of 10 tubes gives collector areas of 0.692 and 1.47m^2 for HPCPC60R12.5BT and HPCPC30R12.5BT respectively. Figure 7.16 shows the HPCPC60R12.5BT configuration with water manifold.

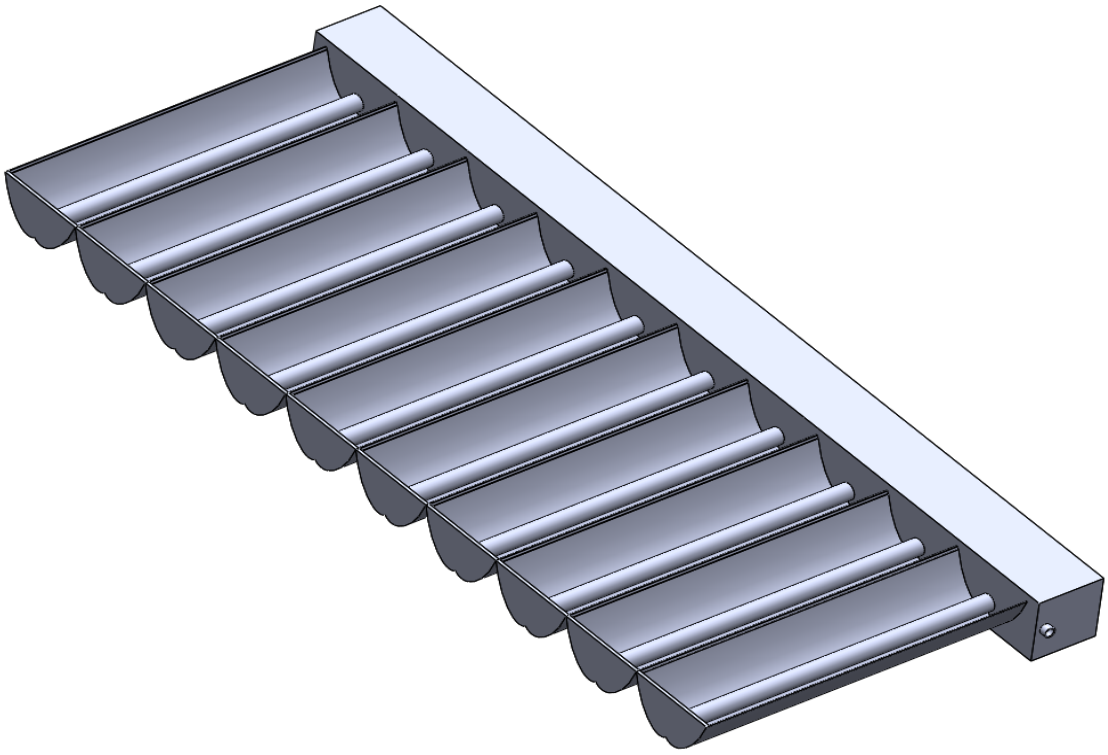

Figure 7.16 A complete HPCPC60R12.5BT with ten tubes and water manifold

Table 7.3 shows the boundary conditions and material properties applied in optical and thermal simulation of the array of 10 tubes. The optical simulation was set based on the

validated procedure shown in Figure 5.12 using the irradiance of March as input. Figure 7.17 and 7.18 show rays falling on the two collectors simulated at solar hour angle of 30^{o}.

Table 7.3 Boundary conditions and material properties for the optical and thermal simulation

S/N	Parameter	Values
1	Reflectivity of the concentrator	0.95
2	Receiver absorptivity	0.98
3	Inlet water temperature (K)	298
4	Irradiance (W/m^2)	March from chapter 3
5	Cooling water flow rate (kg/s)	0.0056

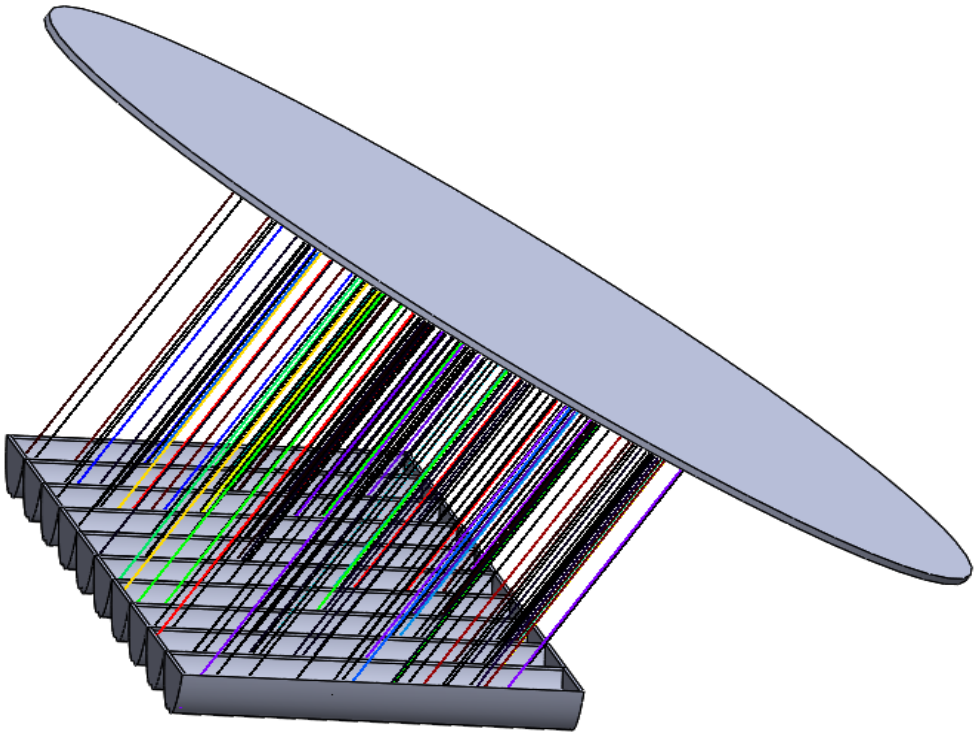

Figure 7.17 Incident rays falling on the HPCPC60R12.5BT at 30^{o} solar hour angle

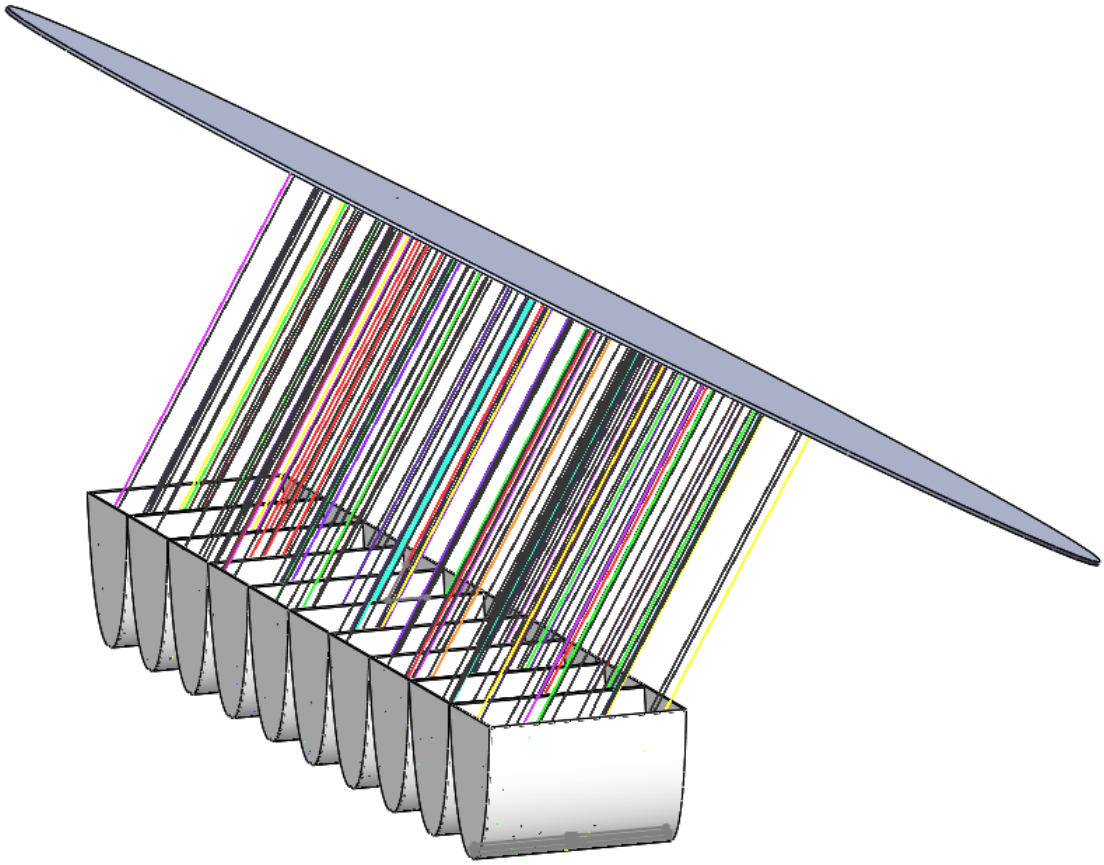

Figure 7.18 Incident rays falling on the HPCPC30R12.5BT at 30^{o} solar hour angle

The incoming power at the evaporator and the received power at the condenser section of the thermosyphon heat pipe at different solar hour angles for the two collectors are shown in Figures 7.19 and 7.20. These powers were used as input in the Ansys fluent to obtain the outlet temperature of the cooling water and the heat generated. It can be seen from these figures that the HPCPC30R12.5BT produces higher power than HPCP60R12.5BT at all solar times due to its higher concentration ratio and the wider collection area than its counterpart.

The thermal simulation model for the array of 10 tubes was set as explained in section 7.4.1 and 7.4.2.1 and the outlet temperature and the heat generated were obtained at different solar times for the two collectors as shown in Figures 7.21 and 7.22.

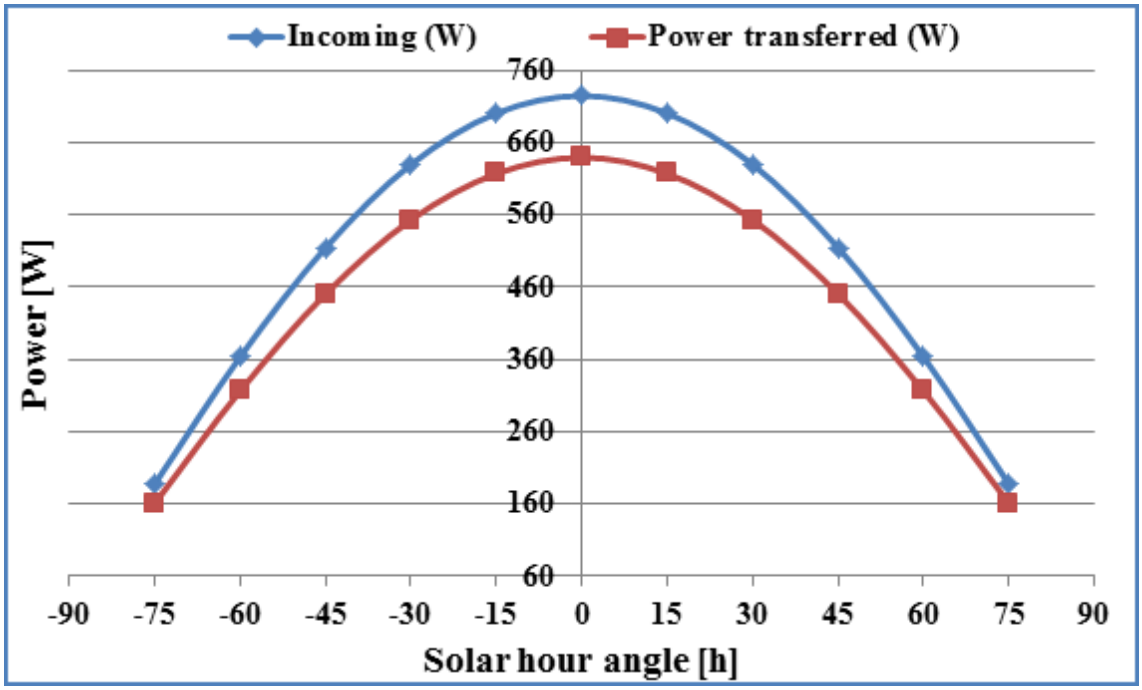

Figure 7.19 Incoming and total power transferred to the condenser section of array of 10 tubes (HPCPC60R12.5BT)

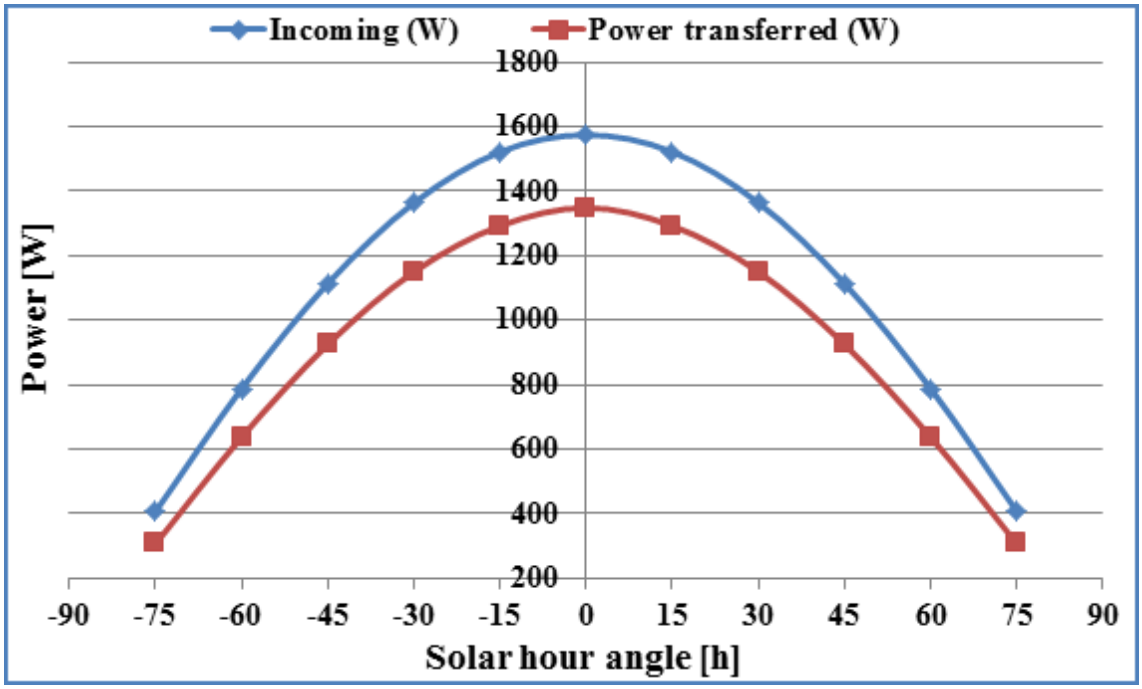

Figure 7.20 Incoming and total power transferred to the condenser section of array of 10 tubes (HPCPC30R12.5BT)

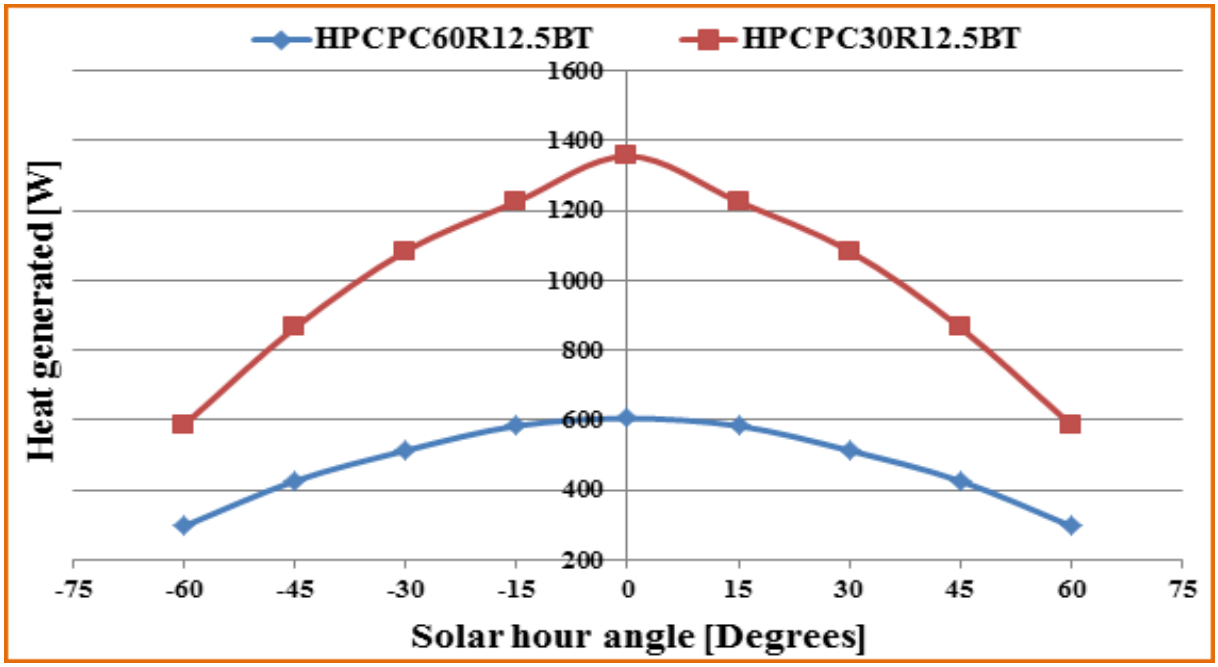

Figure 7.21 Heat generated by array of 10 tubes for the two collectors at different solar hour angles

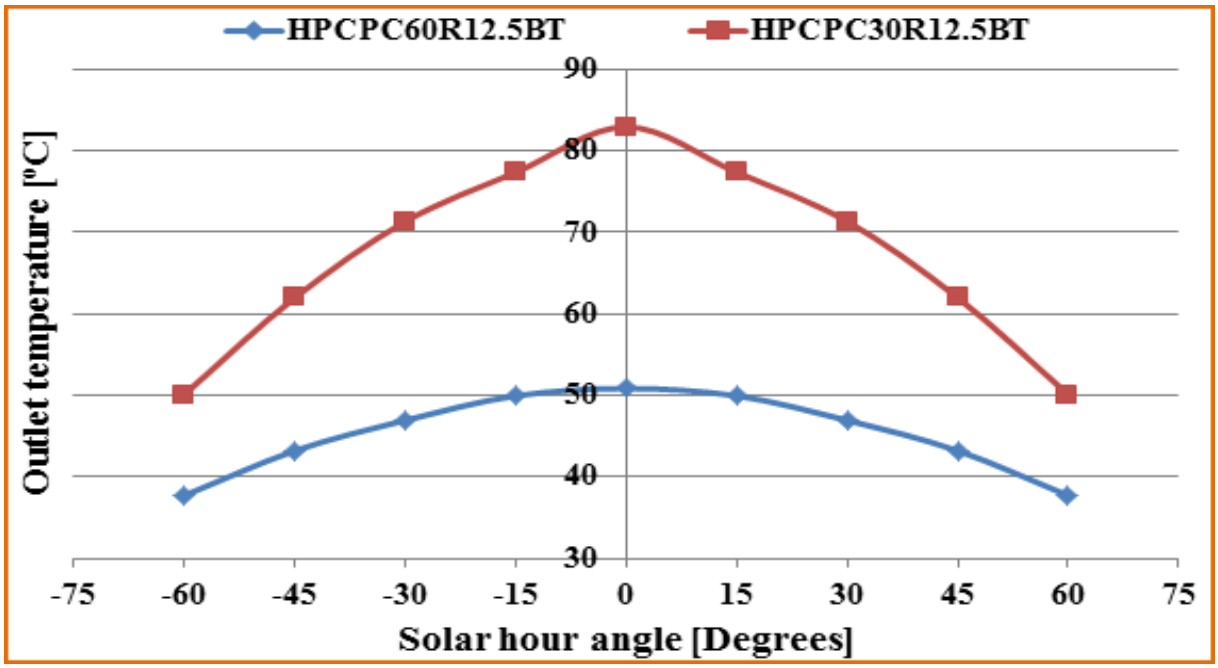

Figure 7.22 Water outlets temperature from array of 10 tubes for the two collectors at different solar hour angles

Figure 7.21 shows that array of 10 tubes of the HPCPC30R12.5BT can produce maximum heat of 1355W at noon and daily average of 987W and 1100W for 9 and 7 hours of operation respectively. It means when 5 and10 units of the array of 10 tubes are connected in parallel, 5.5kW and 11 kW daily average power can be produced respectively. Also each array of this collector can produce hot water above 50^{o}C throughout the day (Figure 7.22) with maximum of 83^{o}C at noon corresponding to 13.5kW power for 10 units of the array of 10 tubes.

While a single array of 10 tubes of HPCPC60R12.5BT can produce maximum power of 605W at noon and daily average of 471 and 521 W for 9 and 7 hours of operation respectively. This shows that daily average power of 2.6kW and 5.2kW can be generated by 5 and 10 units of this collector respectively. Each unit can also produce hot water above 40^{o}C throughout the day (Figure 7.22) with maximum of 51^{o}C at noon corresponding to 6kW power for 10 units.

The outlet temperatures of these collectors can also be increase when the cooling water enters at high temperature than the one assumed in the simulation (25^{o}C). Figure 7.23 shows the temperature gradient of the cooling water in the manifold when the power input to each tube is 134.87W. The water outlet temperatures for each power inputs for the HPCPC configurations simulated were determined from the Ansys as mass weighted average and showed in Figure 7.22.

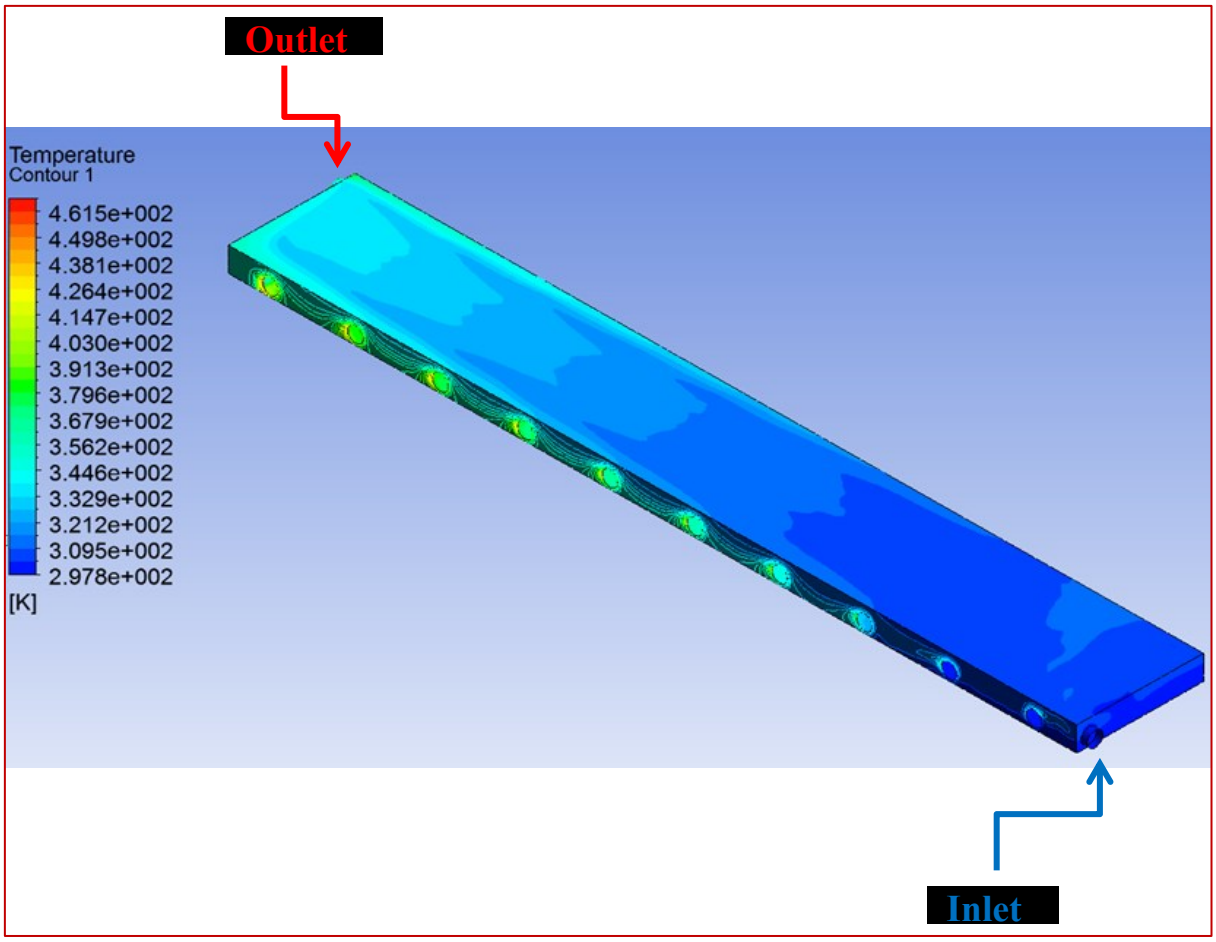

Figure 7.23 Temperature profile of water domain (HPCPC30R12.5BT)

7.5. Applications of HPCPC in powering cooling systems in Kano, Nigeria

The thermal energy generated from the solar collectors described in section 7.4 can be used in powering cooling systems for refrigeration and air-conditioning in Kano. Having solar cooling system in Kano at the hot time of the year and when the radiation is high will assist in providing comfort to the people. Coincidently this is also the time when many of the few power plants break down due to the high ambient temperature reducing the overall power generation.

Although the solar thermal cooling systems have been developed many years ago, but in terms of applications, the technology is still in early stage of development in many parts of the world [183] especially in developing countries like Nigeria. Solar cooling system consists of solar collector, refrigeration system and cooling load and the choice of a right cooling technology for a particular system depends on the requirements in terms of power, cooling demand and temperature level. Figure 7.24 shows various systems through which solar thermal collectors can be utilized in achieving cooling effects. The figure shows two solar driven cooling systems; solar thermal driven and PV electricity driven. It can be seen from the figure that solar thermal driven air-conditioning can be achieved from absorption, adsorption, desiccant, ejector and Rankine cycles.

Solar thermal cooling system is preferred to the PV due to its ability to utilize most of the radiation falling on it compared to PV. Also the efficiency of solar thermal collector in running cooling system will be higher than that of the PV because it converts the solar radiation directly into heat which is used in running the cooling system [3, 184, 185].

Basically, a solar thermal cooling system consists of array of solar collectors, with or without thermal storage tank and heat driven cooling system as shown in Figure 7.25. The heat from the solar collector, Q_g is passed to the generator where the sorbent is activated to absorbing the refrigerant in the absorber. The refrigerant evaporates in the evaporator and condenses in the condenser by releasing heat of condensation, Q_c to the atmosphere. On returning from the absorber, the regenerated sorbent absorbs the refrigerant vapour from the evaporator, releasing the sorption heat, Q_a to the atmosphere. Then heat is extracted from the load in the evaporator by the condensed refrigerant from the condenser producing cooling effect.

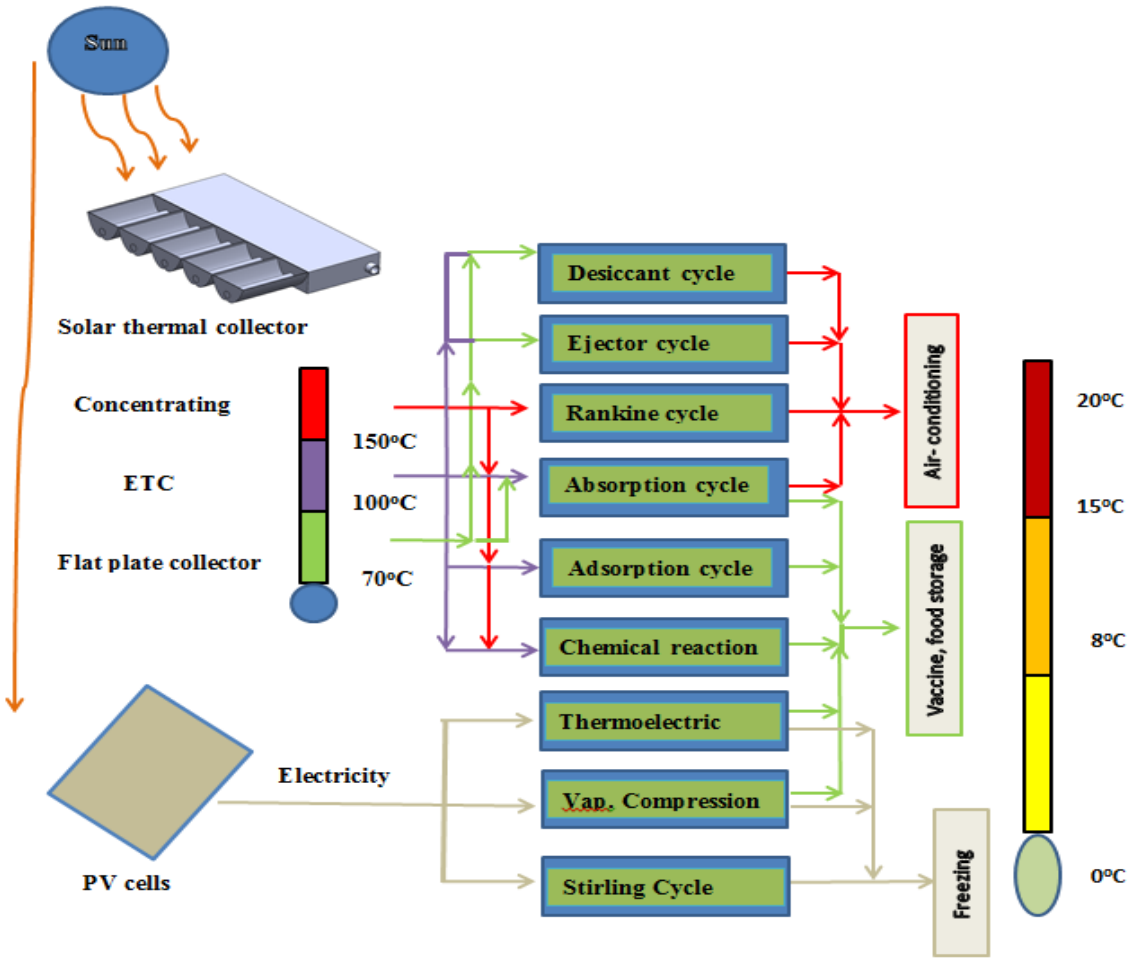

Figure 7.24 Solar cooling technologies [186]

The performance of refrigeration/ air-conditioning systems are usually expressed in terms of coefficient of performance (COP) which can be defined as the ratio of the energy that can be removed from cold place to that input to the system as [186]:

$$COP = \frac{Q_{cooling}}{Q_{in}} \tag{7.1}$$

Where $Q_{cooling}$, is the cooling load and Q_{in} is the power from the thermal solar collector.

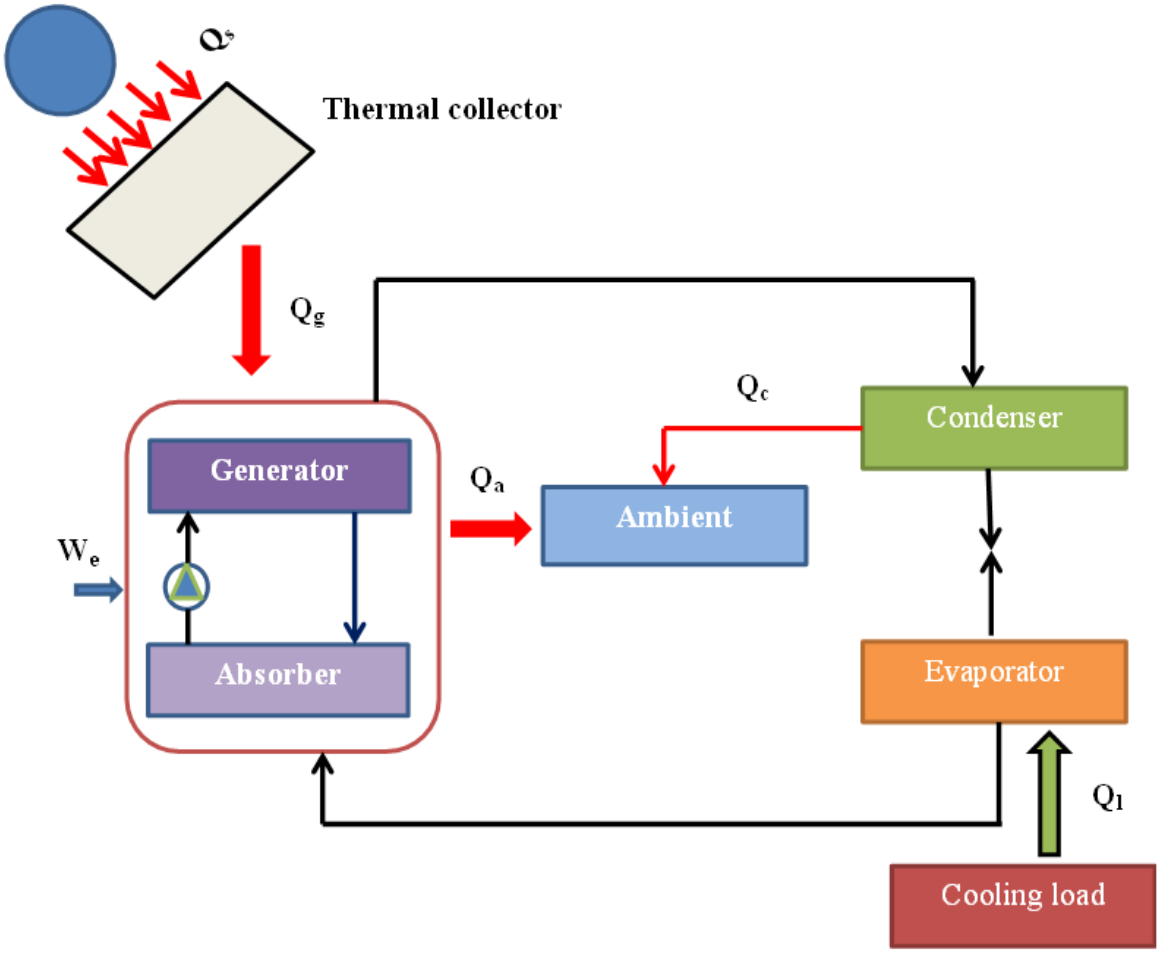

Figure 7.25 Schematic diagram of Solar sorption refrigeration system [187]

Adsorption chillers utilizing silica gel – water pair could be powered by hot water at temperature between 60 and 85°C and could provide cooling load from 5 to 10 kW with coefficient of performance (COP) of 0.3 – 0.5 [188-190]. When a COP of 0.5 is assumed daily average cooling loads of 5.5kW and 2.6 kW can be obtained from HPCPC30R12.5BT and HPCPC60R12.5BT respectively. Also the HPCPCs developed in this study can power most of the marketed systems listed in Table 7.4 for closed systems utilizing water chillers.

Table 7.4 Solar sorption for cooling applications available in market [187]

Parameters	State of the sorption material			
	Liquid			Solid
Sorption material	Water	Lithium- bromide		Silica gel
Refrigerant	Ammonia	Water		Water
Type of cycle	1 - effect	1 - effect	2effects	1 – effect
COP range	0.5 – 0.75	0.65– 0.8	1.1 – 1.4	0.5– 0.75
Driving temperature range (^{o}C)	70 -100 120 - 180	70 - 100	140- 180	65 - 90
Types of the collector	FPC, ETC	FPC,ETC		FPC, ETC

7.6. Summary

The experimental thermal performance of the developed HPCPCs with reflectivity of 60 and 80% was presented at different irradiance and inclination angles of the thermosyphon heat pipe. Also the predicted thermal performance of the array of 10 tubes for solar cooling applications under the climatic conditions of Kano was presented

Some of the outcomes of this chapter can be summarized as follows:

i. The developed HPCPC in this work can function well with inclination angle up to 40^{o} where it gives maximum efficiency at 10^{o} of 76% and for angles between 20 – 30^{o} of 72% and at 45^{o} it has 66% which is higher than that at zero degrees angle (60%).

ii. Single array of HPCPC30R12.5BT consisting of 10 tubes can produce maximum heat of 1355W at noon and daily average of 987W and 1100W for 9 and 7 operation hours respectively with temperature above 50^{o}C throughout the day.

iii. A single array of 10 HPCPC60R12.5BT tubes can produce maximum power of 605W at noon and daily average of 471 and 521 W for 9 and 7 operation hours respectively. This shows that daily average power of 2.6kW and 5.2kW can be generated by 5 and 10 units of this collector respectively.

iv. HPCPC can meet the heat required for driving solar cooling system in Kano and areas with similar climatic conditions

Chapter Eight

8. Conclusions and Recommendations for future works

8.1. Introduction

Interest in harnessing of renewable energy is increasing due to the energy issues all over the world and the problems associated with the use of conventional fossil fuel. While developed nations are faced with problems of global warming, developing countries are faced with inadequate generation and supply of energy.

Although renewable energy like solar is one of the alternative to the fossil fuel and potential contributor to the energy, the technology is faced by low efficiency which leads to high initial cost. Detailed modelling and optimization to enhance the efficiency of the solar systems is important in designing cost effective systems.

Nigeria is faced with serious challenges in power supply ranging from regular outage, inadequate supply, unbalanced energy consumption patterns, inefficient and unreliable supply to inadequate technological capacity and inefficient utilization. On the other hand, it has high potentials of solar radiation in most parts of the country, but little attention is given to its development. Several factors contributed to the slow development of the solar systems in Nigeria including high cost, zero incentive, low awareness, inadequate research, etc. and this makes it impossible for the solar technology to meet the required input to the energy mix of 14% (2008), 23% (2015) and 36% (2030) as projected by presidential committee on power development.

The present study is an investigation on the ways of enhancing the performance of a low concentrating heat pipe based compound parabolic concentrator solar collector by considering the three major factors that affects the performance of collector; ***solar radiation available*****,** ***design and the collector orientation*** which led to the performance predictions of solar collector for powering cooling systems for northwest states in Nigeria. It also aimed at fully modelling the solar radiation of Kano, Nigeria to serve as electronic platform for research on solar energy in the region and similar locations. The collector is to operate under many climate conditions but with more emphasis to the climate of Kano, Nigeria and other northwest states in the country.

8.2. Theoretical and experimental investigations

Detailed geometrical, optical and thermal investigations on the symmetric CPC (2 – 5X) were carried out. Detailed modelling and optimization of solar radiation collection was undertaken.

8.2.1. Solar radiation modelling

Two models were developed for characterizing the solar parameters for regions in the northern hemisphere. The model was validated using meteorological data of Birmingham, UK, and then the solar radiation of Kano, Nigeria was fully modelled and optimized. The radiation model showed that:

i. Kano has high radiation falling on its horizontal surface almost throughout the year, annual average clearness index and daylight hours of 0.63 and 12.00 respectively.

ii. The amount of diffuse radiation component is significant in some months with July having highest (47.55%) and the least in December (27.1%), which shows that CPC ia a good option for the region.

iii. Tilting a solar collector to an angle relative to the horizontal surface of Kano affects the amount of the radiation falling on it depending on the tilt factors. Based on the results obtained, the followings are recommended for Kano:

a. Fixed collector: For the collector to be fixed at an angle throughout the year, the best tilt is to the latitude of Kano ($\beta = \phi = 12.05^{o}$) because of uniformity and having radiation gain in seven month (highest of 13.2% in December) and annual average of 7.3%.

b. Monthly adjustment: To slope the collector to the optimum tilt angle for each month which gives 28.6 and 24.8% increase in December and January respectively.

c. For seasonal tilt:

- $\beta = 27.05^{o}$ ($\phi + 15^{o}$) is the best angle for the months between October and March, with the highest increase in December (24%) and seasonal average of 14%.

- $\beta = 0$ ($\phi - 12.05^{o}$) is the best angle for the months between April and September.

8.2.2. Geometric characterization and optical simulation

A computer program was developed to study the geometric characteristics of CPC and two dimensional advanced ray tracing technique was used to investigate the effects of acceptance

angle, receiver radius, gap effects, truncation effects, length and orientation of the collector. Also various reflector shapes for use in building solar simulator were studied as well as the novel idea of using double receiver in one concentrator. Results showed that:

1. Acceptance angle of the HPCPC is the most important parameter in determining its geometric characteristics because it affects the collector height and aperture, concentration ratio, average number of reflections, etc.
2. Truncating HPCPC60, HPCPC40 and HPCPC30 by 70% increases the acceptance angle by 28.7, 30 and 33.4% respectively leading to corresponding decrease in concentration ratios of 21.7, 22 and 22.24% respectively. Based on these investigations new correlations relating collector height, aperture width and acceptance angles were generated as:

$$H = r \Big/ 0.0645(2\theta_a)^{1.8494} \quad (1)$$

$$A_w = r \Big/ 0.0766(2\theta_a)^{0.964} \quad (2)$$

Combining (1) and (2) gives

$$H = 1.19A_w \Big/ (2\theta_a)^{0.8854} \quad (3)$$

3. Truncation increased the optical efficiencies achieving daily average of 86.2, 75.4 and 66.3% for HPCPC60R12.5, HPCP40R12.5 and HPCPC30R12.5 respectively and corresponding concentration ratios of 1.56, 2.28 and 3.02 at 70% truncation level. Also best truncation levels were determined for the configurations simulated.
4. Novel approach of using two receivers or elliptical shape in single CPC was introduced for optical performance enhancement, economic and other logistic reasons.

Both double tube horizontally aligned and elliptical receivers outperformed single cylindrical with 15 and 17% in optical efficiency

5. Optical losses in the CPC mainly occur due to the average number of reflection of the rays, gap between the receiver and the reflector and the sun position.

8.2.3. CFD modelling and Experiment on a two –phase closed thermosyphon

Since the receiver of the HPCPC is thermosyphon heat pipe, a CFD model was developed using VOF in Ansys Fluent to study the effects of heat inputs, water flow rate, inclination angle, etc. The model was validated through experiment. The results of the two showed that:

i. The overall thermal resistance decreases with increase in the heat input due to the effective nucleate boiling activities in the evaporator

ii. The performance of the thermosyphon increases with the heat input till when the pipe reaches its maximum operation limit

iii. Inclining thermosyphon to an angle from the horizontal enhanced its performance especially at lower heat inputs. Performance enhancement of 17.8, 13.9 and 3.4% were achieved for heat inputs of 31.8, 51.7 and 109W respectively

iv. This model was used to study the effects of cooling water flow rate, pipe thickness and can be used for various investigation on thermosyphon

8.2.4. Thermal performance – CFD and experimental

Experimental thermal performance of single and double receiver HPCPC and determination of best inclination angle of thermosyphon heat pipe in HPCPC was carried out. Also

performance prediction of HPCPC60R12.5T and HPCPC30R12.5T with array of 10 tubes was carried out using Ansys Fluent. Results showed that:

i. The HPCPC can function well with thermosyphon inclination angle up to 40^{o} where it gives maximum efficiency at 10^{o} of 76% and for angles between 20 – 30^{o} of 72% and at 45^{o} it has 66% which is higher than that at zero degrees angle (60%).

ii. The double pipe aligned horizontally outperformed single tube by 21, 19.8 and 17.4% in terms of rate of heat transfer to the cooling water for HPCPC30, HPCPC40 and HPCPC60 respectively for seven hours operations in a day. While for nine hours operations, the percentage increase is 16.7, 18 and 18.3% for HPCPC30, HPCPC40 and HPCPC60 respectively.

iii. Single unit of HPCPC30R12.5BT consisting of 10 tubes can produce maximum heat of 1355W at noon and daily average of 987W and 1100W for 9 and 7 operation hours respectively with temperature above 50^{o}C throughout the day. It means when 5 and10 units of this collector are installed in parallel, 5.5kW and 11 kW daily average powers can be generated respectively.

iv. While a single unit of HPCPC60R12.5BT can produce maximum power of 605W at noon and daily average of 471 and 521 W for 9 and 7 operation hours respectively. This shows that daily average power of 2.6kW and 5.2kW can be generated by 5 and 10 units of this collector respectively. Each unit can also produce hot water above 40^{o}C throughout the day (Figure 7.19) with maximum of 51^{o}C at noon corresponding to 6kW power for 10 units.

8.3. Future works

It has been proved that good design and correct orientation results in efficient heat pipe based compound parabolic collector. The collector is suitable for many applications with long operation hour and reasonable optical and thermal efficiencies. However, the present study presents steps and models for further work in enhancing the performance of the CPC. The following recommendations are put forward:

- The novel idea of using double receivers and elliptical shape receivers in single concentrator should be investigated further for different cross-sectional areas. Also detailed experimental and simulation works should be conducted on different configurations
- Since the potential of solar cooling system depends on the climatic conditions of a region, research on the optimum design of solar cooling system and working medium for Kano is recommended
- To develop a transient model to study the performance of the solar cooling system in Kano at different solar hour angles
- To develop a complete HPCPC with array of 10 tube and testing under real sun for water heating, solar cooling and preservations.

APPENDIX A: EES codes for optimization of collector tilt angle

"Optimization of tilt angle (monthly average)"

```
Lat =12.05                                                    "Latitude"
GR = 0.2                                                      "Ground reflection"
{Tit = Table A.1                                              "Tilt angle"
Soldecl = Table A.1                                           "Solar declination angle"
GRH =     Table A.1                                           "Global radiation on horizontal surface"
n =       Table A.1                                           "Mean day of the year"
```

"Codes for OCTOBER to MARCH"

```
Solset1 = arccos (-tan(lat)*tan(Soldecl))                     "Solar sunset hour angle 1"
TF=(cos(Lat-Tit)*cos(Soldecl)*sin(Solset1)+(pi#/180)*Solset1*sin(Lat-
Tit)*sin(Soldecl))/(cos(Lat)*cos(soldecl)*sin(solset1)+ (pi#/180)*solset1*sin(Lat)*sin(soldecl))
                                                              "Tilt Factor"
ETR=
((86400*G_sc#)/pi#)*(1+0.033*cos(360*n/365))*(cos(lat)*cos(soldecl)*sin(solset1)+(pi#*solset1/180)*sin(lat)*sin
(soldecl))                                                    "Extraterestrial radiation"
CI = GRH/ETR                                                  "Clearness index"
RDG = 0.775+0.00606*(solset1-90) - (0.505+0.00455*(solset1-90))*cos (115*CI-103)
                                                              "Ratio of diffuse to the global    radiation"
DRH = GRH*RDG                                                 "Diffuse radiation on horizontal surface"
GRT = GRH*(1-RDG)*TF + DRH*((1+cos(Tit))/2)+GRH*GR*((1-cos(tit))/2)    "Global radiation on tilt surface"
```

"Codes for APRIL to SEPTEMBER"

```
Solset1 = arccos(-tan(lat)*tan(Soldecl))                      "Solar sunset hour angle"
Solset2 = arccos(-tan(lat-Tit)*tan(Soldecl))                  "Solar sunset hour angle at tilt"
TF=(cos(Lat-Tit)*cos(Soldecl)*sin(Solset2)+(pi#/180)*Solset2*sin(Lat-
Tit)*sin(Soldecl))/(cos(Lat)*cos(soldecl)*sin(Solset2)+(pi#/180)*Solset2*sin(Lat)*sin(soldecl))
                                                              "Tilt Factor"
ETR=
((86400*G_sc#)/pi#)*(1+0.033*cos(360*n/365))*(cos(lat)*cos(soldecl)*sin(solset1)+(pi#*solset1/180)*sin(lat)*sin
(soldecl))                                                    "Extraterrestrial radiation"
CI = GRH/ETR                                                  "Clearness index"
RDG = 0.775+0.00606*(solset1-90) - (0.505+0.00455*(solset1-90))*cos(115*CI-103)
                                                              "Ratio of diffuse to the global radiation"
DRH = GRH*RDG                                                 "Diffuse radiation on horizontal surface"
GRT = GRH*(1-RDG)*TF + DRH*((1+cos(Tit))/2)+GRH*GR*((1-cos(tit))/2)    "Global radiation on tilt surface"
```

Table A.1 Inputs to the EES model

Month	**Soldec**	**GRH, MJ/(m^2.day)**	**n**	**Tilt angles (^{o})**
January	-20.9	22.72	17	0 - 90
February	-13.0	24.85	47	0 - 90
March	-2.4	26.78	75	0 - 90
April	9.4	23.96	105	0 - 90
May	18.8	21.32	135	0 - 90
June	23.1	19.41	162	0 - 90
July	21.2	16.86	198	0 - 90
August	13.5	16.86	228	0 - 90
September	2.2	19.97	258	0 - 90
October	-9.6	22.87	288	0 - 90
November	-18.9	25.45	318	0 - 90
December	-23.0	24.06	344	0 - 90

Appendix B: Instrument Calibration and Uncertainties calculations

1. Uncertainty in water flow rate measurement

The overall uncertainty associated with the measurement of the flow rate consists of the uncertainties with water collection method and the calibration (curve fittings) as:

$$U_{WF} = \sqrt{U_{V_W}{}^2 + U^2{}_{T,curve-fit}} \quad \textbf{(B.1)}$$

The volume flow rate is determined as:

$$V_w = \frac{Volume\ collected\ (V_f)}{Time\ taken\ (t)} \quad \textbf{(B.2)}$$

The uncertainty associated with the cylinder used is ±2.5mL and with the collecting time is ±1 second.

The uncertainty with the determination of volume flow rate method is obtained by rule of square root sum as:

$$U_{V_W} = \sqrt{\left(\partial U_{V_W} / \partial V_f \, \Delta V_f\right)^2 + \left(\partial U_{V_W} / \partial t \, \Delta t\right)^2} \quad \textbf{(B.3)}$$

$$U_{V_W} = \sqrt{\left(1/t \, \Delta V_f\right)^2 + \left(-V_f / t^2 \, \Delta t\right)^2}$$

$$U_{V_W} = \sqrt{\left(1/1\min * 2.5mL\right)^2 + \left(-500mL/(1\min)^2 * \left(1/60\min\right)\right)^2} \quad = \pm 8.7\text{mL/min}$$

The uncertainty due to the curve fit error is calculated in Table B.1

Table B.1 Curve fit error for flow rate measurement

Data point (N)	**Average voltage signal, x**	**Measured Vol. flow rate, mL/min**	**Curve fit vol. flow rate,** $V_{corrected} = 222.79x - 2.8341$	**Deviation squared**
1	0.01	0	-0.6062	0.3674784
2	0.5238	119.047619	113.863302	26.877143
3	0.837235294	179.6407186	183.6935512	16.425452
4	1.1234375	241.9354839	247.4565406	30.482067
5	1.815363636	405.4054054	401.6107645	14.399299
Sum				88.55144
Degree of freedom(N-1) = 4				
Standard deviation σ = 4.7050887				
Standard deviation of the mean $S_{\bar{x}}$ = 2.1041796				
Student distribution factor $t_{N-1,95\%}$ = 2.776				
U_{curve_fit} = 5.84mL/min				

Then the overall uncertainty is obtained using equation A.1 as:

$$U_{WF} = \sqrt{8.7^2 + 5.84^2} = \pm 10.48 \text{mL/min} = \pm \frac{10.48}{500} * 100 = \pm 2.096\ \%\ Fs$$

2. Uncertainty in temperature measurement

The uncertainty in the thermocouple reading is given by:

$$U_{TH} = \sqrt{U^2_{ST} + U^2_{curve-fit}} \qquad \textbf{(B.4)}$$

Where U_{ST} and $U_{curve-fit}$ are the uncertainties of the standard thermocouple and curve fit respectively.

The standard device used in the calibration is high precision Resistance Temperature Detector (RTD) which was calibrated in the ice water mixture. The RTD was placed in ice water mixture and the temperature was recorded at different points as shown in Figure A.1

The uncertainty of curve fitting given by:

$$U_{curve-fitting} = t_{N-1,95\%} S_{\bar{x}} \quad \textbf{(B.5)}$$

Where $S_{\bar{x}}$, is the standard deviation of the mean and $t_{N-1,95\%}$, is the student distribution factor.

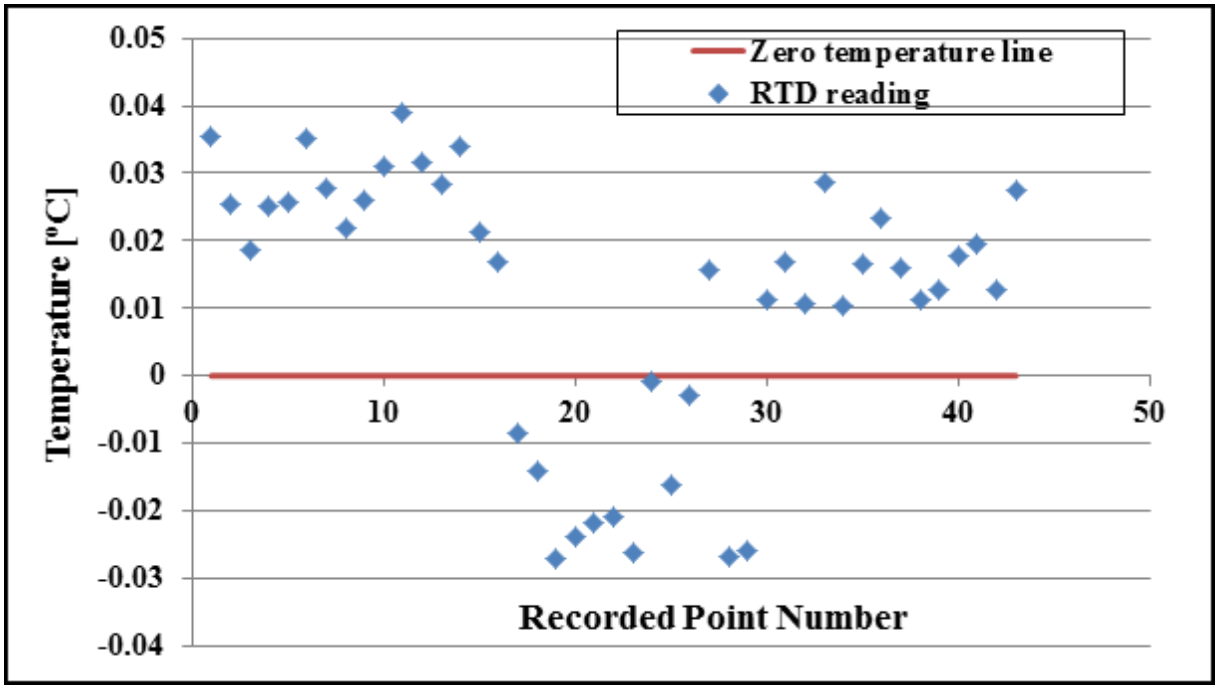

Figure B.1 Uncertainty in the RTD thermocouple reading

The error of the RTD is within ±0.03 and average of ±0.025, which seem negligible, so the uncertainty with the thermocouple reading is only associated with curve fittings as shown in the Table B.2

Table B.2: Calculations of curve fittings uncertainty for the surface-one thermocouple

Data point (N)	RTD reading	Average measured temperature ($T_{measured}$)	Curve fit temperature (°C) $T_{corrected} = 0.9922 * T_{measured} + 0.2558$	Deviation squared
1	23.437381	23.42166667	23.49477767	0.003294362
2	41.866811	41.94541667	41.87404242	5.22907E-05
3	66.773682	66.94333333	66.67697533	0.009352292
4	96.564585	96.60625	96.10852125	0.207994874
5	99.726036	100.7303704	100.2004735	0.225090204
Sum				0.445784022
Degree of freedom (N-1) = 4				
Standard deviation σ = 0.333835297				
Standard deviation of the mean $S_{\bar{x}}$ = 0.149295684				
Student distribution factor $t_{N-1,95\%}$ = 2.57				
U_{curve_fit} = 0.38K				

Engineering Equation solver (EES) is utilized in most of the uncertainties calculations for the various devices and measurement approaches.

9. References

[1]. International Energy Agency, *World Energy Outlook*, 2014, OECD/ IEA: CORLET Paris cedex France.

[2]. Sambo, A.S. *Renewable Energy Technology for National Development: Status, Prospects and Policy Directions*. in *Annual General Meeting of the Nigerian Society of Engineers*. 2001. Bauchi: Nigeria Society of Engineers.

[3]. Kim, D.S., Infante Ferreira, C.A., *Solar refrigeration options – a state-of-the-art review.* International Journal of Refrigeration, 2008. **31**(1): p. 3-15.

[4]. Sims, R.E.H., *Renewable energy: a response to climate change.* Solar Energy, 2004. **76**(1–3): p. 9-17.

[5]. Schimmelpfenning, D., *The option value of renewable energy The case of climate change.* Energy Economics, 1995. **17**(4): p. 311-317.

[6]. Lewis, N.S., Nocera, D.G. *Powering the planet: Chemical challenges in Solar Energy Utilization*. in *National Academy of Sciences*. 2006.

[7]. Nabin, S., *Design and Performance evaluation of a low concentrating Line - axis Dielectric Photovoltaic System*, in *Shool of Engineering and Physical Sciences*2012, Heriot - Watt University.

[8]. Sambo, A.S., Bala, E.J. *Penetration of Solar Photovoltaic into Nigeria's Energy supply mix*. in *World Renewable Energy Forum (WREF)*. 2012. Denver, Colorado USA: Curran Association Inc.

[9]. Sambo, A.S., *Matching Electricity Supply with Demand in Nigeria*, 2008, Energy Commission of Nigeria (ECN). p. 17 - 21.

[10]. World Bank IBRD - IDA, *Data on Electric Power consumption (kWh per capita)*, 2015, World Bank Group.

[11]. Oji, J.O., Idusuyi, N., Aliu, T.O., Petinrin, M.O., Odejobi, O.A., Adetunji, A.R., *Utilization of Solar Energy for Power Generation in Nigeria.* International Journal of Energy Engineering, 2012. **2**(2): p. 54 - 59.

[12]. Charles, A., *How 100% renewable energy possible for Nigeria ?*, 2014, Global Energy Network Institute (GENI).

[13]. Malato Rodríguez, S., Blanco Gálvez, J., Maldonado Rubio, M.I., Fernández Ibáñez, P., Alarcón Padilla, D., Collares Pereira, M., Farinha Mendes, J., Correia de Oliveira, J., *Engineering of solar photocatalytic collectors.* Solar Energy, 2004. **77**(5): p. 513-524.

[14]. Azhari, A.A., Khonkar, H.E., *A thermal comparison performance of CPC with modified (dual-cavity) and non-modified absorber.* Renewable Energy, 1996. **9**(1-4): p. 584-588.

[15]. Tripanagnostopoulos, Y., Yianoulis, P., *CPC solar collectors with multichannel absorber* Solar Energy, 1996. **58**: p. 49 - 61.

[16]. Farouk, K.A., Eames, P.C., Norton, B., *Experimental analysis and performance of an asymmetric inverted absorber Compound Parabolic Concentrating solsr collector at various absorber gap configurations.* Renewable Energy, 1997. **10**: p. 235 - 238.

[17]. Manrique, J.A., *A Compound parabolic concentrator.* International Communications in Heat and Mass Transfer, 1984. **11**: p. 267 - 273.

[18]. Rabl, A., *Active Solar Collectors and their Applications*. First ed1985, New York: Oxford University Press.

[19]. Duffie, J.A., Beckham, W.A., ***Solar Engineering of thermal processes***. 3rd ed2006, USA: John Wiley & son Inc.

[20]. Kaligorous, S., ***Solar Energy Engineering: Processes and systems***2009, Academic press: Elsevier Science.

[21]. Kalogirou, S.A., *Solar thermal collectors and applications.* Progress in Energy and Combustion Science, 2004. **30**(3): p. 231-295.
[22]. Rabl, A., *Comparison of solar concentrators.* Solar energy, 1976. **18**: p. 93 - 111.
[23]. Jan, F.K., Frank, K., *Solar heating and cooling, active and passive design*. Second edition ed1982, USA: Hemisphere Publishing Corporation.
[24]. El -Assay, A.Y., Clark, J.A., *A thermal - optical analysis of compound parabolic concentrator for single and multi flows including super heater.* Warme - und Stoffubertragung (heat and mass transfer), 1987. **21**: p. 189 - 198.
[25]. Kumar, T.M., *Optics and heat transfer for asymmetric compound parabolic photovoltaic for building integrated photovoltaic*, 2003, University of Ulster, Uk: UK.
[26]. Tatara, R.A., Thodos, G., Lee, Y.N., *Performance of an array of compound parabolic concentrators with plain tubular receivers.* Renewable Energy, 1991. **1**: p. 21 - 26.
[27]. Fraidenraich, N., de Lima, C.F., Tiba, C., de S. Barbosa, E.M., *Simulation model of a CPC collector with temperature-dependent heat loss coefficient.* Solar Energy, 1999. **65**(2): p. 99-110.
[28]. Nkwetta, D., Mervyn, S., Zacharopoulos, A., Hyde, T., *In-door experimental analysis of concentrated and non-concentrated evacuated tube heat pipe collectors for medium temperature applications.* Energy and Buildings, 2012. **47**: p. 674-681.
[29]. Rabl, A., *Optical and thermal properties of compound parabolic concentrators.* Solar Energy, 1976. **18**(6): p. 497-511.
[30]. Abdel-Khalil, S.I., Li, M.W., Randall, K.R., *Natural convection in compound parabolic concentrators - a finite element solution.* ASME journal of heat transfer, 1978. **100**: p. 199 - 204.
[31]. Abdel-khalil, S.I., Li, M.W. *Natural convection in two dimensional compound parabolic concentrators*. in *Proceedings of ASME Winter Annual Meeting*. 1978. San Francisco.
[32]. Hsieh, C.K., *Thermal analysis of CPC collectors.* Solar Energy, 1981. **27**(1): p. 19-29.
[33]. Hsieh, C.K., *Design of a system using CPC collectors to collect solar energy and to produce industrial process steam* 1979, Argonne National Laboratory, Rep. ANL. p. 79 - 102.
[34]. Norton, B., Prapas, D.E., Eames, P.C., Probert, S.D., *Measured Performances of curved inverted - Vee absorber compound parabolic concentrating solar - energy collectors.* Solar Energy, 1989. **43**(5): p. 267 - 279.
[35]. Meyer, B.A., Mitchell, J.W., El-wakil, M.M., *Convective heat transfer in V - trough linear concentrators.* Solar Energy, 1982. **28**: p. 33 - 40.
[36]. Fasulo, A., Odicino, L., Perello, D., *Development of CPC with low thermal losses* Solar wind technology, 1987. **4**: p. 157 - 162.
[37]. Eames, P.C., Norton, B., *Detailed parametric analyses of heat transfer in CPC solar energy collectors.* Solar Energy, 1993. **50**(4): p. 321-338.
[38]. Prapas, D.E., Norton, B., Melidis, P.E., Probert, S.D., *Convective heat transfers within air spaces of compound parabolic concentrating solar-energy collectors.* Applied Energy, 1987. **28**(2): p. 123-135.
[39]. Chew, T.C., Wijeysundera, N.E., Tay, A.O., *An experimental study of free convection in compound parabolic concentrators (CPC) cavities.* ASME journal of Solar Energy Engineering, 1988. **110**: p. 293 - 298.
[40]. Eames, P.C., Norton, B., *Validated, unified model for optics and heat transfer in line-axis concentrating solar energy collectors.* Solar Energy, 1993. **50**(4): p. 339-355.
[41]. Fraidenraich, N., Chigueru, T., Bráulio, B., Brandao, B., Olga, C.V., *Analytic solutions for the geometric and optical properties of stationary compound parabolic concentrators with fully illuminated inverted V receiver.* Solar Energy, 2008. **82**(2): p. 132-143.

[42]. Kothdiwala, A.F., Eames, P.C., Norton, B., Zacharopolous, A., *Comparison between inverted absorber asymmetric and symmetric tubular - absorber compound parabolic concentrating solar collectors.* Renewable Energy, 1999. **18**: p. 277 - 281.
[43]. Akio , S., Shigeo, K., *Yearly distributed insolation model and optimum design of a two dimensional compound parabolic concentrator.* Solar Energy, 1995. **54**: p. 327 - 331.
[44]. Carvalho, M.J., tillares-Pereira, M., Correia de Oliveira, J., Farinha Mendes, J., Haberle, A., Wittier, V., *Optical and thermal testing of a new 1.12X CPC solar collector.* solar energy Materials and Solar cells, 1995. **37**: p. 175 -190.
[45]. Mills, D.R., Bassett, I.M., Derrick, G.H., *Relative cost-effectiveness of CPC reflector designs suitable for evacuated absorber tube solar collectors.* Solar Energy, 1986. **36**(3): p. 199-206.
[46]. Grimmer, D.P., *A Comparison of compound parabolic and simple parabolic concentrating solar collectors.* Solar Energy, 1979. **22**: p. 21 - 25.
[47]. Tchinda, R., Kaptouom, E., Njomo, D., *Study of the C.P.C. collector thermal behaviour.* Energy Conversion and Management, 1998. **39**: p. 1395 - 1406.
[48]. Tchinda, R., *Thermal behaviour of solar air heater with compound parabolic concentrator.* Energy Conversion and Management, 2008. **49**(4): p. 529-540.
[49]. Kim, Y., Han, G., Seo, T., *An evaluation on thermal performance of CPC solar collector.* International Communications in Heat and Mass Transfer, 2008. **35**(4): p. 446-457.
[50]. Grass, C., Schoelkopf, W., Staudacher, L., Hacker, Z., *Comparison of the optics of non-tracking and novel types of tracking solar thermal collectors for process heat applications up to 300 °C.* Solar Energy, 2004. **76**(1-3): p. 207-215.
[51]. Abdul-jabbar, N.K., Salman, S.A., *Effect of two - axis sun tracking on the performance of compound parabolic concentrators.* Energy Conversion and Management, 1998. **39**: p. 1073 - 1079.
[52]. Tripanagnostopoulos, Y., Yianoulis, P., Papaeflhimiou, S., Souliotis, M., Nousia, T., *Cost effective asymmetric CPC solar collectors.* Renewable Energy, 1999. **16**: p. 628 - 631.
[53]. Tripanagnostopoulos, Y., Yianoulis, P., Papaefthimious, S., Zafeiratos, S., *CPC Solar collectors with flat bifacial absorbers* Solar Energy, 2000. **69**: p. 191 - 203.
[54]. Adsten, M., Helgesson, A., Karlsson, B., *Evaluation of CPC-collector designs for stand-alone, roof- or wall installation.* Solar Energy, 2005. **79**(6): p. 638-647.
[55]. Zambolin, E., DelCol, D., *Experimental analysis of thermal performance of flat plate and evacuated tube solar collectors in stationary standard and daily conditions.* Solar Energy, 2010. **84**(8): p. 1382-1396.
[56]. Adsten, M., Hellström, B., Karlsson, B., *Measurement of radiation distribution on the absorber in an asymmetric CPC collector.* Solar Energy, 2004. **76**(1-3): p. 199-206.
[57]. Khonkar, H.E.I., Sayigh, A.A.M., *Optimization of the tubular absorber using a Compound parabolic concentrator.* Renewable Energy, 1994. **6**: p. 17 -21.
[58]. Eames, P.C., Norton, B., *Thermal and optical consequences of the introduction of baffles into compound parabolic concentrating solar energy collector cavities.* Solar Energy, 1995. **55**: p. 139 -150.
[59]. Oommen, R., Jayaraman, S., *Development and performance analysis of compound parabolic solar concentrators with reduced gap losses—'V' groove reflector.* Renewable Energy, 2002. **27**(2): p. 259-275.
[60]. Farouk, K.A., Eames, P.C., Norton, B., *Optical performance of an asymmetric inverted absorber compound parabolic concentrating solar collector.* Renewable Energy, 1996. **9**: p. 576 - 579.
[61]. Nkwetta, D., Mervyn, S., Zacharopoulos, A., Hyde, T., *Optical evaluation and analysis of an internal low-concentrated evacuated tube heat pipe solar collector for powering solar air-conditioning systems.* Renewable Energy, 2012. **39**(1): p. 65-70.

[62]. Nkwetta, D.N., Smyth, M., *Performance analysis and comparison of concentrated evacuated tube heat pipe solar collectors.* Applied Energy, 2012. **98**(0): p. 22-32.
[63]. Liu, Z., Hu, R., Lu, L., Zhao, F., Xiao, H., *Thermal performance of an open thermosyphon using nanofluid for evacuated tubular high temperature air solar collector.* Energy Conversion and Management, 2013. **73**(0): p. 135-143.
[64]. Chamsa-ard, W., Sukchai, S., Sonsaree, S., Sirisamphanwong, C., *Thermal Performance Testing of Heat Pipe Evacuated Tube with Compound Parabolic Concentrating Solar Collector by ISO 9806 - 1.* Energy Procedia, 2014. **56**(0): p. 237-246.
[65]. Al-Dadah, R.K., Jackson, G., Rezk, A., *Solar powered vapor absorption system using propane and alkylated benzene AB300 oil.* Applied Thermal Engineering, 2011. **31**(11–12): p. 1936-1942.
[66]. Wei, L., Yuan, D., Tang, D., Wu, B., *A study on a flat-plate type of solar heat collector with an integrated heat pipe.* Solar Energy, 2013. **97**(0): p. 19-25.
[67]. Hussein, H.M.S., Mohamad, M.A., El-Asfouri, A.S., *Transient investigation of a thermosyphon flat-plate solar collector.* Applied Thermal Engineering, 1999. **19**(7): p. 789-800.
[68]. Huang, J., Pu, S., Gao, W., Que, Y., *Experimental investigation on thermal performance of thermosyphon flat-plate solar water heater with a mantle heat exchanger.* Energy, 2010. **35**(9): p. 3563-3568.
[69]. Chun, W., Kang, Y.H., Kwak, H.Y., Lee, Y.S., *An experimental study of the utilization of heat pipes for solar water heaters.* Applied Thermal Engineering, 1999. **19**(8): p. 807-817.
[70]. Vasiliev, L.L., *Heat pipes in modern heat exchangers.* Applied Thermal Engineering, 2005. **25**(1): p. 1-19.
[71]. Skeiker, K., *Optimum tilt angle and orientation for solar collectors in Syria.* Energy Conversion and Management, 2009. **50**(9): p. 2439-2448.
[72]. Shariah, A., Al-Akhras, M.A., Al-Omari, I.A., *Optimizing the tilt angle of solar collectors.* Renewable Energy, 2002. **26**(4): p. 587-598.
[73]. Tang, R., Wu, T., *Optimal tilt-angles for solar collectors used in China.* Applied Energy, 2004. **79**(3): p. 239-248.
[74]. Gunerhan, H., Hepbasli, A., *Determination of the optimum tilt angle of solar collectors for building applications.* Building and Environment, 2007. **42**(2): p. 779-783.
[75]. Elminir, H.K., Ghitas, A.E., El-Hussainy, F., Hamid, R., Beheary, M.M., Abdel-Moneim, K.M., *Optimum solar flat-plate collector slope: Case study for Helwan, Egypt.* Energy Conversion and Management, 2006. **47**(5): p. 624-637.
[76]. Farouk, K.A., Norton, B., Eames, P.C., *The effect of variation of angle of inclination on the performance of low - concentration ratio compound parabolic concentrating solar collectors.* Solar Energy, 1995. **55**: p. 301 - 309.
[77]. Norton, B., Kothdiwala, A.F., Eames, P.C., *Effect of Inclination on the Performance of CPC Solar Energy Collectors* Renewable Energy, 1994. **5**: p. 357 -367.
[78]. Chow, T.T., He, W., Ji, J., *Hybrid photovoltaic-thermosyphon water heating system for residential application.* Solar Energy, 2006. **80**(3): p. 298-306.
[79]. Chami, N., Zoughaib, A., *Modeling natural convection in a pitched thermosyphon system in building roofs and experimental validation using particle image velocimetry.* Energy and Buildings, 2010. **42**(8): p. 1267-1274.
[80]. Wonston, S., Kiatsiriroat, T., *Effects of inclined heat transfer rate on thermosyphon heat pipe under sound wave.* Asian Journal on Energy and Environment, 2009. **10**: p. 214 - 220.
[81]. Pouland, M.E., Fung, A. *Potential benefits from thermosyphon - PCM(TP) integrated design for buildings applications in Toronto*. in *Canadian conference on building simulation (eSim 2012)*. 2012. Toronto.

[82]. Emami, M.R.S., Noie, S.H., khoshnoodi, M., *Effect of aspect ratio and filling ratio on the thermal performance of an inclined two – phase closed thermosyphon.* Iranian Journal of science and technology, 2008. **32**: p. 39 - 51.
[83]. Gabriela, H., Angel, H., *Heat transfer characteristics of a two - phase closed thermosyphons using nanofluids* Experimental thermal and fluid science, 2011. **35**: p. 550 - 557.
[84]. Jouhara, H., Ajji, Z., Koudsi, Y., Ezzuddin, H., Mousa, N., *Experimental investigation of an inclined-condenser wickless heat pipe charged with water and an ethanol-water azeotropic mixture.* Energy, 2013. **61**: p. 139-147.
[85]. Noie, S.H., Emami, M.R.S., Khoshnoodi, M., *Effect of inclination angle and filling ratio on thermal performance of a two-phase closed thermosyphon under normal operating conditions.* Heat Transfer Engineering, 2007. **28**(4): p. 365-371.
[86]. Hahne, E., Gross, U., *The influence of the inclination angle on the performance of a closed two-phase thermosyphon.* Journal of Heat Recovery Systems, 1981. **1**(4): p. 267-274.
[87]. Chehade, A.A., Louahlia - Gualos, H., Masson, S.L., Victor, I., Abouzahab - Damaj, N., *Experimental investigation of thermosyphon loop thermal performance* Energy Conversion and Management, 2014. **84**: p. 671 - 680.
[88]. Asghar, A., Masoud, R., Ammar, A.A., *CFD modeling of flow and heat transfer in a thermosyphon.* International Communications in Heat and Mass Transfer, 2010. **37**: p. 312 - 318.
[89]. Başaran, T., Küçüka, S., *Flow through a rectangular thermosyphon at specified wall temperatures.* International Communications in Heat and Mass Transfer, 2003. **30**(7): p. 1027-1039.
[90]. Zhang, M., Liu, Z., Ma, G., Cheng, S., *Numerical simulation and experimental verification of a flat two-phase thermosyphon.* Energy Conversion and Management, 2009. **50**(4): p. 1095-1100.
[91]. Asmaie, L., Haghshenasfard, M., Mehrabani-Zeinabad, A., Esfahany, M.N., *Thermal performance analysis of nanofluids in a thermosyphon heat pipe using CFD modeling.* Heat and Mass Transfer, 2013. **49**(5): p. 667-678.
[92]. Liu, Z., Li, Y., Bao, R., *Thermal performance of inclined grooved heat pipes using nanofluids.* International Journal of Thermal Sciences, 2010. **49**(9): p. 1680-1687.
[93]. De Schepper, S.C.K., Heynderickx, G.J., Marin, G.B., *Modeling the evaporation of a hydrocarbon feedstock in the convection section of a steam cracker.* Computers & Chemical Engineering, 2009. **33**(1): p. 122-132.
[94]. Fadhl, B., Wrobel, L.C., Jouhara, H., *Numerical modelling of the temperature distribution in a two-phase closed thermosyphon.* Applied Thermal Engineering, 2013. **60**(1–2): p. 122-131.
[95]. Tripanagnostopoulos, Y., Souliotis, M., *Integrated collector storage solar systems with asymmetric CPC reflectors.* Renewable Energy, 2004. **29**: p. 223-248.
[96]. Souliotis, M., Tripanagnostopoulos, Y., *Study of the distribution of the absorbed solar radiation on the performance of a CPC-type ICS water heater.* Renewable Energy, 2008. **33**(5): p. 846-858.
[97]. Souliotis, M., Quinlan, P., Smyth, M., Tripanagnostopoulos, Y., Zacharopoulos, A., Ramirez, M., Yianoulis, P., *Heat retaining integrated collector storage solar water heater with asymmetric CPC reflector.* Solar Energy, 2011. **85**(10): p. 2474-2487.
[98]. Yadak, Y.P., Yadav, A.K., Anwar, N., Eames, P.C., Norton, **B.**, *The fabrication and testing of a line-axis compound parabolic concentrating collcector.* Renewable Energy, 1996. **9**: p. 572 - 575.
[99]. Smyth, M., McGarrigle, P., Eames, P.C., Norton, B., *Experimental comparison of alternative convection suppression arrangements for concentrating integral collector storage solar water heaters.* Solar Energy, 2005. **78**(2): p. 223-233.

[100]. Schmidt, C., Goetzberger, A., Schmid, J., *Test results and evaluation of integrated collector storage systems with transparent insulation.* Solar Energy, 1988. **41**(5): p. 487-494.
[101]. Schmidt, C., Goetzberger, A., *Single-tube integrated collector storage systems with transparent insulation and involute reflector.* Solar Energy, 1990. **45**(2): p. 93-100.
[102]. Tripanagnostopoulos, Y., Yianoulis, P., *Integrated collector-storage systems with suppressed thermal losses.* Solar Energy, 1992. **48**(1): p. 31-43.
[103]. Smyth, M., Eames, P.C., Norton, B., *A comparative performance rating for an integrated solar collector/storage vessel with inner sleeves to increase heat retention.* Solar Energy, 1999. **66**(4): p. 291-303.
[104]. González, M.I., Rodríguez, L.R., Lucio, J.H., *Evaluation of thermal parameters and simulation of a solar-powered, solid-sorption chiller with a CPC collector.* Renewable Energy, 2009. **34**(3): p. 570-577.
[105]. González, M.I., Rodríguez, L. R., *Solar powered adsorption refrigerator with CPC collection system: Collector design and experimental test.* Energy Conversion and Management, 2007. **48**(9): p. 2587-2594.
[106]. Tamanot -Telto, Z., Critoph, R.E., *Solar sortion refrigerator using a CPC collector.* Renewable Energy, 1999. **16**: p. 735 -738.
[107]. NKwetta, D., Mervyn, S., *The potential applications and advantages of powering solar air-conditioning systems using concentrator augmented solar collectors.* Applied Energy, 2012. **89**(1): p. 380-386.
[108]. Blanco, J., Malato, S., Fernández, P., Vidal, A., Morales, A., Trincado, P., Oliveira, J.C., Minero, C., Musci, M., Casalle, C., Brunotte, M., Tratzky, S., Dischinger, N., Funken, K.H., Sattler, C., Vincent, M., Collares-Pereira, M., Mendes, J.F., Rangel, C.M., *Compound parabolic concentrator technology development to commercial solar detoxification applications.* Solar Energy, 1999. **67**(4–6): p. 317-330.
[109]. Malato, R.S., Blanco, J.G., Maldonado, M.I., Fernández, I.P., Alarcón, P.D., Collares, P.M., Farinha, M.J., Correia de Oliveira, J., *Engineering of solar photocatalytic collectors.* Solar Energy, 2004. **77**(5): p. 513-524.
[110]. Vilar, V.J.P., Pinho, L.X., Pintor, A.M.A., Boaventura, R.A.R., *Treatment of textile wastewaters by solar-driven advanced oxidation processes.* Solar Energy, 2011. **85**(9): p. 1927-1934.
[111]. Ajona, J.I., Vidal, A., *The use of CPC collectors for detoxification of contaminated water: Design, construction and preliminary results.* Solar Energy, 2000. **68**(1): p. 109-120.
[112]. Fernández, P., Blanco, J., Sichel, C., Malato, S., *Water disinfection by solar photocatalysis using compound parabolic collectors.* Catalysis Today, 2005. **101**(3-4): p. 345-352.
[113]. Mohd, Y., Othman, B.Y., Kamaruzzaman, S., Mohd Nazari, A., *Performance analysis of a double -pass photovoltaic/thermal (PV/T) solar collector with CPC and fins.* Renewable energy, 2005. **30**(13): p. 2005 - 2017.
[114]. Mallick, T.K., Eames, P.C., Norton, B., *Using air flow to alleviate temperature elevation in solar cells within asymmetric compound parabolic concentrators.* Solar Energy, 2007. **81**(2): p. 173-184.
[115]. Sellami, N., Mallick, T.K., *Optical efficiency study of PV Crossed Compound Parabolic Concentrator.* Applied Energy, 2013. **102**(0): p. 868-876.
[116]. Mallick, T.K., Eames, P.C., Hyde, T.J., Norton, B., *The design and experimental characterisation of an asymmetric compound parabolic photovoltaic concentrator for building façade integration in the UK.* Solar Energy, 2004. **77**(3): p. 319-327.
[117]. Baig, H., Sarmah, N., Heasman, K.C., Mallick, T.K., *Numerical modelling and experimental validation of a low concentrating photovoltaic system.* Solar Energy Materials and Solar Cells, 2013. **113**(0): p. 201-219.

[118]. Sarmah, N., Richards, B.S., Mallick, T.K., *Evaluation and optimization of the optical performance of low-concentrating dielectric compound parabolic concentrator using ray-tracing methods.* Applied Optics, 2011. **50**(19): p. 3303-3310.
[119]. Linkous, C., Muradov, N., Ramser, S., *Consideration of reactor design for solar hydrogen production from hydrogen sulphide using semiconductor particulates.* International Journal of hydrogen energy, 1995. **20**(9): p. 701-710.
[120]. Koca, A., Sahin, M., *Photocatalytic hydrogen production by direct sunlight from sulphide solution.* International Journal of hydrogen energy, 2002. **27**(4): p. 363-367.
[121]. Jing, D., Liu, H., Zhang X, Z., Liang, Z., Guo, L., *Photocatalytic hydrogen production under direct solar light in a CPC based solar reactor: Reactor design and preliminary results.* Energy Conversion and Management, 2009. **50**(12): p. 2919-2926.
[122]. McLoughlin, O.A., Ibáñez, P.F., Gernjak, W., Rodríguez, S.M., Gill, L.W., *Photocatalytic disinfection of water using low cost compound parabolic collectors.* Solar Energy, 2004. **77**(5): p. 625-633.
[123]. Sambo, A.S., *Empirical models for the correlation of global solar radiation with meteorological data for Northern Nigeria.* Solar & Wind Technology, 1986. **3**(2): p. 89-93.
[124]. Sambo, A.S., *The measurement and prediction of global and diffuse components of solar radiation for Kano in northern nigeria.* Solar & Wind Technology, 1988. **5**(1): p. 1-5.
[125]. Lam, J.C., Li, D.H.W., *Correlation between global solar radiation and its direct and diffuse components.* Building and Environment, 1996. **31**(6): p. 527-535.
[126]. Khorasanizadeh, H., Mohammadi, K., *Introducing the best model for predicting the monthly mean global solar radiation over six major cities of Iran.* Energy, 2013. **51**(0): p. 257-266.
[127]. Wong, L.T., Chow, W.K., *Solar radiation model.* Applied Energy, 2001. **69**(3): p. 191-224.
[128]. Oliveira, A.P., Escobedo, J.F., Machado, A.J., Soares, J., *Correlation models of diffuse solar-radiation applied to the city of São Paulo, Brazil.* Applied Energy, 2002. **71**(1): p. 59-73.
[129]. Sabziparvar, A.A., Shetaee, H., *Estimation of global solar radiation in arid and semi-arid climates of East and West Iran.* Energy, 2007. **32**(5): p. 649-655.
[130]. Sabziparvar, A.A., *A simple formula for estimating global solar radiation in central arid deserts of Iran.* Renewable Energy, 2008. **33**(5): p. 1002-1010.
[131]. Fadare, D.A., *Modelling of solar energy potential in Nigeria using an artificial neural network model.* Applied Energy, 2009. **86**(9): p. 1410-1422.
[132]. Alfa, B., Jiya J. D., Sambo A. S. and Asere A. A., *Prediction of hourly solar radiation using neural networks.* Nigerian Journal of Renewable Energy, 2001. **9**: p. 42 - 46.
[133]. Jiya, J.D., Alfa, B., *Parametirization of solar radiation using neural network* Nigerian Journal of Renewable Energy, 2002. **10**: p. 6 - 10.
[134]. Khatib, T., Mohamed, A., Mahmoud, M., Sopia, K., *Modeling of daily solar energy on a horizontal surface for five main sites in Malaysis.* International Journal of Green Energy, 2011. **8**: p. 795 - 819.
[135]. Tiwari, G.N., *Solar Energy Fundamentals, Design, Modelling and Applications*. 4th ed2011, Alpha Science International Ltd: Center for Energy Studies.
[136]. Goswami, D.Y., Jan, F.K., Frank, F., *Principle of solar Engineering* Second ed1999, George H. Bechanan Co. Philadelphia P.A., USA: Taylor and Francis.
[137]. Yadav, A.K., Chandel, S.S., *Tilt angle optimization to maximize incident solar radiation: A review.* Renewable and Sustainable Energy Reviews, 2013. **23**(0): p. 503-513.
[138]. Liu, B.Y.A., Jordan, R.C., *Daily insolation on surfaces tilted toward equator.* ASHRAE Journal, 1962. **3**: p. 53.
[139]. Klein, S.A., *Calculation of monthly average insolation on tilted surfaces.* Solar Energy, 1977. **19**: p. 325.
[140]. Nigerian Meteorological Agency, *Meteorological data*, 2011: Corporate office headquaters, Maitama Abuja.

[141]. Chawla, K.M., *A step by step guide to selecting the right solar simulator for your solar cell testing application*: Pet Photo emission Tech Inc.
[142]. ASTM E927-10, *Standard Specification for Solar simulation for Terrestrial Photovoltaic Testing*, 2010, ASTM International: West Conshohocken, PA.
[143]. IEC 60904 -9, *Photovoltaic devices: Solar Simulator Performance Requirements*, 2007.
[144]. Meng, Q., Wang, Y., Zhang, L., *Irradiance characteristics and optimization design of a large-scale solar simulator.* Solar Energy, 2011. **85**(9): p. 1758-1767.
[145]. Grandi, G., Bardhi, M., *Effective low -cost hybrid LED - Halogen solar simulator.* IEEE Transactions on Industry Applications, 2014. **50**.
[146]. Grandi, G., Ienina, A., Bardhi, M., *Effective Low-Cost Hybrid LED-Halogen Solar Simulator.* Ieee Transactions on Industry Applications, 2014. **50**(5): p. 3055-3064.
[147]. Petrasch, J., Coray, P., Meier, A., Brack, M., Haberling, P., Wuillemin, D., Steinfeld, A., *A novel 50 kW 11,000 suns high - flux solar simulator based on an array of xenon lamps.* Journal of Solar Energy Engineering, 2007. **129**(4): p. 405 - 411.
[148]. Sarwar, J., Georgakis, G., LaChance, R., Ozalp, N., *Description and characterization of an adjustable flux solar simulator for solar thermal, thermochemical and photovoltaic applications.* Solar Energy, 2014. **100**(0): p. 179-194.
[149]. Codd, D.S., Carlson, A., Rees, J., Slocum, A.H., *A low cost high flux solar simulator.* Solar Energy, 2010. **84**(12): p. 2202-2212.
[150]. Dong, X., Ashman, P.J., Nathan, G.J. *A high - flux solar simulator system for investigating the influence of concentrated solar radiation on turbulent reacting flows*. in *Annual Conference, Australian Solar Energy Society*. 2012. Melbourne: Austrial Solar Council.
[151]. Li, Z., Tang, D., Du, J., Li, T., *Study on the radiation flux and temperature distributions of the concentrator–receiver system in a solar dish/Stirling power facility.* Applied Thermal Engineering, 2011. **31**(10): p. 1780-1789.
[152]. Kuhn, P., Hunt, A., *A new solar simulator to study high temperature solid-state reactions with highly concentrated radiation.* Solar Energy Materials, 1991. **24**(1–4): p. 742-750.
[153]. Krueger, K.R., Wojciech, L., Jane, H.D., *Operational performance of the university of Minnesota 45kWe high- flux solar simulator*, in *6th International Conference on Energy Sustainability and 10th Fuel cell Science, Engineering and Technology Conference*2012, ASME: San Diego CA.
[154]. Wang, W., Aichmayer, L., Laumert, B., Fransson, T., *Design and validation of a low-cost high-flux solar simulator using Fresnel lens concentrators.* Proceedings of the Solarpaces 2013 International Conference, 2014. **49**: p. 2221-2230.
[155]. Li, J., Gonzalez-Aguilar, J., Pérez-Rábago, C., Zeaiter, H., Romero, M., *Optical Analysis of a Hexagonal 42kWe High-flux Solar Simulator.* Energy Procedia, 2014. **57**(0): p. 590-596.
[156]. Hirsch, D., Zedtwitz, P.V., Osinga, T., Kinmore, J., Steinfeld, A., *A new 75 kW high - flux solar simulator for high - temperature thermal and thermochemical research.* Journal of Solar Energy Engineering, 2003. **125**: p. 117 - 120.
[157]. Stuckelberger, M., Perruche, B., Bonnet-Eymard, M., Riesen, Y., Despeisse, M., Haug, F.-J., Ballif, C., *Class AAA LED-Based Solar Simulator for Steady-State Measurements and Light Soaking.* Ieee Journal of Photovoltaics, 2014. **4**(5): p. 1282-1287.
[158]. Dennis, T., Schlager, J.B., Bertness, K.A., *A Novel Solar Simulator Based on a Supercontinuum Laser for Solar Cell Device and Materials Characterization.* Ieee Journal of Photovoltaics, 2014. **4**(4): p. 1119-1127.
[159]. Chaves, J., *Introduction to Nonimaging Optics*2008, USA: CRC Press Taylor and Francis Group

[160]. Eames, P.C., Smyth, M., Norton, B., *The experimental validation of a comprehensive unified model for optics and heat transfer in line-axis solar energy systems.* Solar Energy, 2001. **71**(2): p. 121-133.
[161]. Mallick, T.K., *Optics and Heat Transfer for Asymmetric Compound Parabolic Photovoltaic Concentrators for Building Integrated Photovoltaics* in *Faculty of Engineering*2003, University of Ulster.
[162]. Saleh Ali, I.M., O'Donovan, T.S., Reddy, K.S., Mallick, T.K., *An optical analysis of a static 3-D solar concentrator.* Solar Energy, 2013. **88**(0): p. 57-70.
[163]. Karthikeyan, H., Vaidyanthan, S., Sivaraman, B., *Thermal performance of a two -phase closed thermosyphon using aqueous solution.* International journal of Engineering Science and Techonolgy, 2010. **2**(5): p. 913 - 918.
[164]. Grooten, M.H.M., Vander Geld, O.W.M., *Effects of angle of inclination on the operation limiting heat flux of long R - 134a filled thermosyphons.* Journal of heat transfer, 2010. **132**(5).
[165]. Reay, D.A., Kew, P.A., McGlen, R.J., *Chapter 7 - Applications of the heat pipe*, in *Heat Pipes (Sixth Edition)*2014, Butterworth-Heinemann: Oxford. p. 175-206.
[166]. Joudi, K.A., Witwit, A.M., *Improvements of gravity assisted wickless heat pipes.* Energy Conversion and Management, 2000. **41**(18): p. 2041-2061.
[167]. Peterson, G.P., *An introduction to heat pipe, modelling, testing and Applications*1994, New York, USA: John Wiley and Sons Inc.
[168]. Vasilier, L.L., *Review heat pipe in modern heat exchangers.* Applied Thermal Engineering, 2005. **25**: p. 1 - 9.
[169]. Abreu, S.L., Colle, S., *An experimental study of two-phase closed thermosyphons for compact solar domestic hot-water systems.* Solar Energy, 2004. **76**(1–3): p. 141-145.
[170]. Pastukhov, V.G., Maidanik, Y.F., Vershinin, C.V., Korukov, M.A., *Miniature loop heat pipes for electronics cooling.* Applied Thermal Engineering, 2003. **23**(9): p. 1125-1135.
[171]. Vasiliev, L.L., *Micro and miniature heat pipes – Electronic component coolers.* Applied Thermal Engineering, 2008. **28**(4): p. 266-273.
[172]. ESDU 80013, *Heat pipes - General information on thier use, Operation and design*, 1980, ESDU: ESDU International Plc.
[173]. James, P.H., Thomas, F., *Advances in heat transfer*. Vol. 9. 1973, Academic Press.
[174]. Japikse, D., *Advances in thermosyphon technology, Advances in heat transfer*. Vol. 9. 1973.
[175]. Mochizuki, M., Nguyen, T., Sugihara, S., Mashiko, K., Saito, Y., Nguyen, T., Wuttijumnong, V., *Nuclear reactor must need heat pipe for cooling*, in *International heat pipe Symposium (IHPS)*2011: Taipei, Taiwan.
[176]. Nguyen - Chi, H., Groll, M., *Entrainment or Flooding limit in a closed two - phase thermosyphon* in *Advances in heat pipe technology: IV international heat pipe conference*1982, Pergamon Press, Oxford: London.
[177]. Elsayed, A.M., *Heat transfer in helically coiled small diameter tubes for miniture cooling*, in *Mechanical Engineering Department*2011, University of Birmingham, UK.
[178]. Alizadehdakhel, A., Rahimi, M., Alsairafi, A.A., *CFD modeling of flow and heat transfer in a thermosyphon.* International Communications in Heat and Mass Transfer, 2010. **37**(3): p. 312-318.
[179]. Tannehill, J., Anderson, D.A., Pletcher, R.H., *Computational Fluid Mechanics and Heat transfer*. 2nd ed1997, US: Taylor and Francis.
[180]. ANSYS FlUENT, *Theory guide; Multiphase flows*, in *Release 14.0*2011: Ansys Inc. p. 491 - 616.
[181]. Yang, Z., Peng, X.F., Ye, P., *Numerical and experimental investigation of two phase flow during boiling in a coiled tube.* International Journal of Heat and Mass Transfer, 2008. **51**(5–6): p. 1003-1016.

[182]. Cengel, Y.A., *Heat transfer: A Practical Approach*2003, McGraw - Hill Higher Education, New York: McGraw - Hill Higher Education.
[183]. Junusevicius, K., Streckiene, G., Miseviciute, V., *Simulation and Analysis of Small-Scale Solar Adsorption Cooling System for Cold Climate*

International Journal of Environmental Science and Development, 2015. **6**(1).
[184]. Siddiqui, M.U., Said, S.A.M., *A review of solar powered absorption systems.* Renewable and Sustainable Energy Reviews, 2015. **42**(0): p. 93-115.
[185]. Otanicar, T., Taylor, R.A., Phelan, P.E., *Prospects for solar cooling – An economic and environmental assessment.* Solar Energy, 2012. **86**(5): p. 1287-1299.
[186]. Pridasawas, W., *Solar - driven Refrigeration system with focus on Ejector Cycle*, in *Department of Energy Technology* 2006, Royal Institute of Technology, KTH.
[187]. Allouhi, A., Kousksou, T., Jamil, A., Bruel, P., Mourad, Y., Zeraouli, Y., *Solar driven cooling systems: An updated review.* Renewable and Sustainable Energy Reviews, 2015. **44**(0): p. 159-181.
[188]. Wang, R.Z., Ge, T.S., Chen, C.J., Ma, Q., Xiong, Z.Q., *Solar sorption cooling systems for residential applications: Options and guidelines.* International Journal of Refrigeration, 2009. **32**(4): p. 638-660.
[189]. Wang, R.Z., *Efficient adsorption refrigerators integrated with heat pipes.* Applied Thermal Engineering, 2008. **28**(4): p. 317-326.
[190]. Liu, Y.L., Wang, R.Z., Xia, Z.Z., *Experimental study on a continuous adsorption water chiller with novel design.* International Journal of Refrigeration, 2005. **28**(2): p. 218-230.